

Stereological Estimation of Anisotropic Microstructural Features

**Applying an Oriented Cylinder Model to Dual
Phase Steel**

**Stereological Estimation of Anisotropic
Microstructural Features**
**Applying an Oriented Cylinder Model to Dual
Phase Steel**

Proefschrift

ter verkrijging van de graad van doctor
aan de Technische Universiteit Delft,
op gezag van de Rector Magnificus prof. ir. K. C. A. M. Luyben,
voorzitter van het College voor Promoties,
in het openbaar te verdedigen op donderdag 12 december 2013 om 15:00 uur

door

Kimberly Sue MCGARRITY

Master of Science Michigan State University
geboren te St. Cloud, Minnesota, USA.

Dit proefschrift is goedgekeurd door de promotoren:

Prof. dr. ir. G. Jongbloed
Prof. dr. ir. J. Sietsma

Samenstelling promotiecommissie:

Rector Magnificus,	voorzitter
Prof. dr. ir. G. Jongbloed,	Technische Universiteit Delft, promotor
Prof. dr. ir. J. Sietsma,	Technische Universiteit Delft, promotor
Prof. dr. ir. L. A. I. Kestens	Universiteit Gent
Dr. ir. F. H. van der Meulen	Technische Universiteit Delft
Prof. dr. ir. A. H. van den Boogaard	Universiteit Twente
Dr. A. J. van Es	Universiteit van Amsterdam
Dr. P. J. J. Kok	Tata Steel RD&T
Prof. dr. B. de Pagter	Technische Universiteit Delft, reservelid



This research was carried out under project number M41.10.09330 in the framework of the Research Program of the Materials innovation institute (M2i) in the Netherlands (www.m2i.nl).

Keywords: Banded Steel; Stochastic modelling; Wicksell's Problem; Microstructures

Printed by: ...

Front & Back: Kimberly S. McGarrity

Copyright © 2013 by K. S. McGarrity

M2i PhD Series, Delft 2013-01

ISBN 978-94-91909-02-3

An electronic version of this dissertation is available at
<http://repository.tudelft.nl/>.

Contents

1	Introduction	1
2	Quantifying 2D and 3D Microstructural Banding	7
2.1	Introduction	8
2.2	Background	9
2.2.1	Quantifying Microstructural Banding	9
2.2.2	3D Data Acquisition	12
2.3	Experimental Procedure	13
2.3.1	Data Acquisition	13
2.3.2	Image processing	15
2.4	Results and Discussion	17
2.4.1	Threshold Banding	17
2.4.2	2D Banding Parameters	18
2.4.3	Initial 3D Microstructure Analysis	24
2.4.4	Band Connectivity	25
2.4.5	3D Banding Parameters	27
2.5	Conclusion	30
3	Oriented Circular Cylinder Model and Non-parametric Estimators	33
3.1	Introduction	34
3.2	Cylinder Model	36
3.3	Non-parametric Estimation	40
3.4	Asymptotic distributions of the Plug-in Estimators	43
3.4.1	Asymptotic distributions for the estimators of $N(t)$ and $F(t)$	44
3.4.2	Asymptotic distribution for the estimator of the covariance	46
3.4.3	Estimating the Expectations	48
3.4.4	Estimating ξ_g^j	51
3.4.5	Asymptotic distribution for the estimator of the height distribution	54
3.5	Asymptotic distributions of the Isotonic Estimators	54

3.6	Discussion	62
3.7	Conclusion	64
4	Model Validation and Application to Dual Phase Steel	65
4.1	Introduction	66
4.2	Physical Simulation	66
4.3	Numerical Simulation	75
4.4	Applying the Model to Microstructures	85
4.4.1	Expectations and Covariance	86
4.4.2	Isotonic Estimation	91
4.5	Conclusion	94
5	Kernel Smoothed Estimation of the Distribution and Density Functions	95
5.1	Introduction	96
5.2	Kernel Estimators for $N(t)$	97
5.3	Kernel density estimators	103
5.4	Application to numerical simulation and steel microstructures	105
5.5	Conclusion	115
6	Sensitivity to Deviations of Model Assumptions	117
6.1	Introduction	118
6.2	Cut Plane Angle	118
6.3	Deviation from Ideal Cylinders	125
6.3.1	Determining Bounding Rectangle	127
6.3.2	Normalized Symmetric Difference Volume (NSDV)	130
6.3.3	Correlating NSDV and Estimation Results	131
6.4	Conclusion	137
A	Appendix	139
A.1	CLT for Infinite Variance Random Variables	139
A.2	Proof of some Lemmas and statements	140
A.2.1	Proof of Equation (3.4.4)	140
A.2.2	Proof of Lemma 3.4.1	141
A.2.3	Proof of Relation (3.4.22)	143
A.2.4	Relationships for the quantities of interest	143
A.3	Estimation of the heights distribution	145

B Appendix	147
B.1 Calculation of CDFs, Moments and Isotonic Estimators	147
B.1.1 General Calculations	147
B.1.2 Numerical Simulation	150
B.1.3 Physical Simulation	157
C Appendix	159
C.1 Proof of equation (5.2.6)	159
C.2 Convergence conditions for the proofs of Lemmas 5.2.1 and 5.3.1	160
C.3 Proof of equation (5.2.9) for Volume	162
C.4 Calculation of asymptotically MSE optimal bandwidth	163
C.5 Proof of equation (5.2.10)	163
C.6 Proof of equation (5.3.4) for Volume	165
Summary	167
Samenvatting	169
References	171
Curriculum Vitæ	179
List of Publications	181

List of Symbols, Assumptions, Lemmas, Theorems and Corollaries

\xrightarrow{P}	Convergence in probability
\rightsquigarrow	Convergence in distribution
A_b	Area fraction of the banded phase within the banded region
<i>a.s.</i>	Almost surely
B_n	Band number of the n^{th} band
$C_b^{2D(3D)}$	Band Continuity Index in two and three dimensions
$C_p^{2D(3D)}$	Band Perpendicular Continuity Index in two and three dimensions
$C(B_n)$	Center position of band B_n
CDF	Cumulative Distribution Function
$E_k[Y]$	Expectation of random variable Y under density k
$F_T(t) = 1 - N(t)/N(0)$	CDF for the quantity of interest t
$f(x, h)$	Joint pdf of X and H (unobservable)
$g(z, h)$	Joint pdf of Z and H (observable)
\mathbb{G}	Empirical distribution function
H	Random variable: Height of cylinder or rectangle
<i>i.i.d</i>	identical independently distributed
$\overline{K}(v) = \int_{u=0}^{\infty} u^{-\frac{1}{2}} K(u+v) du$	Alternative Kernel function definition [1]
$\overline{K}'(v) = \frac{\partial}{\partial v} \overline{K}(v)$	Derivative of $\overline{K}(v)$

$\lambda_C(B_n)$	Distance between centers of bands B_n and B_{n-1}
$m_F^{\pm} = E_f[X^{+1/2}]$	Expectation of the radius of the cylinder
$m_G^{\pm} = E_g[Z^{-1/2}]$	Expectation of one over rectangle half-width
pdf	Probability density function
\mathbb{R}	Real line
\mathcal{N}	Normal density function
N_{part}	Number of particles of banded phase that make up the band
$N_{q(h;t)}(t) = N(t)$	Integral in the numerator for $F_T(t)$
$N_n(t) = \frac{1}{n} \sum_{i=1}^n [Z_i - q(H_i, t)]^{-\frac{1}{2}} 1_{[Z_i > q(H_i; t)]}$	Plug-in estimator of $N(t)$
$\tilde{N}_n(t) = U_n^{*,r}(t)$	Isotonic estimator of $N(t)$
$\tilde{N}_n(t) = \frac{1}{b_n} \int_{s=-\infty}^{\infty} N_n(s) K\left(\frac{t-s}{b_n}\right) ds$	Kernel smoothed
$= \frac{1}{b_n n} \sum_{i=1}^n \bar{K}(v)$	estimator of $N(t)$
$\tilde{v}_n(t) = \frac{\partial}{\partial t} \tilde{N}_n(t)$	Kernel smoothed
$= \frac{1}{b_n^2} \int_{s=-\infty}^{\infty} N_n(s) K'\left(\frac{t-s}{b_n}\right) ds$	estimator for
$= \frac{1}{b_n^2 n} \sum_{i=1}^n \bar{K}'(v)$	the pdf
ND	Normal Direction
NSDV	Normalized Symmetric Difference Volume
$p(h; u)$	Quantities of interest ($= t$):
	$\frac{u}{\sqrt{u}/h}$ squared radius
	$2\pi(u + \sqrt{uh})$ aspect ratio
	πhu surface area
$\dot{p}(h; u)$	Derivative of $p(h; u)$ with respect to u
	$\frac{t}{(ht)^2}$ squared radius
$q(h; t)$	Inverse of $p(h; u)$ ($= u$):
	$\left[\sqrt{\frac{h^2}{4} + \frac{t}{2\pi}} - \frac{h}{2} \right]^2$ aspect ratio
	$\frac{t}{\pi h}$ surface area
$\dot{q}(h; t)$	Derivative of $q(h; t)$ with respect to t
RD	Rolling Direction
$\sigma_{\sqrt{X}, H}$	Covariance of \sqrt{X} and H
$\tau_q(z)$	Integral: $\int_{h=0}^{\infty} g(z + q(h; t), h) dh$
TD	Transverse Direction
$U_n(t)$	Integral: $\int_{u=0}^t N_n(t) dt$ for Isotonic Estimator
$U_n^*(t)$	Concave majorant of $U_n(t)$
$U_n^{*,r}$	Right hand derivative at t of $U_n^*(t) = \tilde{N}_n(t)$

V_b	Volume fraction of the banded phase within the banded region
$W(B_n)$	Width of band B_n
X	Random variable: Squared radius of cylinder
ξ_g^j	Integral: $\int_{h=0}^{\infty} h^j g(0, h) dh$
Z	Random Variable: Squared half-width of observed rectangle

Assumptions

- Assumption 3.4.1 requires that the expectation of the squared half-width of the observed rectangles is finite. This implies that the squared radius of the unobservable cylinders is also finite.
- Assumption 3.4.2 requires that all moments, at least up to the fifth moment, of the observed rectangle height are finite.
- Assumption 3.4.3 requires that the expectation of the observed rectangle height divided by the rectangle half-width is finite.
- Assumption 3.4.4 requires that the derivative of τ_q is continuous and uniformly bounded (finite) to the right of zero.
- Assumption 3.4.5 requires that the quantities ξ_g^j are finite.
- Assumption 3.4.6 requires that the derivative of the joint probability density g of the observed rectangle height and squared half-width is finite.
- Assumption 3.4.7 requires that the first and second moments of $Z^{1/2}H^j$ be finite, where $j = (0, 1)$.
- Assumption 3.5.1 requires that the integral of $N(t)$ be finite, which leads to the expectation of the function $U_n(t)$ being finite.
- Assumption 5.2.1 requires that at least up to the second derivative of the function $N(t)$ exists and is finite.
- Assumption 5.2.2 requires that the joint distribution function $g(z, h)$ be bounded and uniformly continuous with a bound on its derivative.
- Assumption 5.3.1 requires that at least up to the second derivative of the function $\nu(t)$ exists and is finite.

Lemmas

- Lemma 3.4.1 states that the estimator of the random vector T_n follows the central limit theorem with a rate of convergence of δ_n and an asymptotic variance of Ξ .
- Lemma 3.5.1 states that under Assumption 3.5.1, the isotonic estimator of $N(t)$ converges almost surely to $N(t)$ when the number of observations is large enough for all quantities of interest, $q(h; t)$.
- Lemma 5.2.1 states that under Assumptions 5.2.1 and 5.2.2, and for a kernel bandwidth b_n such that $0 < b_n \rightarrow 0$ as the number of observations $n \rightarrow \infty$, then the asymptotic variance for the Kernel Estimator of $N(t)$ is known for the squared radius and the volume.
- Lemma 5.3.1 states that under Assumptions 5.2.2 and 5.3.1, and for a kernel bandwidth b_n such that $0 < b_n \rightarrow 0$ as the number of observations $n \rightarrow \infty$, then the asymptotic variance for the Kernel Estimator of the derivative of $N(t)$ is known for the squared radius and volume.

Theorems

- Theorem 3.4.1 restates the Central Limit Theorem for random variables with infinite variances (Theorem A.1) in a formulation that is useful for the cylinder model developed in Chapter 3.
- Theorem A.1 (as given in Theorem 4 of Chapter 9 by Chow & Teicher) states that the estimators for the expectation of random variables with infinite variance, for which the conventional Central Limit Theorem does not hold, have a rate of convergence of $\sqrt{\ln(n)}/n$ and a finite asymptotic variance.
- Theorem 3.4.2 states that the empirical estimator for the function $N(t)$ follows the Central Limit Theorem given in Theorem 3.4.1 and has an asymptotic variance of $\tau_q(0)$ for all quantities of interest, $q(h; t)$.
- Theorem 3.4.3 states that the empirical estimator for the covariance between the cylinder radius and height follow the Central Limit Theorem given in Theorem 3.4.1 with the asymptotic variance ν^2 .
- Theorem 3.4.4 states that the estimator of the CDF of the cylinder heights follows the Central Limit Theorem given in 3.4.1 with the asymptotic variance ν^2 .

- Theorem 3.5.1 states that the isotonic estimator of $N(t)$ follows the Central Limit Theorem given in Theorem 3.4.1 with an asymptotic variance of $\frac{1}{2}\tau_q(0)$ for all quantities of interest, $q(h; t)$.
- Theorem 5.2.1 gives the asymptotic mean squared error for the Kernel Estimators of $N(t)$ for the squared radius and volume.
- Theorem 5.3.1 gives the asymptotic mean squared error for the Kernel Estimators of the derivative of $N(t)$ for the squared radius and volume.

Corollaries

- Corollary 3.4.1 follows from Theorem 3.4.2 and states that the empirical estimators for the CDF of all quantities of interest, $q(h; t)$, follow the Central Limit Theorem given in Theorem 3.4.1 with the stated asymptotic variance.
- Corollary 3.4.2 follows from Theorem 3.4.3 and states that the empirical estimators for the expectations give in in eq. (3.4.12) follows the Central Limit Theorem given in Theorem 3.4.1 with the asymptotic variances listed in eq. (3.4.13).
- Corollary 3.5.1 follows from Theorem 3.5.1 and states that the isotonic estimators for the CDF of all quantities of interest, $q(h; t)$, follow from the Central Limit Theorem given in Theorem 3.4.1 with the stated asymptotic variance, which is half of that for the empirical estimators.

Introduction

The basic recipe for making steel is to extract liquid metal from iron ore or scrap, allow it to cool and roll it out to a usable size before it has reached room temperature. There are many adaptations to this recipe that create the myriad of steel varieties used in everything from sinks to cars to bridges to hip joints. Often, besides iron and carbon, other types of atoms, both metallic and non-metallic, are added to the alloy. The material can be heated and cooled multiple times, at different temperatures, and/or for different lengths of time, and/or applying different heating and cooling rates, to achieve various results. Also, the application of plastic deformation can significantly change the properties. Each of these adaptations in each of their possible combinations has an effect on mechanical and other properties, such as strength, ductility, brittleness, resistance to corrosion or cracking, electrical resistivity and magnetic behavior. To understand these effects requires understanding the material down to the microstructural and even atomic level.

Atoms interact with each other in many different ways. The types of atoms and their relative proportions, as well as the heat and rolling treatment, have a strong impact on the way in which the atoms arrange themselves in space. Each crystal structure of atoms is called a phase. Many materials, like the ones presented in this thesis, contain more than one phase. A grouping of atoms makes up the basic unit of a material, called a crystal or grain. The phase, size, shape, distribution and orientation of the grains within a material is what distinguishes it from any other material. The arrangement of the grains and phases with respect to one another defines the microstructure. When

the mechanical properties of steel are discussed, they are often linked to the microstructure.

While the microstructure of a material is the arrangement of grains and phases in a three dimensional (3D) space, the typical procedure to study materials is to observe them in two dimensions (2D). To do this, usually a small sample from inside material is removed and the exposed surface is examined under a microscope. For many materials, this is reasonable because the grains of the microstructure are isotropic, *i.e.* roughly the same size and shape, which is often approximately spherical. The grains are uniformly distributed throughout the material and the atomic lattice orientation of a grain, relative to its neighboring grains, is considered random. For these types of microstructures it can be assumed that any sample taken from any place within the material is representative of the entire microstructure. Therefore, observing the surface of a sample in one place is the same as observing any other exposed surface from any other place within the material, and the 2D picture provides useful information about the properties of the material.

However, not all microstructures are isotropic and random. An example of such a microstructure, and one that is currently of interest to industry, is a banded microstructure (see, for example Figure 2.3.1). Microstructural bands form when grains of the same phase agglomerate inside the material. Usually, this phase is referred to as the banded phase and the other phase is the background or matrix phase. When seen in 2D it often appears that the phases have formed layers, but it is more likely that the banded phase has taken on a large irregular shape, something more like plates or cigars, inside the matrix phase [2, 3]. This is not usually visible from a single 2D image of the material, and viewing at a single location does not guarantee a representative view of the microstructure. For these kinds of materials, knowledge of the entire 3D microstructure is important.

There are several methods available to observe materials in 3D, but they tend to be costly. Possibly the most accessible means of observing a microstructure in 3D is through serial sectioning [4–11]. Basically, this method is performed by polishing a sample surface and observing it with a camera under an optical microscope (though electrons and X-rays can also be used). Subsequently, a layer of material, of a controlled thickness, is removed and the surface is again polished and observed. This continues until the observer has determined that a sufficient depth has been reached. Usually this means that at least one of the features of interest has been seen in its entirety. This technique, while relatively inexpensive monetarily, requires significant amounts of time and destroys the sample. Serial sectioning is also limited in utility by the size of the microstructural feature of interest. If a feature of interest is too

small, it may not be possible to remove a small enough layer of the material to observe the feature with conventional sectioning techniques. If the feature of interest is too large compared to the necessary resolution of the imaging technique and layer removal depth, it will require too much time to obtain.

For the smaller features, other techniques can be used. Focused Ion Beam (FIB) etching can remove sub-micron layers from the material, X-rays have sub-micron resolution, and electron and atom probe microscope techniques can have nearly atomic resolutions. Like serial sectioning, FIB and atom probe microscopy require significant amounts of time to remove the layers and the material is destroyed during observation [7, 10, 12, 13]. In contrast, 3D X-ray techniques are non-destructive and can be used to observe both small and large microstructural objects [14–16]. They can even be used to observe the evolution of the microstructure *in situ*, something not possible with serial sectioning. However, the monetary cost of X-rays is exorbitant. Often powerful enough X-rays can only be created at a synchrotron, and obtaining access to one of those laboratories is difficult.

Modeling and simulation is a way to infer microstructural features of interest in 3D without destroying the material or requiring large amounts of money [10, 16]. Simulations often take in empirical information gathered directly from experimental observations and use well established physical mathematical models to evolve the microstructure in time and space. This allows for observation of the microstructure evolution due to processing or the external environment. Another advantage of simulations is that they can be performed at multiple length scales. It is possible to observe the behavior of the microstructure at the atomic level, tracking the movement of each atom as the environment changes. It is also possible to look at the microstructure on a larger scale, observing the evolution of the grains and phases. However, there are two major limitations to models and simulations. The first comes from the physical mathematical models. Sometimes the underlying formulas are too complicated to use in their full form, and so approximations are made. These approximations only hold under certain circumstances, and so it is imperative that the assumptions are carefully met. Also, many models only account for one type of phenomenon occurring at a time. While this is often sufficient for practical purposes, it can become difficult to simulate several phenomena occurring at the same time. Sometimes, the mechanisms driving the microstructural evolution are not even known, and so the physical modeling breaks down and cannot produce the desired microstructural features being studied. The second limitation is that the absolute size of the simulation is restricted by the computer on which it is performed. A detailed simulation on a small length scale can only be observed in a small volume, meaning that only a tiny portion

of the microstructure can be simulated at one time. Large length scales allow for larger observable volumes, but often important details cannot be captured because they occur on length scales too small to be included. The cost associated with running large and detailed enough simulations is computer run time, often weeks to months.

To circumvent the necessity of such costly techniques, the discipline of stereology was developed [5]. Stereology is concerned with estimating 3D information from 2D observations. It is impossible to look at a single 2D picture and correctly reconstruct the full 3D object. However, it is possible, with only a few reasonable assumptions, usually about the shape and spatial distribution of the objects being considered, to estimate the general content of the microstructure. The 2D observations are simply portions of the 3D object observed when the 3D object has been intersected, usually by a plane. Given the assumptions, there are well established relationships between the 2D observed objects and the 3D objects they could have come from. These inverse relationships do not provide a unique one-to-one mapping from the 2D observations to their corresponding 3D object, but rather a distribution of possible 3D objects, which is why it is impossible to reconstruct the 3D from a single 2D observation.

When considering an isotropic and random microstructure, it is possible to estimate characteristics like the spatial distribution of the grains or objects of interest, the distribution and mean of the sizes and orientations of the grains or objects of interest, and the volume fraction of the phases or objects of interest. There are many different kinds of estimators that can be used for this [17–34]. A parametric estimator can be used if a known family of functions reasonably represents the distribution being estimated. This kind of estimator requires that the unknown function parameters are estimated from the data, where the parameters are related to the moments of the distribution. In practice, this means that often only the sample mean and perhaps the standard deviation of the 2D observations are need to estimate the unobservable 3D distribution. However, if such an assumption is not possible, non-parametric estimators can be used. These estimators tend to require more observations to achieve the same precision as their parametric counterparts, but they can capture the behavior of any underlying distribution while the parametric estimators cannot. When the isotropic and random assumption no longer holds, as in the case of microstructural banding, the basic stereological model must be modified.

The purpose of this thesis is to explore the 3D nature of banded microstructures and to introduce and validate a new stereological model that represents this and possibly other anisotropic non-random microstructural fea-

tures. Along with the model, non-parametric estimators, used to estimate the distributions and expectations of various quantities of interest related to the mechanical properties of the material, are studied. The accuracy and precision of these estimators are determined as a function of the number of observations available. The sensitivity of the model to objects that deviate from the necessary assumptions is also ascertained. Both the model and the estimators perform well for the banded microstructures, despite the small number of observations and the deviations of the bands from the ideal assumptions of the model.

Outline of Thesis

In Chapter 2, banded microstructures and the various techniques used to estimate the degree of banding in a material from a single 2D image are introduced. Two banded microstructures are studied in detail in both 2D and 3D. The latter comes from a set of serial sectioned optical micrographs. A new technique for quantifying the degree of banding in a 2D microstructural image is introduced and applied to several microstructures with a broad range of banding. Finally, this technique is extended to 3D, and from studying the two serial sectioned materials, the 2D results are shown to be reasonable estimates for what can be expected in 3D.

In Chapter 3, a stereological model using oriented cylinders intersected by a cut plane parallel to the cylinders' axes of symmetry is presented. From the rectangles observed on the cut plane, relationships between the rectangle dimensions, the half-width and height, and various quantities of interest of the cylinders, such as radius, height, surface area and volume, are established. The expectations of these quantities can be estimated from the empirical means of the rectangle dimensions. The distribution functions of these quantities can be estimated non-parametrically from the rectangle dimensions. The asymptotic behavior of these estimators is established in preparation for applying the model to the banded microstructures.

In Chapter 4, the model and estimation procedures are studied using two simulations. One simulation mimics the physical scenario of cylinders in an opaque medium and slicing the medium in a random location. The second simulation uses only the known mathematical relations between the 2D and 3D distributions to obtain the working data sets. For this simulation, a distribution for the radius and height of the cylinders is chosen and the corresponding distribution of the rectangle half-widths and heights is determined. Observations from both distributions are drawn and the model is applied. The asymptotic behavior of the estimators is explored and discussed. Finally, the

model is applied directly to the banded steel microstructures and the estimation results are assessed in light of the simulation results.

The natural outcome of the estimators introduced in Chapter 3 are the cumulative distribution functions (CDF). However, the derivative of this function, the probability density function (pdf) is often more useful in practice. Therefore, the focus of Chapter 5 is on obtaining an estimate of the pdf. This is accomplished with Kernel functions that smooth the plug-in estimators used for estimating the CDF and their derivatives for estimating the pdf. The asymptotic behavior of these estimators is explored with the numerical model and the estimators are applied to the steel microstructures.

In Chapter 6, the limitations of the oriented cylinder model are explored. The model requires that the objects observed are circular cylinders, that the cylinders are all oriented in the same direction and that the cut plane is exactly parallel to the axes of symmetry. Microstructural features can deviate significantly from perfect geometric shapes and there is no guarantee that the cut plane is exactly parallel to the axes of symmetry. Therefore, the physical simulation is employed to explore the reliability of the estimation results when the cut plane intersects the box of cylinders at an angle. A different physical simulation is used to explore the sensitivity of the model when the observed objects deviate from the perfect geometric shape.

Quantifying 2D and 3D Microstructural Banding

Two dual phase steels with markedly different microstructural banding were serial sectioned using optical microscopy for characterization and quantification of microstructural banding in both two and three dimensions (2D and 3D). Two parameters, bounded on a scale of zero to one, are defined: Band Continuity Index $C_b^{2D(3D)}$ and Perpendicular Continuity Index $C_p^{2D(3D)}$. The first parameter quantitatively describes the continuity of the microstructural phase of interest within the band and the second describes the distribution of the bands within the material. For both parameters, a value of zero indicates no banding and value of one indicates strong banding. While the results show that the connectivity of the bands in 3D is different from what is observed in 2D, the quantification of banding with these parameters in 2D provide useful information about the behavior of the banding in 3D.

2.1 Introduction

Microstructural banding is an important phenomenon in steel manufacturing. Bands in a material can cause the mechanical properties to be anisotropic [2]. Anisotropy can be useful in certain applications where strength is desired in one direction and flexibility in the other. On the other hand, it can cause serious problems such as having high susceptibility to cracking and corrosion due to the long interphase grain boundaries. Banded material is also difficult to machine. Much work has been done to understand the mechanisms of formation of the banded structure [3, 35–42] and how the mechanical properties are affected by the presence of banding [2, 38, 41–51], and others have studied means of preventing or manipulating the banding to control the mechanical properties [3, 39, 40, 52, 53]. It is important to be able to quantify the banding in order to control it. However, quantifying the amount of banding in a microstructure is non-trivial, and has been undertaken by few researchers over the years [46, 47, 54–57]. These methods, while assigning values to specific quantities, often do not provide an intuitive meaning for those values. Rather, the values are not bounded and so the results are best understood when the quantities of interest are compared between two or more structures.

Until now banding has only been studied and quantified using 2D images under the assumption that the observations extend to 3D without actual validation [46, 47, 54, 55, 57]. While it is well known that for random structures this assumption holds [58, 59], it has not yet been demonstrated for materials with high degrees of correlation and anisotropy, such as banded materials. One of the aims of this work is to carefully analyze the banding behavior of two distinctly different microstructures, using serial sectioning to obtain 3D information about the microstructure.

The aim of this chapter is to provide a set of parameters that combine the ideas behind some of the existing methods explored in Section 2.2 in a new way. Two parameters are presented that are bounded on the interval $[0,1]$, and are calculated from standard material values. This provides a means of quantifying the amount of banding in any single structure in a meaningful way, without the need for comparison. The first parameter is called the Band Continuity Index $C_b^{2D(3D)}$ and it describes the strength of banding along the direction of the bands. It is calculated for each band, and the average over the bands is taken to represent the structure as a whole. The second parameter is called the Perpendicular Continuity Index $C_p^{2D(3D)}$ and it describes the strength of banding with respect to the distribution of the bands throughout the material. The bounds on these parameters have intuitive and succinct meanings: as they approach zero the structure is not banded, and as they approach one

the structure is strongly banded (each parameter provides a portion of the definition of “strongly banded” as will be discussed in the sequel). In this work both parameters are defined in 2D and 3D. Comparing these parameters shows that, indeed, the description of banding in 2D is a reasonable representation of the banding in 3D.

2.2 Background

2.2.1 Quantifying Microstructural Banding

Since banding is a sort of anisotropy in the distribution of phases within a microstructure, there are several means of extracting the information with respect to orientation. Komenda and Sandström wrote a survey of some of these different methods [46]. The first method mentioned was originally proposed by Saltykov [17] in 1958 and was adapted by the ASTM for use as a standard for quantifying banding in microstructures [55]. The proposed method uses test lines in the directions both parallel and perpendicular to the bands or oriented grains. The number of intersections per test line length in each direction is counted and the user obtains N_{\perp} and N_{\parallel} . From these two quantities several values are computed: the average center-to-center distance between bands \bar{N}_{\perp}^{-1} , the mean free path spacing $(1 - f_V)/N_{\perp}$ where f_V is the volume fraction, and the anisotropy index N_{\perp}/N_{\parallel} . These values give a qualitative measure of the amount of banding or anisotropy in the material limited by the dependence on magnification, etching, image quality and image processing. These values take on meaning only when compared to other structures under the same measurement conditions. Another quantity calculated from N_{\perp} and N_{\parallel} is called the anisotropy coefficient Ω_{12} , which gives a quantitative measure of the anisotropy of the material with a value of zero being completely isotropic and a value of one being completely oriented. However, this quantity, as stated in the ASTM standard, cannot distinguish between a banded and an oriented structure. Therefore, none of these quantities can be used to definitively describe the amount of banding in a microstructure¹.

Along similar lines, another method referred to in the survey uses the chord distribution of ferrite grains (assuming the grains are spherical) both parallel and perpendicular to the direction of banding. In banded ferrite-pearlite structures, two distributions arise along the direction of banding. When the absolute frequency of the chord lengths is plotted, these two distributions are distinguished by two different slopes. The larger slope comes from the small ferrite regions within the pearlite bands and the smaller slope comes from the

¹Stated in the ASTM standard E1268 [55] in section 13. Precision and Bias

ferrite grains between the bands. In the perpendicular direction only one distribution is found. The ratio of the transverse slope to the smaller slope from the parallel direction is proposed as a means of quantifying the orientation of the microstructure. No means of interpreting or bounding this ratio is given in the survey.

A third method calculates the degree of clustering and the geometry of clustering. For a homogeneous dual phased material, the spatial distribution of particles is assumed to be random and uniform, *i.e.* from a Poisson process. This gives rise to a random particle size and position. Given the particle density for each of the two phases, the theoretical nearest neighbor distance between two particles of the same phase can be calculated. For a banded structure, the nearest neighbor distance will deviate from the theoretical distance because the distribution is no longer uniformly random. The degree of clustering is defined as $\overline{\Delta}diff = (\overline{\Delta}t - \overline{\Delta}m)/\overline{\Delta}m$, where $\overline{\Delta}t$ is the theoretical and $\overline{\Delta}m$ is the measured average nearest neighbor distance. In a random microstructure, the neighbor distance and the direction in which the neighbor is found are independent. For a banded microstructure this is not the case; there is a particular direction in which neighbors are found to be closer, called the dominant direction. The fraction of nearest neighbor distances that are found in the dominant direction describes the geometry of clustering, also considered the degree of orientation. Both the degree of clustering and the degree of orientation are presumably bounded on $[0,1]$, with zero meaning that the structure is isotropic and non-oriented, and one meaning the structure is strongly non-isotropic and highly oriented. However, it is not clear that this method, as with the anisotropy coefficient from the ASTM standard, can distinguish between a banded structure and an oriented structure.

A fourth method was developed using an automatic structure analyzer. The method is, very briefly, to divide the image into strips parallel to the bands. The volume fraction of the banded phase of each strip is calculated and the distribution of the volume fractions is determined. The average volume fraction of the distribution is calculated and each strip is compared to this average. If the volume fraction for any given strip is greater than the average then a band exists in the strip, otherwise it does not. To assess the degree of banding, the mean deviation of the strips from the average is divided by the number of times there is a change between positive and negative deviations from the average volume fraction. It is mentioned that a volume fraction change of less than 20% of the maximum difference is not counted as a change in volume fraction, so as to account for measurement errors. This method is sensitive to the size and number of strips into which the image is divided.

The method put forth by the authors of this survey [46, 47] is an extension

to the chord distribution method mentioned above. The authors also include the Feret diameter measurements for the various phases of the material in the direction of and transverse to the bands. The Feret diameter can be thought of as the average diameter of a particle if it were measured by a caliper in all possible directions. The ratio between the slopes of the absolute frequency of Feret or chord diameters measured in the parallel and perpendicular directions to the bands gives information about the anisotropy of the material. A ratio of 1.0 is considered isotropic while anything higher than 1.3 is considered anisotropic. This method gives a lower bound for the isotropy of the material, but there is no upper bound given and so the degree of anisotropy is not absolute.

Other authors [54] considered banding to be a sort of periodicity in the distribution of the phases of a microstructure and chose to use 2D Fourier analysis on the images. In that work the 2D Fourier transform of the raw image is considered with the 2D Fourier space containing frequency (ν) and direction (ϕ) information for each pixel. In the 2D Fourier space, three different distributions can be calculated. First, the Local Orientation Distribution Function is defined to be the number of neighbors with a certain orientation ϕ that surround a given pixel. As each pixel is considered in turn, the distribution of neighbor orientations gives a measure of the anisotropy of the material. Another distribution is the Orthogonal Frequency Distribution, which is the difference between Fourier spectra from two orthogonal directions in the image. If there is a periodicity in the difference, due to the presence of a periodic structure in one direction but not the other, it will show up as a peak or a trough in the distribution. The third distribution measured is the Directional Energy Distribution, or the square of the Fourier amplitude summed over all pixels of a given orientation. The dominant direction will yield a peak at that angle. This method is less sensitive to the image quality and does not require image processing, unlike the methods mentioned previously. However, this method only provides a relative scale for comparison of the degree of banding.

A more recent analysis [57] has made use of the covariance of an image to determine quantities like the center-to-center distances of the bands, which correlate to a wavelength, the intensity of the bands, which correlates to the area fraction of the band, and the shape of the bands. This method provides 3 parameters that can be extracted from the covariogram of an image and used to quantify the banding of a given structure. A more concrete scale for comparison arises in this work, but the values still do not provide a means of stand-alone evaluation for a single structure.

2.2.2 3D Data Acquisition

There are a variety of means available to observe the surface of prepared materials. Optical microscopy, electron microscopy (SEM, TEM, STEM, etc.), diffraction (XRD, EBSD, etc.) and Energy Dispersive Spectroscopy all provide various types of information about a material at various resolutions. Microscopy provides spatial information about the microstructure. Often, the grain boundaries and solute particles are directly observable with the proper etching agent. Diffraction can provide information on the crystallographic orientations and the textures of the microstructures. When these two methods are used in conjunction, much of the microstructure is sufficiently characterized. However, most of this information is limited to the observable 2D surface. Through stereology, some information observed from the image can be extrapolated into 3D [4, 5, 59]. Much of this information is limited to averages; individual details are often not extractable. For example, it is not possible to obtain information about the connectivity, contiguity or real particle shape and size in the depth of the material by only observing a 2D image [6–8, 60]. Obtaining full three dimensional information about a material is important for a full understanding of the mechanical properties of the material [6–8, 60, 61].

There are currently two ways to experimentally obtain the 3D information: serial sectioning combined with one of the above microscopy methods [4–11] and X-ray tomography and diffraction [5, 15, 16]. Serial sectioning is perhaps the oldest technique and has the advantage of being relatively simple since it can be accomplished with polishing equipment and an optical or electron microscope [6, 8–11, 60]. Multiple spatial resolutions can be obtained from microscopes in a single imaging step and orientation information can be obtained from EBSD. Often, the limiting factor with serial sectioning is the amount of material that can be removed with each polishing step. The removal depth must be a small fraction of the grain size in order to retain useful information about the microstructure and, even then, some information is lost [4, 60]. This procedure is time consuming since a large number of images is required to represent a sufficient depth into the material, and often the polishing, etching and imaging must be done in separate locations. This also leads to difficulties in aligning and registering the images [6, 7, 10, 11]. Automation of serial sectioning is of interest [6] and recently, focused ion beam (FIB) etching and Atomic Probe Microscopy and Tomography (APM and APT) have been used to remove significantly thinner layers for increased depth resolution. FIB allows automatic removal of a nearly atomic layer of the material while simultaneously imaging the microstructure with SEM or EBSD [7, 10]. APM and APT allow for 3D reconstruction at the atomic level, back calculating the position and type of atom based on the interaction of the ion with a detector

screen as it is striped from the material [12, 13]. The biggest draw-back of serial sectioning is that it is destructive and therefore, it cannot be used to observe temporal behavior of the microstructure [11, 15, 16].

In comparison, X-ray tomography and 3D X-ray diffraction (XRD) are nondestructive to the sample [14–16]. Powerful enough X-rays can penetrate hundreds of microns into the material with resolution down to the nanometer scale [16]. XRD can also obtain orientation information about the individual grains in the sample. Another advantage of XRD over serial sectioning is the ability to observe the *in situ* development of the microstructure during annealing or recrystallization [14, 15]. The drawback of this technique is the cost of creating X-rays; synchrotron sources are required for penetrating deep enough into the material and providing high enough resolution [15, 16].

Another means of obtaining 3D information is through simulation and modelling. Several simulation techniques, such as Finite Element Methods (FEM), Cellular Automata and Voronoi methods are used to create realistic microstructures. These structures are evolved by means of established physical models for describing the behavior of the microstructures under certain conditions. Currently, serial sectioned data or images taken from the three orthogonal planes of a material are used as input into simulations to obtain the most realistic microstructures possible [10, 16]. The distinct advantage of simulations is that they are extremely cost-effective. Using models and simulations allows for 3D observations of the microstructures during events such as grain nucleation and recrystallization that are not easily accessible with experiments due to equipment, time and/or resource constraints. Most models make assumptions, and often these assumptions are made to simplify the problem. However, the assumptions may not actually hold in the real microstructures, and as more 3D data is being obtained, the model assumptions need to be reconsidered [10, 14, 15, 60].

2.3 Experimental Procedure

2.3.1 Data Acquisition

In this work, two DP800 steels having the same chemical composition (Table 2.1) but different rolling conditions were serial sectioned for comparison. The two steels were chosen because of the stark visual differences in the banding of the microstructures, with Steel B appearing more banded than Steel A (see Figures 2.4.1c and 2.4.1d).

Initially, the samples were prepared in a manner typical for optical microscopy: polishing began with 320 grit wet sandpaper with subsequent processing to finer paper, finishing with 6 μm , 3 μm , and 1 μm polishing cloths

C	Si	Mn	Cr	P	Ac3	Ms
0.072	0.29	2.16	0.65	0.08	850	430

TABLE 2.1: Composition of the DP800 steels. The quantities given are in weight percent and degrees Celsius.

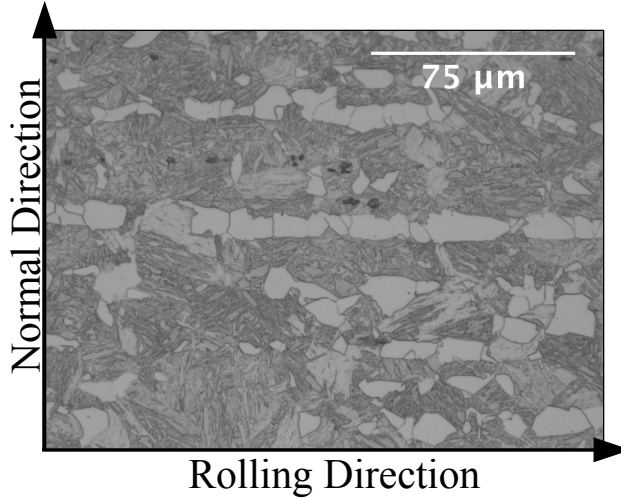


FIGURE 2.3.1: Original image for the ND-RD plane of Steel A.

and the corresponding diamond suspensions. This was followed by etching in 5% Nital, and the samples were examined using a Leica DM-LM microscope with a computer controlled PRIOR Scientific Instruments table. The images were captured with a Leica DFC420C camera, which was controlled by Leica QWin Pro V 3.5.1 (April 2008) software. Images of the planes perpendicular to the rolling (RD), transverse (TD), and normal (ND) directions were taken at 6 different magnifications: 500x, 200x, 100x, 50x, 25x and 12.5x. The analysis of this paper is presented for the plane perpendicular to the RD at the magnification of 500x (see Figure 2.3.1).

For each subsequent section, a layer was removed by polishing. The first 23 layers were removed with the 1 μm polishing cloth and diamond suspension. Each polishing step removed approximately 0.5 μm, as measured and aligned with Vicker's hardness indents just outside the desired field of view. However, this step size required more time than was available to section into the depth of interest, and so a larger step size was used for the second half of the sectioning. Beginning with step 24 both the 3 μm cloth/diamond suspension and the 1 μm cloth/diamond suspension were used. This led to approximately 3 μm

removal with each step.

Figure 2.3.1 shows an original image as taken from the microscope for Steel A. The phases in this microstructure are ferrite (light areas), martensite and retained austenite (dark areas). The images shown are of the plane whose normal is in the TD, which is also the direction along which the sectioning occurs. With Steel A and B, we are primarily interested in characterizing, comparing, and quantifying the banding of the ferrite phase in the microstructures. While the choice of the banded phase will provide different output values, any phase may be chosen to carry out this analysis as demonstrated with Figure 2.4.4, where pearlite and martensite bands are also analyzed.

2.3.2 Image processing

The first step in image analysis is image processing. Because the material under consideration is dual phase steel, reducing the optical micrograph to a binary image is a standard simplification. This initial image processing was performed using the freeware program Fiji [62] on the optical images. All section images (heretofore referred to as slices) were put into a TIFF image stack, which was registered and cropped so that the images were properly aligned and rotated. The remaining image processing steps were carried out on the entire stack. First, the image contrast was enhanced by equalizing and normalizing the grey-scale histogram. Next, the brightness/contrast for the image was adjusted by hand in order to accentuate the differences between the two phases. Finally, the image was thresholded to create a binary mask to separate the two phases. The banded (ferrite) phase was assigned the grey-scale value of 255 and is displayed in the images as black; the background (martensite) was assigned a grey-scale value of 0 and is displayed in the images as white, as is shown in Figure 2.3.2a. All subsequent image processing and data analysis

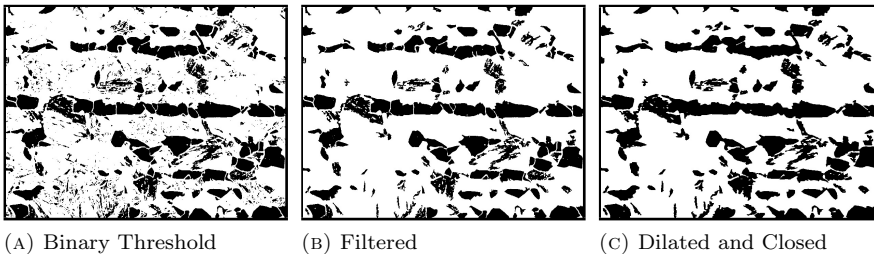


FIGURE 2.3.2: (a) Thresholded binary image of Steel A from Figure 2.3.1. (b) Filtered out grains of area 100 pixels (approximately $24 \mu\text{m}^2$) or smaller. (c) dilated and closed (horizontal line of length 3 pixels or $0.7 \mu\text{m}$). For all images, normal direction (ND) \uparrow , RD \rightarrow .

was carried out on these binary images. The grey-scale assignment was chosen for creating profiles of the images, as discussed below. It is important to note that most often the bands run horizontally across the image, in accordance with the ASTM standard [55]. However, it is possible for the bands to be vertical or at an angle through the image. A simple image rotation can bring the bands into the horizontal position where analysis becomes much simpler.

Since the aim of this work is to quantify the degree of banding of a chosen phase, the small grains of the banded phase (ferrite in the example of Steel A) that are intermixed in the matrix do not contribute to the bands, and so they are filtered out. A Matlab[®] routine was written to filter out grains smaller than a certain pixel size using a breadth first search algorithm. For the image in Figure 2.3.1 grains smaller than 100 pixels (or $24 \mu\text{m}^2$) were filtered out eliminating 1608 pixels out of 508,200. The outcome of filtering can be seen in Figure 2.3.2b.

The bands as a whole contribute most significantly to the overall mechanical properties of the material, and so the individual (ferrite) grains are of no interest in this analysis. Therefore, the images were morphologically processed to eliminate the intraphase grain boundaries so as to better represent the continuity of the bands. After filtering, the images were dilated in the RD using a horizontal line (since the grain boundaries are mostly vertical with respect to the image) with a length of 3 pixels (or $0.7 \mu\text{m}$). Then, the images were morphologically closed using the same structuring element. The results are shown in Figure 2.3.2c. This allows for the grains to merge while respecting the spacing between the bands in the vertical direction.

From the thresholded, filtered, dilated and closed images, a profile was created by taking the row average of the grey-scale values along the RD, which coincides with the banding direction. The peaks in these profiles highlight the regions where bands exist. Comparing Figures 2.3.3a and 2.3.3b it is evident that processing the images has very little effect on the profiles. The amplitudes, positions and widths of the peaks do not change significantly through the processing steps, and therefore, very little information is lost. This implies that the profiles may be used interchangeably without loss of generality, and eliminating the grain boundaries for the purpose of focusing on the bands is justifiable. Therefore, the following discussion will only consider the fully processed images.

2.4 Results and Discussion

2.4.1 Threshold Banding

Because any individual profile is quite rough, a spline fit was constructed using Matlab’s[®] spline fitting function and an automated fitting routine [63] (for comparison) to smooth out the curves. Figures 2.4.1a and 2.4.1b show the actual profile (x’s) and the spline smoothed fit (solid line) for Steel A and Steel B. Using a smooth profile is important for defining a band because the rougher the profile, the more likely it is for a band to be broken into tiny, disconnected bands. This does not accurately reflect the microstructure, and so the smoother spline curve is used instead to define the bands through thresholding.

To determine the (ferrite) bands a grey-scale threshold is chosen and any value that falls above the threshold is considered to be part of a stylized (ferrite) band (demarcated as the region between the dashed and solid line pairs in Figures 2.4.1c and 2.4.1d), and any value below is considered to be part of the (martensite) background. The threshold was chosen using a common iterative thresholding algorithm [64] in image processing, which is a special 1D version of the k-means clustering algorithm [65]. This algorithm can be performed with Matlab’s[®] built-in function “kmeans” in the statistics toolbox. The algorithm converges to a threshold value such that the sum of the grey-scale values that lie above the threshold is equal to the sum of the grey-scale values

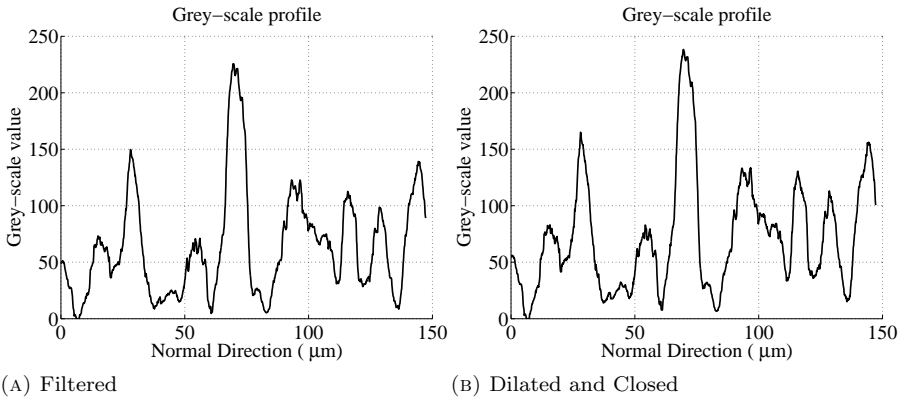


FIGURE 2.3.3: Grey-scale profiles (row averaged along the columns or in the RD) for the images in Figure 2.3.1. There is no significant difference between the profiles due to the processing steps. Between the filtered image (Figure 2.3.3a) and the dilated and closed image (Figure 2.3.3b) the peaks maintain their positions, widths and heights. Therefore, the fully processed images will be used throughout the rest of this paper.

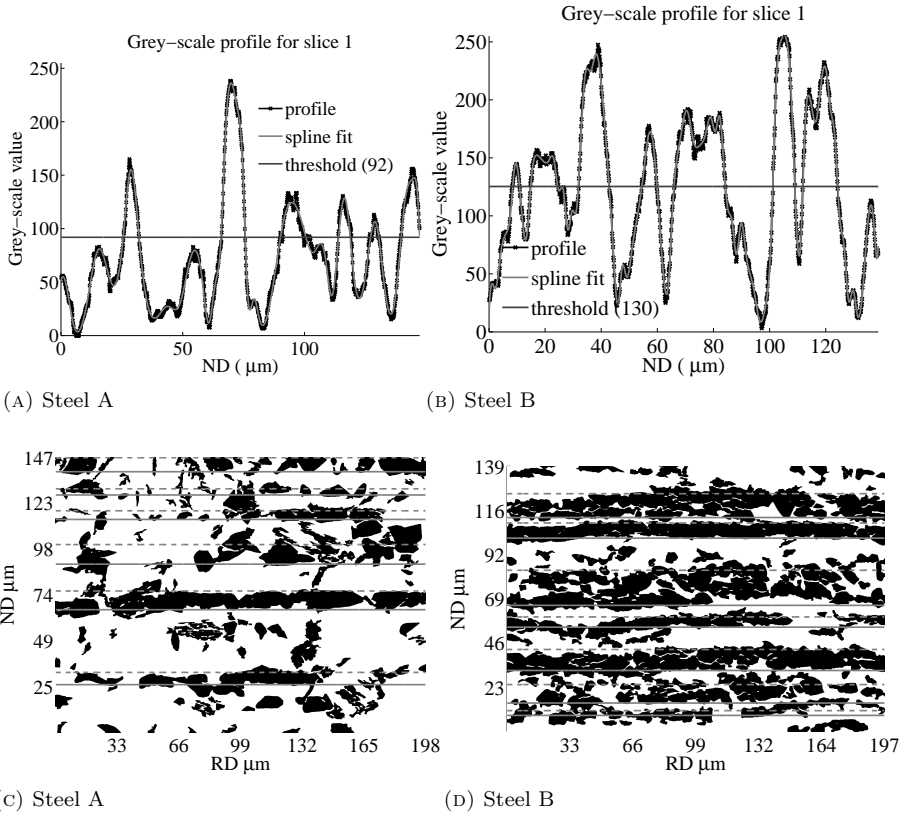


FIGURE 2.4.1: Binary thresholded banded structures for steel A (2.4.1c) and Steel B (2.4.1d) created from the profiles (2.4.1a and 2.4.1b, respectively). The solid and dashed like pairs mark the region defined to be the ferrite band.

that lie below the threshold. This allows the threshold to be determined without any *a priori* knowledge of the microstructure or the profiles. In creating these stylized bands, some of the (ferrite) grains are considered to be part of the background and not part of a band. Thus, even though ferrite, in this example, is considered the banded phase, not all of the ferrite contributes to the bands.

2.4.2 2D Banding Parameters

As mentioned in Section 2.2, there are a few methods for qualitatively describing the amount of anisotropy in microstructures. The ASTM standard

essentially counts the number of particles in the banding and perpendicular directions and takes a ratio of these values [55]. A more recent method quantifies banding by calculating the area fraction, wavelength and shape of the bands [57]. The drawback to some of these methods is that they are scale dependent, for other methods the drawback is an open-ended scale. In this chapter, these ideas are combined to introduce two parameters that are scale-free and absolute. These two parameters, which will be defined for 2D in this section, are: Band Continuity Index C_b^{2D} and Perpendicular Continuity Index C_p^{2D} . These parameters quantitatively describe the banding with respect to both the direction of and perpendicular to the bands. They are bounded on $[0,1]$, thus providing an absolute scale for quantification and characterization of the degree of banding for a chosen phase (ferrite in the current example) in a given microstructure.

The main idea behind the Continuity Indexes is to describe the connectedness of the banded phase. The mechanical properties appear to be dependent upon both the volume fraction [44, 45, 49] and the morphology of the banded phase [48, 50, 51]. Bands that are continuous propagate small cracks [48] along the band/matrix boundary and shear bands [51] through the band causing voids to nucleate [49, 51] due to decreased stress flow. Continuous bands also limit ductility in the direction perpendicular to the bands [42]. Bands that are less continuous, *i.e.* that are interrupted by grains of the other phase absorb the shear bands [51] and increase the ductility of the material overall [45, 49]. The Continuity Indexes directly link to these behaviors by quantifying the connectedness of the bands along the banding direction and the spacing of the bands with respect to the size of the bands and the interaction with the matrix.

Both C_b^{2D} and C_p^{2D} are defined for each band B_n , and the center position $C(B_n)$ of each band is used to uniquely identify the bands in the microstructure. The average C_b^{2D} and C_p^{2D} of all of the bands are used to represent the entire microstructure. With this in mind, the Band Continuity Index $C_b^{2D}(B_n)$ for band B_n is defined as

$$C_b^{2D}(B_n) = A_b(B_n)/N_{part}(B_n), \quad (2.4.1)$$

where $A_b(B_n)$ is the area fraction of the banded phase within the banded region (the dashed and solid line pairs in Figures 2.4.1c and 2.4.1d), and $N_{part}(B_n)$ is the number of particles of the banded phase that make up the band. A particle is defined to be an assembly of grains of the banded phase (ferrite in this case) that are separated only by their grain boundaries and not by the other phase (martensite in this example). The scale ranges from zero to one,

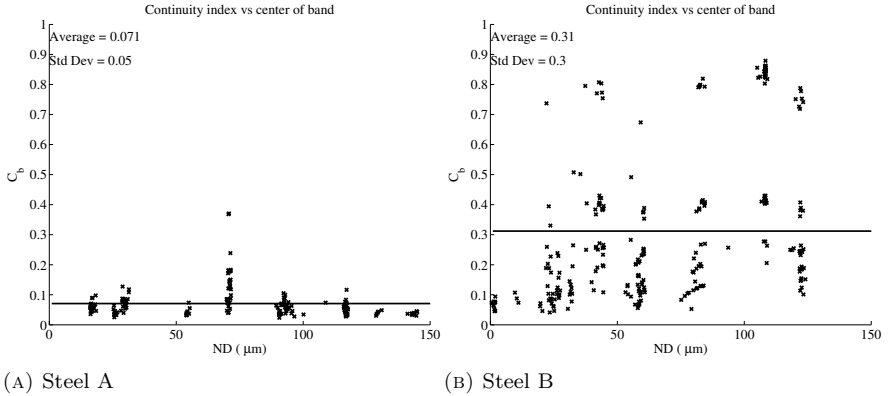


FIGURE 2.4.2: Ferrite band Continuity index C_b^{2D} (given by eq. 2.4.1) of each band B_n plotted against the center position along the ND $C(B_n)$.

with 1 indicating a strong band where $A_b(B_n) = 1$ and $N_{part}(B_n) = 1$, and 0 indicating a weak band with $A_b(B_n) \ll 1$ and/or $N_{part}(B_n) \gg 1$. It should be noted that any value of C_b^{2D} above 0.5 indicates that the band is unbroken, *i.e.* that $N_{part} = 1$, and, therefore, C_b^{2D} is exactly the area fraction of the banded phase in the region defined as the band.

From a simple visual inspection of the microstructures shown in Figures 2.4.1c and 2.4.1d, it is easy to qualitatively discuss the continuity of the bands. For Steel A, the band centered around $71 \mu\text{m}$ clearly has the highest ferrite band area fraction of around 0.7 and it is also seen to be the most continuous band composed of only two ferrite particles. In contrast, the band near $143 \mu\text{m}$ is rather broken with almost no connection between the grains. This band will have a significantly lower Band Continuity Index than the previous band. For Steel B, it is obvious that in general the Band Continuity Index should be higher than for Steel A. The band at $100 \mu\text{m}$ should have the highest Band Continuity Index of any of the bands since the region is almost fully filled by the single ferrite particle.

The qualitative assessment given above is confirmed quantitatively in Figure 2.4.2. The average value of C_b^{2D} for Steel A (see Figure 2.4.2a) is significantly smaller, almost three times less than that for Steel B (see Figure 2.4.2b). For Steel A, most of the bands have similar continuity, less than 0.1. For Steel B there is more spread. Steel B has two strongly connected bands, higher than 0.8. Even the strongest band in Steel A is only half that at 0.4. Overall, from the Band Continuity Index, Steel B is more banded than Steel A.

Turning now to the perpendicular direction, $C_p^{2D}(B_n)$ is defined for band B_n as

$$C_p^{2D}(B_n) = \frac{0.5A_b(B_n)W(B_n) + 0.5A_b(B_{n-1})W(B_{n-1})}{\lambda_C(B_n)}, \quad (2.4.2)$$

where $A_b(B_n)$ is the area fraction of each band as described previously, $W(B_n)$ is the width of the stylized bands in Figures 2.4.1c and 2.4.1d, and $\lambda_C(B_n)$ is the distance between the center of band B_n and band B_{n-1} and can be thought of as a wavelength. C_p^{2D} expresses the fraction of the center-to-center distance between adjacent bands that is taken up by the banded phase. As C_p^{2D} approaches 1 it implies that almost all of the wavelength is covered by the two (ferrite) bands, meaning there is little matrix separation between them and they are merging into a single band, *i.e.* the bands are thick and/or close together. As C_p^{2D} approaches zero it means that the wavelength is composed almost exclusively of the (martensite) matrix and the bands are disappearing, *i.e.* the bands are thin and/or far apart.

Again, from a simple visual inspection of the microstructures in Figures 2.4.1c and 2.4.1d, a qualitative description of the Perpendicular Continuity Index is possible. Overall, the bands in Steel A are thinner and spread further apart than the bands in Steel B. The bands in Steel B appear to be grouped together in pairs. For example, the bands centered around 100 and 120 μm in Steel B are close together, which also indicates that C_p^{2D} should be close to 1. The band centered around 70 μm appears to be grouped with the band centered around 55 μm . However, these two groups of bands are spread apart, the band around 70 μm is further away from the band at 100 μm , resulting in C_p^{2D} being lower.

Figure 2.4.3 shows the Perpendicular Continuity Index for both Steel A and Steel B. The qualitative description just given is confirmed by these plots. The average value of C_p^{2D} for Steel B is again almost three times larger than that of Steel A. The relative uniformity of the band placement in Steel A is seen by the small standard deviation of the points about the mean. For Steel B the bands grouping together in pairs is reflected in the oscillatory pattern observed about the mean and the large standard deviation.

The average C_b^{2D} and C_p^{2D} for 11 different microstructures are plotted in Figure 2.4.4. The average values are used to characterize the banding in the microstructures as a whole. The squares are the values for the banded phase of each microstructure. For Steels A, B, F and K the banded phase is ferrite, for Steels C, E and G-J the banded phase is pearlite and for Steel D the banded phase is martensite. Steel D is a model microstructure created from Voronoi

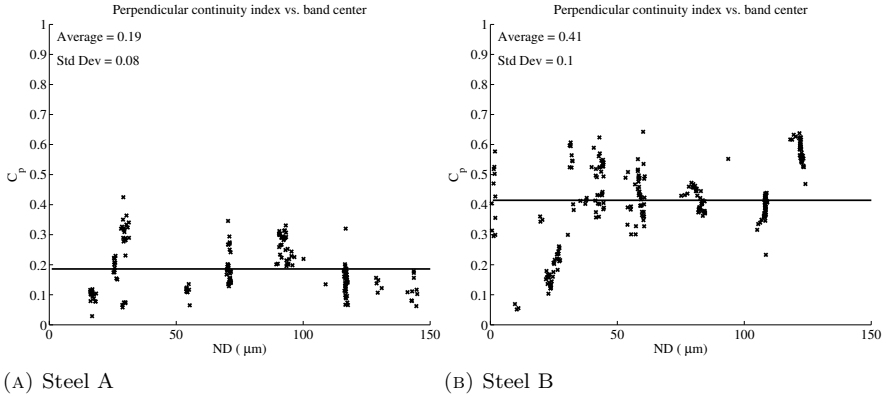


FIGURE 2.4.3: Perpendicular Continuity Index C_p^{2D} (given by eq. 2.4.2) plotted against the center position along the ND $C(B_n)$ of each band.

tessellations, while all other images are from real dual phase microstructures. The diamonds show the values for Steels C, E and G-J if the ferrite phase were taken to be the banded phase.

All of the microstructures have, on average, bands that are broken ($C_b^{2D} < 0.5$) and have bands that are thinner than the width of the background phase that separates them. However, even for these microstructures the quantification has separated them into distinct groups. Steels A, F and K make up the first group. A visual inspection of the microstructure indicates truly weak banding. In all three images, the central band is the dominant band and the other groupings of the banded phase form partial, thin bands, spread far apart throughout the material. Both of these behaviors are reflected in the calculated average values for C_b^{2D} and C_p^{2D} being less than 0.2. Steels C, E and G-J are clustered in the same region in the plot with C_p^{2D} ranging from 0.29 to 0.39 and C_b^{2D} falling below 0.2. This indicates that the bands are interrupted by the background phase. This is obvious from a visual inspection of the microstructures. The higher values for C_p^{2D} reflect the fact that the bands are wider and closer together than for the previously mentioned steels. For Steel B, $C_b^{2D} = 0.31$, which is higher than the other steels. As can be seen from the micrograph, Steel B has more connectivity of the grains within a band and the bands are closer together than the previous microstructures. This indicates much stronger banding. Finally, Steel D has $C_b^{2D} = 0.74$, which is expected since the bands have no background phase interrupting them. Steel D also has $C_p^{2D} = 0.39$, which is only slightly lower than that of Steel B, making it the most banded microstructure shown. It is based on these groupings that the

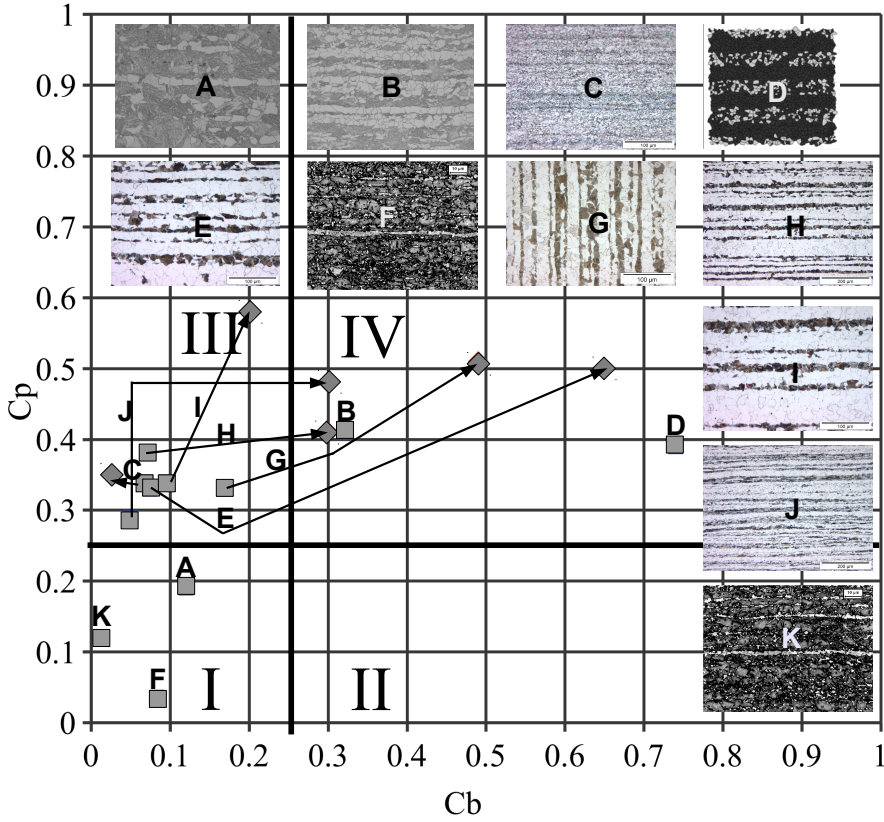


FIGURE 2.4.4: Eleven microstructures are compared using the average Band and Perpendicular Continuity Indexes for each microstructure as a measure of the total bandedness. Steels A, B, F and K consider ferrite (light areas) to be the banded phase, while Steels C, E and G-J consider pearlite and Steel P considers martensite (dark areas) to be the banded phase. The squares are plotted at (C_b^{2D}, C_p^{2D}) and are labeled with the letter corresponding to the microstructure. The diamonds given for Steels C, E and G-J show the results of the analysis if instead of pearlite, the banded phase was taken to be the ferrite. The arrows connect the squares and diamonds for the given microstructure. Note that choosing the other phase as banded does not affect the process of quantification, but it does give significantly different results.

quadrant lines have been drawn.

Considering the diamonds, if the role of the phases is reversed (*i.e.* if the ferrite is considered to be the banded phase and the martensite and pearlite are considered to be the background phase) then the results of the analysis are

significantly different for several of the microstructures. For Steels G and I, the ferrite bands are wide and close together. The ferrite bands of Steel E are continuous since $N_{part} = 1$. Steel J has ferrite bands that are both thicker and more continuous than the pearlite bands. The ferrite in Steel H is also more continuous as indicated by the increase in C_b^{2D} . The only structure that did not change much is Steel C. The ferrite is somewhat less continuous than the pearlite and the ferrite bands are only slightly wider and/or closer together than for the pearlite. At first glance, Steel I appears as if the band continuity index should be higher than it is, but a closer look at the microstructure reveals that the ferrite is interrupted by the pearlite more than one might initially suspect.

2.4.3 Initial 3D Microstructure Analysis

The first step to characterising the bands in 3D is to look at the profiles, as described in the previous section, for each slice in the stack. These profiles highlight the regions where bands exist before imposing boundaries on them through the thresholding procedure. In Figures 2.4.5a and 2.4.5b the profiles are stacked consecutively in the slicing (or transverse) direction. This provides a glimpse of how the ferrite bands behave in the TD or sectioning direction.

Observing the stacked profiles for Steel A (Figure 2.4.5a) and the images of the microstructure at various sectioning depths (Figures 2.4.5c - 2.4.5f), several conclusions can be drawn about the behavior of the ferrite bands in the direction of the sectioning. First, the strongest peak of the profiles is found in the center, around $70 \mu\text{m}$, and it remains the strongest through the sectioning direction. This corresponds to the obvious band in the center of the optical micrographs which remains visible, but towards the end of the sectioning depth appears to break into pieces corresponding to the slightly lower amplitude in the profiles. In contrast, while the peaks around $14 \mu\text{m}$ and $30 \mu\text{m}$ remain through the TD with only small changes in position and width, they appear to merge together to form one larger band and then break apart again to form two bands at various locations in the depths. This behavior can also be seen in the micrographs. Finally, looking at the peaks around $95 \mu\text{m}$ and $120 \mu\text{m}$ they appear to start and end in the sectioning direction, which is also supported by the micrographs. From this, it is reasonable to conclude that these peaks really do represent the bands observed in the actual images for various slices.

Now, conclusions can be drawn for Steel B without necessarily needing to see the actual microstructure. The profile for Steel B is shown in Figure 2.4.5b. For this material, it appears that all of the bands are strong through the entire depth of the material. Unlike Steel A, it appears that some of the bands shift their center positions, giving a slightly wavy look to the bands in

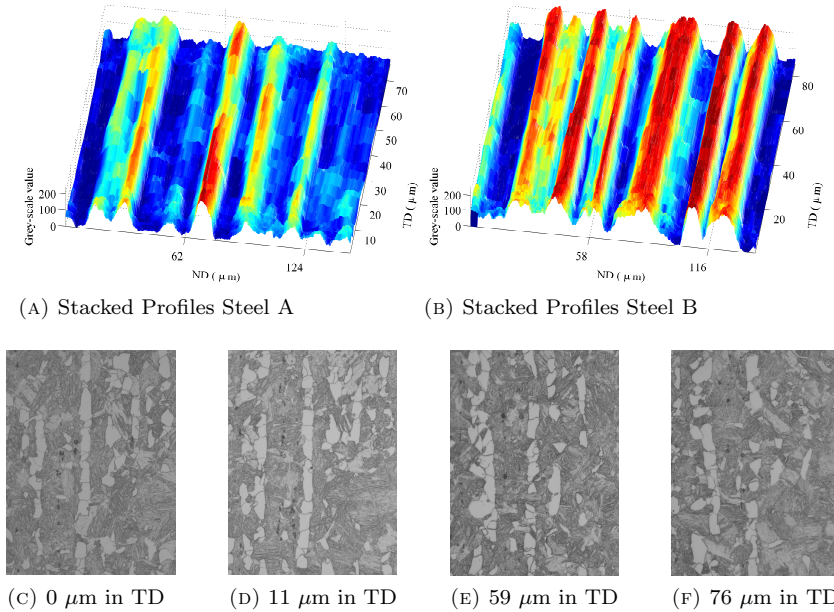


FIGURE 2.4.5: Figures 2.4.5a (Steel A) and 2.4.5b (Steel B) show the grey-scale filtered profiles (averaged along the rolling direction) for all 55 slices in the stack. Figures 2.4.5c-2.4.5f show actual images of Steel A normal to the RD at various distances in the TD. (Normal Direction \rightarrow , Rolling Direction \downarrow .)

the depth. Like Steel A, there is a band centered near $30 \mu\text{m}$ that appears to split into two bands in the sectioning depth. From these simple grey-scale profiles, significant qualitative information about the 3D nature of the bands may be obtained.

2.4.4 Band Connectivity

Connectivity plays an important role in mechanical properties of steel. Information about connectivity is completely lost when only a 2D image is considered. Therefore, using the stylized bands, as defined in section 2.4.1 and shown in Figures 2.4.1c and 2.4.1d, the connectivity of the bands in the direction of sectioning is explored.

Since the stylized bands are uniform along the RD, a single value, the vertical (ND) center position $C(B_n)$ of band B_n provides a unique label for each band. Using $C(B_n)$ the bands can be tracked through the TD to observe the behavior in the third dimension. A breadth-first search was carried out on

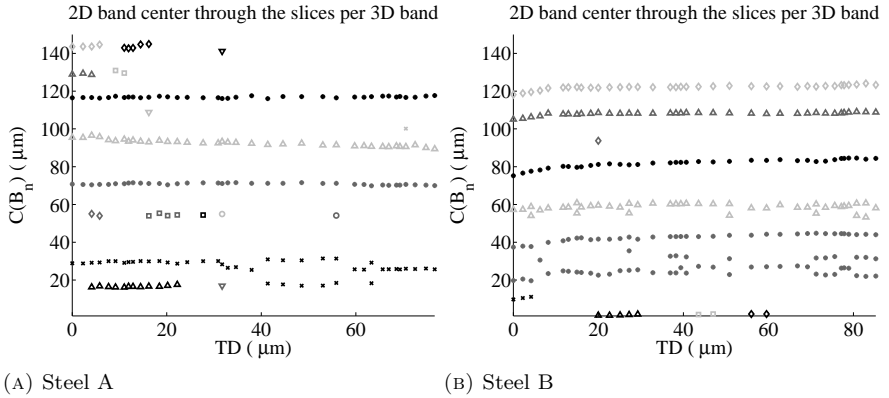


FIGURE 2.4.6: Center position $C(B_n)$ along the ND of the images for each band B_n followed through the TD (the serial sectioning). The symbols correspond to individual bands that are connected through the sectioning.

the stylized bands to ascertain how connected they are through the transverse (sectioning) direction. Figure 2.4.6 shows this connectivity with each symbol representing a single, connected band through the sectioning direction. This figure is important because it demonstrates the problem of relying on a single 2D image for characterising and quantifying banding in the 3D microstructure. The connectivity of the bands is lost in any given 2D image. For Steel A, this is evident when observing the bands centered between $20 \mu\text{m}$ and $30 \mu\text{m}$. The band near $20 \mu\text{m}$ appears to be three different bands through the depth. This information is completely lost, especially if comparing images taken at, say, $10 \mu\text{m}$ and $50 \mu\text{m}$ in the TD. It would not be obvious that these two bands are not the same, even though they appear in the same location. On the same token, it is not possible to see that the two bands observed at $50 \mu\text{m}$ in the TD, and the single band observed at $70 \mu\text{m}$ along the TD are, in fact, connected. The same can be said about the bands centered between $20 \mu\text{m}$ and $40 \mu\text{m}$ for Steel B.

Figure 2.4.7 shows 3D images of both Steel A (2.4.7a) and Steel B (2.4.7b) looking into the depth of the sectioning direction. These images were created by the ImageJ 3D viewer plug-in [66] as implemented in the Fiji software [62]. These images confirm what was concluded with the stylised bands. The connectivity in 3D is different than what is observable in 2D. For example, in Steel B the pair of bands at the bottom of the images are seen to be connected in 3D, while they appear unconnected in many of the 2D slices.

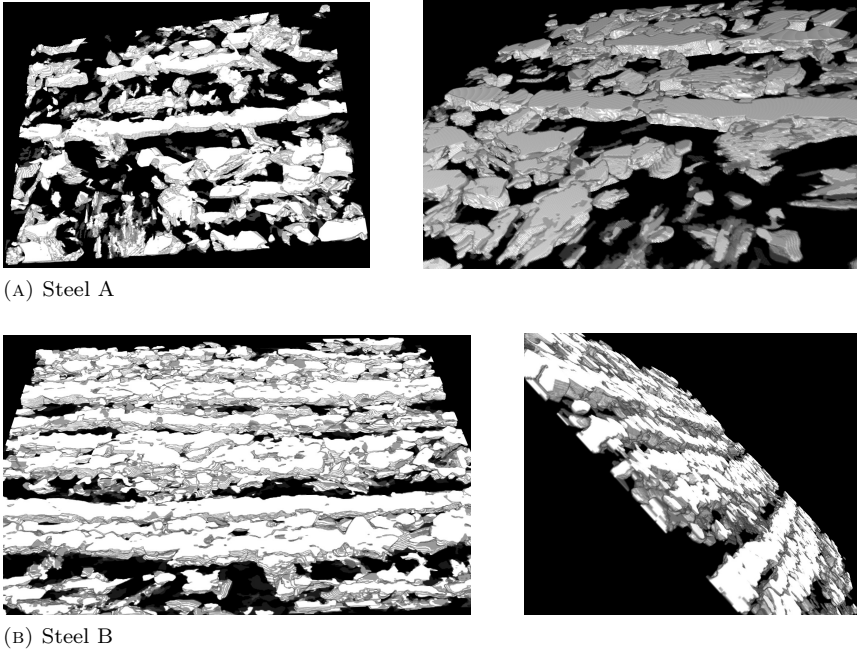


FIGURE 2.4.7: Rotated views of the 3D reconstructions from the first 24 slices ($12\ \mu\text{m}$ into the depth) of Steel A (2.4.7a) and Steel B (2.4.7b). The ferrite bands appear less structured in Steel A than in Steel B. Much of the ferrite does not obviously contribute to a band, making Steel A arguably weakly banded. The opposite is true for Steel B.

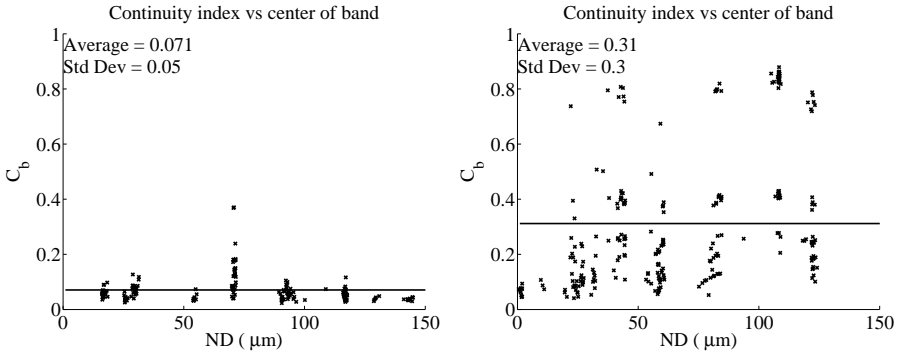
2.4.5 3D Banding Parameters

The 2D Band Continuity Index C_b^{2D} for both Steel A and Steel B, shown in Figures 2.4.8a and 2.4.8b, respectively, is given by eq. (2.4.1). This index is easily extended to 3D in the following way:

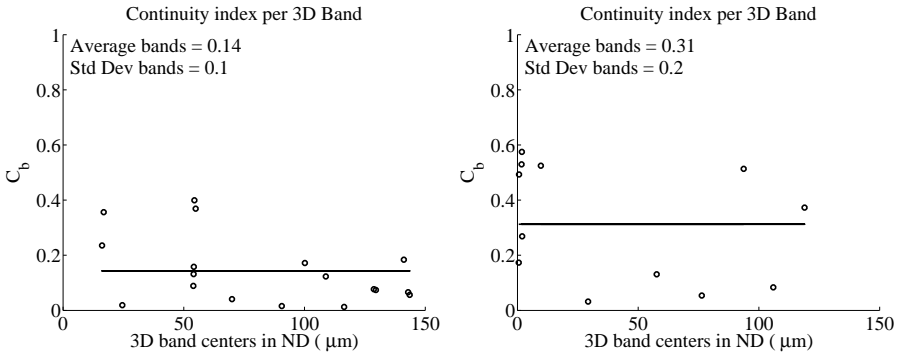
$$C_b^{3D}(B_n) = V_b(B_n)/N_{part}(B_n) \quad (2.4.3)$$

where $V_b(B_n)$ is the volume fraction of the banded phase, as determined from the entire 3D connected band, B_n . For $N_{part}(B_n)$, the definition of a particle is the same as given for 2D. Figures 2.4.8c and 2.4.8d show a comparison of the 2D and 3D results for the C_b calculations of Steel A and Steel B, respectively. The average values for the 2D and 3D Band Continuity Indexes could be considered to be the same to within one standard deviation.

While this conclusion is perhaps unsurprising, it is useful. The equality of the area and volume fractions has been well established [58, 59]. However, the



(A) 2D Band Continuity Index C_b^{2D} Steel A (B) 2D Band Continuity Index C_b^{2D} Steel B



(C) 3D Band Continuity Index C_b^{3D} Steel A (D) 3D Band Continuity Index C_b^{3D} Steel B

FIGURE 2.4.8: Figures 2.4.8a and 2.4.8b show the 2D Band Continuity Index C_b^{2D} for each of the 55 slices for both steels. Figures 2.4.8c and 2.4.8d show the 3D Band Continuity Index C_b^{3D} of the entire microstructure for both steels. The average value is given in each plot and is represented by the solid line. The 2D and 3D values for C_b differ slightly, but within the set of standard deviations, they could be considered to be the same.

contiguity of the phase is not necessarily constant in the third dimension. It could be that any one slice significantly over or under represents the connectivity of the banded phase, but without explicitly testing this, it is impossible to know for certain. The fact that the 2D and 3D quantification results are essentially equivalent confirms two things. First, this verifies that C_b is reasonable and useful. Second, it confirms the assumption that a 2D banded image reasonably reflects the 3D banded microstructure.

The 2D Perpendicular Continuity Index, C_p^{2D} , shown in Figures 2.4.9a and

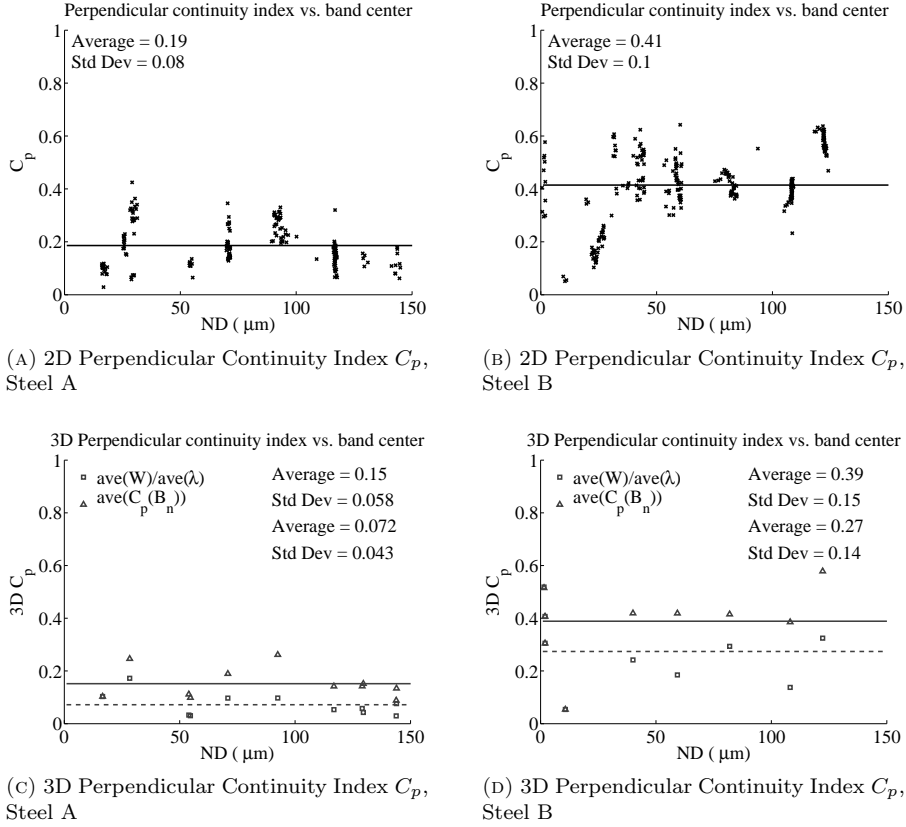


FIGURE 2.4.9: Figures 2.4.9a and 2.4.9b show the 2D Perpendicular Continuity Index C_p^{2D} of both steels for each of the 55 slices. Figures 2.4.9c and 2.4.9d show the 3D Perpendicular Continuity Index C_p^{3D} of both steels for the entire microstructure. The average values are given in each plot and are represented by the solid lines. The solid line corresponds to calculating the average of the C_p^{2D} values for each band over the set of stacked images and the dashed line corresponds to calculating C_p^{3D} from the band width and center-to-center distances for a given band averaged over the stack of images. The 2D and 3D values for C_p differ slightly, but within the set of standard deviations, they could be considered to be the same.

2.4.9b, is given by eq. (2.4.2). This index is also easily extended into 3D in the following way:

$$C_p^{3D}(B_n) = \frac{\frac{1}{2}V_b(B_n)W(B_n) + \frac{1}{2}V_b(B_{n-1})W(B_{n-1})}{\lambda_C(B_n)} \quad (2.4.4)$$

where the band volume fraction V_b is used instead of A_b as in the 2D calculation.

As discussed earlier, due to the connectivity, sometimes what is shown as two separate bands in 2D is actually one band in 3D. This makes the 3D value much more difficult to determine than in 2D. Figures 2.4.9c and 2.4.9d show C_p^{3D} calculated in two different ways for Steel A and Steel B, respectively. The first way is to calculate C_p^{3D} on each 2D image, using the 3D connectivity of the bands. If two adjacent bands are connected in 3D, then both bands are considered as one in the calculation. This affects the determination of both $W(B_n)$ and $\lambda_C(B_n)$. Then, for each band the value is averaged over the slices. The second way is to calculate the average widths and center-to-center distances of each 3D connected band from the set of 2D slices and then to use these average values to calculate C_p^{3D} . The crosses in Figures 2.4.9c and 2.4.9d show the results for this calculation. While these two methods yield slightly different values, as of yet, there is no reason to choose one method over the other, and so both have been included in this analysis.

From Figure 2.4.9, it can be concluded that for either method of calculating C_p^{3D} , the results again confirm that the 2D is reflective of the 3D behavior, despite the fact that the band connectivity is different. Again, this result is not surprising, but it is significant, both with respect to the implications for these banded microstructures, and for the utility of the parameters themselves.

2.5 Conclusion

Two parameters, Band Continuity Index C_b^{2D} and Perpendicular Continuity Index C_p^{2D} , have been introduced to quantify the degree of banding in Dual Phase steel microstructures on a bounded and absolute scale of zero to one. The Band Continuity Index combines the idea of area fraction and number of particles to quantify how broken a band is. When C_b^{2D} approaches 0, the bands are broken into many small disconnected particles. When it approaches 1, the band is continuously connected across the image. The Perpendicular Continuity Index combines the ideas of band width and band wavelength to quantify how close the bands are throughout a material. When C_p^{2D} approaches 0 the bands are separated from each other by large sections of the matrix or other phase. When it approaches 1 the bands are close together with only a small section of the matrix separating them. Both quantities have direct links to and implications for the mechanical properties of the material. These two parameters could also be used to generate realistic microstructures for models and simulations, given that models often use area fractions, number of particles, band spacing and band widths as input parameters.

The 3D nature of the microstructural bands in two of the dual phase steels, as observed from serial sectioned optical micrographs has also been presented in this chapter. Much can be assumed about the behavior of the bands in 3D from only 2D images, as expected from the extensive studies of random microstructures. However, the connectivity of the bands is not directly nor accurately observable in 2D images. Therefore, the two parameters developed in 2D have also been extended to 3D. It is shown that these parameters yield separate results in 2D and 3D that are within one standard deviation of each other. This is enough for these values to be reasonably considered the same. While this conclusion is perhaps not surprising, it is important. The values calculated from a single 2D image reasonably represent what is expected of the 3D image.

Oriented Circular Cylinder Model and Non-parametric Estimators

Oriented circular cylinders in an opaque medium are used to represent certain microstructural objects in steel. The opaque medium is sliced parallel to the cylinder axes of symmetry and the cut-plane contains the observable rectangular profiles of the cylinders. A one-to-one relation between the joint density of the squared radius and height of the 3D cylinders and the joint density of the squared half-width and height of the observable 2D rectangles is established. A nonparametric estimation procedure is proposed to estimate the distributions and expectations of quantities of interest, such as the cylinder radius, height, aspect ratio, surface area and volume from the observed 2D rectangle widths and heights. Also, the covariance between the radius and height of a cylinder is estimated. The asymptotic behavior of these estimators is established to yield confidence intervals for the expectations of the quantities of interest.

3.1 Introduction

One of the biggest challenges of studying materials like steel is the inability to see inside of an opaque medium. While there are methods to obtain 3D information, as discussed in Chapter 1 and Section 2.2, they tend to be costly both in terms of time and resources. Therefore, one can turn to the discipline of stereology for tools that can be used to confront these issues in the sense that there are well established models that provide means of estimating various 3D quantities from (relatively inexpensive) 2D observations and measurements (see e.g. [4, 5, 59]). One of the classical problems in stereology comes from a study by Wicksell [67] where the size distribution of spherical corpuscles in spleens is estimated based on measuring the circular cross-sections from slices of the spleens. Wicksell derived the relationship between the distribution of the unobservable sphere radii and the distribution of the observable cross-sectional circle radii. He then used the empirical data and a histogram estimator to solve his particular problem.

This basic stereological model has been applied in a variety of disciplines where it is not possible to obtain full 3D measurements of objects simply by looking at them; this includes biology [4, 67–70], geology [25, 28], astronomy [34], and materials science [18, 23, 26, 27, 29–33, 71–77]. Not surprisingly, the method has also gained considerable attention in the statistics literature. There, the main focus is on computation and asymptotic behaviour of the proposed estimators [17–34].

In several applications the particles of interest are spheres, or close enough to be treated as such. However, in many other applications the particles are not spherical at all, and so it is important to also consider models with non-spherical particles. The basic model has been extended to include randomly oriented cylinders [26, 77–80], polygons [25, 28, 29, 81], spheroids and ellipsoids [23, 25, 32, 74, 80], and non-regular shapes [27, 29, 30, 73, 75, 82].

All of this has led to a large body of work from which information of interest to scientists, engineers and industry can be drawn. The tools that have been created are powerful in their versatility. They can be applied to real materials, to models and simulations. They can also be studied from a theoretical point of view. The specific motivation for this work comes from the banded steel microstructures introduced in Chapter 2 and shown in Figures 2.3.1 and 3.1.1. This particular material is interesting to industry because it has anisotropic properties, high susceptibility to cracking and corrosion, and it is more difficult to machine than non-banded material. Currently, there is no reliable way to prevent or control the banding under certain necessary processing environments. Being able to quantitatively describe the sizes of the bands

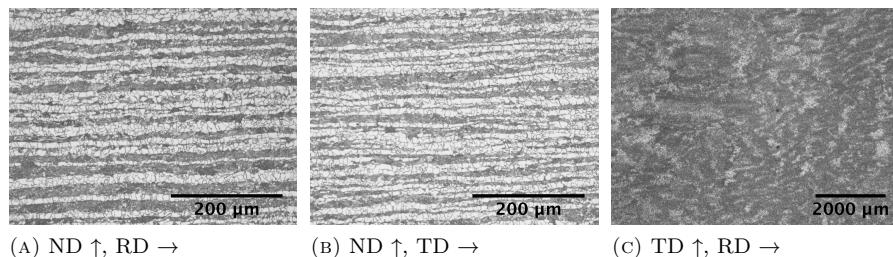


FIGURE 3.1.1: Optical images of Steel B. Figure 3.1.1a shows a typical banded microstructure where the normal direction is the direction along which the steel is cut. The rolling direction is to the right (the transverse direction is into the page). Figure 3.1.1b shows the same steel with the cut still along the normal direction, but the transverse direction is to the right (the rolling direction is into the page). Figure 3.1.1c shows a slice taken perpendicular to the normal direction, looking down on top of the bands.

in 3D will greatly aid industry in assessing the quality of the material and the extent of the effects the bands have on the material coming off the production line. Ultimately, this will also aid in understanding and controlling the process that leads to band formation, thereby making it possible to eliminate them from the material when they are undesirable.

Figure 3.1.1 shows the three orthogonal directions of Steel B, introduced in Chapter 2. Figure 3.1.1a shows a typical banded microstructure where the normal direction (ND) is the direction along which the steel is cut. In this image, the rolling direction (RD) is to the right and the transverse direction (TD) is into the page. Figure 3.1.1b shows the same steel with the cut still along the ND, but the TD is to the right and the RD is into the page. Figure 3.1.1c shows a slice taken perpendicular to the ND, looking down on top of the bands. While it is clear from these images that the bands are rather complicated structures, it is also reasonable to assume that since the phases are stacked like layers, they have an oriented plate-like (albeit nebulous) structure. Therefore, the bands can be represented by oriented cylinders. For simplicity, the cylinders are taken to be circular.¹ Following the example set forth by Wicksell when he considered spherical corpuscles observed in spleens [67], the marginal distributions of the radius and height of the cylinders are considered. While most stereological models assume that non-spherical objects are randomly oriented, in this case, it is clear that this assumption is not

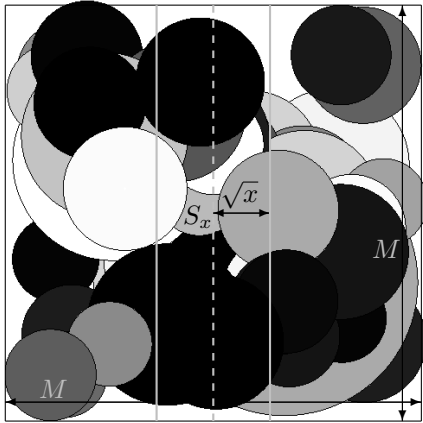
¹While it is clear that the objects are not truly symmetric, the circular assumption means that only observations in one direction, namely the rolling direction for this work, are required. Non-symmetric shapes such as ellipses might be more representative, but requires information from at least two orthogonal directions, and the results are more complicated than what is presented in this thesis.

appropriate. By imposing the orientation constraints, one can explore other properties of the cylinders such as the volume, surface area, and aspect ratio. These quantities are important to estimate because they are linked to the mechanical properties of the material. For example, the surface area can be linked to the interface area between two phases, which influences properties like strength and resistance to corrosion or cracking.

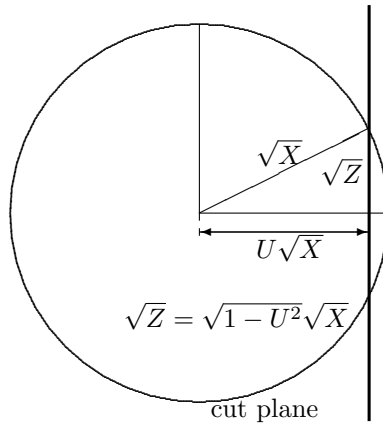
In this chapter, two non-parametric estimators are proposed for estimating the distributions of the 3D cylinder quantities of interest from the 2D rectangle half-width and height observations. One estimator enforces a monotonicity constraint for the distribution functions, inspired by the work of Groeneboom and Jongbloed [22], the other does not. An empirical estimator is used to estimate the expectations of the 3D quantities of interest from the 2D rectangle half-width and height observations. The rates of convergence and asymptotic distributions for all of these estimators are derived. This establishes a means of estimating the confidence intervals for the expectations when the model is applied to the steel microstructures in Chapter 4.

3.2 Cylinder Model

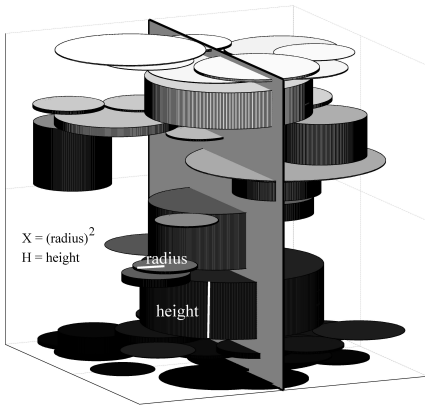
To represent the bands shown in Figure 3.1.1, the following model is proposed (see Figure 3.2.1). Cylinders are generated with a joint density, f for the squared radius, X (the choice to consider the *squared* radius is inspired by Hall and Smith [1]), and height, H . The centers of these cylinders are distributed according to a Poisson process, *i.e.* randomly and uniformly distributed throughout an opaque medium and the cylinders are placed such that their axes of symmetry all have the same orientation, as in Figure 3.2.1c. The center of a cylinder with radius \sqrt{x} will be intersected by the plane if and only if its center falls within slab S_x as shown in Figure 3.2.1a. This leads to biased observations on the cut plane since cylinders with larger radii have a higher probability of being intersected. More specifically, the joint cumulative distribution function (CDF) F of (X, H) , given that the plane intersects the



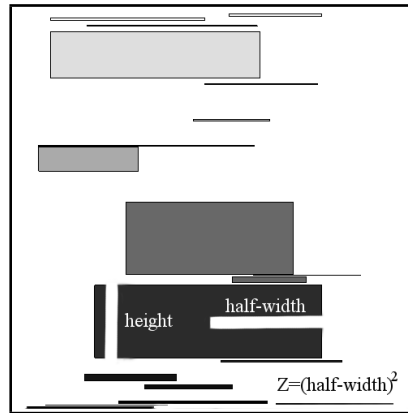
(A) Top view (equivalent to Figure 3.1.1c) of cylinders in an $M \times M \times M$ box with a cut plane (dashed line) and slab S_x (solid lines) into which cylinder centers should fall to be cut by the plane.



(B) Schematic View, \sqrt{X} is the cylinder radius, \sqrt{Z} is the rectangle half-width, U is a uniform random variable.



(C) View of cut plane through the box



(D) Observations on the cut plane

FIGURE 3.2.1: Visualization of the cylinder model. Figure 3.2.1a shows the top view, equivalent to Figure 3.1.1c, of an $M \times M \times M$ box. The dashed line represents the intersecting plane through the center of the box, along the ND. The slab labeled S_x is denoted by the solid grey lines. A cylinder whose radius is equal to \sqrt{x} and whose center falls within S_x will be cut by the plane. Figure 3.2.1b shows a single cylinder that has been intersected by the cut-plane. The distance of the center of the cylinder to the cut plane is a uniform random variable U on $(0, \sqrt{x})$ due to the Poisson process assumption on the radial position of the cylinder centers. The observed rectangle half-width \sqrt{Z} is a random fraction of the radius. Figure 3.2.1c shows the cylinders in full, cut by the plane. Figure 3.2.1d shows the rectangles observable on the cut plane.

cylinder, can be written as

$$\begin{aligned}
 F(x, h) &= P(X \leq x, H \leq h | \text{plane intersects cyl.}) = \\
 &= \frac{P(X \leq x, H \leq h \text{ and plane intersects cyl.})}{P(\text{plane intersects cyl.})} \\
 &= \frac{\int_{y=0}^x \int_{m=0}^h \sqrt{y} f(y, m) \, dm \, dy}{\int_{y=0}^{\infty} \int_{m=0}^{\infty} \sqrt{y} f(y, m) \, dm \, dy} = \frac{\int_{y=0}^x \int_{m=0}^h \sqrt{y} f(y, m) \, dm \, dy}{m_F^+} \\
 &= \int_{y=0}^x \int_{m=0}^h \frac{\sqrt{y}}{m_F^+} f(y, m) \, dm \, dy
 \end{aligned}$$

Here, the density function f is weighted by the ratio of the radius of the cylinder to the expected radius, $E_f[\sqrt{X}] \equiv m_F^+$, which is assumed to be finite (see Assumption 3.4.1). Since the centers of the circles are uniformly distributed throughout the medium, the distance from the center of a cylinder that has been cut to the intersecting plane is a uniform random variable, as shown in Figure 3.2.1b. This is analogous to the relationship between the circle radii and sphere radii in the method set forth by Wicksell [67]. Once a cylinder has been cut, the observable portion is seen as a rectangle on the cut plane, as shown in Figure 3.2.1d.

The rectangles have observable squared half-widths, z , and heights, h , that have a joint density g . Since the cylinders are all cut parallel to their axis, all of the height information for the cut cylinders is preserved and directly observable on the cut-plane. (This shows that the distribution of the cylinder centers along the direction of the heights does not require the Poisson process assumption.) The half-widths of the observed rectangles are related to the cylinder radii through the relationship displayed in Figure 3.2.1b. From these 2D observations, one can estimate the 3D distribution where the relationship between g and f can be obtained using a variant of the well-known formula relating the density of the rectangle half-width (and height) to the distance of cylinder center to the cut plane and the density of the cylinder radius (and height):

$$g(z, h) = \frac{\int_{x=z}^{\infty} (x-z)^{-\frac{1}{2}} f(x, h) \, dx}{2 \int_{x=0}^{\infty} \sqrt{x} f_X(x) \, dx} = \frac{1}{2 m_F^+} \int_{x=z}^{\infty} (x-z)^{-\frac{1}{2}} f(x, h) \, dx. \tag{3.2.1}$$

This relation can be inverted to obtain the joint density for the cylinder radius

and height as a function of the observable rectangle joint density:

$$f(x, h) = -\frac{\partial}{\partial x} \frac{\int_{z=x}^{\infty} (z-x)^{-\frac{1}{2}} g(z, h) dz}{\int_{z=0}^{\infty} z^{-\frac{1}{2}} g_Z(z) dz} = -\frac{\partial}{\partial x} \frac{\int_{z=x}^{\infty} (z-x)^{-\frac{1}{2}} g(z, h) dz}{m_G^-} \quad (3.2.2)$$

where $m_G^- \equiv E[Z^{-1/2}]$ is the expectation of one over the rectangle half-width and is also assumed to be finite (see Assumption 3.4.1). From this relationship, the distributions of univariate quantities of interest such as the height H , the squared radius X , the aspect ratio $R = \sqrt{X}/H$, the surface area $S = 2\pi(X + \sqrt{X}H)$, and the volume $V = \pi XH$ can be calculated.

The CDF for the observed height takes on the form:

$$F_H(h) = \int_{t=0}^h f_H(t) dt = \frac{1}{m_G^-} \int_{t=0}^h \int_{z=0}^{\infty} z^{-\frac{1}{2}} g(z, t) dz dt. \quad (3.2.3)$$

Note that this CDF still contains the weight associated with the biasing from the radius of the cylinder. This accounts for any dependence that might exist between the cylinder height and radius. Should such a dependence exist, then the observed rectangle height distribution will also be biased. See Figure A.3.1 and Appendix A.3 for a more detailed discussion of the biasing of the height observations associated with a dependence of the height and radius.

For each of the other quantities of interest, define

$$q(h; t) = \begin{cases} t & \text{(squared radius: } T = X) \\ (ht)^2 & \text{(aspect ratio: } T = \sqrt{X}/H) \\ \left[\sqrt{\frac{h^2}{4} + \frac{t}{2\pi}} - \frac{h}{2} \right]^2 & \text{(surface area: } T = 2\pi(X + \sqrt{X}H)) \\ \frac{t}{\pi h} & \text{(volume: } T = \pi XH) \end{cases} \quad (3.2.4)$$

(see Appendix A.2.4 for a comprehensive review of the relationships between X , H , Z and $q(h; t)$). These quantities are chosen such that the random variable of interest, $T > t$ if and only if $X > q(H; t)$. Hence, using eq. (3.2.2),

$$1 - F_T(t) = \int_{h=0}^{\infty} \int_{x=q(h;t)}^{\infty} f(x, h) dx dh = \frac{N(t)}{N(0)} \quad (3.2.5)$$

where N is a bounded and decreasing function that can be rewritten as

$$N(t) = N_{q(\cdot;t)}(t) = \int_{h=0}^{\infty} \int_{z=q(h;t)}^{\infty} (z - q(h; t))^{-\frac{1}{2}} g(z, h) dz dh. \quad (3.2.6)$$

Note that eq. (3.2.6) expresses the CDF of the unobservable 3D cylinder properties in terms of a function N involving only the joint density g of the observable pairs (Z, H) . This suggests natural ways to estimate the CDFs of these quantities, as will be discussed in Section 3.3. Also note that under Assumption 3.4.1,

$$N(t) \leq N(0) = E_g \left[Z^{-\frac{1}{2}} \right] < \infty. \tag{3.2.7}$$

Along with the distribution functions, it is useful to estimate the expectations of the quantities of interest. It is especially important to be able to express these 3D quantities entirely as functions of the density g of the observable variables (Z, H) . This can be done using eq. (3.2.1) with $\alpha, \beta > -1$ (given that the moments exist)

$$E_g \left[Z^\alpha H^\beta \right] = \int_{h=0}^\infty \int_{z=0}^\infty z^\alpha h^\beta g(z, h) dz dh = \frac{\sqrt{\pi} \Gamma(\alpha + 1)}{2 m_F^+ \Gamma(\alpha + \frac{3}{2})} E_f \left[X^{\alpha + \frac{1}{2}} H^\beta \right], \tag{3.2.8}$$

where m_F^+ is the same as that given in eq. (3.2.1) and Γ is the Gamma function. (See Appendix B.1 for the full derivation.)

From these cross-moments, another important quantity of interest can be calculated: the covariance between the radii and heights of the cylinders. From the moments given in eq. (3.2.8) the following expression is obtained for the covariance between the unobservable radius \sqrt{X} and height H in terms of the observable rectangle half-width \sqrt{Z} and height H (see Table B.1):

$$\begin{aligned} \text{Cov}_f(\sqrt{X}, H) &= \sigma_{\sqrt{X}H} = E_f \left[\sqrt{X}H \right] - E_f \left[\sqrt{X} \right] E_f[H] \\ &= \frac{(\pi/2)E_g[H]}{E_g \left[Z^{-\frac{1}{2}} \right]} - \frac{\pi/2}{E_g \left[Z^{-\frac{1}{2}} \right]} \frac{E_g \left[Z^{-\frac{1}{2}} H \right]}{E_g \left[Z^{-\frac{1}{2}} \right]} \end{aligned} \tag{3.2.9}$$

The stated quantities of interest associated with the density f are now expressed in terms of the density g of the observable quantities. The next section will describe empirical and isotonic estimation procedures that can be used to estimate the unknown distributions and covariance.

3.3 Non-parametric Estimation

The main statistical problem to solve is to estimate the quantities defined in terms of the joint density f , as introduced in Section 3.2, based on the observed

data from the joint density g . A natural estimator to begin with in this case is the empirical or plug-in estimator.

Plugging the empirical distribution of the observed data pairs (Z_i, H_i) ($1 \leq i \leq n$) into relations eq. (3.2.3) and eq. (3.2.6) yields

$$\widehat{F}_{H,n}(h) = \frac{\sum_{i=1}^n Z_i^{-\frac{1}{2}} 1_{[H_i < h]}}{\sum_{i=1}^n Z_i^{-\frac{1}{2}}} \quad (3.3.1)$$

as an estimator for the CDF of the heights and

$$N_n(t) = N_{n,q(\cdot;t)}(t) = \frac{1}{n} \sum_{i=1}^n (Z_i - q(H_i;t))^{-\frac{1}{2}} 1_{[Z_i > q(H_i;t)]} \quad (3.3.2)$$

as estimators for the various choices of N dependent on $q(h;t)$. These estimators of N can be plugged into eq. (3.2.5) to obtain the estimators for the CDFs of the various quantities of interest.

The expectations of interest in eq. (3.2.8) can be estimated by the empirical mean:

$$\widehat{E} [Z^\alpha H^\beta] = \frac{1}{n} \sum_{i=1}^n Z_i^\alpha H_i^\beta. \quad (3.3.3)$$

In this way, the covariance between \sqrt{X} and H can be estimated by

$$\widehat{\sigma}_{\sqrt{X}H} = \frac{(\pi/2) \sum_{i=1}^n H_i}{\sum_{i=1}^n Z_i^{-\frac{1}{2}}} - \frac{\pi/2}{n^{-1} \sum_{i=1}^n Z_i^{-\frac{1}{2}}} \frac{\sum_{i=1}^n H_i Z_i^{-\frac{1}{2}}}{\sum_{i=1}^n Z_i^{-\frac{1}{2}}}. \quad (3.3.4)$$

The empirical plug-in estimator works well for estimating the expectations and covariance and it yields a monotonic function for the estimate of the distribution function of the height. This is not true, however, for N_n . This estimator for N , which in view of eq. (3.2.5) is a non-increasing, non-monotonic function; it even has infinite discontinuities due to the vanishing denominator when $q(H_i;t) = Z_i$. See, for example, Figure 3.3.1. Therefore, inspired by the approach of Groeneboom and Jongbloed [22], the isotonic estimator is introduced, which enforces monotonicity, to obtain estimates for N and consequently the underlying distribution functions of X , R , S and V .

Briefly, the isotonic estimator is the (non-increasing) function \widehat{N}_n that minimizes

$$N \mapsto \int_0^\infty N(y)^2 dy - 2 \int_0^\infty N_n(y) N(y) dy \quad (3.3.5)$$

over all non-increasing functions on $[0, \infty)$. It is tempting to ‘complete the square’ and choose to minimize the function $\int (N(y) - N_n(y))^2 dy$ instead of eq. (3.3.5), which should lead to the same solution since the added constant, $\int_0^\infty N_n(y)^2 dy$, does not depend on N . However, N_n is not square integrable, and so this added constant is infinite, making this problem ill defined. Therefore, one should only minimize eq. (3.3.5).

To solve the minimization problem (continuous isotonic regression), use Lemma 2 from Anevski and Soulier [83] (see also [84]), where a characterization is given for the solution of our minimization problem. Integrating the empirical estimator in eq. (3.3.2) with respect to t , yields

$$U_n(t) = \int_{u=0}^t N_n(u) du = \int_{u=0}^t \frac{1}{n} \sum_{i=1}^n (Z_i - q(H_i; u))^{-\frac{1}{2}} 1_{[Z_i > q(H_i; u)]} du. \quad (3.3.6)$$

Then, define U_n^* to be the least concave majorant of U_n , enforcing monotonicity of its derivative. Finally, for $t \geq 0$, $\hat{N}_n(t) = U_n^{*,r}(t)$ is the right hand derivative of U_n^* evaluated at t .

Sections 3.4 and 3.5 will consider the rates of convergence asymptotic and distributions for the plug-in estimators and the isotonic estimator in turn.

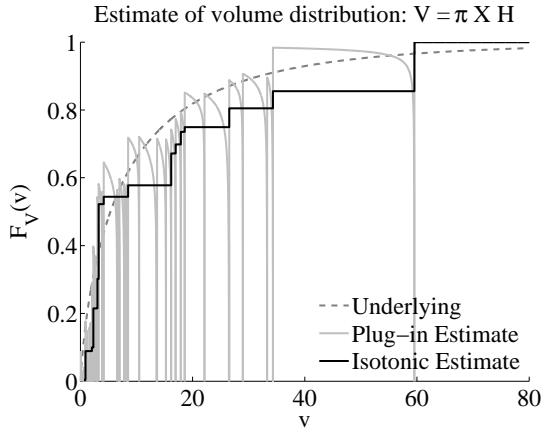


FIGURE 3.3.1: The estimates for the underlying distribution of the volume (given by the physical simulation in Section 4.2) for $n = 50$ cylinders. The underlying distribution is given by the dashed grey line, the empirical plug-in estimate is given by the solid light grey line, and the isotonic estimate is given by the solid black line.

3.4 Asymptotic distributions of the Plug-in Estimators

There are a few assumptions on the observed variables that are required for the derivation of consistency and the various asymptotic distributions to hold.

Assumption 3.4.1. $0 < E_g \left[Z^{-\frac{1}{2}} \right] < \infty$. Equivalently, via eq. (3.2.1) and eq. (3.2.8): $0 < E_f \left[\sqrt{X} \right] < \infty$

Assumption 3.4.2. $E_g[H^{5+\epsilon}] < \infty$ for some $\epsilon > 0$

Assumption 3.4.3. $E_g \left[Z^{-\frac{1}{2}} H \right] < \infty$

Under Assumptions 3.4.1, 3.4.2, and 3.4.3, the plug-in estimators for the distribution function of H , the quantities $N(t)$ for X , R , S and V (for fixed t), and the covariance in eq. (3.3.1), eq. (3.3.2) and eq. (3.3.4), respectively, are consistent by the law of large numbers. From eq. (3.2.1), eq. (3.2.2) and eq. (3.2.8) it follows that the random variables $Z^{-\frac{1}{2}}$, $HZ^{-\frac{1}{2}}$ and $[Z - q(H; t)]^{-\frac{1}{2}} 1_{[Z > q(H; t)]}$ have infinite variances. This means that the standard (finite variance) central limit theorem cannot be used to derive relevant asymptotic distributions. The theorem below states a central limit result for random variables with infinite variances that will be needed in the sequel.

Theorem 3.4.1. Let Y_i , for $i = 1, 2, \dots$, be i.i.d. random variables. Denote the distribution of Y_i by K and define $\bar{Y}_n = \frac{1}{n} \sum_{i=1}^n Y_i$. If $E_K[Y_i] < \infty$ and $P_K(Y_i > c) \sim \frac{\kappa}{c^2}$ as $c \rightarrow \infty$ and $E_K[Y_i^2 1_{[Y_i \in [0, c]]}] \sim \kappa \ln(c^2)$, where $\kappa > 0$ is a constant, then

$$\sqrt{\frac{n}{\ln(n)}} (\bar{Y}_n - E_K[Y_i]) \rightsquigarrow \mathcal{N}(0, \kappa).$$

Proof. Theorem 4 from Chapter 9 of Chow & Teicher [85] is used (for completeness it is restated in Appendix A.1). To this end, note that because $P_K(Y_i > c) \sim \frac{\kappa}{c^2}$ and $E_K[Y_i^2 1_{[Y_i \in [0, c]]}] \sim \kappa \ln(c^2)$, the following condition holds:

$$\lim_{c \rightarrow \infty} \frac{\int_{|y| > c} dK(y)}{\frac{1}{c^2} \int_{|y| < c} y^2 dK(y)} = \lim_{c \rightarrow \infty} \frac{P(Y_i > c)}{\frac{1}{c^2} E_K[Y_i^2 1_{[Y_i \in [0, c]]}]} = \lim_{c \rightarrow \infty} \frac{\kappa}{\kappa \ln(c^2)} = 0.$$

Now, choose $c_n = \sqrt{n \ln(n) \kappa}$ and define $A_n = \frac{n}{B_n} \int_{|y| < B_n} y dK(y)$ and $B_n = \sup \left\{ c : \frac{1}{c^2} \int_{|y| < c} y^2 dK(y) \geq \frac{1}{n} \right\}$. This leads to $B_n \sim c_n$ and $A_n \sim$

$\sqrt{\frac{n}{\ln(n)\kappa}}E_K[Y_i]$ for $n \rightarrow \infty$ since $E_K[Y_i] < \infty$. Consequently, the central limit theorem holds where, for $y \in \mathbb{R}$,

$$\lim_{n \rightarrow \infty} P\left(\frac{1}{B_n} \sum_{i=1}^n Y_i - A_n < y\right) = \lim_{n \rightarrow \infty} P\left(\sqrt{\frac{n}{\ln(n)\kappa}}(\bar{Y}_n - E_K[Y_i]) < y\right) = \Phi(y),$$

where Φ is the CDF of the standard normal distribution. □

3.4.1 Asymptotic distributions for the estimators of $N(t)$ and $F(t)$

Using Theorem 3.4.1, the asymptotic distribution for estimators of $N(t)$ are derived for the various choices of q given in eq. (3.2.4). Define the marginal density function of the random variable Z shifted by the quantity of interest $q(H; t)$ as

$$\tau_q(z) = \tau_{q(\cdot; t)} = \int_{h=0}^{\infty} g(z + q(h; t), h) dh. \tag{3.4.1}$$

Assumption 3.4.4. τ'_q is continuous and uniformly bounded by some $M < \infty$ in a right neighborhood of 0.

If Assumption 3.4.4 holds, then eq. (3.4.1) has the important property that for $\delta \downarrow 0$,

$$\int_{z=0}^{\delta} \tau_q(z) dz = \delta \tau_q(0) + o(\delta) \tag{3.4.2}$$

Theorem 3.4.2. Let (Z_i, H_i) ($i = 1, 2, \dots$) be an i.i.d. sequence with density g given in eq. (3.2.1), $t \geq 0$ fixed, and let q be any of the choices given by eq. (3.2.4). Furthermore, let N_n be defined as in eq. (3.3.2) and let Assumption 3.4.1 hold and Assumption 3.4.4 be satisfied for $q(\cdot; t)$ and g . Then

$$\sqrt{\frac{n}{\ln(n)}}(N_n(t) - N(t)) \rightsquigarrow \mathcal{N}(0, \tau_q(0)). \tag{3.4.3}$$

Proof. Define the i.i.d. sequence Y_1, Y_2, \dots by $Y_i = [Z_i - q(H_i; t)]^{-\frac{1}{2}} 1_{[Z_i > q(H_i; t)]}$ for $i = 1, 2, \dots$ with distribution function K_Y . Note that $N_n(t) = n^{-1} \sum_{i=1}^n Y_i$ and $E[Y_i] = N(t) < \infty$ by Assumption 3.4.1 and eq. (3.2.7). Using eq. (3.4.2),

the tail probabilities of Y_i behave like

$$\begin{aligned}
 P(Y_i > y) &= P\left(\frac{1_{[Z_i > q(H_i; t)]}}{\sqrt{Z_i - q(H_i; t)}} > y\right) = P\left(q(H_i; t) < Z_i < \frac{1}{y^2} + q(H_i; t)\right) \\
 &= \int_{h=0}^{\infty} \int_{z=q(h; t)}^{\frac{1}{y^2} + q(h; t)} g(z, h) dz dh = \int_{h=0}^{\infty} \int_{z=0}^{\frac{1}{y^2}} g(z + q(h; t), h) dz dh \\
 &= \int_{z=0}^{\frac{1}{y^2}} \int_{h=0}^{\infty} g(z + q(h; t), h) dz dh = \int_{z=0}^{\frac{1}{y^2}} \tau_q(z) dz \\
 &= \frac{1}{y^2} \tau_q(0) + o(y^{-2}).
 \end{aligned}$$

By applying eq. (3.4.2) as $y \rightarrow \infty$ it is seen that $\kappa = \tau_q(0)$ in Theorem 3.4.1. The expectation of Y_i^2 truncated at $c_n = \sqrt{n \ln(n)} \kappa$ is

$$E[Y_i^2 1_{Y_i \in [0, c_n]}] = \int_{y=0}^{c_n} y^2 dK_Y(y) = \int_{y=0}^{c_n} 2y (K_Y(c_n) - K_Y(y)) dy \sim \ln(c_n^2) \tau_q(0). \quad (3.4.4)$$

(The above relationship is proven in Appendix A.2.1.) Therefore, from Theorem 3.4.1 the result follows. \square

By Theorem 3.4.2, the asymptotic variances for the estimators $N_n(t)$ based on the quantities q for the squared radius, aspect ratio, surface area and volume, respectively, are given by

$$\begin{aligned}
 \int_{h=0}^{\infty} g(t, h) dh &= g_Z(t), \quad \int_{h=0}^{\infty} g(h^2 t^2, h) dh, \quad (3.4.5) \\
 \int_{h=0}^{\infty} g\left(\left[\sqrt{\frac{h^2}{4} + \frac{t}{2\pi}} - \frac{h}{2}\right]^2, h\right) dh &\text{ and } \int_{h=0}^{\infty} g\left(\frac{t}{\pi h}, h\right) dh.
 \end{aligned}$$

Note that for the squared radius, result eq. (3.4.5) is not new. Since it is independent of height, this result is the same as the result stated in Theorem 2 by Groeneboom and Jongbloed [22] for spherical particles in Wicksell's problem. The asymptotic distributions of $N_n(t)$ can be used to obtain the asymptotic distributions of the corresponding distribution functions of interest, evaluated at t . Note that for all choices of q in eq. (3.2.4), $N_n(0) = \frac{1}{n} \sum_{i=1}^n Z_i^{-\frac{1}{2}}$ and $N(0) = E_g \left[Z^{-\frac{1}{2}} \right] = m_G^- = \pi / (2m_F^+)$.

Corollary 3.4.1. *Based on the estimators $N_n(t)$ of Theorem 3.4.2, define $F_n(t) = 1 - N_n(t)/N_n(0)$ as estimator for F_T defined in eq. (3.2.5). Then, under the conditions of Theorem 3.4.2, for $n \rightarrow \infty$*

$$\sqrt{\frac{n}{\ln(n)}} (F_n(t) - F(t)) \rightsquigarrow \mathcal{N}\left(0, \frac{N(0)^2 \tau_q(0) + N(t)^2 g_Z(0)}{N(0)^4}\right) \quad (3.4.6)$$

The proof follows from Theorem 3.4.2 using Slutsky's lemma.

3.4.2 Asymptotic distribution for the estimator of the covariance

Finding the asymptotic distribution of the covariance estimator is more complicated than for any single expectation estimator. Therefore, this asymptotic distribution is considered first and the results are then applied to the simpler estimators for the various expectations. From Assumption 3.4.2 the variance of H is finite. Therefore, the standard central limit theorem for finite variance random variables holds for the sample mean of the H_i 's and an approximating quantity is defined for the covariance that depends only on the terms involving $Z^{-\frac{1}{2}}$ (compared to eq. (3.3.4)):

$$\tilde{\sigma}_{\sqrt{X}H} = \frac{(\pi/2)E_g[H_i]}{n^{-1} \sum_{i=1}^n Z_i^{-\frac{1}{2}}} - \frac{\pi/2}{n^{-1} \sum_{i=1}^n Z_i^{-\frac{1}{2}}} \frac{\sum_{i=1}^n H_i Z_i^{-\frac{1}{2}}}{\sum_{i=1}^n Z_i^{-\frac{1}{2}}}.$$

Note that $\delta_n^{-1} (\hat{\sigma}_{\sqrt{X}H} - \tilde{\sigma}_{\sqrt{X}H}) \xrightarrow{P} 0$, where $\delta_n = \sqrt{\frac{\ln(n)}{n}}$. Hence, to derive the asymptotic distribution of $\delta_n^{-1} (\hat{\sigma}_{\sqrt{X}H} - \sigma_{\sqrt{X}H})$, it suffices to derive the asymptotic distribution of $\delta_n^{-1} (\tilde{\sigma}_{\sqrt{X}H} - \sigma_{\sqrt{X}H})$. Considering this distribution, define the function $\phi : (0, \infty)^2 \mapsto \mathbb{R}$ as

$$\phi(u, v) = \frac{\pi}{2} \left(\frac{E_g[H]}{u} - \frac{v}{u^2} \right).$$

Moreover, define

$$T_n = \frac{1}{n} \sum_{i=1}^n \begin{pmatrix} Z_i^{-\frac{1}{2}} \\ H_i Z_i^{-\frac{1}{2}} \end{pmatrix}, \quad (3.4.7)$$

leading to $\tilde{\sigma}_{\sqrt{X}H} = \phi(T_n)$. In order to pin down the asymptotic variance of $\tilde{\sigma}_{\sqrt{X}H}$ two more assumptions and the following lemma are required.

Assumption 3.4.5. $\xi_g^j = \int_{h=0}^{\infty} h^j g(0, h) dh < \infty$ for $j = 0, 1, 2$

Assumption 3.4.6. For some constant $K < \infty$, $|\frac{\partial}{\partial z}g(z, h)| \leq K$ for all $z, h \geq 0$

Lemma 3.4.1. Let T_n be as defined in eq. (3.4.7). Assume that Assumptions 3.4.1, 3.4.2, 3.4.3, 3.4.5 and 3.4.6 hold, then

$$\delta_n^{-1} (T_n - E_g[T_n]) \rightsquigarrow \mathcal{N}(0, \Xi), \quad \text{where} \quad \Xi = \begin{pmatrix} \xi_g^0 & \xi_g^1 \\ \xi_g^1 & \xi_g^2 \end{pmatrix}. \quad (3.4.8)$$

The proof of this lemma can be found in Appendix A.2.2. Now apply the Δ -method to the quantity $\phi(T_n)$, yielding

$$\begin{aligned} \delta_n^{-1} (\tilde{\sigma}_{\sqrt{X}H} - \sigma_{\sqrt{X}H}) &= \delta_n^{-1} (\phi(T_n) - \phi(E_g[T_n])) \rightsquigarrow \mathcal{N}(0, \nu^2) \\ \text{where} \quad \nu^2 &= (\nabla\phi(E_g[T_n]))^T \Xi (\nabla\phi(E_g[T_n])) \\ \text{and} \quad \nabla\phi(u, v) &= \begin{pmatrix} \frac{\partial}{\partial u}\phi(u, v) \\ \frac{\partial}{\partial v}\phi(u, v) \end{pmatrix} = \frac{\pi}{2} \frac{1}{u^3} \begin{pmatrix} 2v - E_g[H]u \\ -u \end{pmatrix}. \end{aligned}$$

This provides ν^2 in terms of the joint densities of the observable variables:

$$\begin{aligned} \nu^2 &= \frac{\pi^2}{4 E_g^4[Z^{-\frac{1}{2}}]} \left\{ 4 \xi_g^0 \left(\frac{E_g^2[Z^{-\frac{1}{2}}H]}{E_g^2[Z^{-\frac{1}{2}}]} - \frac{E_g[Z^{-\frac{1}{2}}H] E_g[H]}{E_g[Z^{-\frac{1}{2}}]} + \frac{E_g^2[H]}{4} \right) \right. \\ &\quad \left. + 2 \xi_g^1 \left(E_g[H] - \frac{E_g[Z^{-\frac{1}{2}}H]}{E_g[Z^{-\frac{1}{2}}]} \right) + \xi_g^2 \right\}. \quad (3.4.9) \end{aligned}$$

Given the cross moment relationships in eq. (3.2.8) and that

$$\xi_g^j = \frac{E_f[X^{-\frac{1}{2}}H^j]}{2E_f[X^{\frac{1}{2}}]}, \quad (3.4.10)$$

ν^2 can also be expressed in terms of the underlying joint distribution of the

cylinder radii and heights:

$$\nu^2 = \frac{4 E_f^3 [X^{\frac{1}{2}}]}{\pi^2} \left\{ 4 E_f [X^{-\frac{1}{2}}] \left(E_f^2 [H] - \frac{E_f [H] E_f [X^{\frac{1}{2}} H]}{4 E_f [X^{\frac{1}{2}}]} + \frac{E_f^2 [X^{\frac{1}{2}} H]}{E_f^2 [X^{\frac{1}{2}}]} \right) + 2 E_f [X^{-\frac{1}{2}} H] \left(\frac{E_f [X^{\frac{1}{2}} H]}{E_f [X^{\frac{1}{2}}]} - E_f [H] \right) + E_f [X^{-\frac{1}{2}} H^2] \right\} \quad (3.4.11)$$

This proves the following theorem for the plug-in estimator for $\sigma_{\sqrt{XH}}$.

Theorem 3.4.3. *Let $\sigma_{\sqrt{XH}}$ and $\hat{\sigma}_{\sqrt{XH}}$ be defined as in eq. (3.2.9) and eq. (3.3.4), respectively. Under the assumptions of Lemma 3.4.1, for ν^2 defined in eq. (3.4.9) and eq. (3.4.11),*

$$\sqrt{\frac{n}{\ln n}} (\hat{\sigma}_{\sqrt{XH}} - \sigma_{\sqrt{XH}}) \rightsquigarrow \mathcal{N}(0, \nu^2) \text{ as } n \rightarrow \infty$$

3.4.3 Estimating the Expectations

From eq. (3.2.8) and eq. (3.3.3), it is simple to verify that the various 3D quantities of interest are given by the 2D observable quantities as follows (with

the empirical estimators given below the defined moments):

$$\begin{aligned}
 \text{Radius} \quad E_f \left[X^{\frac{1}{2}} \right] &= \frac{\pi}{2} \frac{1}{E_g \left[Z^{-\frac{1}{2}} \right]} \\
 &\rightarrow \hat{E}_f \left[X^{\frac{1}{2}} \right] = \frac{\pi}{2} \left(\frac{1}{n} \sum_{i=1}^n Z_i^{-\frac{1}{2}} \right)^{-1} \\
 \text{Squared Radius} \quad E_f[X] &= \frac{2E_g \left[Z^{\frac{1}{2}} \right]}{E_g \left[Z^{-\frac{1}{2}} \right]} \\
 &\rightarrow \hat{E}_f[X] = \left(\frac{2}{n} \sum_{i=1}^n Z_i^{\frac{1}{2}} \right) \left(\frac{1}{n} \sum_{i=1}^n Z_i^{-\frac{1}{2}} \right)^{-1} \\
 \text{Height} \quad E_f[H] &= \frac{E_g \left[Z^{-\frac{1}{2}} H \right]}{E_g \left[Z^{-\frac{1}{2}} \right]} \\
 &\rightarrow \hat{E}_f[H] = \left(\frac{1}{n} \sum_{i=1}^n Z_i^{-\frac{1}{2}} H_i \right) \left(\frac{1}{n} \sum_{i=1}^n Z_i^{-\frac{1}{2}} \right)^{-1} \\
 \text{Volume} \quad \pi E_f[XH] &= \frac{2\pi E_g \left[Z^{\frac{1}{2}} H \right]}{E_g \left[Z^{-\frac{1}{2}} \right]} \\
 &\rightarrow \pi \hat{E}_f[XH] = \left(\frac{2}{n} \sum_{i=1}^n Z_i^{\frac{1}{2}} H_i \right) \\
 \text{Surface Area} \quad 2\pi \left(E_f[X] + E_f \left[X^{\frac{1}{2}} H \right] \right) &= 2\pi \left(\frac{2E_g \left[Z^{\frac{1}{2}} \right]}{E_g \left[Z^{-\frac{1}{2}} \right]} + \frac{\pi E_g[H]}{2E_g \left[Z^{-\frac{1}{2}} \right]} \right) \\
 &\rightarrow 2\pi \left(\hat{E}_f[X] + \hat{E}_f \left[X^{\frac{1}{2}} H \right] \right) = \\
 &= 2\pi \left[\left(\frac{2}{n} \sum_{i=1}^n Z_i^{\frac{1}{2}} H_i \right) \left(\frac{1}{n} \sum_{i=1}^n Z_i^{-\frac{1}{2}} \right)^{-1} + \left(\frac{\pi}{n} \sum_{i=1}^n H_i \right) \left(\frac{2}{n} \sum_{i=1}^n Z_i^{-\frac{1}{2}} \right)^{-1} \right] \\
 \text{Aspect Ratio} \quad E_f \left[X^{\frac{1}{2}} H^{-1} \right] &= \frac{\pi E_g \left[H^{-1} \right]}{E_g \left[Z^{-\frac{1}{2}} \right]} \\
 &\rightarrow \hat{E}_f \left[X^{\frac{1}{2}} H^{-1} \right] = \left(\frac{\pi}{n} \sum_{i=1}^n H_i^{-1} \right) \left(\frac{1}{n} \sum_{i=1}^n Z_i^{-\frac{1}{2}} \right)^{-1}
 \end{aligned} \tag{3.4.12}$$

Due to the dependence on H^{-1} of the aspect ratio, several more assumptions are required to continue this analysis. For brevity and simplicity, the expectation of the aspect ratio will not be considered any further.

To obtain the asymptotic distributions, Lemma 3.4.1 and the delta method can be used with the following assumption.

Assumption 3.4.7. $E_g \left[Z^{\frac{1}{2}} H^j \right] < \infty$ and $E_g \left[\left(Z^{\frac{1}{2}} H^j \right)^2 \right] < \infty$, where $j = 0, 1$.

Under Assumption 3.4.7, the expectations can be treated as constants in the modified function ϕ , as discussed for the expectation of the height in the previous section. The coefficients s and t for linearizing (3.4.7) are taken to be zero where appropriate. Then, the asymptotic variance for the estimation of the quantities of interest given above are:

Radius	$\nu_g^2 = \left(\frac{\pi}{2}\right)^2 \xi_g^0 \left(E_g \left[Z^{-\frac{1}{2}} \right]\right)^{-4}$
Squared Radius	$\nu_g^2 = 4\xi_g^0 \left(E_g \left[Z^{-\frac{1}{2}} \right]\right)^{-4} \left(E_g \left[Z^{\frac{1}{2}} \right]\right)^2$
Height	$\nu_g^2 = \left(E_g \left[Z^{-\frac{1}{2}} \right]\right)^{-4} \left\{ \xi_g^0 \left(E_g \left[Z^{-\frac{1}{2}} H \right]\right)^2 - 2\xi_g^1 E_g \left[Z^{-\frac{1}{2}} H \right] E_g \left[Z^{-\frac{1}{2}} \right] + \xi_g^2 \left(E_g \left[Z^{-\frac{1}{2}} \right]\right)^2 \right\}$
Volume	$\nu_g^2 = 4\pi^2 \xi_g^0 \left(E_g \left[Z^{-\frac{1}{2}} \right]\right)^{-4} \left(E_g \left[Z^{\frac{1}{2}} H \right]\right)^2$
Surface Area	$\nu_g^2 = \xi_g^0 \left(E_g \left[Z^{-\frac{1}{2}} \right]\right)^{-4} \left(4\pi E_g \left[Z^{\frac{1}{2}} \right] + \pi^2 E_g[H]\right)^2$

(3.4.13)

This leads to the following corollary to Theorem 3.4.3.

Corollary 3.4.2. Let $E_f[T]$ and $\widehat{E}_f[T]$ be defined as in eq. (3.4.12), where T is any of the quantities of interest listed in eq. (3.4.12). Under the assumptions of Lemma 3.4.1 and Assumption 3.4.7, for ν_g^2 as defined in eq. (3.4.13),

$$\sqrt{\frac{n}{\ln(n)}} \left(\widehat{E}_f[T] - E_f[T] \right) \rightsquigarrow \mathcal{N} \left(0, \nu_g^2 \right) \text{ as } n \rightarrow \infty$$

Theorem 3.4.3 and Corollary 3.4.2 can be used to obtain the 95% confidence intervals for the unknown expectations being estimated by $\widehat{E}_f[T]$:

$$\widehat{E}_f[T] \pm 1.96\nu_g \sqrt{\frac{\ln(n)}{n}}. \quad (3.4.14)$$

Here, the asymptotic variance depends on the moments of g as well as the ξ_g^j for $j = 0, 1, 2$. Theorem 3.4.3 and Corollary 3.4.2 show that the expectations of the quantities of interest can be estimated consistently with a rate of $\sqrt{\ln(n)/n}$. However, to use the asymptotic results to construct confidence intervals, the ξ_g^j must be known, which they are not. Therefore, in Section 3.4.4, an estimator for the ξ_g^j is considered.

3.4.4 Estimating ξ_g^j

Since $\xi_g^j = \int_{h=0}^{\infty} h^j g(0, h) dh$, and observations of $Z_i = 0$ have zero probability, a sequence $0 \leq b_n \downarrow 0$ is defined, where b_n is a bandwidth or cutoff value that will be used to estimate the density g on the line $z = 0$. With this, the following estimator can be defined:

$$\widehat{\xi}_g^j = \frac{1}{n} \sum_{i=1}^n H_i^j b_n^{-1} 1_{[0, b_n]}(Z_i). \quad (3.4.15)$$

Then

$$E \left[\widehat{\xi}_g^j \right] = \int_{h=0}^{\infty} h^j b_n^{-1} \int_{z=0}^{b_n} g(z, h) dz dh,$$

yielding a bias for the estimator of

$$\begin{aligned} E \left[\widehat{\xi}_g^j \right] - \xi_g^j &= \int_{h=0}^{\infty} h^j b_n^{-1} \int_{z=0}^{b_n} (g(z, h) - g(0, h)) dz dh \\ &= \int_{h=0}^{\infty} h^j b_n^{-1} \int_{z=0}^{b_n} z \frac{\partial}{\partial z} g(z, h) \Big|_{z=0} dz dh + o(b_n) \\ &= \frac{1}{2} b_n \int_{h=0}^{\infty} h^j \frac{\partial}{\partial z} g(z, h) \Big|_{z=0} dh + o(b_n) = c_g^j b_n + o(b_n). \end{aligned} \quad (3.4.16)$$

Note that the bias vanishes as the bandwidth goes to zero.

The variance of this estimator is found to be

$$\begin{aligned}
 \text{Var}(\widehat{\xi}_g^j) &= \text{Var}\left(\frac{1}{n} \sum_{i=1}^n b_n^{-1} H_i^j 1_{[0, b_n]}(Z_1)\right) = \frac{1}{nb_n^2} \text{Var}\left(H_1^j 1_{[0, b_n]}(Z_1)\right) \\
 &= \frac{1}{nb_n^2} \left\{ E\left[(H_1^j)^2 1_{[0, b_n]}(Z_1)\right] - \left(E\left[H_1^j 1_{[0, b_n]}(Z_1)\right]\right)^2 \right\} \\
 &= \frac{1}{nb_n^2} \left\{ E\left[H_1^{2j} 1_{[0, b_n]}(Z_1)\right] - \left(E\left[H_1^j 1_{[0, b_n]}(Z_1)\right]\right)^2 \right\} \\
 &= \frac{1}{nb_n^2} \left\{ b_n \xi_g^{2j} + b_n^2 c_g^{2j} + o(b_n^2) - [b_n \xi_g^j + b_n^2 c_g^j + o(b_n^2)]^2 \right\} \\
 &= \frac{1}{nb_n} \left\{ \xi_g^{2j} + b_n c_g^{2j} + o(b_n) - b_n (\xi_g^j)^2 - 2b_n^2 \xi_g^j c_g^j - b_n^3 (c_g^j)^2 + o(b_n^3) \right\} \\
 &= \frac{1}{nb_n} \left\{ \xi_g^{2j} + b_n (c_g^{2j} - (\xi_g^j)^2) + o(b_n) \right\} \\
 &= \frac{\xi_g^{2j}}{nb_n} + \frac{c_g^{2j} - (\xi_g^j)^2}{n} + o(b_n).
 \end{aligned} \tag{3.4.17}$$

Note that the variance increases as the bandwidth decreases. This is in contrast to the dependence of the bias on the bandwidth. Therefore, it is important to find the optimal bandwidth where the bias and the variance are balanced. The mean squared error (MSE) is a standard quantity used to find this optimum.

The MSE is defined as the variance plus the squared bias. In this case, asymptotically, it is

$$\text{MSE}(\widehat{\xi}_g^j) = \text{Var}(\widehat{\xi}_g^j) + \left(E[\widehat{\xi}_g^j] - \xi_g^j\right)^2 = \frac{\xi_g^{2j}}{nb_n} + \frac{c_g^{2j} - (\xi_g^j)^2}{n} + (c_g^j b_n)^2. \tag{3.4.18}$$

Balancing the squared bias and variance in the MSE suggests that the bandwidth $b_n \sim n^{-1/3}$. To find the optimal bandwidth, let $b_n = \tau n^{-1/3}$ and

minimize the MSE with respect to τ .

$$\begin{aligned}
 \text{MSE} &= \frac{\xi_g^{2j}}{n b_n} + \frac{c_g^{2j} - (\xi_g^j)^2}{n} + (c_g^j b_n)^2 \\
 &= \frac{\xi_g^{2j}}{n \tau n^{-\frac{1}{3}}} + \frac{c_g^{2j} - (\xi_g^j)^2}{n} + \left(c_g^j \tau n^{-\frac{1}{3}}\right)^2 \\
 \frac{\partial \text{MSE}}{\partial \tau} &= 0 = -\tau^{-2} \xi_g^{2j} n^{-\frac{2}{3}} + 0 + 2\tau n^{-\frac{2}{3}} (c_g^j)^2 \\
 2\tau n^{-\frac{2}{3}} (c_g^j)^2 &= \tau^{-2} \xi_g^{2j} n^{-\frac{2}{3}} \\
 \tau^3 &= \frac{\xi_g^{2j}}{2 (c_g^j)^2} \\
 \tau &= \left(\frac{\xi_g^{2j}}{2 (c_g^j)^2} \right)^{\frac{1}{3}}
 \end{aligned}$$

Therefore, the optimal bandwidth is

$$b_n = \tau n^{-\frac{1}{3}} = \left(\frac{\xi_g^{2j}}{2n (c_g^j)^2} \right)^{\frac{1}{3}} \quad (3.4.19)$$

leading to the optimal vanishing rate for the MSE of $\hat{\xi}_g^j$ to be $n^{-2/3}$. Therefore, ν_g for all quantities of interest eq. (3.4.13) can be estimated consistently, even at a rate of $n^{-1/3}$.

Define $\hat{\nu}_g$ as the estimate of ν_g that includes now $\hat{\xi}_g^j$ along with the empirical means as estimators T_n for the expectations and covariance. Then, the following set,

$$\left[T_n - 1.96 \hat{\nu}_g \sqrt{\frac{\ln(n)}{n}}, T_n + 1.96 \hat{\nu}_g \sqrt{\frac{\ln(n)}{n}} \right] \quad (3.4.20)$$

constructs an approximate 95% confidence interval for the expectations and covariance. This confidence interval is important when assessing the results of the model applied to the steel microstructures in Chapter 4.

3.4.5 Asymptotic distribution for the estimator of the height distribution

Consider the plug-in estimator for the distribution function of heights, given in eq. (3.3.1). As mentioned before, under Assumption 3.4.2, the law of large numbers immediately gives that $\widehat{F}_{H,n}(h) \xrightarrow{P} F_H(h)$ as $n \rightarrow \infty$. The asymptotic distribution is given in the theorem below.

Theorem 3.4.4. *Consider $F_H(h)$ and $\widehat{F}_{H,n}(h)$ as given in eq. (3.2.3) and eq. (3.3.1), respectively. Under Assumptions 3.4.1 and 3.4.5,*

$$\sqrt{\frac{n}{\ln n}} \left(\widehat{F}_{H,n}(h) - F_H(h) \right) \rightsquigarrow \mathcal{N}(0, \nu^2)$$

where

$$\nu^2 = 4m_F^{+2} \left(F_H(h) \int_h^\infty g(0, y) dy + (1 - F_H(h)) \int_0^h g(0, y) dy \right) / \pi^2. \tag{3.4.21}$$

Proof. Consider the random vectors

$$T_n = \frac{1}{n} \sum_{i=1}^n \begin{pmatrix} Z_i^{-\frac{1}{2}} \\ Z_i^{-\frac{1}{2}} 1_{[H_i < h]} \end{pmatrix}$$

with

$$E [T_n] = \begin{pmatrix} \pi / (2m_F^+) \\ \int_{z=0}^\infty \int_{v=0}^h z^{-\frac{1}{2}} g(z, v) dv dz \end{pmatrix}.$$

For T_n it is shown in Appendix A.2.3 that

$$\sqrt{\frac{n}{\ln n}} (T_n - E [T_n]) \rightsquigarrow \mathcal{N}(0, \Xi) \tag{3.4.22}$$

where the entries of Ξ are given by $\xi_{12} = \xi_{21} = \xi_{22} = \int_{y=0}^h g(0, y) dy$ and $\xi_{11} = g_Z(0)$. The result follows by applying the Δ -method to the function $\phi(u, v) = v/u$ at T_n , yielding asymptotic normality with variance ν^2 . \square

3.5 Asymptotic distributions of the Isotonic Estimators

In this section, the consistency and asymptotic behavior of the isotonic estimators, \widehat{N}_n , as described in Section 3.3 are studied. To do so requires one further assumption and the subsequent lemma.

Assumption 3.5.1. $\int_0^\infty N(t) dt < \infty$

Lemma 3.5.1. Let $U_n(t)$ given in eq. (3.3.6) be the empirical estimator of $U(t) = \int_{u=0}^t N(u) du$. Suppose that assumption 3.5.1 holds. Then,

$$\widehat{N}_n(t) \rightarrow N(t) \text{ a.s. for all } t \geq 0. \quad (3.5.1)$$

Proof. Fix $t > 0$. The estimator $U_n(t)$ is consistent by the strong law of large numbers. Since $U_n(t)$ and U are monotone increasing, continuous and bounded, this implies

$$\sup_{t \in [0, \infty)} |U_n(t) - U(t)| \rightarrow 0, \text{ a.s.} \quad (3.5.2)$$

Since U is a concave function, for any $\epsilon > 0$, $U \pm \epsilon$ are also concave functions. Therefore, almost surely, for all n sufficiently large,

$$U - \epsilon \leq U_n \leq U + \epsilon \quad \implies \quad U - \epsilon \leq U_n^* \leq U + \epsilon$$

as U_n^* is the *least* concave majorant of U_n . Since this holds for each $\epsilon > 0$, this leads to

$$\sup_{t \in [0, \infty)} |U_n^*(t) - U(t)| \rightarrow 0$$

with probability one. Arguing as Robertson *et al.* do in Lemma 7.2.1 [86] implies eq. (3.5.1).

For $t = 0$, a different argument is needed. Note that

$$\widehat{N}_n(0) = \lim_{t \downarrow 0} \frac{U_n^*(t)}{t} = \sup_{t > 0} \frac{U_n(t)}{t},$$

so that

$$\left| \widehat{N}_n(0) - N(0) \right| = \left| \sup_{t > 0} \frac{U_n(t)}{t} - \sup_{t > 0} \frac{U(t)}{t} \right| \leq \sup_{t > 0} \left| \frac{U_n(t) - U(t)}{t} \right|. \quad (3.5.3)$$

Using the empirical process notation also used by Kosorok [87], one can write for any choice for q

$$\frac{U_n(t) - U(t)}{t} = (\mathbb{P}_n - P)\phi_t,$$

where \mathbb{P}_n denotes the empirical distribution of the observed pairs (Z_i, H_i) and P the corresponding underlying joint distribution of (Z, H) (with density g). For example, for the volume

$$\phi_t(z, h) = \frac{2\pi h}{t} \left(\sqrt{z} - \sqrt{z - \frac{t}{\pi h}} 1_{[z > t/(\pi h)]} \right). \tag{3.5.4}$$

In view of eq. (3.5.3), it suffices to show that the classes $\Phi = \{\phi_t : t > 0\}$, for all quantities of interest T , are Glivenko-Cantelli. For this, note that ϕ_t can be viewed as the minimum of two functions $\phi_t^{(1)}$ and $\phi_t^{(2)}$. For eq. (3.5.4) one can take

$$\begin{aligned} \phi_t^{(1)}(z, h) &= \frac{2\pi h}{t} \sqrt{z} \quad \text{and} \\ \phi_t^{(2)}(z, h) &= \frac{2\pi h}{\sqrt{t}} 1_{[0 < z \leq t/(\pi h)]} + \frac{2\pi h}{t} \left(\sqrt{z} - \sqrt{z - \frac{t}{\pi h}} \right) 1_{[z > t/(\pi h)]}. \end{aligned}$$

Therefore, $\Phi \subset \Phi^{(1)} \wedge \Phi^{(2)}$, where $\Phi^{(1)}$ and $\Phi^{(2)}$ are Vapnik-Červonenkis (VC). Kosorok’s preservation Lemma 9.9 [87], implies that $\Phi^{(1)} \wedge \Phi^{(2)}$ is also VC. Hence, Φ is VC. It is also straightforward to show that Φ has an integrable envelope (for the class corresponding to the volume, $(z, h) \mapsto z^{-1/2}$ can be chosen). By Theorem 9.3 from Kosorok [87], it can be concluded that the class Φ is Glivenko-Cantelli. \square

Theorem 3.5.1. *Suppose $t \geq 0$ and F_T from eq. (3.2.5) has a density f that is strictly positive and continuous in a neighborhood of t (a right neighborhood if $t = 0$) and that $q(h; t)$ is defined as in eq. (3.2.4). Further, suppose that Assumptions 3.4.1, 3.4.4 and 3.5.1 hold. Then,*

$$\sqrt{\frac{n}{\ln n}} \left(\hat{N}_n(t) - N(t) \right) \rightsquigarrow \mathcal{N} \left(0, \frac{1}{2} \tau_q(0) \right) \tag{3.5.5}$$

as $n \rightarrow \infty$.

The striking difference with Theorem 3.4.2 is the factor 1/2 in the asymptotic variance. This means that enforcing monotonicity in the estimator both improves on the empirical estimator because the resulting estimator satisfies the natural monotonicity constraint, and leads to a more accurate estimator asymptotically.

Proof. Recall that $U(t) = \int_{y=0}^t N(y) dy$ and $U_n(t) = \int_{y=0}^t N_n(y) dy$. Given this, the definitions for the isotonic estimator given in Section 3.3, and defining

the term ‘slocom’ as the slope of the least concave majorant, can be written as follows:

$$\delta_n^{-1} [U_n^{*,r}(t) - N(t)] = \text{slocom} [v \mapsto \delta_n^{-2} (U_n(t + \delta_n v) - U_n(t) - N(t)\delta_n v)], \quad (3.5.6)$$

where δ_n is a vanishing sequence of positive numbers. Here properties of convex minorants are used, e.g. that adding an affine function to U_n only changes the derivative of its concave majorant by adding the slope of the affine function to it. Using that N is continuously differentiable in a neighborhood of t , $U'(t) = N(t)$ and Taylor’s formula, the term inside the slocom can be approximated by the sum of a random term and a deterministic term:

$$\begin{aligned} \delta_n^{-2} \{[U_n(t + \delta_n v) - U(t + \delta_n v)] - [U_n(t) - U(t)]\} + \frac{v^2}{2} U''(t) + o(1) \\ = W_n(v) + \frac{v^2}{2} U''(t) + o(1), \quad (3.5.7) \end{aligned}$$

where the $o(1)$ term converges to zero uniformly on compacta. The random term $W_n(v)$ has an expected value of zero since $E[N_n(t)] = N(t)$. This function can be written as

$$\begin{aligned} W_n(v) &= \delta_n^{-2} \{[U_n(t + \delta_n v) - U(t + \delta_n v)] - [U_n(t) - U(t)]\} \\ &= \delta_n^{-2} \int_{y=t}^{t+\delta_n v} [N_n(y) - N(y)] dy \\ &= \delta_n^{-2} \int_{h=0}^{\infty} \int_{z=0}^{\infty} \int_{y=t}^{t+\delta_n v} [z - q(h; y)]^{-\frac{1}{2}} 1_{[z > q(h; y)]} dy d(\mathbb{G}_n - G)(z, h) \\ &= \delta_n^{-2} \int_{h=0}^{\infty} \int_{z=0}^{\infty} \phi_{n,v}(z, h) d(\mathbb{G}_n - G)(z, h) \\ &= \delta_n^{-2} \left\{ \int_{h=0}^{\infty} \int_{z=0}^{\infty} \phi_{n,v}(z, h) d\mathbb{G}_n(z, h) - E[\phi_{n,v}](Z, H) \right\}. \end{aligned}$$

To determine the asymptotic behavior of W_n , turn now to the functions $\{\phi_{n,v} : v \in \mathbb{R}\}$ and obtain $\text{Cov}(\phi_{n,u}(Z, H), \phi_{n,v}(Z, H))$ for $u \leq v$.

To find the expectation of the product $\phi_{n,u}\phi_{n,v}$ begin by writing

$$\phi_{n,v}(z, h)\phi_{n,u}(z, h) = \int_{w=t}^{t+\delta_n v} \frac{1_{[z > q(h; w)]}}{\sqrt{z - q(h; w)}} dw \int_{y=t}^{t+\delta_n u} \frac{1_{[z > q(h; y)]}}{\sqrt{z - q(h; y)}} dy.$$

Applying the change of variables from eq. (A.2.6) gives

$$\begin{aligned} & \phi_{n,v}(z, h)\phi_{n,u}(z, h) \\ &= \int_{x=q(h;t)}^{q(h;t+\delta_n v)} \frac{\dot{p}(h; x)}{\sqrt{z-x}} 1_{[z>x]} dx \int_{m=q(h;t)}^{q(h;t+\delta_n u)} \frac{\dot{p}(h; m)}{\sqrt{z-m}} 1_{[z>x]} dm \\ &= \int_{x=q(h;t)}^{q(h;t+\delta_n v)} \int_{m=q(h;t)}^{q(h;t+\delta_n u)} \frac{\dot{p}(h; x)\dot{p}(h; m)}{\sqrt{(z-x)(z-m)}} 1_{[z>m]} 1_{[z>x]} dm dx \end{aligned}$$

where $\dot{p}(h; u)$ eq. (A.2.2) is the derivative of $p(h; u)$ eq. (A.2.1) with respect to u . This leads to

$$E[\phi_{n,v}\phi_{n,u}] = \int_{h=0}^{\infty} \int_{z=0}^{\infty} \phi_{n,v}(z, h)\phi_{n,u}(z, h) g(z, h) dz dh.$$

From the indicator functions, the smallest value z can take on is the minimum of x and m . Therefore, the condition that $z > q(h; t)$ and the integral over $z \in [0, q(h; t)]$ is zero is needed. Break up the remaining portion of the integral over z , to obtain the following decomposition, recalling that $u \leq v$:

$$\begin{aligned} E[\phi_{n,v}\phi_{n,u}] &= \int_{h=0}^{\infty} \left\{ \int_{z=q(h;t)}^{q(h;t+\delta_n u)} \int_{x=q(h;t)}^z \int_{m=q(h;t)}^z \right. \\ &+ \left. \int_{z=q(h;t+\delta_n u)}^{q(h;t+\delta_n v)} \int_{x=q(h;t)}^z \int_{m=q(h;t)}^{q(h;t+\delta_n u)} + \int_{z=q(h;t+\delta_n v)}^{\infty} \int_{x=q(h;t)}^{q(h;t+\delta_n v)} \int_{m=q(h;t)}^{q(h;t+\delta_n u)} \right\} \\ &\quad \frac{\dot{p}(h; x)\dot{p}(h; m)}{\sqrt{(z-x)(z-m)}} dm dx g(z, h) dz dh. \end{aligned}$$

Define the function

$$\kappa_n(u; z, h, t) = \int_{m=q(h;t)}^{q(h;t+\delta_n u)} \frac{\dot{p}(h; m)}{\sqrt{z-m}} dm.$$

Given that $\delta_n \downarrow 0$, the first two integrals over z are negligibly small compared to the last term. Therefore, the last term dominates the expectation leading to

$$\begin{aligned} E[\phi_{n,v}\phi_{n,u}] &= \int_{h=0}^{\infty} \int_{z=q(h;t+\delta_n v)}^{\infty} \kappa_n(v; z, h, t)\kappa_n(u; z, h, t)g(z, h) dz dh + O(\delta_n^2) \\ &= I_n + o(\delta_n). \end{aligned}$$

Note that the functions $x \mapsto \dot{p}(h; x)$ in eq. (A.2.2) are constant or decreasing in x and from eq. (A.2.5) $\dot{p}(h; q(h; t)) = \dot{q}(h; t)^{-1}$. This means that

$$\begin{aligned} \dot{p}(h; q(h; t + \delta_n u)) \zeta_n(u; z, h, t) &= \frac{\zeta_n(u; z, h, t)}{\dot{q}(h; t + \delta_n u)} \leq \\ &\leq \kappa(u; z, h, t) \leq \dot{p}(h; q(h; t)) \zeta_n(u; z, h, t) = \frac{\zeta_n(u; z, h, t)}{\dot{q}(h; t)}, \end{aligned}$$

where

$$\begin{aligned} \zeta_n(u; z, h, t) &= \int_{m=q(h; t)}^{q(h; t + \delta_n u)} \frac{1}{\sqrt{z - m}} dm \\ &= 2 \left(\sqrt{z - q(h; t)} - \sqrt{z - q(h; t + \delta_n u)} \right) \\ &= 2\sqrt{z - q(h; t)} \left(1 - \sqrt{1 - \frac{q(h; t + \delta_n u) - q(h; t)}{z - q(h; t)}} \right) \\ &= 2\sqrt{z - q(h; t)} \left(1 - \sqrt{1 - \frac{\delta_n u \dot{q}(h; t)}{z - q(h; t)}} \right) \end{aligned}$$

This bounds the integral I_n as follows

$$\begin{aligned} &\int_{h=0}^{\infty} \frac{1}{\dot{q}(h; t + \delta_n v) \dot{q}(h; t + \delta_n u)} \\ &\quad \int_{z=q(h; t + \delta_n v)}^{\infty} \zeta_n(u; z, h, t) \zeta_n(v; z, h, t) g(z, h) dz dh \leq I_n \leq \\ &\leq \int_{h=0}^{\infty} \frac{1}{\dot{q}(h; t) \dot{q}(h; t)} \int_{z=q(h; t + \delta_n v)}^{\infty} \zeta_n(u; z, h, t) \zeta_n(v; z, h, t) g(z, h) dz dh. \end{aligned}$$

Focusing on the integral over z gives

$$\begin{aligned} &\int_{z=q(h; t + \delta_n v)}^{\infty} \zeta_n(u; z, h, t) \zeta_n(v; z, h, t) g(z, h) dz = 4 \int_{z=q(h; t + \delta_n v)}^{\infty} [z - q(h; t)] \times \\ &\quad \times \left(1 - \sqrt{1 - \frac{\delta_n u \dot{q}(h; t)}{z - q(h; t)}} \right) \left(1 - \sqrt{1 - \frac{\delta_n v \dot{q}(h; t)}{z - q(h; t)}} \right) g(z, h) dz. \end{aligned}$$

Using the Taylor expansion for a function $\alpha \mapsto \sqrt{1 + \alpha}$ near zero results in $\sqrt{1 + \alpha} = 1 + \alpha/2 - \xi_\alpha^2/8$ for $\xi_\alpha \in [0, \alpha]$. Apply this to the functions $\zeta_n(u; z, h, t)$ and obtain

$$\begin{aligned}
& \int_{z=q(h;t+\delta_n v)}^{\infty} \zeta_n(u; z, h, t) \zeta_n(v; z, h, t) g(z, h) dz dh = \\
& = 4 \int_{z=q(h;t+\delta_n v)}^{\infty} \frac{[z - q(h; t)]}{4} \left(\left[\frac{\delta_n u \dot{q}(h; t)}{z - q(h; t)} \right] \left[\frac{\delta_n v \dot{q}(h; t)}{z - q(h; t)} \right] \right) g(z, h) dz + O(\delta_n^2) \\
& = (\delta_n u)(\delta_n v) \dot{q}(h; t)^2 \int_{z=q(h;t+\delta_n v)}^{\infty} \frac{g(z, h)}{[z - q(h; t)]} dz + O(\delta_n^2) \\
& = -\delta_n^2 uv \dot{q}(h; t)^2 g(q(h; t), h) \ln(\delta_n) + O(\delta_n^2) \\
& = \frac{1}{2} \delta_n^2 uv \dot{q}(h; t)^2 g(q(h; t), h) \ln(\delta_n^{-2}) + O(\delta_n^2).
\end{aligned}$$

This leads to

$$\begin{aligned}
& \frac{1}{2} \delta_n^2 uv \ln(\delta_n^{-2}) \int_{h=0}^{\infty} \frac{\dot{q}(h; t)^2}{\dot{q}(h; t + \delta_n v) \dot{q}(h; t + \delta_n u)} g(q(h; t), h) dh + O(\delta_n^2) \leq \\
& \leq I_n \leq \frac{1}{2} \delta_n^2 uv \ln(\delta_n^{-2}) \int_{h=0}^{\infty} \frac{\dot{q}(h; t)^2}{\dot{q}(h; t)^2} g(q(h; t), h) dh + O(\delta_n^2).
\end{aligned}$$

Using the linear approximation of \dot{q} near t ,

$$\dot{q}(h; t + \delta_n v) = \dot{q}(h; t) + \ddot{q}(h; t) \delta_n v + o(\delta_n v) = \dot{q}(h; t) + O(\delta_n v),$$

the lower bound of I_n becomes

$$\begin{aligned}
& \frac{1}{2} \delta_n^2 uv \ln(\delta_n^{-2}) \int_{h=0}^{\infty} \frac{\dot{q}(h; t)^2}{\dot{q}(h; t)^2} g(q(h; t), h) dh + O(\delta_n^2) = \\
& = \frac{1}{2} \delta_n^2 uv \ln(\delta_n^{-2}) \int_{h=0}^{\infty} g(q(h; t), h) dh + O(\delta_n^2).
\end{aligned}$$

Finally yielding

$$E[\phi_{n,u}(Z, H) \phi_{n,v}(Z, H)] = \frac{1}{2} \delta_n^2 uv \ln(\delta_n^{-2}) \tau_q(0) + O(\delta_n^2).$$

This leads to a covariance of

$$\text{Cov}(\phi_{n,u}, \phi_{n,v}) = \frac{1}{2} \delta_n^2 uv \ln(\delta_n^{-2}) \tau_q(0) + O(\delta_n^2).$$

Therefore, $\delta_n = \sqrt{\frac{\ln(n)}{n}}$ is taken, the covariance for $W_n(u)$ and $W_n(v)$ is

$$\begin{aligned} \text{Cov}(W_n(u), W_n(v)) &= \delta_n^{-4} n^{-1} \text{Cov}(\phi_{n,u}, \phi_{n,v}) \\ &= \frac{uv}{2} \left[1 - \frac{\ln(\ln(n))}{\ln(n)} \right] \tau_q(0) + O\left(\frac{1}{\ln(n)}\right) \\ \text{and} \quad \text{Var}(W_n(v)) &= \frac{v^2}{2} \left[1 - \frac{\ln(\ln(n))}{\ln(n)} \right] \tau_q(0) + O\left(\frac{1}{\ln(n)}\right), \end{aligned}$$

which leads to

$$\begin{aligned} \text{Var}(vW_n(u) - uW_n(v)) &= \\ &= v^2 \text{Var}(W_n(u)) - 2uv \text{Cov}(W_n(u), W_n(v)) + u^2 \text{Var}(W_n(v)) \end{aligned}$$

From this, conclude that the finite dimensional distribution of W_n converges to the finite dimensional distribution of W , where W is defined on \mathbb{R} by $W(v) = vX$ with $X \sim \mathcal{N}(0, \frac{1}{2}\tau_q(0))$. Moreover, conclude that W_n converges to W in $C(\mathbb{R})$ equipped with the topology of uniform convergence on compacta. Following the same reasoning as in Lemma 4 from Groeneboom and Jongbloed [22], it follows that by taking some M sufficiently large, with probability arbitrarily close to one, the concave majorant of the function in eq. (3.5.7) will have at least one change of slope in $[-M, 0)$ and one in $(0, M]$. This implies that the topology of uniform convergence on compacta is strong enough to ensure convergence in distribution of the slocom of eq. (3.5.7) to slocom($v \mapsto vX + \frac{1}{2}v^2U''(t)$) = X . \square

Analogous to Corollary 3.4.1, is the following.

Corollary 3.5.1. *Suppose that $q(h; t) > 0$ for all h and $t > 0$, and that $F_T(t)$ has a density f which is strictly positive at t and continuous in a neighborhood of t . Then, under the assumptions of Theorem 3.5.1,*

$$\sqrt{\frac{n}{\ln(n)}} \left(1 - \frac{\hat{N}_n(t)}{\hat{N}_n(0)} - F_T(t) \right) \rightsquigarrow \mathcal{N} \left(0, \frac{N(0)^2 \tau_q(0) + N(t)^2 g_Z(0)}{2N(0)^4} \right) \quad (3.5.8)$$

as $n \rightarrow \infty$.

The proof of this corollary is analagous to the proof of Corollary 2 given in Groeneboom and Jongbloed [22], in our case applying Theorem 3.5.1 from above. Recall that consistency at zero follows from Lemma 3.5.1. Note, again, the factor of $\frac{1}{2}$ compared to eq. (3.4.6).

3.6 Discussion

There are two main ideas presented in this chapter. The first is the inverse problem addressed by the cylinder model. Often, it is difficult to know about the full 3D nature of a material or object being studied. Instead, the observations tend to be 2D slices through the material. In order to be able to say something about the 3D nature of the material, certain assumptions must be made. In the case of the Oriented Cylinder Model introduced in this chapter, the assumptions are that the objects in the material can be represented by circular cylinders whose axes of symmetry are all oriented in the same direction and that the cut through the material is along that axis. It is also assumed that the cylinders are uniformly distributed throughout the material. From this, the portions of the cylinders that have been intersected are observed as rectangles on the 2D slice. The width of the rectangle is directly related to the radius of the cylinder and the height of the rectangle is exactly the height of the cylinder. There is an inherent bias in these observations because cylinders with larger radii are more likely to be intersected when the material is sliced, and therefore the smaller cylinders are underrepresented by the observations on the slice. This bias can be accounted for.

In cases where the true underlying distribution of the radius and height of the cylinders is unknown, it can be estimated from the observed width and height of the rectangles. Equation (3.2.2) shows the known relationship between the joint probability density function, f , of the cylinder squared radius and height, (X, H) , and the joint probability density function, g of the rectangle squared half-width and height, (Z, H) . Using this equation turns out to be a bit difficult, but the cumulative distribution functions, F_X and F_H given by eqs. (3.2.5) and (3.2.3), respectively, are less so. Therefore, the focus is on estimating these distributions, and eventually the CDFs for the volume, squared radius and aspect ratio of the cylinders. However, it is also possible to calculate the expectations of these various quantities and the covariance between the radius and height of the cylinders. These quantities provide a summary of the interesting aspects of the cylinders in the box (the objects of interest in the material being represented by the cylinders). Equation (3.2.8) provides the relationship between the unobservable expectations of the cylinder quantities and the observable expectations of the rectangle quantities. Equation (3.2.9) takes those relationships and provides the covariance of the cylinder radius and height calculated from the expectations of the observable rectangles.

Focusing on eq. (3.2.5), the CDF of the squared radius (and eventually volume, squared radius and aspect ratio) can be broken down into the function $N(t)$ given in eq. (3.2.6) and a constant $N(0)$. The function $N(t)$ comes from

substituting eq. 3.2.2 for the joint pdf of the cylinder squared radius and height in eq. 3.2.5. Since the true underlying distribution of the rectangle width and height is generally unknown, $g(z, h)$ can be estimated by the empirical distribution which comes directly from the observations. This means that the function N can be estimated by $N_n(t)$ given in eq. 3.3.2. In this equation, the Z_i and H_i are the squared half-width and height of rectangle i observed on the 2D slice. Extending this idea to the other quantities, eq. (3.3.1) is the empirical estimator for the CDF of the height. Equation (3.3.3) provides the empirical estimator for the expectations in eq. (3.2.8), which are simply the empirical means of the quantities of interest, while eq. (3.3.4) provides the estimator for the covariance. Therefore, all of the quantities of interest related to the 3D cylinders can be estimated by plugging in the squared half-width and height observations of the 2D rectangles into the appropriate equations.

The only problem with these empirical estimators is that the function $N_n(t)$ has infinities that occur when the observed Z_i are equal to the variable t . This corresponds to a cylinder of radius t being cut exactly in the center. The CDF is always monotonic, meaning, in this case, that the function always increases with its independent variable. The empirical estimator of N is non-monotonic because of these discontinuities, leading to a non-monotonic estimate of the CDF. While this is not necessarily an unreasonable estimator, enforcing monotonicity might provide a better estimate. Therefore, the isotonic estimator given in eq. (3.3.6) and in the description following, is introduced. This estimator still uses the observed rectangle widths and heights as the only input variables, but it provides a monotonic estimate of the CDFs and, as discussed in the sequel, has a smaller asymptotic variance which makes it a better estimator than the empirical estimator.

The second idea presented in this chapter is that of the asymptotic variances and rates of convergence of the estimators. Together, these two quantities construct confidence intervals for the unknown quantities being estimated. From the various theorems and corollaries given in this chapter, every estimator has the same rate of convergence: $\sqrt{\ln(n)/n}$, where n is the number of observed rectangles. Equation (3.4.3) gives the asymptotic variance for the empirical estimator of N while eq. (3.5.5) gives it for the isotonic estimator. This, in turn leads to eqs. (3.4.6) and (3.5.8) for the asymptotic variances of the empirical and isotonic estimators of the CDFs of the various quantities of interest. Equation (3.4.9) gives the asymptotic variance for the empirical estimator of the covariance and eq. (3.4.13) gives the asymptotic variances for the empirical estimators of the expectations of interest. Finally, eq. (3.4.21) gives the asymptotic variance for the estimator of the CDF for the height of the cylinders.

While these asymptotic variances are all known, they are often functions of the unknown distributions or the unknown functions being estimated. This means that for all practical purposes, the asymptotic variances must also be estimated in order to be used for building confidence intervals or sets. For the asymptotic variances of the estimators of the various expectations, this can be done rather easily, especially with the estimators for the quantities ξ_g^j given in eq. (3.4.15). Obtaining confidence bands for the CDFs, on the other hand, is more difficult and not actually dealt with in this thesis.

Chapter 4 puts these two main ideas together and examines the obtainable results. This is done first through simulation, where the 3D distributions and expectations are known. Then, the model is applied to Steel A and Steel B, for which the distributions are unknown.

3.7 Conclusion

Oriented cylinders in an opaque medium that have been intersected by a cut plane have been considered. The distribution functions and expectations of various quantities of interest for the 3D cylinders can be estimated using the observed rectangle projections on the cut plane. The quantities of interest that have been considered are the squared radius, height, surface area and volume of the cylinders, as well as the covariance of the cylinder height and radius. All quantities have been shown to be estimated consistently, and the asymptotic behavior of the estimators has been derived. This leads to a construction of the 95% confidence intervals of the expectations. These estimators will be studied with simulations and applied to steel microstructures in the coming chapters.

4

Model Validation and Application to Dual Phase Steel

In this chapter, the mathematical model and estimation procedures developed in Chapter 3 are validated and illustrated using two different kinds of simulations. The first simulation is called the physical simulation where cylinders are distributed in a unit box. The second simulation is called the numerical simulation where observations are drawn from the mathematically related 2D and 3D distribution functions. These simulations demonstrate the advantage of using a non-parametric model. The asymptotic behavior of the model, as described in Chapter 3, is demonstrated with the simulations. The effectiveness of the model at estimating the underlying distributions as well as the expectations of the quantities of interest is also shown. Finally, the model is applied to the two banded microstructures introduced in previous chapters. These microstructures are considered both in 2D and in 3D, for which nearly 90 μm of depth have been observed via serial sectioning as described in Chapter 2.

4.1 Introduction

The model established in Chapter 3 was designed to provide valuable information about the three dimensional nature of the microstructures of Steel A and Steel B, shown in Figures 2.3.1 and 3.1.1, respectively. The bands, especially of Steel B, are thought to be plate-like and the bands seen in the micrographs are the rectangular sections observed on the cut plane. However, before applying the model to the steel microstructures, it will be validated through two different simulations. These simulations are set up to demonstrate the validity of the model and to explore the various results that the model puts forward.

Two different types of simulations are used to explore the model. The first simulates the physical system of the microstructure. The second simulation draws observations directly from the related underlying 2D and 3D distributions. The so-called physical simulation demonstrates the validity of the model under conditions similar to those arising from observing a single image of a microstructure, along with all the drawbacks of a finite 2D and 3D observation windows and finite cylinder sizes. The so-called numerical simulation demonstrates the validity of the model without the drawbacks associated with physical systems. It allows for outlier observations and demonstrates the ability of the model to encompass such outliers. The simulations use two different underlying distributions to demonstrate the advantage of the non-parametric model and its ability to successfully capture the behavior of the underlying marginal distributions. The simulations also demonstrate the effectiveness of the model at estimating the covariance of the height and radius of the cylinders, as well as the expectations of the quantities of interest. Finally, the model is applied to the steel microstructures and the results are considered in light of the simulation results.

4.2 Physical Simulation

The so-called physical simulation mimics the situation where cylinders, whose axes of symmetry are all oriented in the same direction, are placed inside of a box. The box is cut and portions of the intersected cylinders are observed as rectangles on the cut plane. This simulates the physical scenario of materials that have been cut and whose cut surface is prepared and observed via micrographic imaging. The physical simulation is set up in the following way. A unit box is used to represent the piece of material being observed. The bottom center of the cylinders are distributed with a Poisson process, i.e. they are independently, uniformly and randomly distributed inside the box. The radius of the cylinders are uniformly distributed on the interval $[a, b] = [0.1, 0.4]$. This interval was chosen to ensure that the cylinders were smaller than the

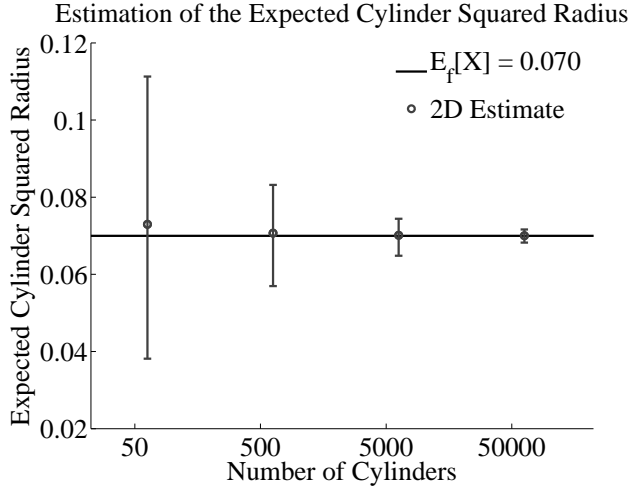
box, but not so small that the number of observations on the cut plane would be too low. The height of the cylinders is uniformly distributed on the interval $[0, c] = [0, 0.2]$. This interval was chosen to keep the heights less than the largest possible radius, and to ensure that the cylinders would be mostly plate-like with varying thickness. In this simulation, the heights and radii of the cylinders are independent. The joint density function of the cylinder squared radius and height is

$$f(x, h) = \frac{1}{2c(b-a)} x^{-\frac{1}{2}} = \beta x^{-\frac{1}{2}} \quad x \in [0.01, 0.16] \text{ and } h \in [0, 0.2]. \quad (4.2.1)$$

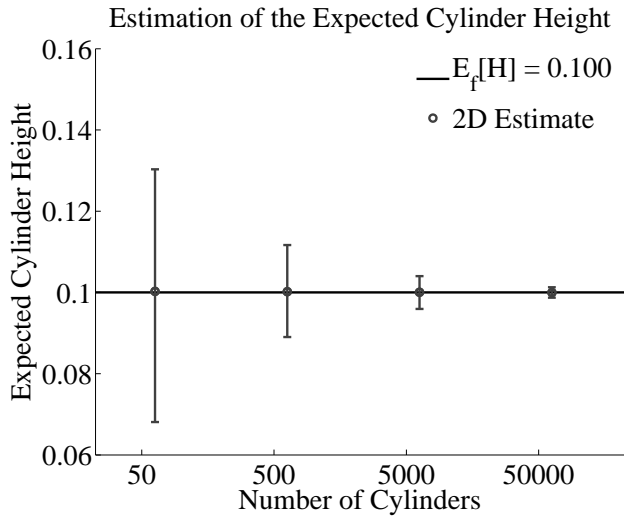
The box is sliced in a random location, parallel to the cylinder axes of symmetry and the rectangles observed on the plane are measured to obtain the pairs (Z, H) of the squared half-width and height. From these observations, the distribution functions and the expectations of the quantities of interest can be estimated and compared to the calculated underlying distributions and moments (see Appendix B.1.3). The only deviation of this simulation from a truly physical system is that no care is taken to keep the cylinders from overlapping. In a real physical system, it is often not possible to ascertain whether an observed object is actually two overlapping objects. In this simulation, there is no barrier to observing overlap, and so it is allowed.

Theorem 3.4.3 and Corollary 3.4.2 give the rate of convergence of the model as $\sqrt{\ln(n)/n}$ for the estimators of the 3D cylinder quantities using the 2D rectangle observations, where n is the number of 2D observations on the cut plane. Therefore, to explore this, the simulation is run with $N = 50, 500, 5000$ and 50000 cylinders in the box. Note that in this situation, n is always less than N . For each N , the simulation was run 1000 times. This allows the effect of the variance of the estimators to be observed. This is important for determining confidence intervals of the expected values, which, as in the case of the microstructures, must also be approximated when the underlying distribution is unknown. On average, over the 1000 simulation runs, the number of observations on the cut plane is roughly half of the number of cylinders in the box. Therefore, a direct comparison of the 2D estimation and the 3D estimation results is not reasonable, and so in what follows, only the 2D estimation results are shown.

Figures 4.2.1, 4.2.2 and 4.2.3 show the results of the estimations of the expectations eq. (3.4.12) and the covariance eq. (3.3.4) from the observed rectangle pairs (Z, H) . In all figures, the black line indicates the true expected value in 3D. The grey circles indicate the mean from the 1000 runs of the estimates of the expected values calculated from the 2D rectangle observations. The error bars span the 2.5 and 97.5 quantiles for the 1000 simulation runs.

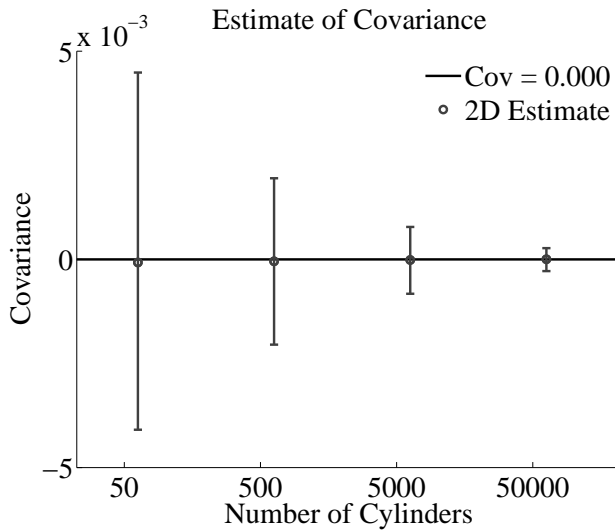


(A)

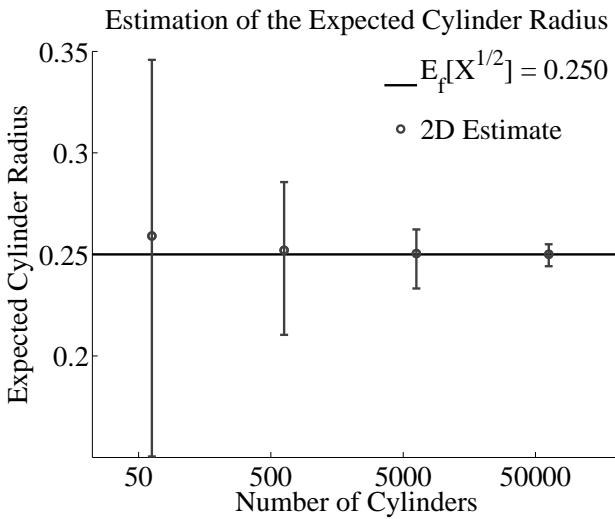


(B)

FIGURE 4.2.1: Estimate of the expected cylinder squared radius X and expected cylinder height H . The error bars span the 2.5 and 97.5 quantiles for the 1000 runs.

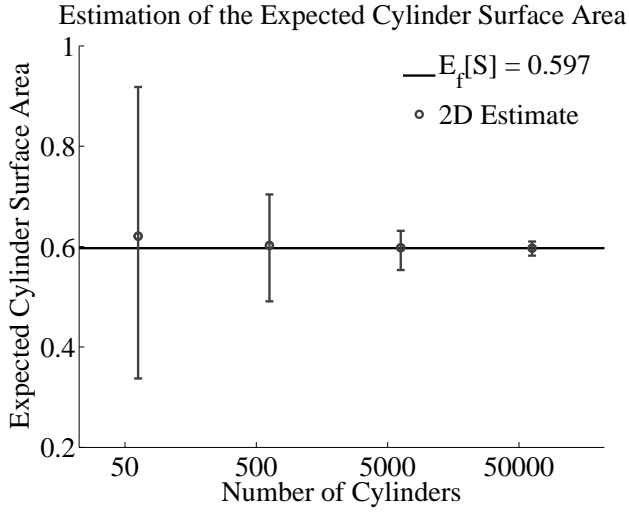


(A)

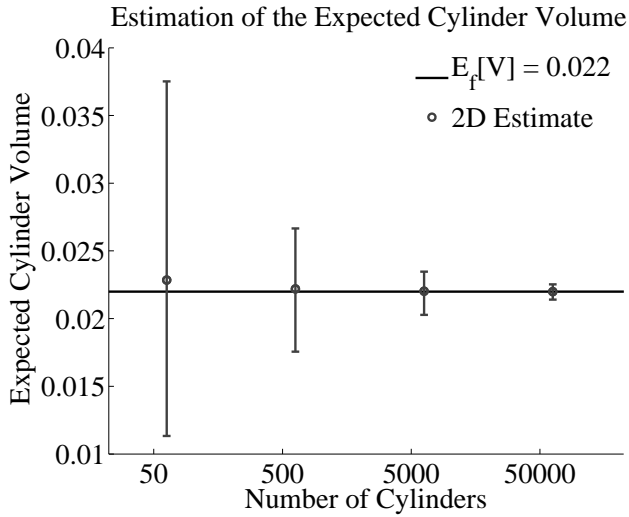


(B)

FIGURE 4.2.2: Estimate of the covariance of the cylinder radius and height and the expected cylinder radius, \sqrt{X} . The error bars span the 2.5 and 97.5 quantiles for the 1000 runs.



(A)



(B)

FIGURE 4.2.3: Estimate of the expected cylinder surface area, expected cylinder volume. The error bars span the 2.5 and 97.5 quantiles for the 1000 runs.

Mean Optimal Bandwidth for ξ_g^j			
N	$j = 0$	$j = 1$	$j = 2$
50	$(31 \pm 2) \times 10^{-3}$	$(34 \pm 2) \times 10^{-3}$	$(38 \pm 2) \times 10^{-3}$
500	$(145 \pm 2) \times 10^{-4}$	$(159 \pm 3) \times 10^{-4}$	$(176 \pm 3) \times 10^{-4}$
5000	$(672 \pm 3) \times 10^{-5}$	$(739 \pm 4) \times 10^{-5}$	$(8170 \pm 4) \times 10^{-5}$
50000	$(3117 \pm 4) \times 10^{-6}$	$(3431 \pm 5) \times 10^{-6}$	$(3792 \pm 6) \times 10^{-6}$

TABLE 4.1: Optimal bandwidths for estimating the ξ_g^j given for the four values of N , the number of cylinders per simulation. The number of rectangle observations is different for each of the 1000 simulation runs. Therefore, the reported optimal bandwidth is the mean optimal bandwidth for the 1000 runs plus or minus one standard deviation.

Corollary 3.4.2 shows the estimators to be asymptotically unbiased. From Figures 4.2.1a and 4.2.2b it is clear that care must be taken when assessing the results for small numbers of observations. Even though asymptotically the estimator is unbiased, due to a finite observation of a quantity with infinite variance, the estimate for any small set of observations could be biased.

The quantities ξ_g^j , for $j = 0, 1$, and 2 , given in eq. (3.4.8) are also important to estimate and validate. These quantities are necessary for constructing the confidence intervals of the expectations of real systems, like the steel microstructures. The estimators eq. (3.4.15) require a bandwidth, which can be thought of as a practical cutoff value for estimating the event where the rectangle half-width is equal to zero. The optimal bandwidth given in eq. (3.4.19) can be calculated for each simulation given the number of observations on the cut plane. Table 4.1 gives the mean optimal bandwidth for each of the estimators for each of the four values of N , along with one standard deviation. Looking down each column of the table shows that as the number of observations increases, the bandwidth does, indeed, become smaller and smaller. The expected rectangle squared half-width is 0.056 and for 50 cylinders (approximately 25 observed rectangles) the bandwidth is 0.031, a large fraction of the expected observation. As the number of observations goes up by an order of magnitude, the bandwidth slowly decreases. Figure 4.2.4 shows the results of these estimators. The black lines indicate the underlying value and the grey circles represent the mean of the estimation results for the 1000 runs. The error bars span the 2.5 and 97.5 quantiles for the 1000 runs. The bias in this estimator is evident. Despite the bias, the true expected value is always covered by the error bars and the bias is shown to be positive, giving an upper bound on the expected value from the estimate. This would lead to slightly larger confidence intervals for the estimates of the expectations eq. (3.4.13) and covariance eq. (3.4.9).

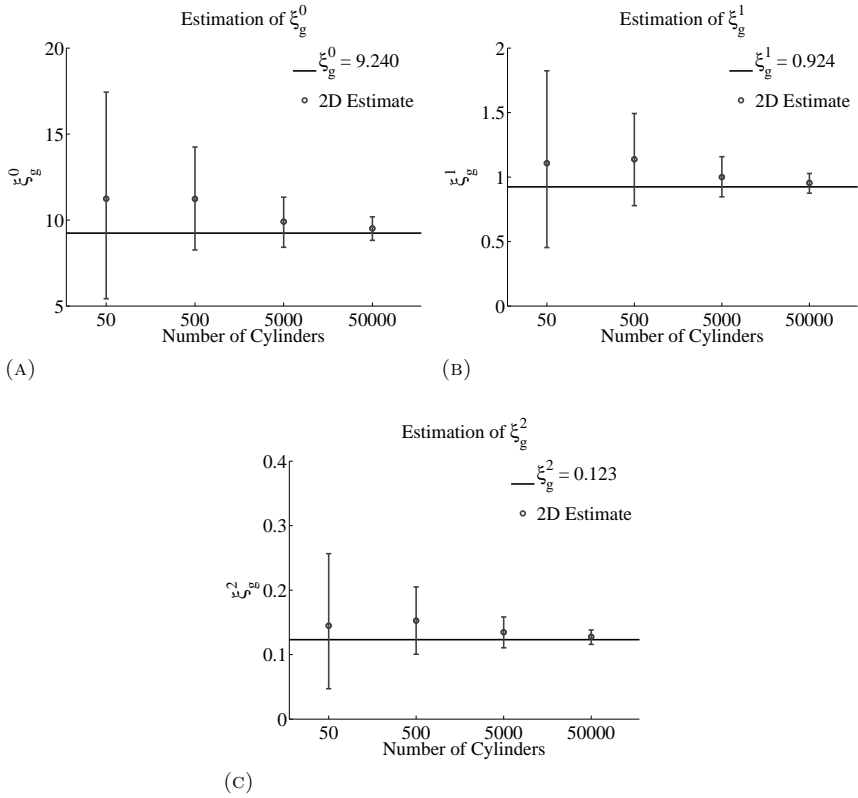


FIGURE 4.2.4: Estimate of the ξ_g^j quantities for $j = 0, 1, 2$ using the optimal bandwidth calculated from eq. (3.4.18) and the underlying distributions. The solid black line represents the underlying value and the grey circles represent the results from the estimator eq. (3.4.15). The bars span the 2.5 and 97.5 quantiles.

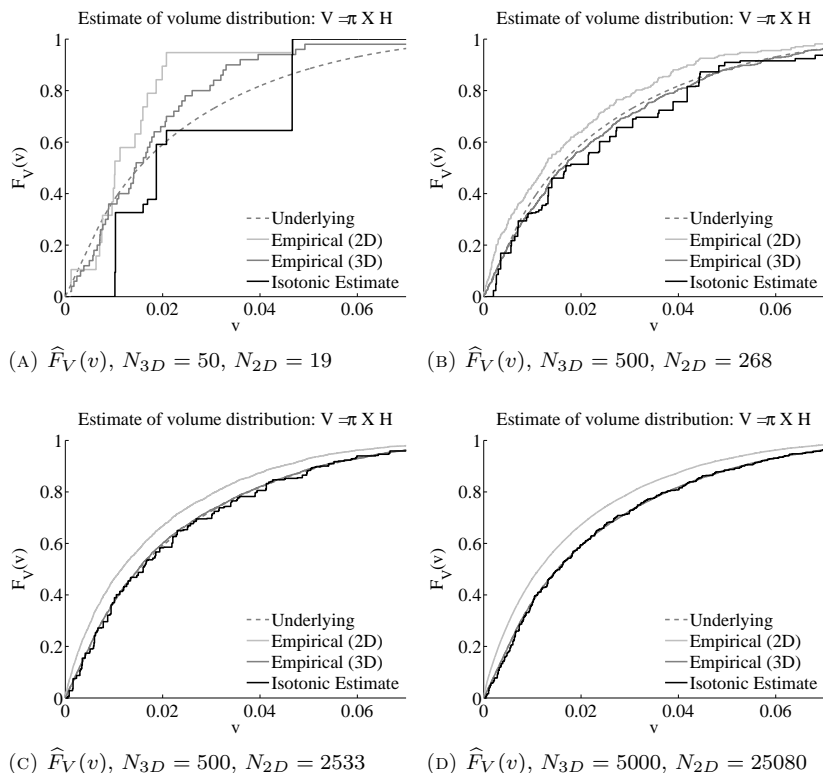


FIGURE 4.2.5: Estimation of the CDF for the cylinder volume. The actual number of rectangle observations, N_{2D} is less than the number of cylinders in the box, N_{3D} . In all figures, the dash-dotted grey line gives the underlying distribution, the solid grey line gives the empirical distribution based on the 3D observations, the light-grey line gives the empirical distribution based on the 2D observations (Z, H) as if they were distributed as the (X, H) , and the black line gives the isotonic estimation of the distribution of the quantity of interest based on the 2D observations.

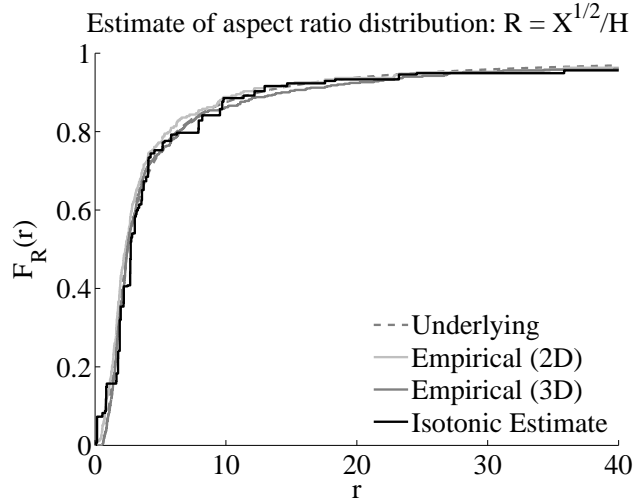
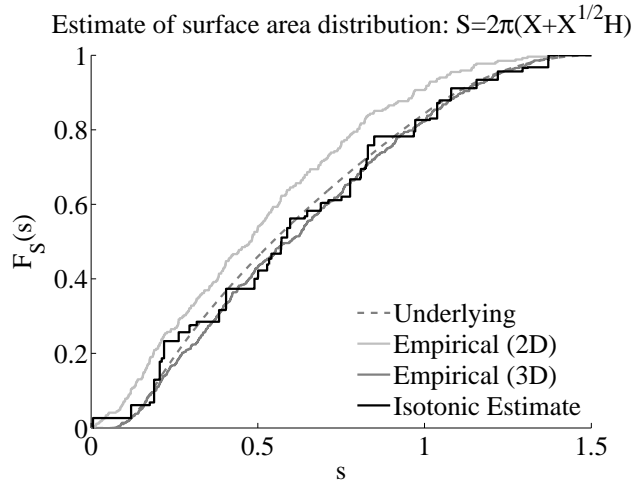
(A) $\hat{F}_R(r)$, $N_{3D} = 500$, $N_{2D} = 268$ (B) $\hat{F}_S(s)$, $N_{3D} = 500$, $N_{2D} = 268$

FIGURE 4.2.6: Isotonic and empirical estimation results for the aspect ratio R and surface area S of the cylinders. In all figures, the dashed grey line gives the underlying distribution. The solid grey line gives the empirical distribution based on the 3D observations. The light-grey line gives the empirical distribution based on the 2D observations (Z, H), treating them as if they were distributed as the (X, H) . The black line gives the isotonic estimation of the distribution of the quantity of interest based on the 2D observations.

Figures 4.2.5 and 4.2.6 show the estimates of the cumulative distribution functions (CDFs) of the quantities of interest. In all figures the underlying distribution is given by the dashed grey line. The empirical distribution from the 2D observations, treating (Z, H) as if they were distributed like (X, H) , are given by the light grey line. The empirical distribution from the 3D observations are given by the solid grey line. The isotonic estimate is given by the black line. Figure 4.2.5 shows the estimates of the CDF for the volume for each of the four values of N , demonstrating visually how the rate of convergence affects the estimator. The results are from a single simulation run for each N . These figures make it clear that the isotonic estimate is superior for these quantities. While treating the 2D observations as if they were distributed like the 3D observations seems to only slightly underestimate the underlying distribution, the isotonic estimator does follow the underlying distribution reasonably well, even for small number of observations on the cut plane, see Figure 4.2.5a. Since in real systems the only observables are those on the cut plane, and most likely the underlying distribution is not known at all, the isotonic estimate can be considered a reasonable approximation to the underlying distribution, even for small numbers of observation points.

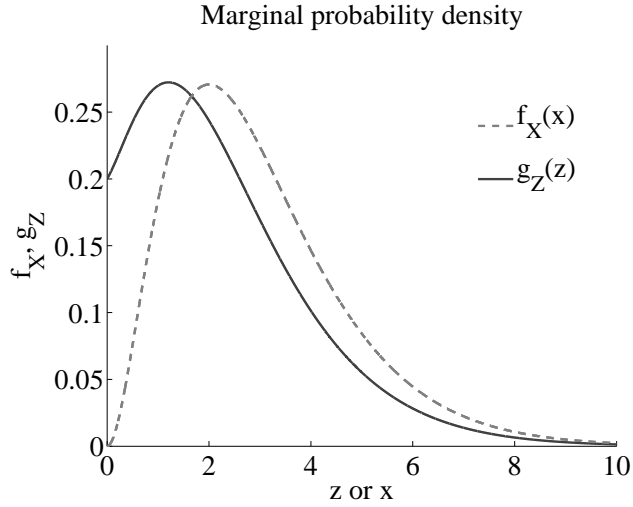
The results for estimating the CDF of the aspect ratio and the surface area of the cylinders are shown in Figure 4.2.6. For the aspect ratio, it seems that the difference between the estimates from the 2D and 3D observations is nearly negligible, but the isotonic estimation results also follow the underlying distribution. Comparing the aspect ratio and surface area, this demonstrates the power of this estimator. Without any assumptions on the form of the distribution, the estimator gives an adequate reproduction of the underlying distribution.

4.3 Numerical Simulation

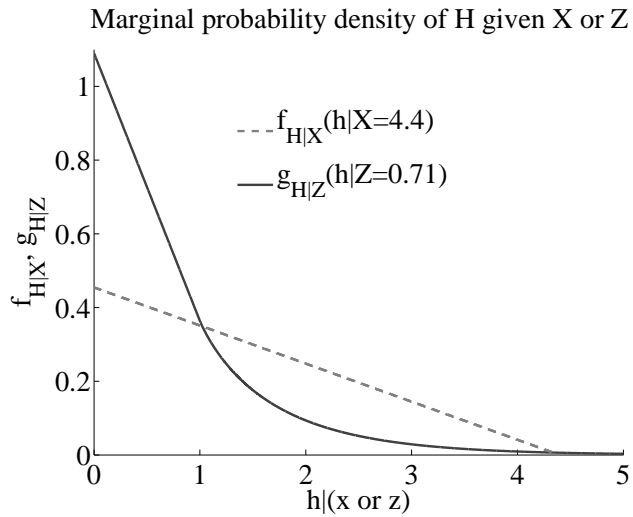
The purpose of the so-called numerical simulation is to work directly with the underlying distributions in order to avoid the limitations of a physical simulation. For this simulation, the squared radius X is assumed to be Gamma(3) distributed and the height H given $X = x$ is triangularly distributed on $[0, x]$. This leads to the following marginal and conditional density functions:

$$f_X(x) = \frac{1}{2}x^2e^{-x}, \quad x \geq 0 \quad f_{H|X}(h|x) = \frac{2}{x^2}(x-h), \quad h \in (0, x). \quad (4.3.1)$$

From eq. (3.2.1) the marginal and conditional densities of the observable



(A)



(B)

FIGURE 4.3.1: Marginal probability density functions (pdf) for the squared radius X and the squared half-width Z as well as the conditional density of the height H . In both figures the light grey dashed line represents the pdf for the cylinder dimensions and the solid dark grey line represents the pdf for the rectangle dimensions.

rectangle quantities are calculated to be (see Appendix B.1.2 for details):

$$\begin{aligned}
 g_Z(z) &= \frac{4}{15} \left(z^2 + z + \frac{3}{4} \right) e^{-z}, & 0 \leq z \\
 g_{H|Z}(h|z) &= \frac{2}{\sqrt{\pi} \left(z^2 + z + \frac{3}{4} \right)} \begin{cases} \left(\frac{1}{2} - h_z \right) \Gamma \left(\frac{1}{2} \right) & 0 < h < z \\ \left(\frac{1}{2} + h_z \right) I_G \left(\frac{1}{2}, h_z \right) + \sqrt{h_z} e^{-h_z} & 0 < z < h \end{cases} & \\
 & & (4.3.2)
 \end{aligned}$$

where $h_z = h - z$ and $I_G(m, x) = \int_{t=x}^{\infty} t^{m-1} e^{-t} dt$ is the incomplete Gamma function.

Figure 4.3.1 shows the pdfs for the squared radius and half-width as well as a single instantiation for the conditional density of the height. The Gamma distribution was chosen for the squared radius because it has the appropriate behavior of not allowing the squared radius to be zero while still allowing for arbitrarily small values to be chosen. The width of the curve around the peak is fairly small while still having a long tail out to large values, allowing for extremely large observations with nonzero probability. The marginal distribution for the height limits the cylinders to being more plate-like than rod-like, with smaller heights having the highest probability.

From the joint densities in eq. (4.3.1), the underlying distributions for the various quantities of interest (V , S , and R) can be calculated (see Appendix B.1.2). As an example, the distribution function for the volume is

$$F_V(v) = 1 - \left[1 + \sqrt{\frac{v}{\pi}} - \frac{v}{2\pi} + \frac{1}{2} \left(\frac{v}{\pi} \right)^{\frac{3}{2}} \right] e^{-\sqrt{\frac{v}{\pi}}} + \frac{v^2}{2\pi^2} Ei \left(\sqrt{\frac{v}{\pi}} \right) \quad (4.3.3)$$

where $Ei(x) = \int_{u=x}^{\infty} e^{-u} u^{-1} du$ is the exponential integral. For this simulation, $N = 50, 500, 5000, \text{ or } 50000$ observations are drawn from the joint density distributions for (X, H) , the 3D observations, and another set of the same size for the density of (Z, H) , the 2D observations. Unlike with the physical model, since $n = N$, a more fair comparison between the estimation results from the 3D observations and the estimation results from the 2D observations is possible. The simulation is run 1000 times for each value of N and the mean of the results and the span between the 2.5 and 97.5 quantiles for the estimates of expectations of the quantities of interest and the covariance are shown in Figures 4.3.2, 4.3.3 and 4.3.4. In all figures, the black line corresponds to the underlying expectation or covariance. The light grey squares represent the estimates from the 3D observations and the dark grey circles represent the estimates from the 2D observations. In these figures, the problem of the apparent bias is even stronger than for the physical simulation. This is due to

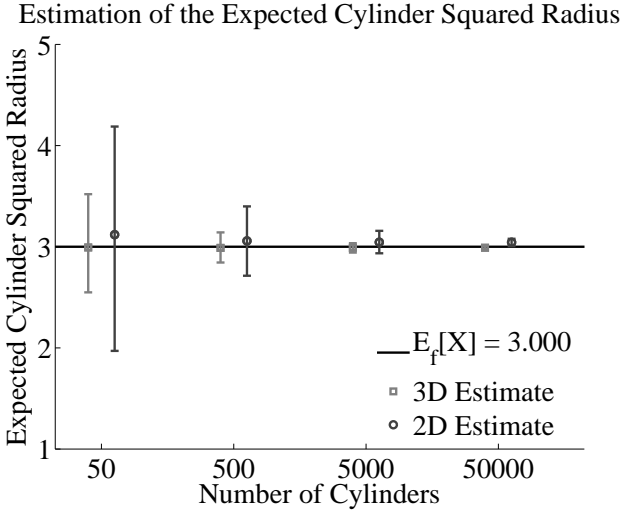
Optimal Bandwidth for ξ_g^j			
N	$j = 0$	$j = 1$	$j = 2$
50	1.22	2.19	4.06
500	0.565	1.02	1.88
5000	0.262	0.472	0.873
50000	0.122	0.219	0.405

TABLE 4.2: Optimal bandwidths for estimating the ξ_g^j are given for the four values of N , the number of cylinders per simulation. The number of rectangle observations on the cut plane are equal to N .

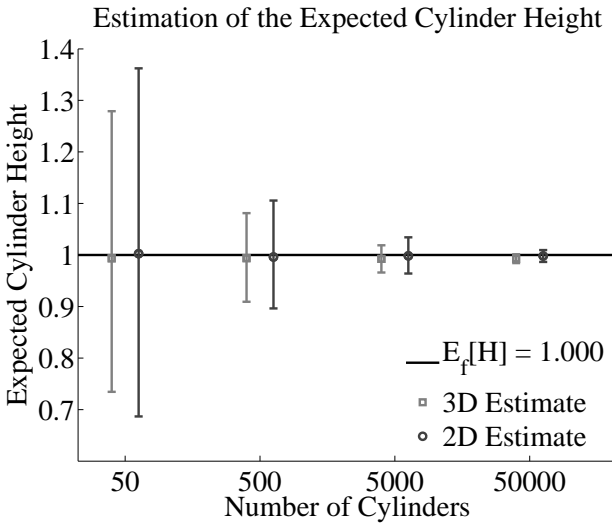
the probability of extreme observations of the squared half-width being rather large (see Figure 4.3.1a). This impacts the estimate of the expectation even for large, though finite, numbers of observations.

Because the number of observations is constant over all 1000 runs, the optimal bandwidth for estimating the ξ_g^j quantities can be calculated once. Table 4.2 shows the optimal bandwidths for each value of N . For this distribution, the expected squared half-width is 2.3. For 50 observations, the bandwidth is a large fraction of the expected value, and for the $j = 2$ it is nearly twice the expected value. This distribution is more sensitive to this estimator than the physical model. Figure 4.3.5 shows the results of the estimation from both the 3D observations eq. (3.4.10) and the 2D observations eq. (3.4.15). While the estimation from the 3D observations is unbiased, in scenarios where the model is intended to be implemented, only the 2D observations are available.

Figure 4.3.6 shows the results of the estimation of the CDFs for the volume of the cylinders. For this simulation, the number of observations in 2D and 3D are equal. Figure 4.3.7 shows the results for 500 observations for the estimates of the aspect ratio and the surface area. All of these distributions are notably different from the distributions in the physical model. Despite this, the isotonic estimator still provides a reasonable estimate of the underlying distributions. This reinforces the justification for a nonparametric model.

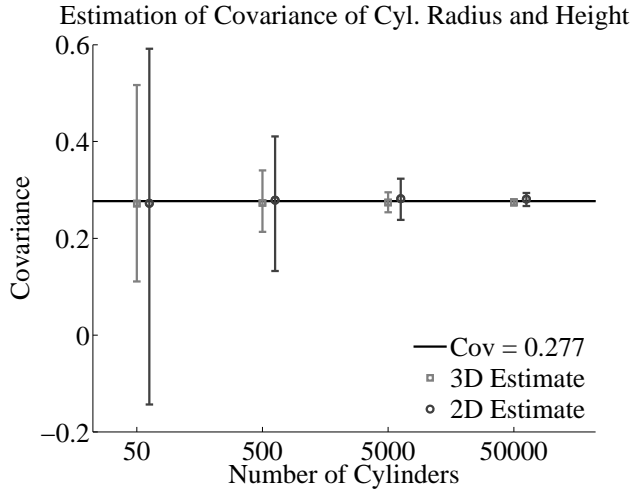


(A)

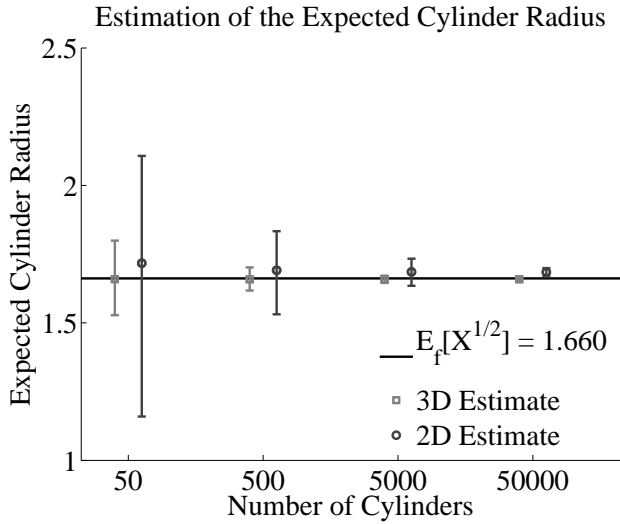


(B)

FIGURE 4.3.2: Estimate of the expected cylinder squared radius X and expected cylinder height H . The solid line shows the underlying expected value. The light grey squares show the mean of the estimation results from the 3D observations. The dark grey circles show the mean of the estimation results from the 2D observations. The error bars span the 2.5 and 97.5 quantiles for the 1000 runs.

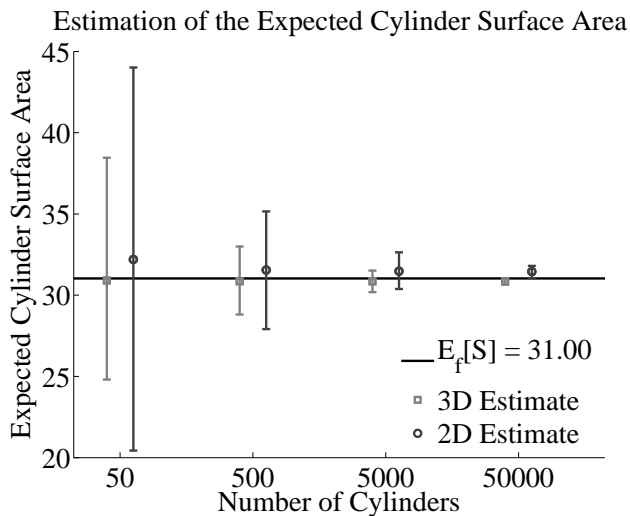


(A)

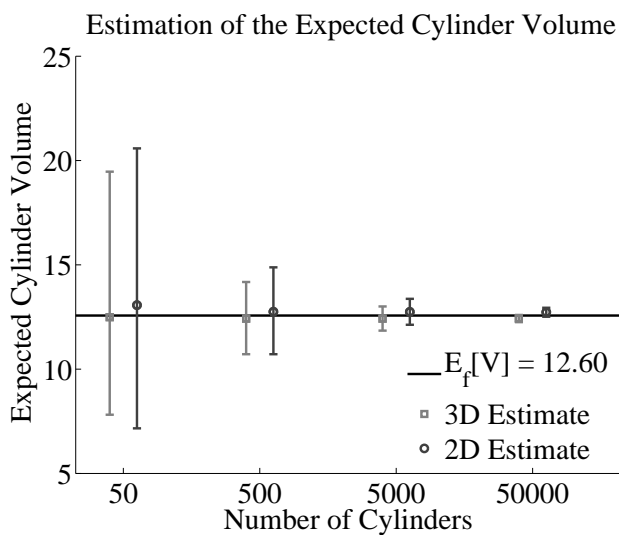


(B)

FIGURE 4.3.3: Estimate of the expected covariance between the cylinder radius and height and estimate of the expected cylinder radius and the estimate of the expected cylinder radius \sqrt{X} . The solid line shows the underlying expected value. The light grey squares show the mean of the estimation results from the 3D observations. The dark grey circles show the mean of the estimation results from the 2D observations. The error bars span the 2.5 and 97.5 quantiles for the 1000 runs.



(A)



(B)

FIGURE 4.3.4: Estimate of the expected cylinder surface area S and the expected cylinder volume V . The solid line shows the underlying expected value. The light grey squares show the mean of the estimation results from the 3D observations. The dark grey circles show the mean of the estimation results from the 2D observations. The error bars span the 2.5 and 97.5 quantiles for the 1000 runs.

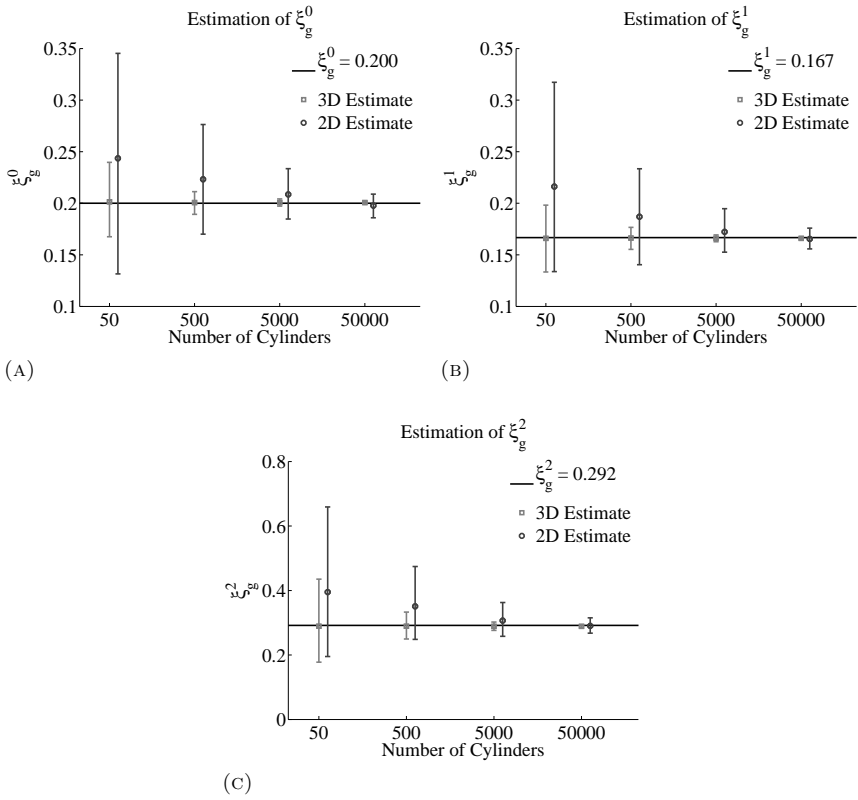


FIGURE 4.3.5: Estimate of the ξ_g^j quantities for $j = 0, 1, 2$ using the optimal bandwidth calculated from eq. (3.4.18) and the underlying distributions. The solid black line represents the underlying value. The light grey squares represent mean of the estimation results from the 3D observations and the dark grey circles represent the mean of the estimation results from the 2D observations. The bars span the 2.5 and 97.5 quantiles.

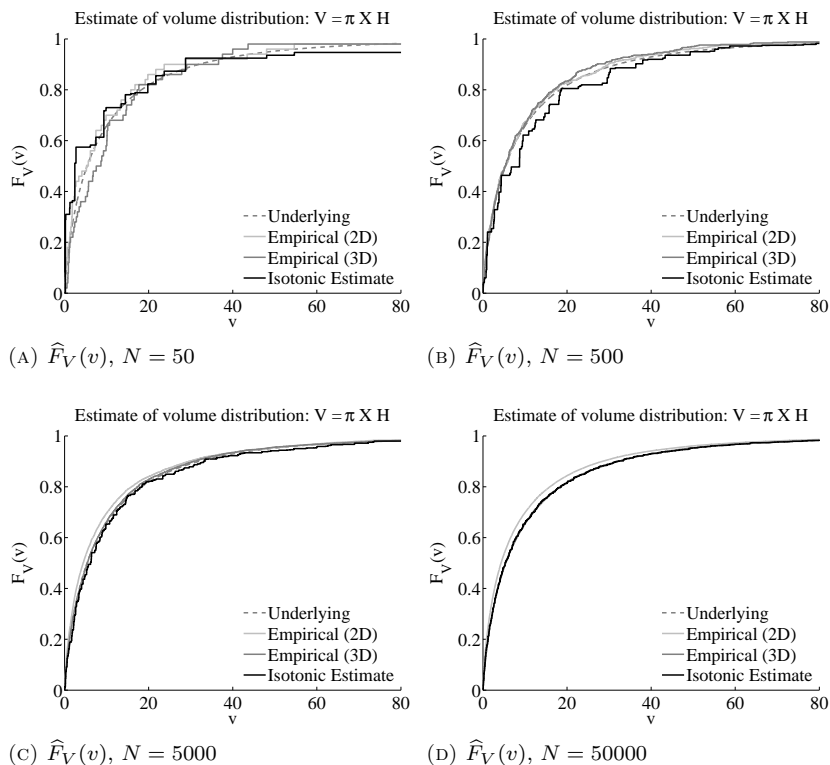
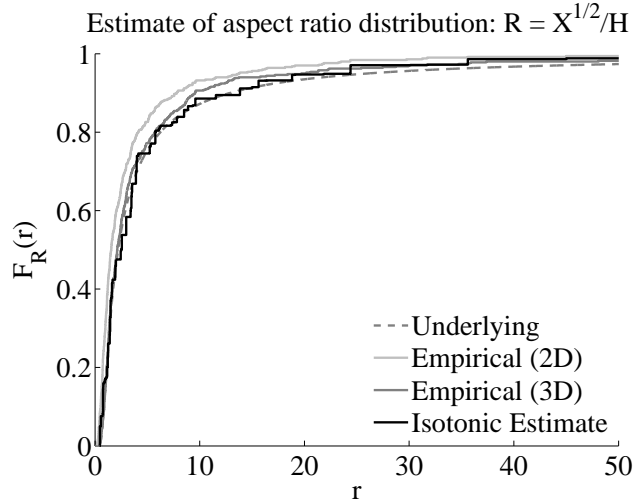
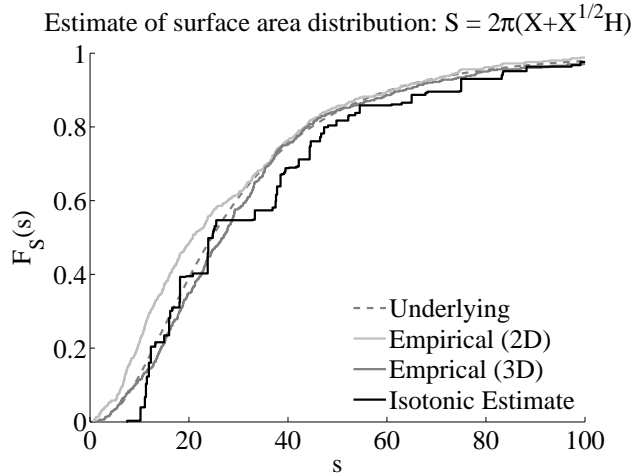


FIGURE 4.3.6: Estimation of the CDF for the cylinder volume. The number of rectangle observations is equal to the number of cylinder observations, N . In all figures, the dashed grey line gives the underlying distribution. The solid grey line gives the empirical distribution based on the 3D observations. The light-grey line gives the empirical distribution based on the 2D observations (Z, H), treating them as if they were distributed as the (X, H) . The black line gives the isotonic estimation of the distribution of the quantity of interest based on the 2D observations.



(A) $\hat{F}_R(r)$, $N = 500$

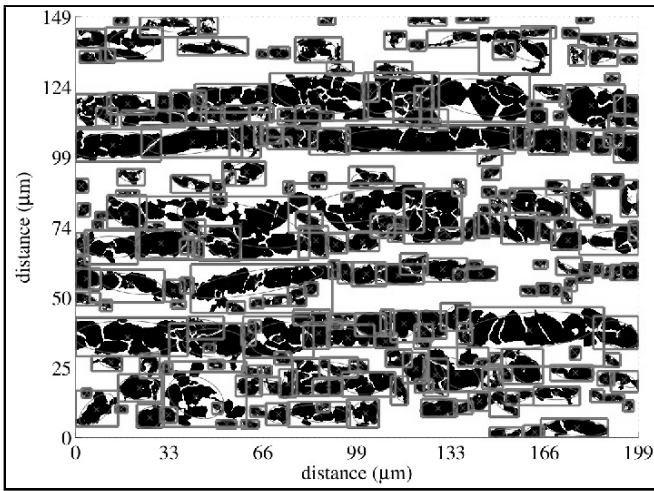


(B) $\hat{F}_S(s)$, $N = 500$

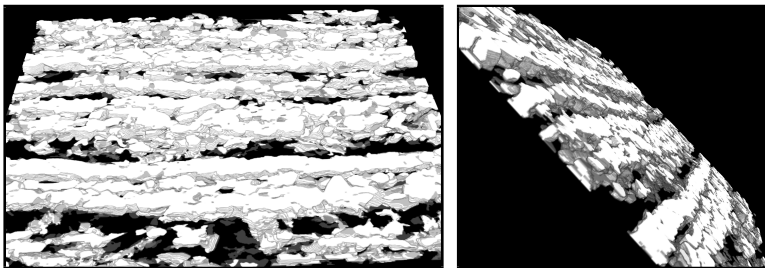
FIGURE 4.3.7: Isotonic and empirical estimation results for the aspect ratio R and surface area S of the cylinders. In all figures, the dashed grey line gives the underlying distribution. The solid grey line gives the empirical distribution based on the 3D observations. The light-grey line gives the empirical distribution based on the 2D observations (Z, H), treating them as if they were distributed as the (X, H) . The black line gives the isotonic estimation of the distribution of the quantity of interest based on the 2D observations.

4.4 Applying the Model to Microstructures

The model and estimation procedures are now applied to the banded steel microstructure shown in Figure 3.1.1. To obtain 3D information about the microstructure, the material was serial sectioned providing images approximately every 2 μm into a depth of about 90 μm . (See Chapter 2 for details on the experimental procedure and image processing.) The bounding boxes, or the smallest rectangle containing all of the object, around the features of interest (heretofore referred to as cylinders) were found for the binary images using Fiji software [62] (see Figure 4.4.1). The serial sectioned binary images



(A) Bounding boxes around features of interest in Steel B.



(B) 3D reconstruction from 2D slices.

FIGURE 4.4.1: Figure 4.4.1a shows the bounding boxes around the features of interest (heretofore referred to as cylinders) in the microstructure. Figure 4.4.1b shows two views of the 3D reconstruction of Steel B's microstructure from the serial sectioned images.

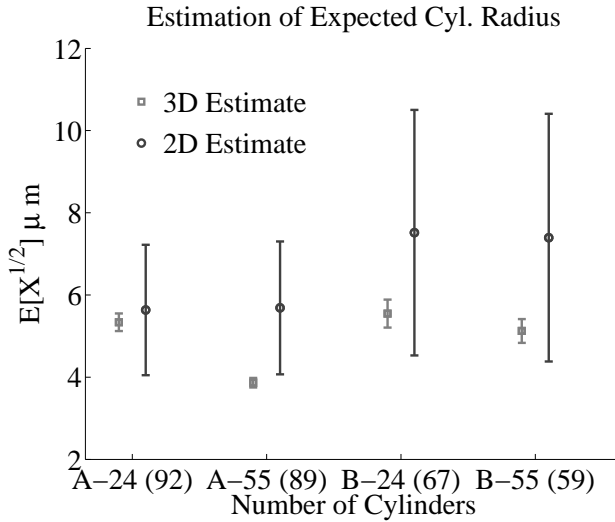
were combined to form a single 3D object and the bounding boxes of the 3D features of interest were found using the 3D analysis function in Fiji [88].

4.4.1 Expectations and Covariance

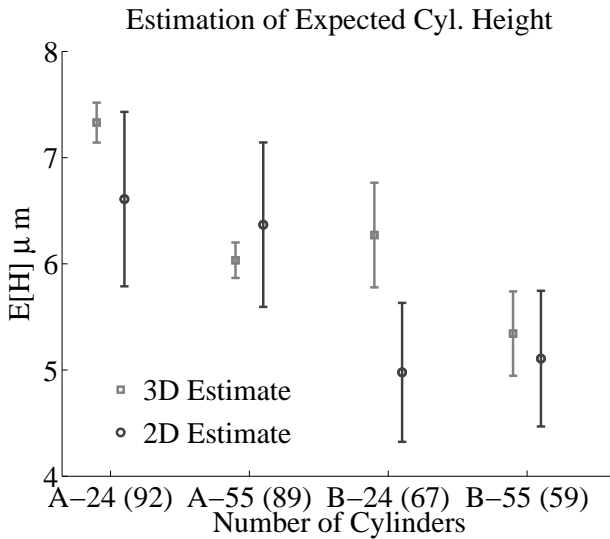
Using the dimensions of the bounding boxes in both 2D and 3D one can apply the model and estimation procedures to the microstructure to see how well the estimators are able to estimate the size of the cylinders. The bounding boxes, shown in Figure 4.4.1a, are taken to be the observed portions of the cylinders on the cut plane. Figure 4.4.1b shows two views of the 3D reconstruction of the serial sectioned data for Steel B's microstructure. Bounding boxes can also be found for these images, and for the purpose of this work, yield the radius and height distribution being estimated.

Figures 4.4.2, 4.4.3 and 4.4.4 give the estimates for the expectations of the quantities of interest and the covariance of the radius and height from both the 2D and 3D observations, dark grey circles and light grey squares, respectively. The x-axis labels refer to the steel, number of slices and number of observations on the cut plane. For example, A-24 (92) encodes Steel A with 24 slices at 0.5 μm steps and 92 rectangles observed on the cut plane. The constructed 95% confidence intervals are given by the error bars. For the estimates from the 3D data the ordinary Central Limit Theorem applies and so the confidence interval can be constructed from the sample deviation divided by the number of observations. For the estimates from the 2D observations, eq. (3.4.20) is used with the appropriate moment and ξ_g^j estimations. The latter are shown in Figure 4.4.5. The bandwidths for the ξ_g^j estimates were chosen by eye to simultaneously minimize the difference between the 2D and 3D estimates while also minimizing the 95% confidence intervals of the expected squared radius and height estimates. There are other ways to choose a bandwidth, but the exploration of these means is beyond the scope of this thesis.

For the expected radius, height, squared radius and surface area estimations, the 2D and 3D estimates mostly coincide to within the 95% confidence interval. For the covariance and the volume estimations this is not true. However, given that the serial sectioned data making up the 3D observations does not represent an entire cylinder, the results shown for the estimations using the 3D values need to be used cautiously. The truncation of the cylinders from the serial sectioning will underrepresent the true 3D size and shape of the cylinders. The rectangles observed on the cut plane can be considered complete observations. Therefore, the estimates from the 2D observations are more reliable, yielding a better representation of the true values.

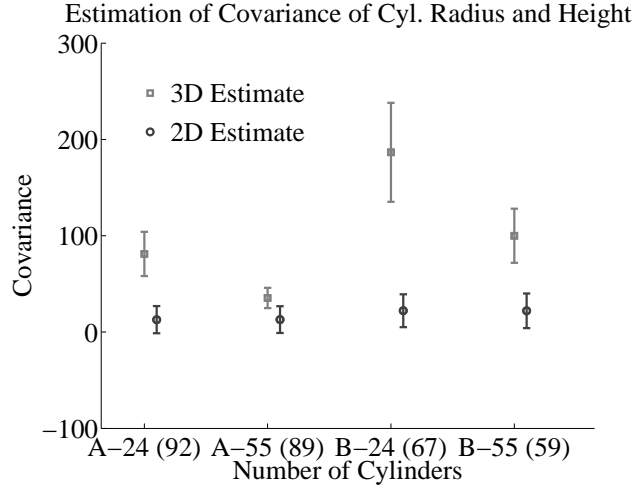


(A)

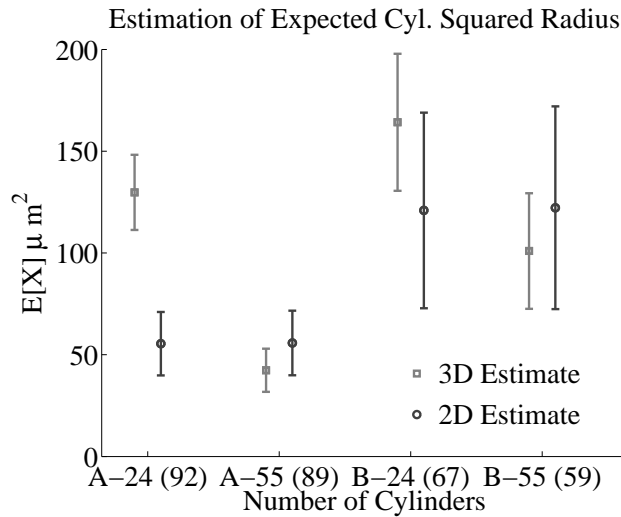


(B)

FIGURE 4.4.2: Results for the expectation and covariance estimations from the microstructure data. The light grey squares correspond to the estimates using the 3D bounding box values. The dark grey circles correspond to the estimates using the observed 2D values. The constructed 95% confidence intervals are given by the error bars, eq. (3.4.20) for the estimates from the 2D observations and the standard deviation divided by the number of observations is used for the estimates from the 3D data. The x-axis labels refer to Steel A or B, the number of slices considered, either 24 at 0.5 μm steps or 55 at 2 μm steps and the number of observations in parentheses on the cut plane.

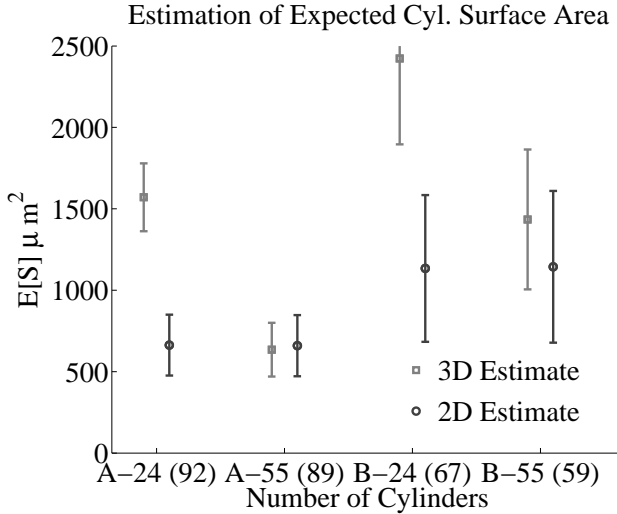


(A)

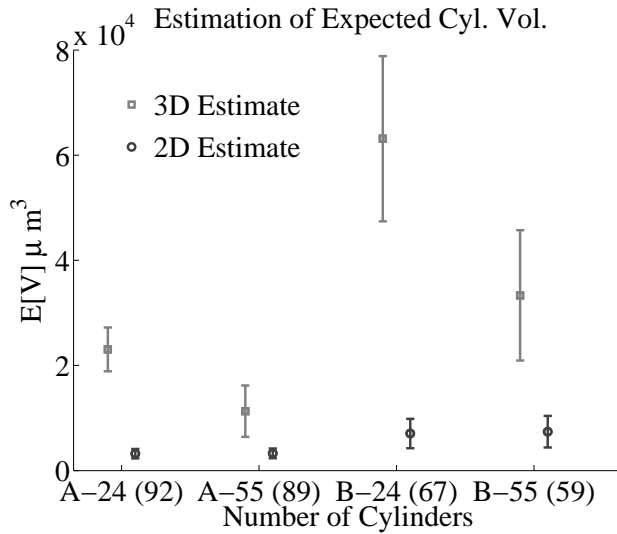


(B)

FIGURE 4.4.3: Results for the expectation and covariance estimations from the microstructure data. The light grey squares correspond to the estimates using the 3D bounding box values. The dark grey circles correspond to the estimates using the observed 2D values. The constructed 95% confidence intervals are given by the error bars, eq. (3.4.20) for the estimates from the 2D observations and the standard deviation divided by the number of observations is used for the estimates from the 3D data. The x-axis labels refer to Steel A or B, the number of slices considered, either 24 at $0.5 \mu\text{m}$ steps or 55 at $2 \mu\text{m}$ steps and the number of observations in parentheses on the cut plane.



(A)



(B)

FIGURE 4.4.4: Results for the expectation and covariance estimations from the microstructure data. The light grey squares correspond to the estimates using the 3D bounding box values. The dark grey circles correspond to the estimates using the observed 2D values. The constructed 95% confidence intervals are given by the error bars, eq. (3.4.20) for the estimates from the 2D observations and the standard deviation divided by the number of observations is used for the estimates from the 3D data. The x-axis labels refer to Steel A or B, the number of slices considered, either 24 at 0.5 μm steps or 55 at 2 μm steps and the number of observations in parentheses on the cut plane.

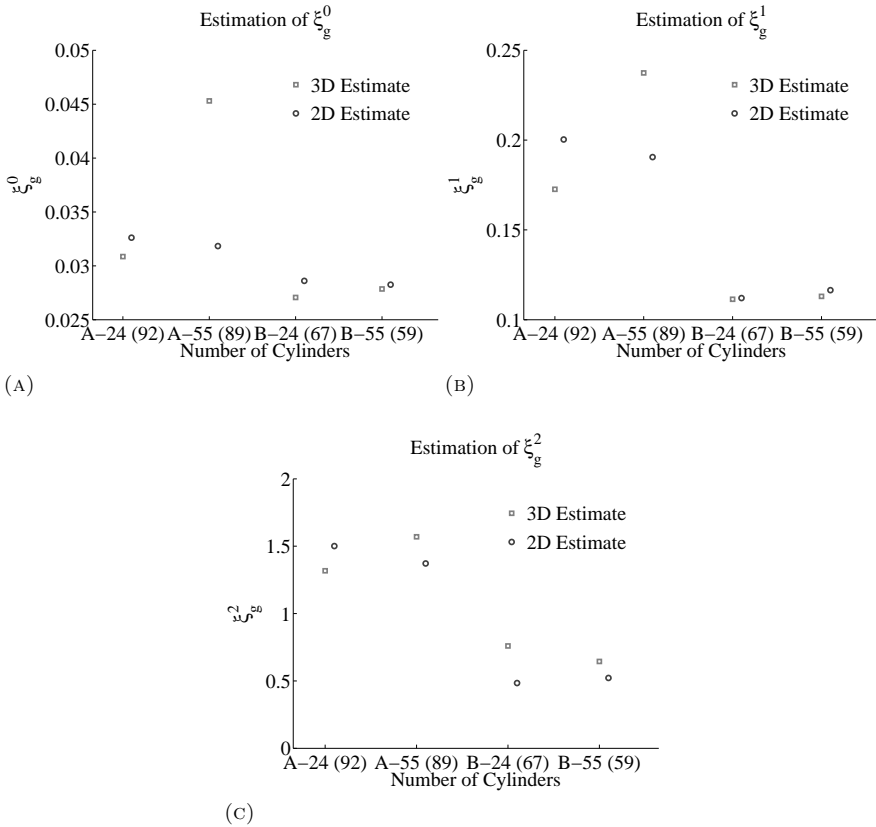


FIGURE 4.4.5: Results for the estimation of the ξ_g^j for $j = 0, 1, 2$ as calculated from the 2D and 3D observations. The bandwidth is determined by eye to be 6 for Steel A and 12 for Steel B. The x-axis labels refer to Steel A or B, the number of slices considered, either 24 at $0.5 \mu\text{m}$ steps or 55 at $2 \mu\text{m}$ steps and the number of observations in parentheses on the cut plane.

4.4.2 Isotonic Estimation

The isotonic estimator can be applied to estimate the CDF of the quantities of interest.

Figures 4.4.6 and 4.4.7 show the results of the isotonic and empirical estimation procedures for the distribution functions of the quantities of interest applied to the microstructures of Steel B and Steel A, respectively. Figures 4.4.6a and 4.4.7a show the results for the squared radius. In all plots, the light-grey lines show the empirical distribution from the 2D observations treated as if the (Z, H) pairs were distributed as the (X, H) pairs. The grey lines show the empirical distribution from the 3D observations, and the black lines are the isotonic estimation results from the 2D observations.

The empirical distribution of the 2D observations is included in the plots to emphasize the bias in the observations. As described in Section 3.2, the larger cylinders are more likely to be cut by the plane, and this is evident from comparing the empirical distribution of the quantities of interest calculated from the 2D observations to the empirical distribution of the quantities of interest based on the 3D observations. In all cases, the isotonic estimator falls roughly between the 2D and the 3D empirical estimators. This shows that the isotonic distribution is a better estimate of the true underlying distribution than the 2D empirical distribution. Also, given how close the 3D empirical distributions and isotonic estimates are, it is likely that the 3D empirical distributions are representative of the true underlying distribution, assuming the bands are approximately circular plates.

These results are remarkable given that the total number of observations in 2D is less than 100. While a parametric estimator could give a better rate of convergence and a smaller asymptotic variance than the isotonic estimator, at this point, not enough is known about the bands within the steel microstructures to assume a specific of distribution for the height and radius of the cylinders. With the nonparametric model, nothing needs to be assumed and all of the desired information can still be estimated.

There are several other considerations that must be accounted for when looking at these results. It is important to note that the total attained depth from the serial sectioning is not enough to view a cylinder in its entirety through the depth of the sectioning. Therefore, an actual bound on the full radial distribution into the depth of the material is not known. It is also true that edge effects are not accounted for in this analysis. The cylinders are considered to be completely inbounds of the observation window. However, it is likely that cylinders ending at the edge of the image continue beyond and this is not accounted for in this model. These matters will be explored further in Chapter 6.

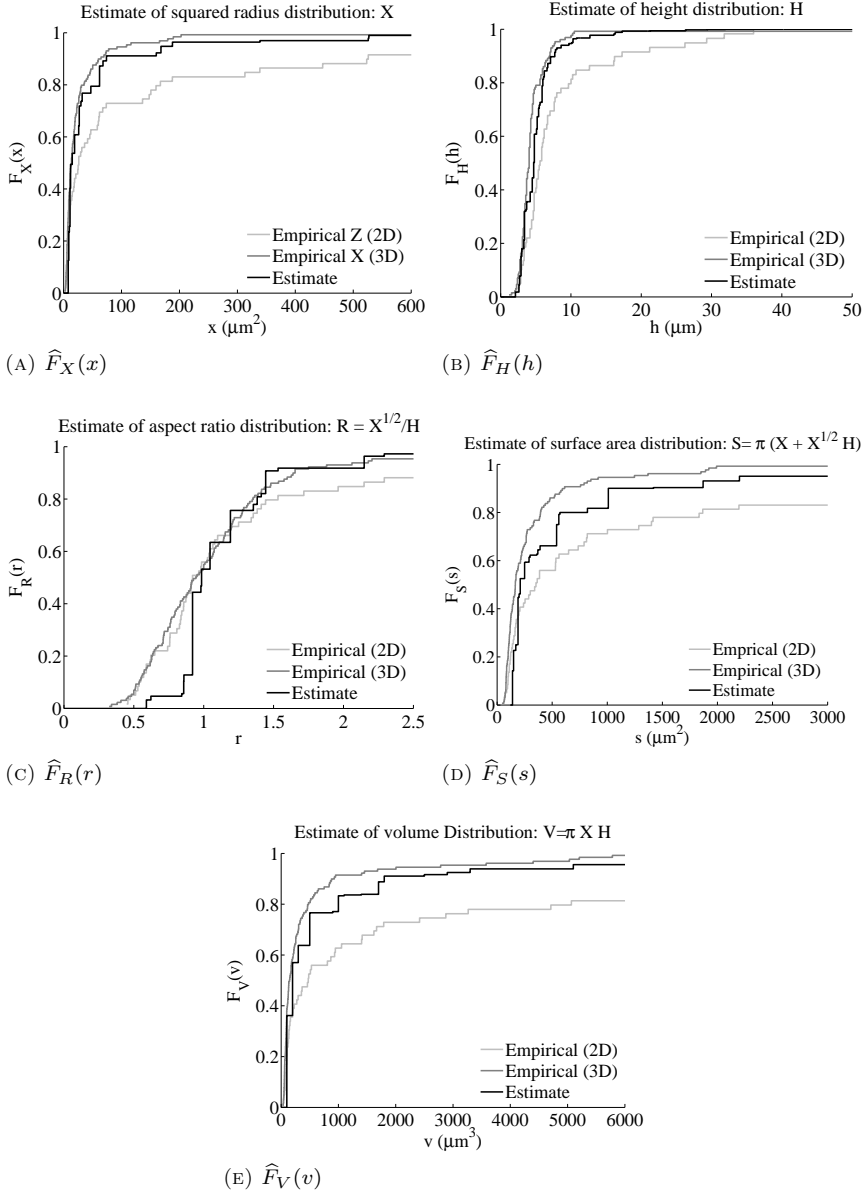


FIGURE 4.4.6: Results of the model and estimation procedures for the squared radius, height, aspect ratio, surface are and volume applied to the microstructure of Steel B shown in figure 4.4.1. The number of rectangles observed on the image is $N = 59$. In all figures, the light-grey lines are the 2D observations from the bounding box. The dark-grey lines are the 3D observations from the 3D bounding boxes. The black lines are the isotonic estimations of the underlying 3D distributions given the 2D observations.

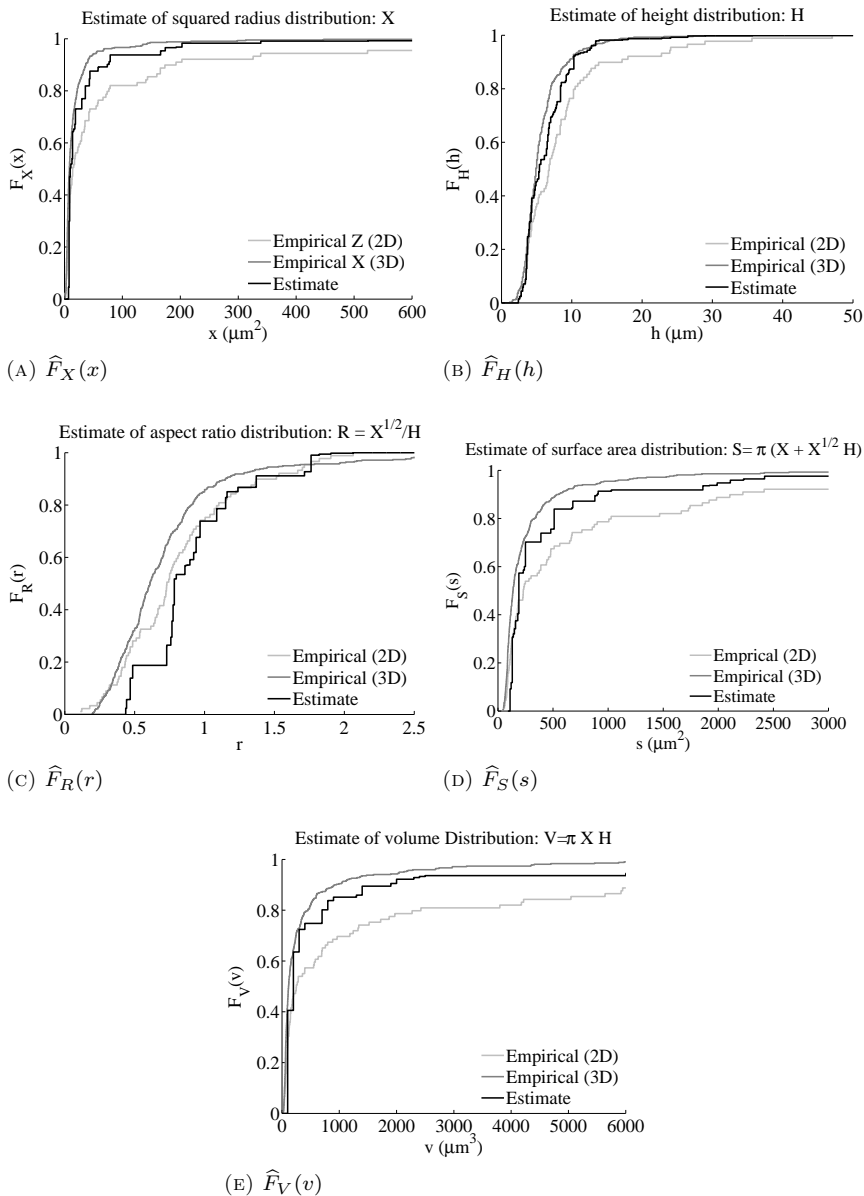


FIGURE 4.4.7: Results of the model and estimation procedures for the squared radius, height, aspect ratio, surface are and volume applied to the microstructure of Steel A shown in figure 2.3.1. The number of rectangles observed on the image is $n = 89$. In all figures, the light-grey lines are the 2D observations from the bounding box. The dark-grey lines are the 3D observations from the 3D bounding boxes. The black lines are the isotonic estimations of the underlying 3D distributions given the 2D observations.

Despite these issues, and the simplicity of the model, the estimated distributions for the 3D quantities of interest are practicable representations of the underlying distributions. As a first step toward understanding and modeling a full 3D microstructure, this provides a solid starting point and a reasonable approximation to what is often not directly observable.

4.5 Conclusion

The oriented cylinder model has been explored and validated through two types of simulations, demonstrating the accuracy and precision of the results for various numbers of observations on the cut plane. The model has been applied directly to two dual phase steel microstructures. Serial sectioned images of the microstructures have been stitched together to yield a 3D structure to which the 2D estimation results can be compared. Given that there are less than 100 observable rectangles on any given section image, the estimation results appear to be reasonable, and the circular cylinder model appears to be representative of the bands in the microstructure.

However, there are several issues inherent to processing images that have not been considered in this chapter. Features of interest like microstructural bands often deviate from perfect cylinders and are not observable as perfect rectangles. How does one go about defining the observed rectangle in this instance? Determining an object of interest in an image is often done through pixel connectivity. Even though the images have undergone morphological processing, as described in Chapter 2, it is not always possible to preserve the true connectivity of the objects. How does this affect the outcome of the estimation under the model assumptions? These issues are considered in Chapter 6.

5

Kernel Smoothed Estimation of the Distribution and Density Functions

Often, it is of more practical interest to have an estimate of the probability density function, which is the derivative of the cumulative distribution function, of the quantities of interest. Since the isotonic estimator presented in Chapter 3 yields a staircase function for the CDFs, its derivative cannot be used to estimate the corresponding pdfs. Therefore, Kernel estimators are introduced in this chapter for both the CDFs and pdfs of the various quantities of interest. The asymptotic behavior of these estimators is derived and the estimators are tested with the second simulation introduced in Chapter 4. Finally, the estimators are applied to the microstructures of Steel A and Steel B.

5.1 Introduction

The outcome of the functional estimators introduced in Chapter 3 are the cumulative distribution functions (CDF). However, the derivative of this function, the probability density function (pdf) is often of more interest in practice. For instance, histograms are commonly used to display an observed data set, and a normalized histogram gives an estimate of the underlying pdf. From the pdf it is easier to determine the modality of a distribution. Also, the pdf provides weights associated with observations that are useful as inputs for physical models and simulations.

Since the non-parametric estimators of the CDF presented in Chapter 3 result in staircase functions, their derivatives are not useful for estimating the corresponding pdfs. At the same time, these staircase functions are estimating an unknown, but most likely smooth underlying distribution function. Therefore, it is not unreasonable to look for an estimator that provides a smoother estimate of the CDF so that its derivative can be used to estimate the pdf.

Kernel estimators are smooth, non-parametric estimators commonly used to estimate pdfs directly from empirical data sets. Kernels are functions that generally satisfy three requirements. The first is that the function is non-negative. Second, the function K should be symmetric, meaning $K(u) = K(-u)$. Finally, $\int K(u)du = 1$, which ensures that the convolution of the kernel function with the data set results in a probability density. The general procedure for estimating the distribution function is to convolve the empirical distribution function of the data set or resulting function with the Kernel function where a smoothing parameter, the bandwidth, is used. The variance and the bias of the estimator are directly affected by the bandwidth. When the bandwidth is small, the bias is low but the variance is large. When the bandwidth is large, the function becomes smoother and the variance decreases but the bias increases. Usually an optimal bandwidth is sought which minimizes the mean squared error (MSE) of the estimator.

Generally, kernel estimators are applied directly to the observed data set. In the case of the inverse problem associated with the cylinder model, applying the kernel to the 2D observations provides an estimate for the marginals of the 2D observations, g_Z and g_H . Using the inverse relationship eq. (3.2.2) with the kernel-estimated density functions will yield an estimate for the marginal density functions of the corresponding distributions for the 3D observations. This was originally proposed by Taylor to estimate the probability density of the radius of spheres in an opaque medium [89] from the observed circles on a plane. Hall and Smith reformulated the estimator in terms of the squared radius [1]. For both estimators, the optimal bandwidth was of order $n^{-1/6}$,

and the MSE rate of convergence using the optimal bandwidth was of order $n^{-2/3}$, where n is the number of observations.

Van Es and Hoogendoorn suggested, for the problem of spheres, that the kernel estimator be applied after the inversion step, on the function N_n given by eq. (3.3.2) [21]. Here, the kernel function replaces the empirical distribution function \mathbb{G}_n and results in a smooth estimator for the CDF. The derivative of the smoothed estimator may be taken to estimate the pdf. Van Es and Hoogendoorn compared the results of their estimator to that of Hall and Smith and determined that there is no reason to prefer one over the other. The optimal bandwidth is still of order $n^{-1/6}$ and the MSE of order $n^{-2/3}$. The only difference is that the estimator proposed by van Es and Hoogendoorn was shown to have a smaller bias near zero [21].

For the problem of cylinders in an opaque medium, because there are two variables to consider, the inverse problem requires a bivariate density for eq. (3.2.2), which is beyond the scope of this work. However, if instead, the kernel estimator is applied to eq. (3.3.2), it remains a univariate density estimation problem. Yet, unlike the problem of spheres considered by van Es and Hoogendoorn and Hall and Smith, estimating the various quantities of interest in the cylinder model still requires the observed pairs, (z, h) . In this chapter, the effect of the two variables on the asymptotic behavior of the kernel estimator is considered.

5.2 Kernel Estimators for $N(t)$

The smoothed estimator of N , based on smoothing N_n given in eq. (3.3.2), is defined as

$$\begin{aligned}\tilde{N}_n(t) &= \frac{1}{b_n} \int_{s=t-b_n}^{t+b_n} K\left(\frac{t-s}{b_n}\right) N_n(s) ds \\ &= \frac{1}{nb_n} \sum_{i=1}^n \int_{s=t-b_n}^{t+b_n} K\left(\frac{t-s}{b_n}\right) [Z_i - q(H_i; s)]^{-\frac{1}{2}} \mathbf{1}_{\{Z_i > q(H_i; s)\}} ds\end{aligned}\tag{5.2.1}$$

where the bandwidth $b_n \downarrow 0$ is the smoothing parameter. As with the estimator for the quantities of ξ_g^j given in Section 3.4.4, the Mean Squared Error (MSE) is used to obtain the optimal bandwidth and asymptotic behavior of these kernel estimators.

For this estimator, the MSE for estimating $N(t)$ (for t fixed) is defined by

$$\text{MSE}(\tilde{N}_n(t)) = \left(E_g \left[\tilde{N}_n(t)\right] - N(t)\right)^2 + \text{Var} \left(\tilde{N}_n(t)\right).$$

To consider the MSE further, the following assumptions and condition are required:

Assumption 5.2.1. *The function N is twice continuously differentiable at t .*

Assumption 5.2.2. *The joint density function g has bounded support on $[0, M] \times [0, M]$ and is Lipschitz continuous on $(0, \infty)^2$.*

Condition 5.2.1. *The kernel K is continuously differentiable on \mathbb{R} and have support on $[-1, 1]$.*

Now, under Assumption 5.2.1 and fixing $t > 0$, the expectation of $\tilde{N}_n(t)$ is

$$E \left[\tilde{N}_n(t) \right] = E \left[\frac{1}{b_n} \int_{s=t-b_n}^{t+b_n} K \left(\frac{t-s}{b_n} \right) N_n(s) ds \right] \quad (5.2.2)$$

$$\begin{aligned} &= \frac{1}{b_n} \int_{s=t-b_n}^{t+b_n} K \left(\frac{t-s}{b_n} \right) E [N_n(s)] ds \\ &= \frac{1}{b_n} \int_{s=t-b_n}^{t+b_n} K \left(\frac{t-s}{b_n} \right) N(s) ds = \int_{u=-1}^1 K(u) N(t - ub_n) du \\ &= \int_{u=-1}^1 K(u) \left[N(t) - ub_n N'(t) + \frac{1}{2} (ub_n)^2 N''(\xi_{u,n}) \right] du \\ &= N(t) + \frac{1}{2} b_n^2 N''(t) \int_{u=-1}^1 u^2 K(u) du + o(b_n^2) \quad \text{for } n \rightarrow \infty. \end{aligned} \quad (5.2.3)$$

This gives a squared bias for the MSE as $n \rightarrow \infty$ of

$$\left(E_g \left[\tilde{N}_n(t) \right] - N(t) \right)^2 = \frac{1}{4} b_n^4 N''(t)^2 \left(\int_{u=-1}^1 u^2 K(u) du \right)^2 + o(b_n^4).$$

Note that this asymptotic bias has been derived independent of the choice of q and with no conditions placed upon the kernel. The variance, however, is sensitive to the choice of q , and in what follows, we choose to consider the squared radius and volume.

First, for the squared radius, using that $t > 0$ and $t > b_n$ for sufficiently

large n , yields

$$\begin{aligned}
 \tilde{N}_n(t) &= \frac{1}{b_n n} \sum_{i=1}^n \int_{s=-\infty}^{\infty} K\left(\frac{t-s}{b_n}\right) [Z_i - s]^{-\frac{1}{2}} 1_{[Z_i > s]} ds \\
 &= \frac{1}{b_n n} \sum_{i=1}^n \int_{u=0}^{\infty} K\left(\frac{t-(Z_i-u)}{b_n}\right) u^{-\frac{1}{2}} du \\
 &= \frac{1}{b_n n} \sum_{i=1}^n \int_{u=0}^{\infty} K\left(\frac{u+t-Z_i}{b_n}\right) \left(\frac{u}{b_n}\right)^{-\frac{1}{2}} b_n^{-\frac{1}{2}} d\left(\frac{u}{b_n}\right) b_n \\
 &= \frac{1}{\sqrt{b_n} n} \sum_{i=1}^n \int_{u=0}^{\infty} K\left(u + \frac{t-Z_i}{b_n}\right) u^{-\frac{1}{2}} du.
 \end{aligned}$$

Defining the function, as suggested by Hall and Smith [1],

$$\bar{K}(v) = \int_0^{\infty} u^{-\frac{1}{2}} K(u+v) du, \quad (5.2.4)$$

leads to the expression for \tilde{N}_n corresponding to the squared radius:

$$\tilde{N}_n(t) = \frac{1}{\sqrt{b_n} n} \sum_{i=1}^n \bar{K}\left(\frac{t-Z_i}{b_n}\right). \quad (5.2.5)$$

(See Figure 5.4.1 for visualization of the function \bar{K} based on two Kernel functions.)

In a similar fashion (see Appendix C.1), the estimator for the function \tilde{N}_n corresponding to the volume can be expressed as

$$\tilde{N}_n(t) = \frac{1}{\sqrt{b_n} n} \sum_{i=1}^n \sqrt{\pi H_i} \bar{K}\left(\frac{t-\pi H_i Z_i}{b_n}\right). \quad (5.2.6)$$

The function \bar{K} behaves as follows.

$$\bar{K}(v) = \begin{cases} 0 & \text{for } v \geq 1 \\ \int_0^{-v+1} u^{-\frac{1}{2}} K(u+v) du & \text{for } -1 < v < 1 \\ \int_{-v-1}^{-v+1} u^{-\frac{1}{2}} K(u+v) du & \text{for } v \leq -1. \end{cases}$$

This implies that for $v < -1$

$$(-v+1)^{-\frac{1}{2}} \leq \bar{K}(v) \leq (-v-1)^{-\frac{1}{2}}, \quad (5.2.7)$$

which leads to the following asymptotic behavior of $\bar{K}(v)$ for $v \rightarrow -\infty$

$$\sqrt{\frac{-v}{-v+1}} \leq \sqrt{-v} \bar{K}(v) \leq \sqrt{\frac{-v}{-v-1}} \implies \sqrt{-v} \bar{K}(v) \rightarrow 1 \text{ for } v \rightarrow -\infty. \quad (5.2.8)$$

This now gives rise to the following lemma for the asymptotic variance of the kernel estimators.

Lemma 5.2.1. *Let $t > 0$ and suppose $0 < b_n \rightarrow 0$ as $n \rightarrow \infty$. Suppose that Assumptions 5.2.1 and 5.2.2 hold. Then*

$$\text{Var} \left(\tilde{N}_n(t) \right) = \tau_q(0) n^{-1} \ln(b_n^{-1}) + O(n^{-1}), \quad (5.2.9)$$

for both the squared radius and volume and any choice of kernels that meet Condition 5.2.1.

Proof. Consider $\tilde{N}_n(t)$ for the squared radius. Using representation eq. (5.2.5) and recalling that $\tau_q(z) = \int_{h=0}^{\infty} g(z + q(h; t), h) dh = g_Z(z + t)$ for the squared radius, leads to

$$\begin{aligned} n \text{Var} \left(\tilde{N}_n(t) \right) &= b_n^{-1} \text{Var} \left(\bar{K} \left(\frac{t - Z_1}{b_n} \right) \right) \\ &= b_n^{-1} \left\{ E \left[\bar{K} \left(\frac{t - Z_1}{b_n} \right)^2 \right] - \left(E \left[\bar{K} \left(\frac{t - Z_1}{b_n} \right) \right] \right)^2 \right\}. \end{aligned}$$

Using continuity of N at t yields

$$E \left[\bar{K} \left(\frac{t - Z_1}{b_n} \right) \right] = \sqrt{b_n} E \left[\tilde{N}_n(t) \right] = \sqrt{b_n} N(t) + o \left(b_n^{\frac{1}{2}} \right),$$

giving, for $n \rightarrow \infty$,

$$n \text{Var} \left(\tilde{N}_n(t) \right) = b_n^{-1} E \left[\bar{K} \left(\frac{t - Z_1}{b_n} \right)^2 \right] - N(t)^2 + o(1).$$

Now, for $\epsilon > 0$ and n sufficiently large such that $b_n < \epsilon$,

$$b_n^{-1} E \left[\bar{K} \left(\frac{t - Z_1}{b_n} \right)^2 \right] = b_n^{-1} \left(\int_{z=t-b_n}^{t+\epsilon} + \int_{t+\epsilon}^{\infty} \right) \bar{K} \left(\frac{t - z}{b_n} \right)^2 g_Z(z) dz = I_1 + I_2.$$

For I_2 , squaring the upper bound on \bar{K} given in eq. (5.2.7) and using that for $z > t + \epsilon > t + b_n$, and $v = (t - z)/b_n < -1$ gives

$$I_2 \leq b_n^{-1} \left(\frac{z - t}{b_n} - 1 \right)^{-1} \leq \frac{1}{\epsilon - b_n} \leq \frac{2}{\epsilon}$$

for all n sufficiently large. For any $c < -1$ and n sufficiently large, I_1 is

$$\begin{aligned} I_1 &= \int_{-\epsilon/b_n}^1 \bar{K}(v)^2 g_Z(t - b_n v) dv \\ &= \int_{-\epsilon/b_n}^c \bar{K}(v)^2 g_Z(t - b_n v) dv + \int_c^1 \bar{K}(v)^2 g_Z(t - b_n v) dv. \end{aligned}$$

For any fixed c , the second term is bounded by $g_Z(t) \int_{v=-1}^1 \bar{K}(v)^2 dv$, which is a constant. Taking $c < -1$ sufficiently small and using eq. (5.2.8) and the fact that ϵ can be chosen to be arbitrarily small, under Assumption 5.2.2 the first term becomes (details can be found in Appendix C.2)

$$\begin{aligned} \int_{-\epsilon/b_n}^c \bar{K}(v)^2 g_Z(t - b_n v) dv &= g_Z(t) \int_{-\epsilon/b_n}^c \frac{1}{-v} dv + O(1) \\ &= \tau_q(0) \ln(b_n^{-1}) + O(1). \end{aligned}$$

The proof of eq. (5.2.9) for the volume is analogous and is given in Appendix C.3. \square

Combining the results of this section provides the following theorem.

Theorem 5.2.1. *Under Assumptions 5.2.1 and 5.2.2, for $b_n \downarrow 0$, as $n \rightarrow \infty$, for $t > 0$*

$$\text{MSE}(\tilde{N}_n(t)) = \frac{1}{4} b_n^4 N''(t)^2 \left(\int u^2 K(u) du \right)^2 + \frac{\tau_q(0) \ln(b_n^{-1})}{n} + O(n^{-1}) + o(b_n^4)$$

for the squared radius and volume and any choice of kernels that meet Condition 5.2.1.

As a consequence, the asymptotically MSE optimal bandwidth is given by

$$b_n = n^{-\frac{1}{4}} \tau_q(0)^{\frac{1}{4}} \left(N''(t) \int u^2 K(u) du \right)^{-\frac{1}{2}},$$

yielding

$$\lim_{n \rightarrow \infty} \frac{n}{\ln n} \text{MSE}(\tilde{N}_n(t)) = \frac{1}{4} \tau_q(0)$$

(see Appendix C.4). The MSE of the initial plug-in estimator N_n defined in (3.3.2) is infinite, because its variance is infinite. A notable property of the estimator $\tilde{N}_n(t)$ is that as long as the bandwidth tends to zero at rate $n^{-1/4}$, the asymptotic MSE does not depend on the constant that is chosen for the bandwidth. In other contexts, including the estimation of the pdf given in Section 5.3, choosing this constant optimally is often a delicate matter. Another notable fact is the value of the asymptotic MSE in relation to asymptotic distribution results of the estimators studied in Chapter 3. Both the empirical (non-smoothed) and isotonic estimators are asymptotically unbiased and normal with variance $\tau_q(0)$ and $\tau_q(0)/2$, respectively (both rescaled with rate $\sqrt{n/\ln n}$). In view of Theorem 5.2.1, these estimators are comparable to smoothed estimators with bandwidths of order n^{-1} and $n^{-1/2}$ respectively. Taking these small bandwidths results in asymptotically unbiased smoothed estimators. However, smoothing with a bandwidth of $b_n \sim n^{-1/4}$ results in a smoother function with a decreased variance while maintaining the asymptotically unbiased nature of the estimator. Attempting to smooth even more by taking a larger bandwidth will make the bias term in the MSE the dominating one, and thereby increase the asymptotic MSE.

Remark Note that this is essentially different from the situation of estimating a distribution function based on an i.i.d. sample from it. The empirical distribution function \mathbb{G}_n evaluated at t then has MSE equal to its variance (since it is unbiased), $G(t)(1 - G(t))/n$. The Kernel smoothed distribution function (using bandwidth b_n) has

$$\text{MSE} \sim \frac{1}{n} G(t)(1 - G(t)) - c_1 \frac{b_n}{n} + c_2 b_n^4 \quad (5.2.10)$$

where $c_1, c_2 \geq 0$ depend on G and the kernel function K . Hence, smoothing only improves the MSE of the empirical distribution function in the lower order terms. It is clear that taking b_n of the order $n^{-1/3}$ is optimal in this second order MSE sense. See Appendix C.5 for the proof of eq. (5.2.10).

All of this leads to a smooth estimate for the CDF as follows:

$$\tilde{F}_T(t) = 1 - \frac{\tilde{N}_n(t)}{\tilde{N}_n(0)}, \quad t \geq 0. \quad (5.2.11)$$

The derivative of this smoothed function may be taken to give an estimate of the density. This will be explored further in the next section.

5.3 Kernel density estimators

In order to obtain a density estimator for the densities f , eq. (5.2.11) may be differentiated. This leads to the following density estimator, for $t > 0$:

$$\tilde{f}_n(t) = \frac{d}{dt} \tilde{F}_T(t) = -\frac{\frac{d}{dt} \tilde{N}_n(t)}{\tilde{N}_n(0)} = -\frac{\tilde{\nu}_n(t)}{\tilde{N}_n(0)},$$

where $\tilde{\nu}_n(t)$ is the estimator of interest and defined to be

$$\tilde{\nu}_n(t) = \frac{d}{dt} \tilde{N}_n(t) = \frac{1}{nb_n^2} \sum_{i=1}^n \int K' \left(\frac{t-s}{b_n} \right) [Z_i - q(H_i; s)]^{-\frac{1}{2}} \mathbf{1}_{[Z_i > q(H_i; s)]} ds. \quad (5.3.1)$$

Note that just as in the setting of estimating $N(t)$, the expectation of the estimators for the function ν related to the various choices of q can be dealt with at once. To this end, it is necessary that

Assumption 5.3.1. *The function ν is twice continuously differentiable at t .*

Indeed, under Assumption 5.3.1 we can write

$$E[\tilde{\nu}_n(t)] = \frac{1}{b_n} \int N(t-bu) K'(u) du = \nu(t) + \frac{1}{2} b_n^2 \nu''(t) \int u^2 K(u) du + o(b_n^2) \quad (5.3.2)$$

for $n \rightarrow \infty$. Just as in the setting of estimating $N(t)$, the variance must be considered for each q , and only the squared radius and volume will be considered here. In order to obtain the asymptotic variance of these estimators, representations eq. (5.2.5) and eq. (5.2.6) are used to write

$$\begin{aligned} \tilde{\nu}_n(t) &= \frac{d}{dt} \tilde{N}_n(t) = \frac{1}{nb_n^{3/2}} \sum_{i=1}^n \bar{K}' \left(\frac{t-Z_i}{b_n} \right) \quad \text{and} \\ \tilde{\nu}_n(t) &= \frac{1}{nb_n^{3/2}} \sum_{i=1}^n \sqrt{\pi H_i} \bar{K}' \left(\frac{t-\pi H_i Z_i}{b_n} \right) \end{aligned} \quad (5.3.3)$$

for the squared radius and volume, respectively. The following lemma deals with the asymptotic variances of these estimators.

Lemma 5.3.1. *Under Assumptions 5.2.2 and 5.3.1 for the squared radius and the volume, as $b_n \downarrow 0$, for $t > 0$*

$$\text{Var}(\tilde{\nu}_n(t)) = \tau_q(0) \frac{\int \bar{K}'(u)^2 du}{nb_n^2} + O((nb_n)^{-1}) \quad (5.3.4)$$

for any choice of kernels that meet Condition 5.2.1.

Proof. Considering the squared radius, by eq. (5.3.3) we can write

$$nb_n^2 \text{Var}(\tilde{\nu}_n(t)) = \frac{1}{b_n} \left\{ E \left[\overline{K}' \left(\frac{t - Z_i}{b_n} \right)^2 \right] - \left(E \left[\overline{K}' \left(\frac{t - Z_i}{b_n} \right) \right] \right)^2 \right\}$$

Using the asymptotic bias eq. (5.3.2) and Assumption 5.3.1, it follows that the second term in the above expression is $o(1)$ for $n \rightarrow \infty$. Under Assumption 5.2.2 the first term in the above expression is (details can be found in Appendix C.2)

$$\frac{1}{b_n} E \left[\overline{K}' \left(\frac{t - Z_i}{b_n} \right)^2 \right] = \int \overline{K}'(u)^2 g_Z(t - b_n u) du = g_Z(t) \int \overline{K}'(u)^2 du + O(b_n)$$

The proof of eq. (5.3.4) for the volume is given in Appendix C.6. □

Defining the Mean Squared Error for the estimators by

$$\text{MSE}(\tilde{\nu}_n(t)) = (E_g[\tilde{\nu}_n(t)] - \nu(t))^2 + \text{Var}(\tilde{\nu}_n(t)),$$

leads to the following result.

Theorem 5.3.1. *Under Assumptions 5.2.2 and 5.3.1 as $n \rightarrow \infty$ and $b_n \downarrow 0$, for $t > 0$*

$$\text{MSE}(\tilde{\nu}_n(t)) = \tau_q(0) \frac{\int \overline{K}'(u)^2 du}{nb_n^2} + \frac{1}{4} b_n^4 \nu''(t)^2 \left(\int u^2 K(u) du \right)^2 + o\left(\frac{1}{nb_n^2}\right) + o(b_n^4)$$

for the squared radius and volume and any choice of kernels meeting Condition 5.2.1.

From Theorem 5.3.1 it can be inferred that the optimal bandwidth corresponds to a balance of the two terms, leading to $b_n \sim n^{-1/6}$. Taking $b_n = \alpha n^{-1/6}$, the asymptotic optimal choice for α is given by

$$\alpha_{opt} = \left[\frac{2\tau_q(0) \int \overline{K}'(u)^2 du}{\nu''(t)^2 \left(\int u^2 K(u) du \right)^2} \right]^{\frac{1}{6}}$$

Contrary to the results for the estimation of N , here the choice of α has an effect on the dominant term in the expansion of the MSE. Therefore, taking the asymptotically optimal bandwidth yields

$$\lim_{n \rightarrow \infty} n^{\frac{2}{3}} \text{MSE}(\tilde{\nu}_n(t)) = 3 \left[\frac{1}{4} \tau_q(0) \nu''(t) \left(\int \overline{K}'(u) du \right) \left(\int u^2 K(u) du \right) \right]^{\frac{2}{3}}.$$

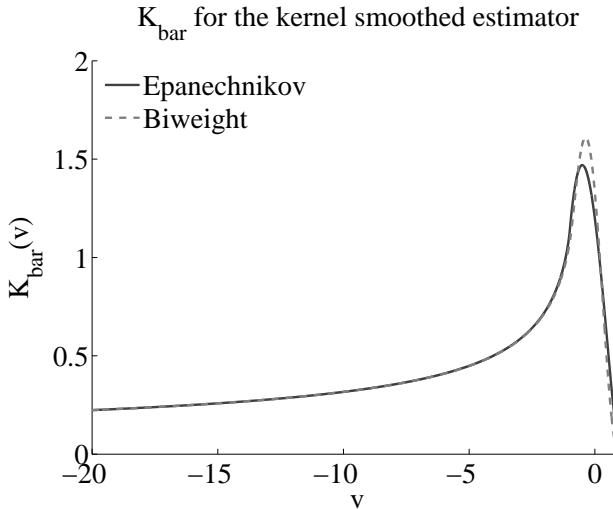


FIGURE 5.4.1: Example of $\bar{K}(v)$ given in eq. (5.2.4) as a function of v using two different kernels, the Epanechnikov and the biweight kernels. In this figure, v is a holding variable, in practice it a function of the quantity of interest t and the observations (Z_i, H_i) ; see, for example, the arguments to the kernel function given in eqs. (5.2.5) and (5.2.6).

Unlike the optimal bandwidth for estimating the CDF, which is asymptotically dependent only on the sample size, finding the optimal bandwidth for estimating the pdf must be done more carefully. This bandwidth depends on the second derivative of the function being estimated, as well as on the integrals related to the kernel. In practice, $\nu''(t)$ is unknown and the integrals for the kernels are not easily calculated. Therefore, other statistical methods, such as cross validation or bootstrapping, could be employed to estimate the optimal bandwidth for the data.

5.4 Application to numerical simulation and steel microstructures

The estimators are applied to the numerical simulation (described in Section 4.3) to visually demonstrate the asymptotic results and compare to the non-smoothed estimators discussed in Chapter 3. Since only the estimators for the squared radius and volume have been presented in the previous sections of this chapter, the results will be confined to these estimators.

For the estimator $\tilde{N}_n(t)$, any available kernel may be used. However, it is necessary for the density estimates that the chosen kernel also be differentiable.

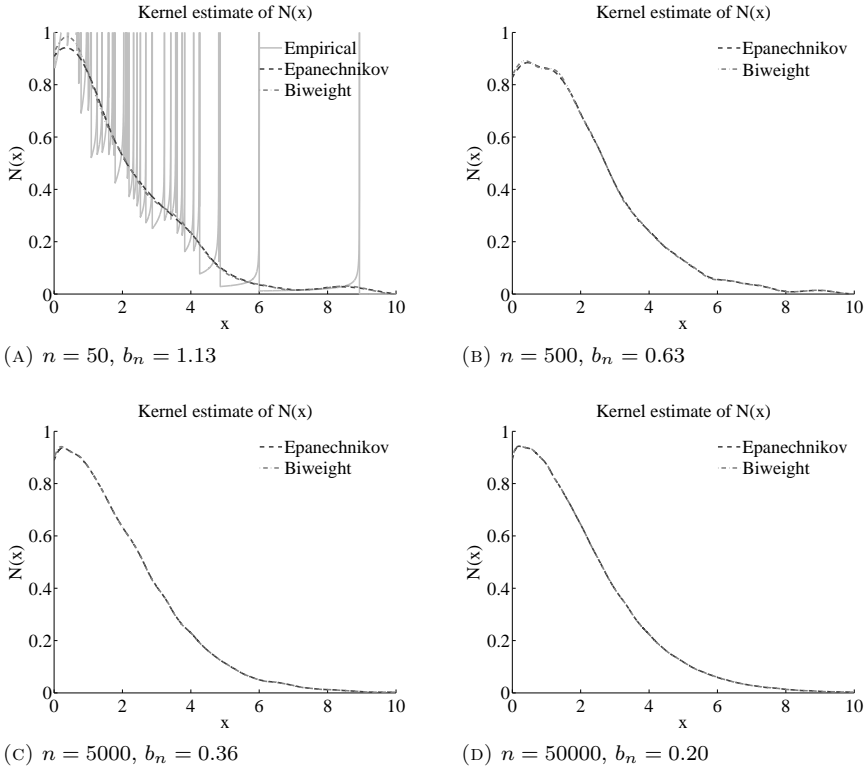


FIGURE 5.4.2: Kernel estimates, $\tilde{N}_n(t)$ given in eq. (5.2.1), for $N(t)$ of the squared radius with $n = 50, 500, 5000,$ and 50000 observations from the numerical simulation. $N(t)$ and its derivative are required for estimating the CDF and the pdf of the quantities of interest. In Figure 5.4.2a the solid line is the empirical plug-in estimator $N_n(t)$. In all figures, the dashed line is the estimate using the Epanechnikov kernel and the dash-dotted line is the estimate using the biweight kernel.

Therefore, the Epanechnikov and biweight kernels were chosen for all estimators. The Epanechnikov kernel is defined as $K(u) = (3/4)(1 - u^2) 1_{[-1,1]}(u)$. The biweight kernel is smoother and defined as $K(u) = (15/16)(1 - u^2)^2 1_{[-1,1]}(u)$. Plugging these kernels into eq. (5.2.4) leads to the new kernels $\bar{K}(v)$ which are shown in Figure 5.2.4 as functions of a holding variable v , which, in practice is a function of the quantities of interest t and the observed pairs (Z_i, H_i) . Equations (5.2.5) and (5.2.6) show what v is in practice for the squared radius and volume, respectively. In the figure, the solid line is the new Kernel using the Epanechnikov kernel and the dashed line is the new Kernel using the biweight

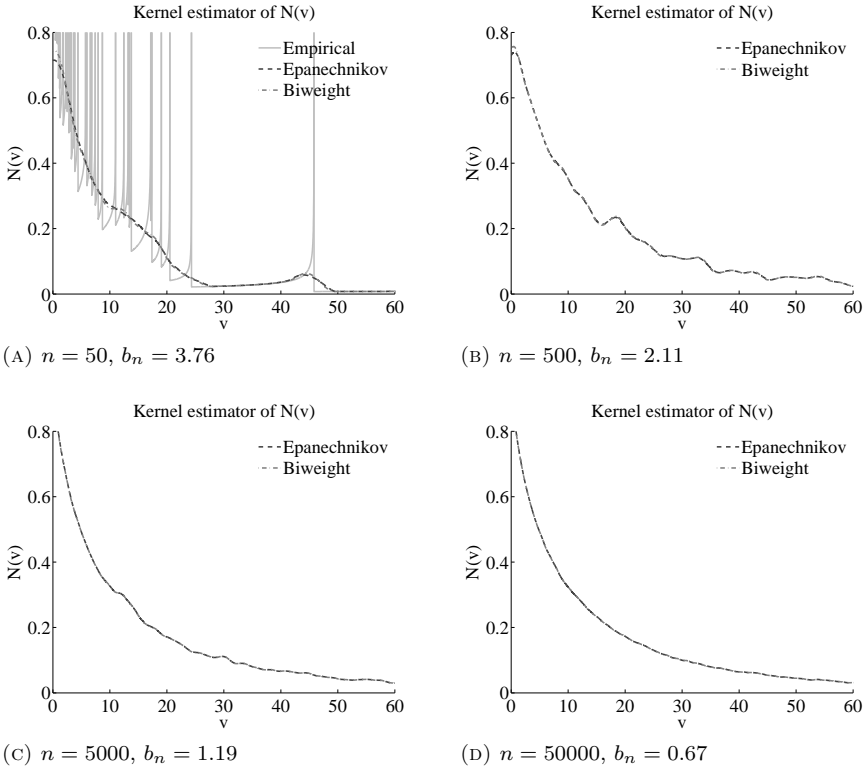


FIGURE 5.4.3: Kernel estimates, $\tilde{N}_n(t)$ given in eq. (5.2.1), for $N(t)$ of the volume with $n = 50, 500, 5000,$ and 50000 observations from the numerical simulation. $N(t)$ and its derivative are required for estimating the CDF and the pdf of the quantities of interest. In Figure 5.4.3a the solid line is the empirical plug-in estimator $N_n(t)$. In all figures, the dashed line is the estimate using the Epanechnikov kernel and the dash-dotted line is the estimate using the biweight kernel.

kernel.

Recall that the CDFs for the quantities of interest t are defined as $F_T(t) = 1 - N(t)/N(0)$, and to obtain an estimate for F_T one must first estimate N . The empirical plug-in estimator for N given in eq. (3.3.2) is non-monotonic and has infinite discontinuities that do not exist in the underlying function. Since the pdf is the derivative of the CDF, it is reasonable to smooth the function N with the newly introduced kernel. Figures 5.4.2 and 5.4.3 show the estimation results of the function $N(t)$ for the squared radius and volume, respectively, from the numerical simulation. In Figures 5.4.2a and 5.4.3a, the light grey lines

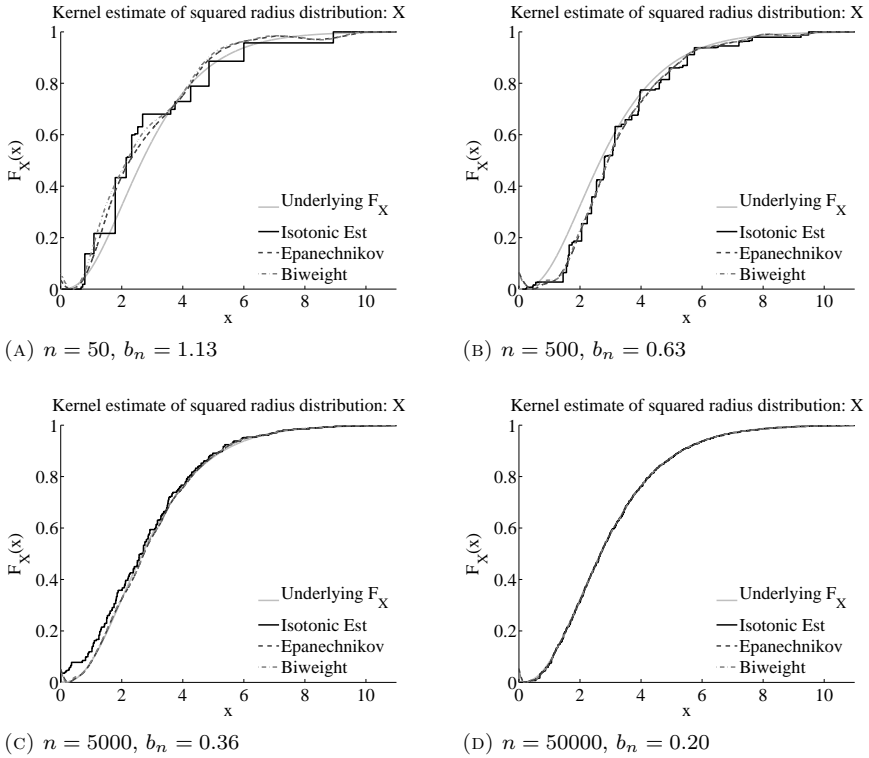


FIGURE 5.4.4: Estimate of the CDF ($F_X(x) = 1 - N(t)/N(0)$) of the squared radius for $n = 50, 500, 5000,$ and 50000 observations from the numerical simulation. The solid light grey line indicates the underlying distribution. The solid black line shows the isotonic estimation results from Chapter 3. The dashed and dash-dotted grey lines show the Kernel estimation results using the Epanechnikov and Biweight kernels, respectively.

represent the results for the empirical plug-in estimator given in eq. (3.3.2), showing the infinite discontinuities. They are then omitted from the remaining images. In all the plots, the dashed dark grey lines and the dash-dotted grey lines represent the results for the smoothed estimator given in eq. (5.2.1) with the Epanechnikov and biweight kernels, respectively. The number of (2D) observations are $n = 50, 500, 5000,$ and 50000 . The bandwidth was chosen to be $3n^{-1/4}$ for the squared radius and $10n^{-1/4}$ for the volume, as they were the smallest bandwidths chosen by eye for a satisfactorily but arbitrarily smooth function. There is no apparent difference between the two kernels chosen. Though, unlike the isotonic estimator, these estimators are non-monotonic.

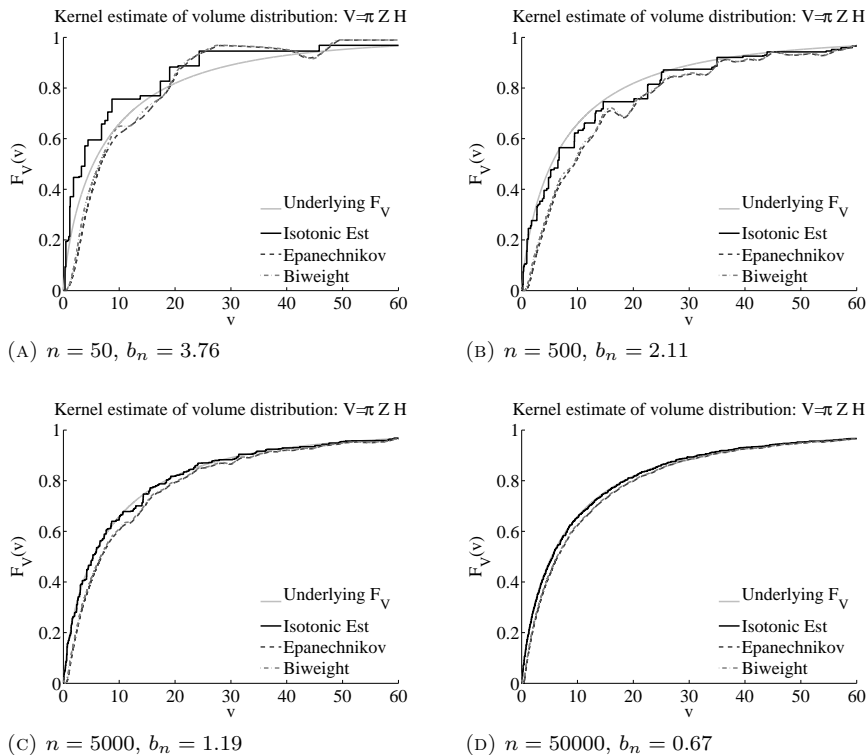


FIGURE 5.4.5: Estimate of the CDF ($F_V(v) = 1 - N(t)/N(0)$) of the volume for $n = 50, 500, 5000$, and 50000 observations from the numerical simulation. The solid light grey line indicates the underlying distribution. The solid black line shows the isotonic estimation results from Chapter 3. The dashed and dash-dotted grey lines show the Kernel estimation results using the Epanechnikov and Biweight kernels, respectively.

This is especially evident with the volume estimators. The spikes to infinity have been smoothed out, but the estimated function is rather wiggly even for large values of n . Since it is the derivative of this function that will eventually lead to an estimate for the probability density, the non-monotonic behavior will result in negative values for the pdf, which is not reasonable.

Figures 5.4.4 and 5.4.5 show the results for the estimator for the CDF given by eq. (5.2.11) for the squared radius and volume, respectively. In all figures the solid light grey line represents the underlying CDF. The solid black line shows the isotonic estimator, a staircase function. The dark grey dashed line shows the results from the Epanechnikov kernel and the grey dash-dotted line

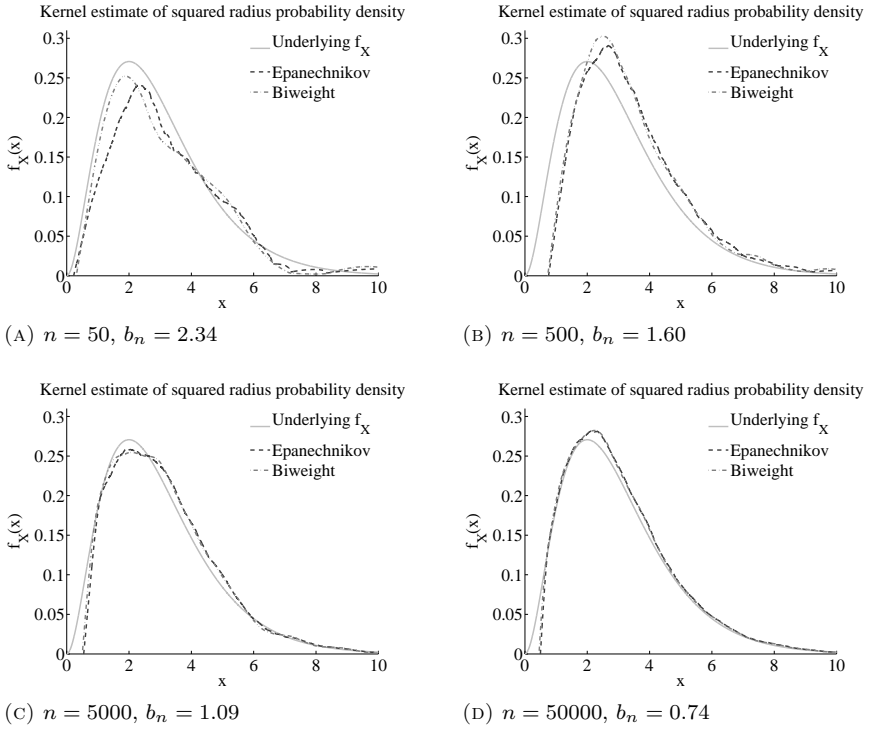


FIGURE 5.4.6: Estimate of the pdf ($f_X(x) = -\frac{d}{dt}N(t)/N(0)$) of the squared radius for $n = 50, 500, 5000,$ and 50000 observations from the numerical simulation. The solid light grey line indicates the underlying distribution. The dashed and dash-dotted grey lines show the Kernel estimation results using the Epanechnikov and Biweight kernels, respectively.

shows the results from the biweight kernel. These figures support the idea of using a smooth estimator for the CDF. For small numbers of observations there does not appear to be any reason to choose the isotonic estimator over the smoothed estimators, and as the number of observations increases, it becomes evident that the smooth estimators are slightly better, especially near $t = 0$. The advantage of the isotonic estimator is the monotonicity of the estimate. Especially in the results for the volume estimate, the non-monotonic results of the smoothed estimators are evident. While choosing large enough observation samples eliminates this problem, the data sets available for the steel microstructures are between 50 and 100, where the non-monotonicity is still observable.

Figures 5.4.6 and 5.4.7 show the results of the estimators for the pdf of

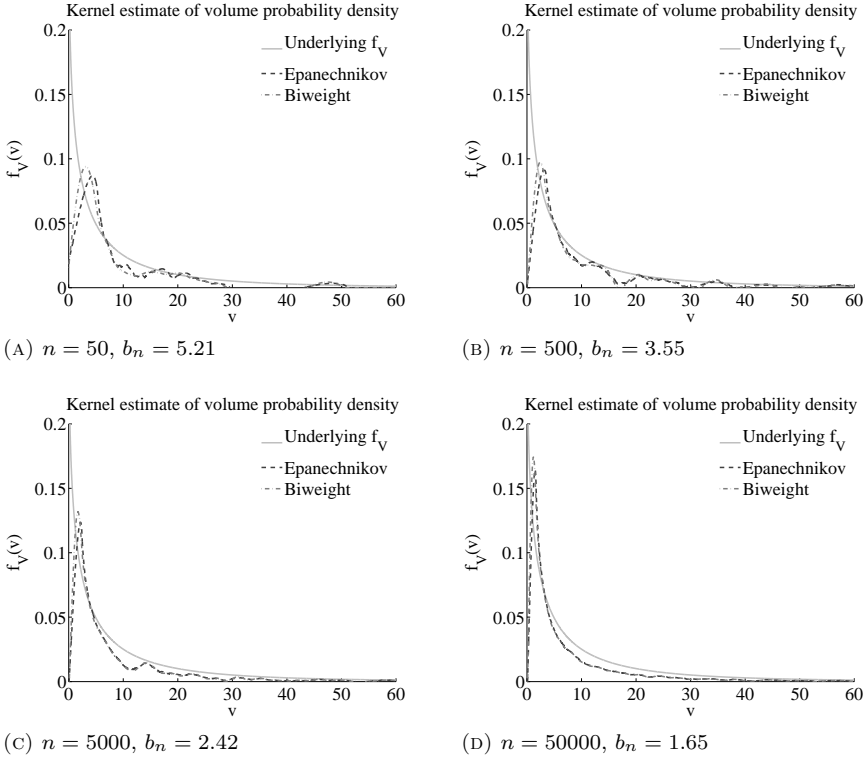


FIGURE 5.4.7: Estimate of the pdf ($f_V(v) = -\frac{d}{dt}N(t)/N(0)$) of the volume for $n = 50, 500, 5000,$ and 50000 observations from the numerical simulation. The solid light grey line indicates the underlying distribution. The dashed and dash-dotted grey lines show the Kernel estimation results using the Epanechnikov and Biweight kernels, respectively.

the squared radius and volume, respectively. In all figures, the light grey solid line represents the underlying density function. The dashed dark grey and dash-dotted grey lines show the results of the smoothed estimators using the Epanechnikov and biweight kernels, respectively. The bandwidths for each estimator were taken to be $4.5n^{-1/6}$ and $10n^{-1/6}$, respectively. These were chosen, as for the estimators above, as the smallest bandwidth to yield estimates that most closely followed the underlying density on visual inspection. Smaller bandwidths resulted in more jaggedness in the estimate, thereby giving a larger variance. Larger bandwidths resulted in a larger bias which manifests as shifts of the function away from zero and a change in the height of the peak. Figure 5.4.6b is a good example of the effect of the bias. Note that the Kernel

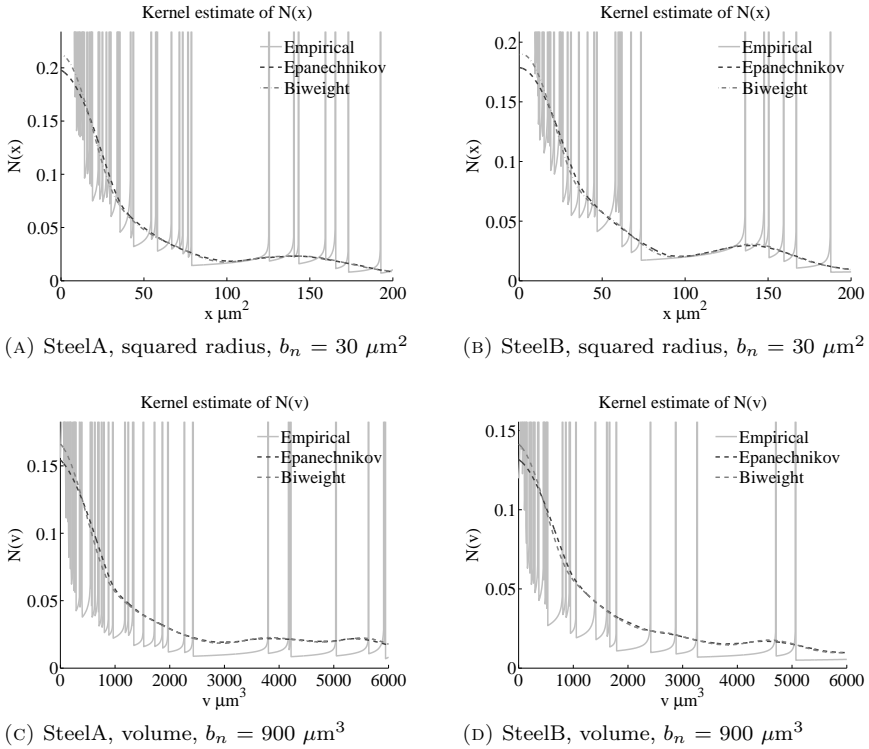


FIGURE 5.4.8: Estimate for $N(t)$ of the squared radius and volume. Note that $n = 89$ and 59 for Steel A and Steel B, respectively.

estimators both go to zero when x is approximately equal to one whereas the underlying distribution goes to zero when x is equal to zero. This has the effect of shifting the peak to the right as well as increasing the height of the peak. With even larger bandwidths, the deviation of the estimate from the underlying becomes even larger.

From these figures, it is not clear that one kernel is superior to the other. Even though the biweight is considered to be a smoother kernel than the Epanechnikov, there does not appear to be an obvious advantage in the resulting estimates. However, a problem arises at zero if the underlying density does not go to zero there, since the kernel functions force the density to zero when the variable is zero, as is the case for the volume with the particular choice of distributions used in the numerical simulation. However, considering boundary behavior is beyond the scope of this work. Therefore, a large bias

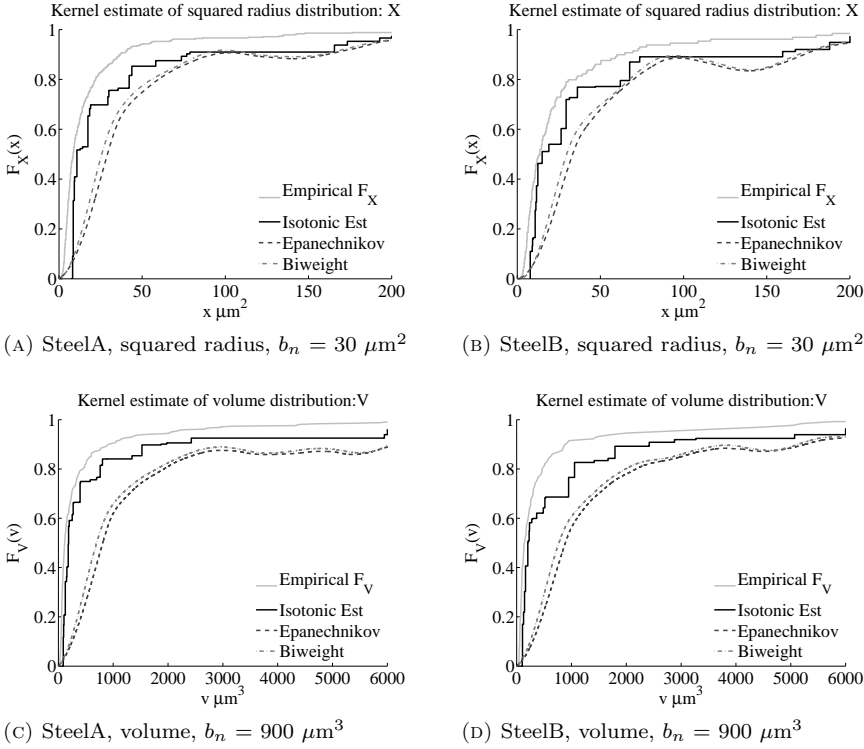


FIGURE 5.4.9: Estimate for $F(t)$ of the squared radius and volume. Note that $n = 89$ and 59 for Steel A and Steel B, respectively.

exists at zero in the estimation of the volume due to this lack of consideration.

Figures 5.4.8, 5.4.9 and 5.4.10 show the results of the estimators applied to the microstructure data from Steel A and Steel B. In all figures, the light grey line represents the empirical estimate. The dark grey dashed and grey dash-dotted lines represent the kernel estimate results for the Epanechnikov and biweight kernels, respectively. The black line in Figure 5.4.9 shows the results of the isotonic estimator.

The estimators appear to provide reasonable estimation results, though in all cases the smoothed estimator over estimates the CDF compared to the empirical and isotonic estimators. Also, the non-monotonicity of the smoothed estimators is evident in these figures. While the pdfs are not, in general, monotonic, the CDFs, by definition must be. Since the pdf is being approximated by the derivative of the smoothed, but here non-monotonic CDF, the result

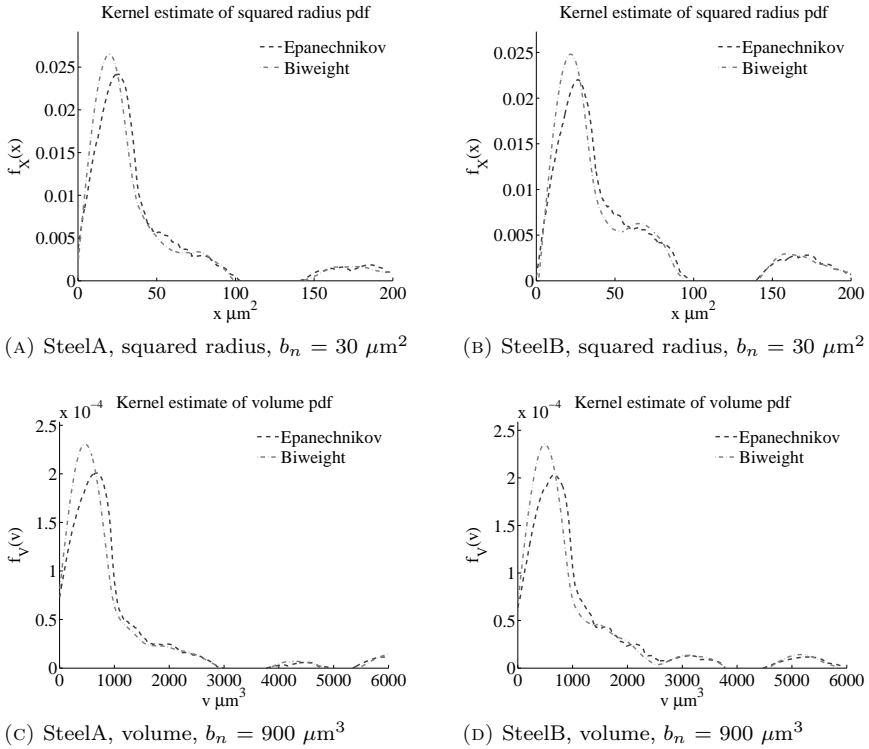


FIGURE 5.4.10: Estimate for $f(t)$ of the squared radius and volume. Note that $n = 89$ and 59 for Steel A and Steel B, respectively.

is that the estimate for the pdf sometimes takes on negative values, which it should not do. While choosing larger bandwidths than $30 \mu\text{m}^2$ for the squared radius and $900 \mu\text{m}^3$ for the volume would have led to monotonic functions, they also smoothed away some of the important features and led to even larger overestimation of the CDFs. As with the simulation results, both kernels appear to yield approximately the same results, neither seeming to outperform the other for the chosen bandwidths.

Interestingly, from these figures, it does not appear that the two steels are very different from each other in 3D. The bands appear to have come from similar distributions, which goes against the intuition arising from the images themselves. This provides a nice example of why a single 2D observation is not always sufficient. While the images of the microstructures of Steel A and Steel B appear to be quite different, perhaps if one could look at all of the

bands inside the material, the differences would be more in how the bands are distributed through out and less in the size and shape of the bands, at least under the assumption that the bands are circular plates. Of course, care must still be taken in drawing such conclusions from these results as the number of observations in 2D is less than 100 for both Steel A and Steel B. Also, the monotonicity is not enforced with the smoothed estimators, and important details in the pdfs may have been lost during the estimation procedure.

5.5 Conclusion

Obtaining an estimate of the probability density function may be more desirable than having an estimate of the cumulative distribution function. The estimators for the CDFs given in Chapter 3 give staircase functions, which cannot be used by straightforward differentiation to estimate the corresponding pdfs. Therefore, kernel estimators for the CDFs were proposed to yield smooth estimators whose derivatives are estimators for the corresponding pdfs. Due to the complex dependence of the estimators on the choice of q , only the simplest dependences of the squared radius and volume were considered in this chapter. However, the surface area and aspect ratio should be similar though more complicated to compute.

The optimal bandwidth to use with the kernels was found to be of order $n^{-1/4}$ for estimating the CDFs and of order $n^{-1/6}$ to estimate the pdfs. This leads to an asymptotic rate of convergence for the MSEs to be $\ln(n)/n$ and $n^{-2/3}$ for the CDFs and pdfs, respectively. It is interesting to note that the smoothed estimators for the CDF have a smaller variance than and the same rate of convergence as the isotonic estimator when the optimal bandwidth is chosen. The estimators were applied to observations drawn from the numerical model introduced in Section 4.3. The results show that the smoothed estimators for the CDFs are reasonable and comparable with the isotonic results. The smoothed estimators for the pdfs are also reasonable, but a bias near zero for the volume is introduced because the behavior of the pdf near zero was not accounted for during the estimation procedure. Last, the estimators were also applied to the microstructures of Steels A and B. The results for the estimate of the CDF were not quite as good as those from the isotonic estimator. The smoothed estimators overestimate the distribution and do not provide monotonic functions, like the isotonic estimator does. This means that the estimate for the pdf takes on negative values, which is not realistic, but at least indicative of the underlying density.

6

Sensitivity to Deviations of Model Assumptions

The cylinder model presented in Chapter 3 has stringent requirements about the angle of the cut plane and the shape of the observed objects. This chapter explores the effects on the accuracy and precision of the estimators when the objects deviate from circular cylinders and the cut plane is not perfectly parallel to the cylinder symmetry axis. It will be shown that the angle of the cut plane skews the height observations, but that the model is less sensitive in the case of thin objects than for thick objects. Continuity of the structures is not always observable on a cut plane and the effect of cylinders appearing either broken into smaller pieces or merging into one larger object is considered. Finally, a quantifier for the degree an object deviates from ideal is suggested and correlated to the estimation results.

6.1 Introduction

It is important to understand the scope and limitations of any model that is used. In Chapter 4 the oriented circular cylinder model presented in Chapter 3 was explored using two different types of simulations. The requisite conditions of circular cylinders oriented in the same direction with the cut plane parallel to the axis of symmetry of the cylinders was strictly followed in these simulations. In this chapter, the sensitivity of the cylinder model when the objects of interest do not completely meet the stringent requirements of the model is considered. When the cut plane is allowed to have an angle relative to the axis of symmetry, the height observations will be of a more complex character, sometimes not even rectangular, since the plane can partially intersect with a cylinder, or intersect in such a way as to result in a height observation that is larger than the actual cylinder height. In Section 6.2 the limitations of the model due to the cut plane not being exactly parallel are explored.

Objects of interest, such as microstructural bands, deviate from perfectly circular cylinders and therefore, do not produce perfect rectangles on the cut plane. In Section 6.3, the effects of microstructural band deviations on the estimation results is explored and a metric to quantify how much an object deviates is suggested. Discussion about the relationship between the metric and the extent to which the results are reliable is presented. In Section 6.3.1 the issue of determining the rectangle dimensions for an object that is not exactly rectangular is considered. Sometimes, it is impossible to determine the connectivity of the microstructural objects in 3D from what is observable on the cut plane. Standard image analysis determines an object by pixel connectivity. This leads to the possibility of two objects merging into one, or a single object appearing to be broken into smaller pieces. It is impossible to know when this occurs and the effect this has on the estimation results is discussed. Quantifying how much an object deviates from ideal is discussed in Section 6.3.2. This is used in Section 6.3.3 to identify the dependence of the accuracy and precision of the estimators to the deviation from ideal.

6.2 Cut Plane Angle

In this section the effect of the cut plane not being completely parallel to the axis of symmetry of the cylinders is explored. When the plane is at an angle, the observed rectangle height is no longer guaranteed to be the same as that of the cylinder. The physical simulation described in Section 4.2 was used to observe the limitations of the model due to this effect. Two different cylinder height distributions were used because this effect is strongly dependent upon the height dimension. The radii and the position of the bottom of the cylinders

were kept the same throughout the simulations. Five different cut plane angles were used: 5°, 10°, 15°, 20° and 30° from the axis of symmetry.

By introducing an angle to the cut plane, the observed objects on the cut plane are no longer rectangular, but instead trapezoidal. Depending on the size of the cylinder, the sides of the trapezoid may even bulge. Therefore, neither the height nor the half-width are straightforward measurements. In this modified physical simulation, the mean of the chords formed by intersections of the top and bottom of the cylinder with the cut plane is used as the observed width corresponding to $\sqrt{Z_i}$. The maximum height of the trapezoid is used as the observed height, H_i .

Figure 6.2.1 shows cylinders inside a box with a cut plane at 0° (Figure 6.2.1a), 5° (Figure 6.2.1b) and 30° (Figure 6.2.1c) angles from parallel. The lower left edge of the plane is always in the same location. The left images show thick plate-like cylinders whose heights are relatively large, while the right images show thin plate-like cylinders whose heights are relatively small. In these figures, the role of the thickness of cylinders is observable. The thickness determines whether the cylinder is within range of the tilted cut plane, and how much of the cylinder is observable should the cut plane intersect it. Comparing the two panels of Figure 6.2.1b demonstrates this well. The middle cylinder in the left panel is intersected at the top, but not at the bottom. Therefore, in the right panel, the corresponding thin cylinder does not intersect with the cut plane. Also, when the plane does intersect with the tall middle cylinder, it only intersects with a small portion of it. This leads to the observed object on the cut plane not being rectangular, but rather trapezoidal or wedge-shaped. This leads to difficulties in determining not only the height but also the half-width of the observed shape. A similar result occurs in Figure 6.2.1c, where the same cylinder is still fully intersected for the thin cylinders, but only the lower portion of it is intersected for the thick cylinders. For the cylinders that are fully intersected by the tilted plane, the observed rectangle has a larger height than the actual cylinder and its sides bow out, also skewing the observed half-width.

Figure 6.2.2 shows the empirical estimation results from the 2D observations made on the angled cut plane (dark grey lines) and the isotonic estimation results (black lines) for the squared radius at cut plane angles of 5° (dash-dotted lines) and 30° (solid lines). The simulations were run with 5000 cylinders in the box and varying observations on the cut planes. The estimation results for the thin cylinders (Figure 6.2.2b) show little difference between the two angles. Due to the cylinders being thin, almost always when the plane intersects it, the height is fully intersected and so for any “rectangle”, the half-width is relatively constant despite the tilt of the plane through the cylinder.

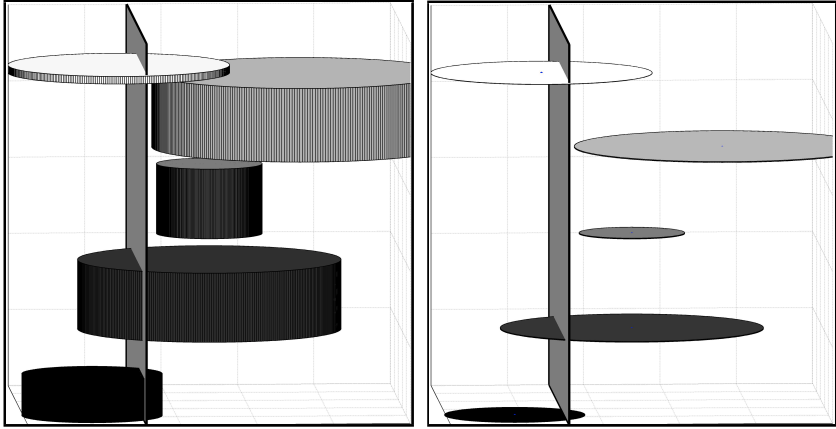
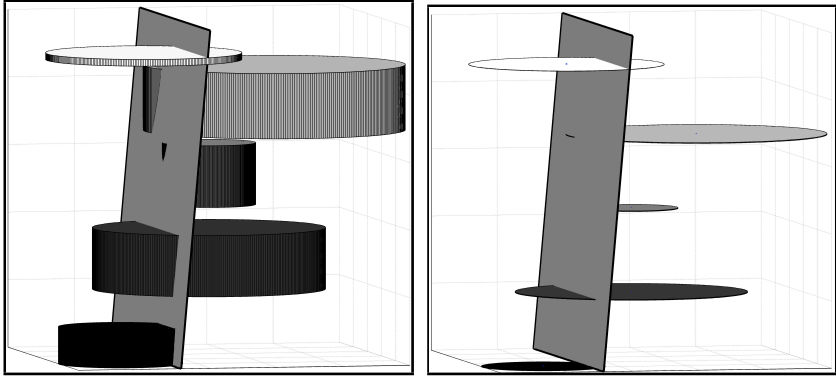
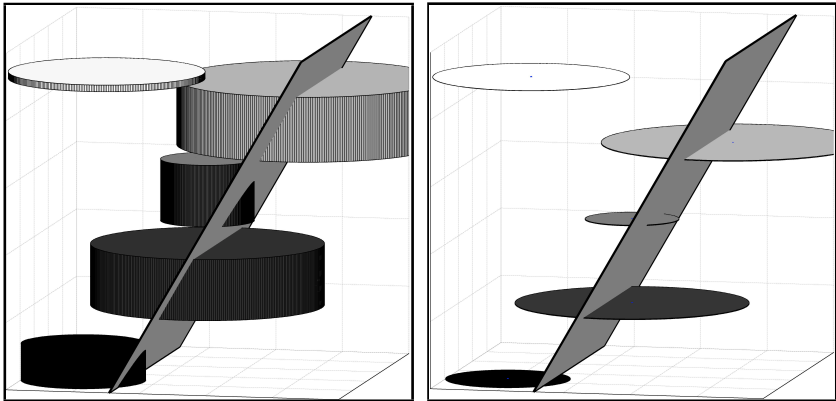
(A) Cut plane at 0° from symmetry axis.(B) Cut plane at 5° from symmetry axis.(C) Cut plane at 30° from symmetry axis.

FIGURE 6.2.1: View of the cut plane through the unit box. Thick ($h_{max} = 0.2$) and thin ($h_{max} = 0.002$) plate-like cylinders are shown to contrast the effect of the cylinder height on the observations.

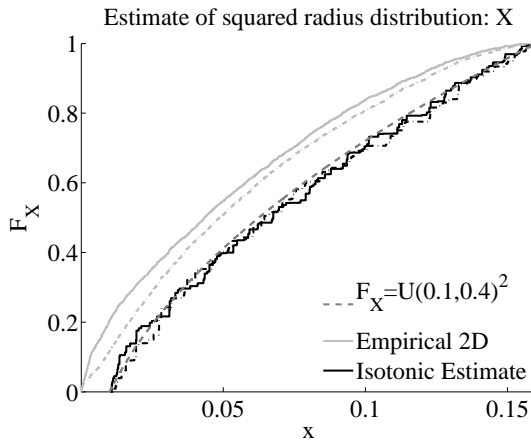
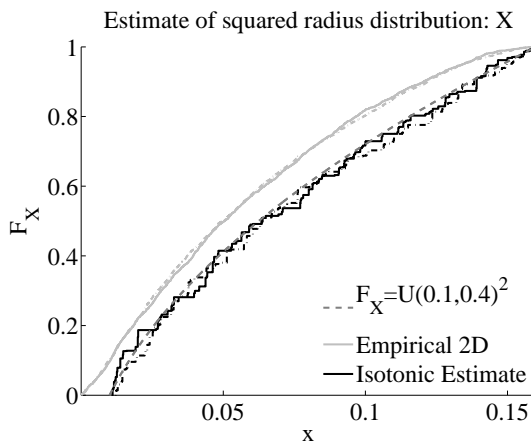
(A) \hat{F}_X for thick cylinders.(B) \hat{F}_X for thin cylinders.

FIGURE 6.2.2: The distribution function of the squared radius, X for 5000 cylinders. The dashed grey line is the underlying (3D) distribution. The dash-dotted (5°) and solid (30°) grey lines are the empirical distributions of the 2D squared half-widths on the angled cut planes. The dash-dotted (5°) and solid (30°) black lines are the isotonic estimates. Note that the angle does not seem to affect the estimation of the squared radius.

For the thick cylinders (Figure 6.2.2a) the effect of the cylinder being only partially intersected is evident. The empirical distribution of the “rectangle” squared half-widths shows that the observations are even smaller for 30° than

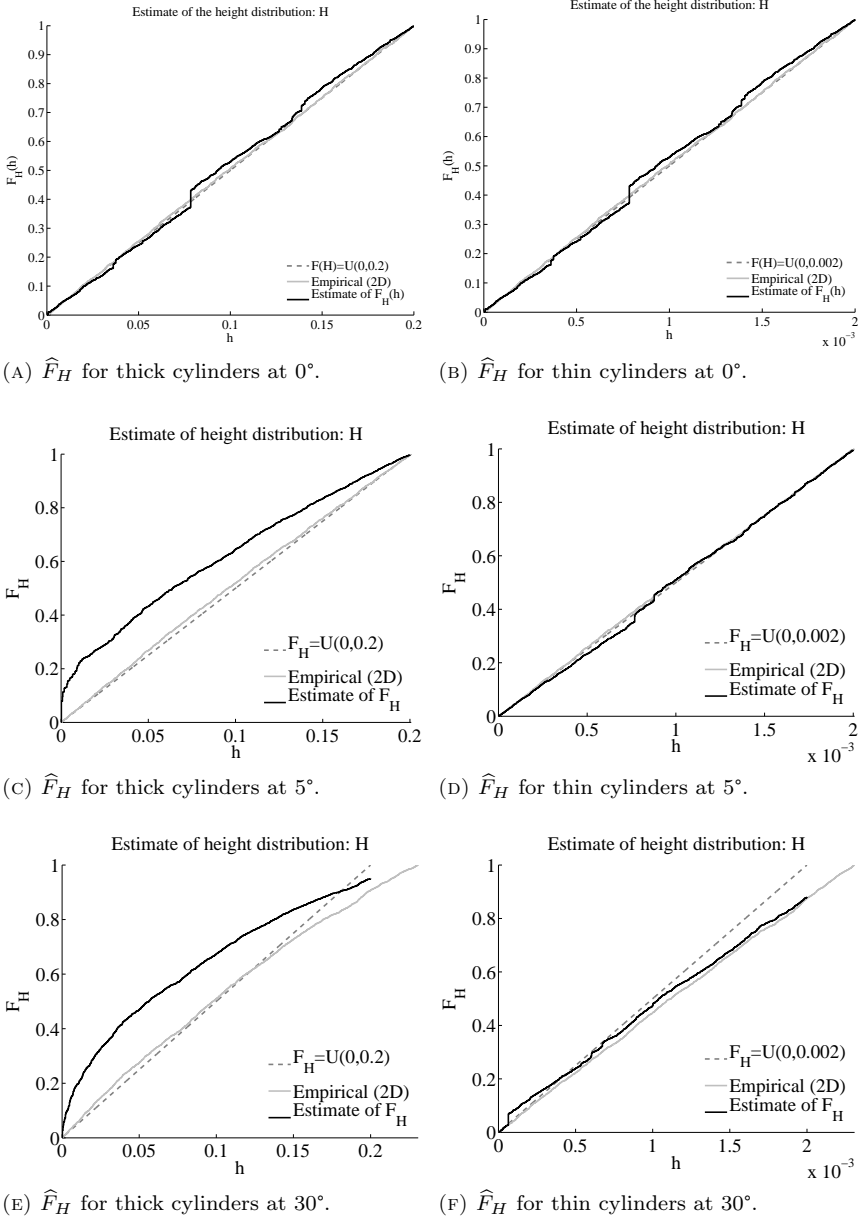


FIGURE 6.2.3: The estimated distribution function of the height, H . The dashed grey line is the underlying distribution. The solid grey line is the empirical distribution of the 2D heights observed on the angled cut plane. The solid black line is the estimate from eq. (3.3.1). Note that the relative height of the cylinders strongly affects the accuracy of the estimator.

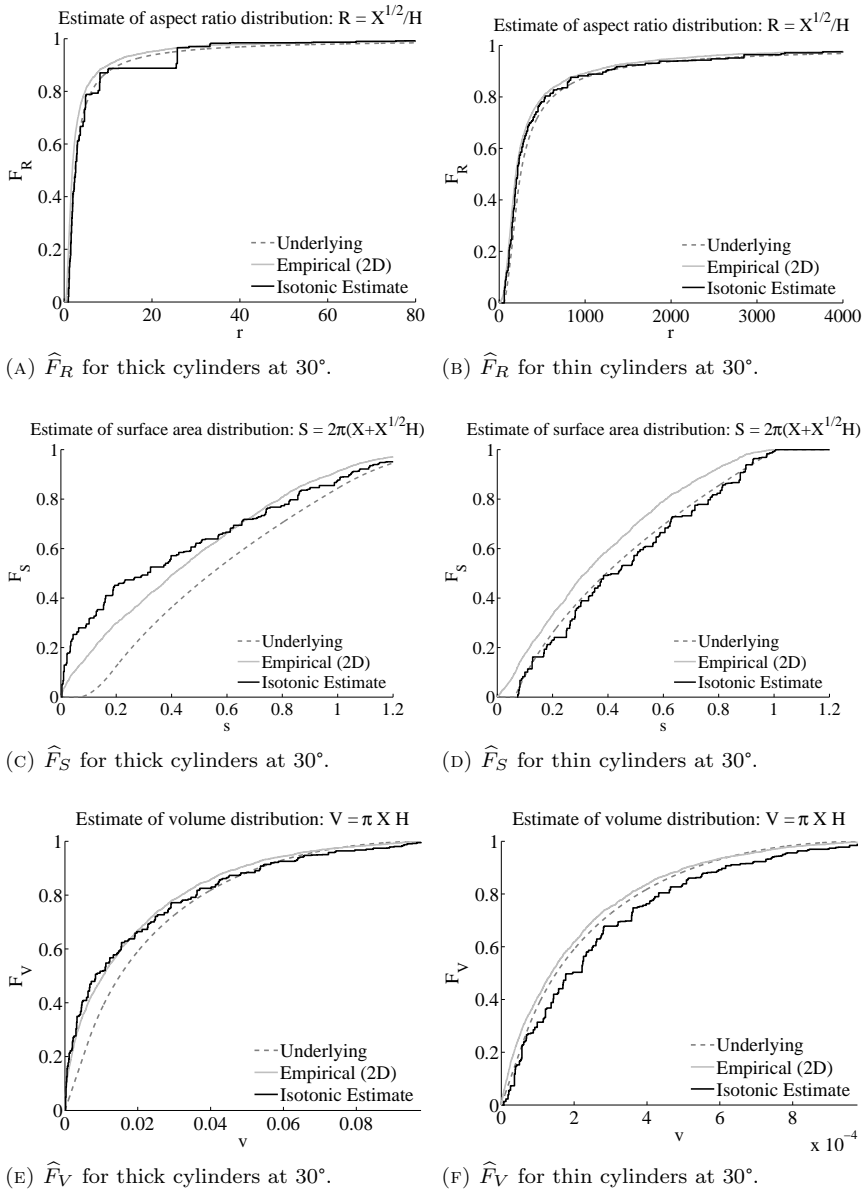


FIGURE 6.2.4: The distribution function of the aspect ratio, R , the surface area, S and volume, V . The dashed grey line is the underlying distribution. The solid grey line is the empirical distribution of the 2D quantities calculated from the observations on the angled cut plane. The solid black line is the isotonic estimate. All figures are for a cut plane angle of 30° with respect to the axis of symmetry. The relative height of the cylinders strongly effects the accuracy of the estimator.

for 5° . Despite this, the isotonic estimator still appears to accurately estimate the true underlying distribution. Therefore, it appears that the isotonic estimator is not sensitive to the angle of the cut plane, even for large angles.

However, the cut plane angle does have a notable effect on the estimation of the height. Figure 6.2.3 shows the height estimation results for the thick (Figures 6.2.3a, 6.2.3c, and 6.2.3e) and thin (Figures 6.2.3b, 6.2.3d, and 6.2.3f) cylinders with cut planes at 0° (Figures 6.2.3a and 6.2.3b), 5° (Figures 6.2.3c and 6.2.3d) and 30° (Figures 6.2.3e and 6.2.3f). The effect of the relative cylinder size is observable here. Even for a cut plane at 5° the height estimation results are skewed towards smaller heights for thick cylinders. This is due to the cut plane intersecting only a small portion of the cylinder, as seen, for example, in figure 6.2.1b. This introduces an artificial correlation between the observed “rectangle” height and half-width, both being smaller than they should be, which leads the estimator eq. (3.3.1) to give inappropriate weighting to the smaller observations. The empirical distribution for the 2D height observations is not nearly as sensitive to this. Even at 30° the empirical distribution for the 2D height observations only slightly under represents the heights for the shorter of the thick cylinders while over representing the heights for the larger cylinders. For the thin cylinders, a small tilt in the cut plane does not have any effect on the empirical distribution nor on the estimate. The artificial correlation seen with the thick cylinders is not introduced in this scenario. At large angles, the empirical distribution of the 2D heights deviates almost immediately to larger heights, but the estimate appears to try to correct for this. It seems to slightly under estimate for very small heights and only slightly overestimate the large heights. Therefore, if the cylinders are thin, the model is not sensitive to deviations of the cut plane from 0° .

Figure 6.2.4 shows the results for the estimators of the CDFs for the aspect ratio, surface area and volume of the thick and thin cylinders with a cut plane at 30° from parallel. Here, again, the effect of the relative height of the cylinders is evident. For the thick cylinders, the surface area and the volume estimates overrepresent the smaller values while for the thin cylinders the surface area estimator is quite accurate. The volume estimator seems to slightly overestimate the volumes of the thin cylinders. The aspect ratio estimation is affected in the opposite way by relative height. This is due to the aspect ratio depending on the inverse of the height.

Based on the chosen simulation settings, the cylinder model appears to be sensitive to the angle of the cut plane with respect to the cylinder axis of symmetry only if the cylinders are thick. Thick cylinders are more likely to be partially intersected by the cut plane than thin ones, leading to under-representation of both the height and the rectangle half-width, and creating

an artificial correlation between the half-widths and heights. The isotonic estimator is robust against the underrepresentation of the half-widths and independent of any induced correlation. However, the estimator for the heights, designed to account for unknown correlation between the cylinder radii and heights, is, by its very nature, not robust against it. For even small deviations of the cut plane, the estimator for the thick cylinders becomes inaccurate. On the other hand, even for large deviations of the cut plane for thin cylinders, the estimation remains reasonably accurate. Therefore, if the observed objects can be considered thin, the artificial correlation is not introduced and the estimation results are fairly reliable.

6.3 Deviation from Ideal Cylinders

Since material microstructures are often not ideal geometric shapes, it is important to consider the impact this has on the results of the model. In Chapter 4, two simulations were used to test the model and observe its behavior under various conditions. However, the simulations were always considered with perfect cylinders. The steel microstructures were also treated as if the objects of interest conformed perfectly to the cylindrical and rectangular shapes. Yet, from Figures 2.3.1 and 3.1.1 it is clear that the objects do not perfectly conform to these shapes. To assess the impact of microstructural objects on the results from the model, another physical simulation is performed. In this simulation, 3D Voronoi diagrams (see Ref. [90] for a complete description) are used to represent realistic dual phase microstructures. This type of simulation is often used in Materials Science to generate realistic microstructures for studying their behavior and properties [82, 90]. The objects of interest are created so that they could be represented by the oriented cylinder model. The density of the Voronoi generating sites allows for control over deviations of the objects of interest from perfect cylinders. The objects of interest are created by placing cylinders into the Voronoi diagram and labeling any cells whose generating sites fall inside of a cylinder as the phase of interest. If the number of Voronoi generating sites is infinite, the objects of interest converge to the ideal generating cylinders. In this way, the information about the generating cylinder and the corresponding Voronoi object is preserved. The Voronoi diagram is cut in a few locations and the cut planes are prepared and analyzed in the same manner as the optical micrographs for Steel A and Steel B (see Chapters 2 and 4).

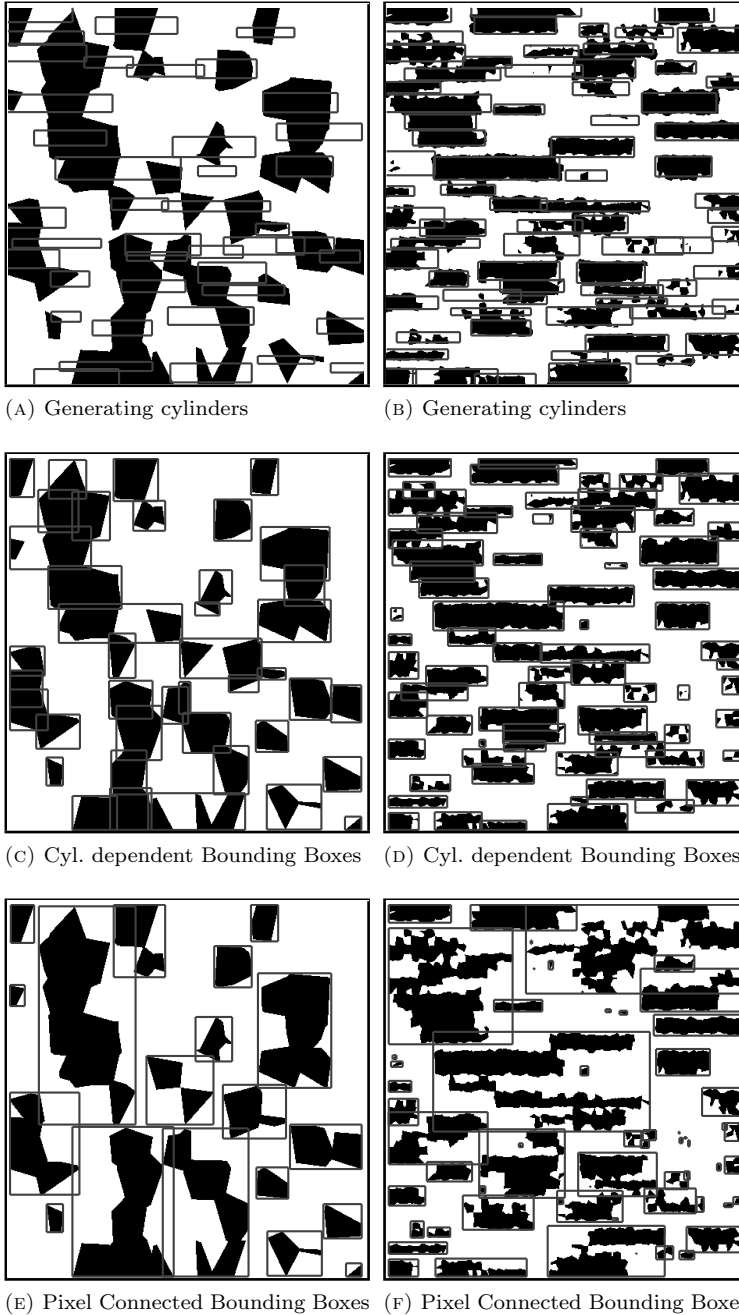


FIGURE 6.3.1: Comparison of the underlying generating cylinders to the bounding boxes of the objects associated with the generating cylinders and to the bounding boxes of the objects determined by pixel connectivity. Figures 6.3.1a, 6.3.1c and 6.3.1e have a Voronoi site density of 100 times that of Figures 6.3.1b, 6.3.1d and 6.3.1f.

6.3.1 Determining Bounding Rectangle

When working with objects that deviate from ideal cylinders, the observations on the cut plane also deviate from ideal rectangles. A possible way to determine the observed rectangle of such an object is to use the bounding box, which is the smallest rectangle that contains the object. Depending on the roughness of the object, the bounding box can lead to an overestimation of the observed half-width and height. Determining the connectivity of the objects on the cut plane into the depth of the material is not possible without knowledge of the entire 3D structure. Therefore, it is possible that some objects will appear as a single object, or a single object will appear broken into smaller objects. This has an effect on the estimation of the underlying distributions and expectations.

Figure 6.3.1 shows cut planes through two different 3D Voronoi diagrams representing dual phase microstructures. Figures 6.3.1a and 6.3.1b show coarse- and fine-grained structures with Voronoi site densities differing by two orders of magnitude. This particular Voronoi grid has been distorted in such a way as to make the cells closer to rectangles than irregular polygons [91]. The rectangles represent the generating cylinders of the visible microstructural objects as if the cylinder were cut exactly in the center. Figures 6.3.1c and 6.3.1d show the bounding boxes around the objects of interest as determined by their generating cylinders. For the fine-grained structures, the objects within the bounding box are sometimes disjointed while at other times the boxes overlap. When these structures are analyzed as a microstructure with no knowledge of the connection through the generating cylinders, the resulting bounding boxes are shown in Figures 6.3.1e and 6.3.1f.

From these figures, two problems arise. The first problem is that of connectivity. When a microstructure is analyzed, objects are determined by pixel connectivity. In this case, where the Voronoi structures represent dual phase steel, a binary image is used. Sometimes, when grey-scale or full color images are used, it can be much easier to determine the boundaries between objects. However, with binary images, this subtlety can be lost leading to the problems observed in Figures 6.3.1e and 6.3.1f where individual objects appear connected and so they are treated as a single object, or where a single object is broken and so it is treated as multiple objects. This leads to a misinterpretation of the corresponding rectangle dimensions and of the number of cylinders in the microstructure. For the coarse structure, there are 190 cylinders in the entire 3D box, 41 of which are intersected by the cut plane. However, only 19 individual objects are recognized through pixel connectivity. For the fine structure, 73 of the 418 cylinders are intersected by the cut plane and only 61 objects are recognized through pixel connectivity. The second problem is

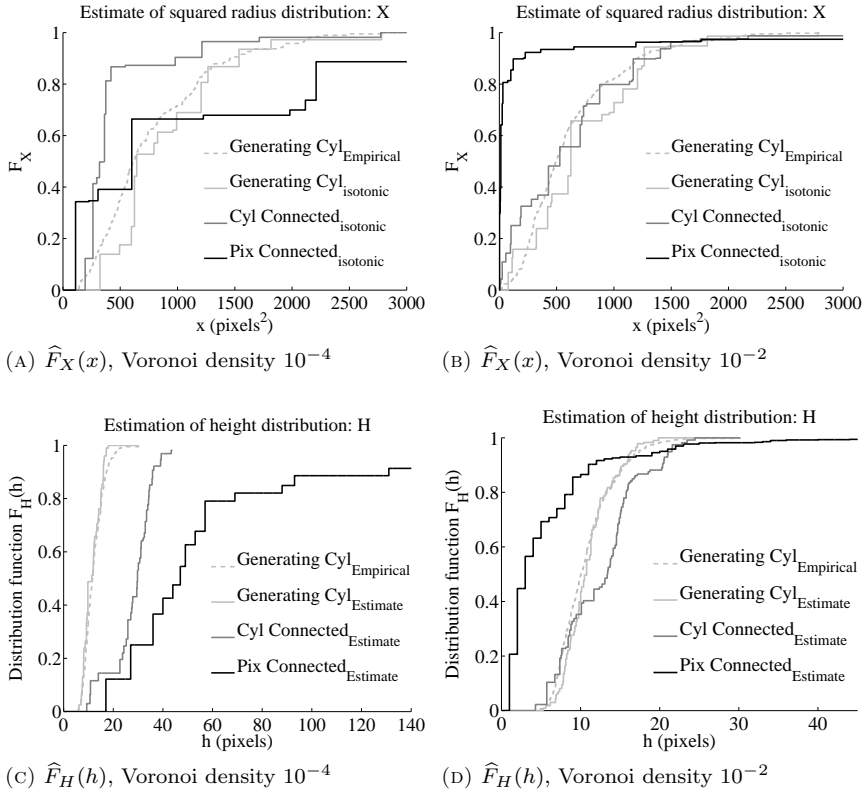


FIGURE 6.3.2: Results of the estimation of the squared radius X and height H of the cylinders for the coarse grained and fine grained structures in Figure 6.3.1. In all figures, the light grey dashed line shows the empirical 3D generating cylinder observations, the solid light grey line shows the Isotonic estimation from the rectangles formed by the generating cylinders on the cut plane. The grey line shows the Isotonic estimation from the bounding boxes of the objects connected through the generating cylinder. The black line shows the Isotonic estimation from the bounding boxes determined by the pixel connectivity. The latter estimation is not at all representative of the true generating cylinder distribution.

that even when the objects are correctly identified, due to the roughness of the objects determining the observed rectangle height is non-trivial. The choice, in this work, of using the bounding box of the connected object leads to the height always being overrepresented. This problem is more serious for in the coarse-grained structures, but is evident even in the fine-grained structures.

The effect of these problems on the estimation of the CDFs for the squared radius and height can be seen in Figure 6.3.2. In all plots, the dashed light

grey line shows the empirical distribution of the generating cylinders. The solid light grey line shows the estimation from the observed rectangles. The grey line shows the estimate from the bounding boxes around the objects connected by the generating cylinders. The black line shows the estimate of the bounding boxes for the objects formed by pixel connectivity. The distribution of the squared radius in Figures 6.3.2a and 6.3.2b suggests that the Isotonic estimator is sensitive to the choice of bounding box. The results are heavily weighted by the small observations from the broken cylinders and the large observations from the merged cylinders. This is true for both the coarse- and fine-grained structures. The results from the bounding box around the cylinder connected objects appears to be somewhat better than the pixel connected objects, especially for the fine-grained Voronoi structure. However, the number of observations on the cut plane, especially for the coarse-grained structure, is quite small and so it is expected that the resulting estimate will not be as good as an estimate made from a larger number of observations. Overall this leads to expecting the fine-grained estimate to be better than the coarse-grained estimate and the cylinder connected object estimation to be better than the pixel connected object estimation.

Since the height information is preserved when the box is cut, the results for the CDF of the height in Figures 6.3.2c and 6.3.2d make a clear statement about the model sensitivity. For the coarse-grained structure, neither choice for the bounding box is representative of the underlying distribution. This is not at all surprising given the large Voronoi cell sizes compared to the heights of the generating cylinders. The result for the bounding boxes of the objects formed by the generating cylinders clearly overrepresents the heights. The estimation results from the bounding boxes of the pixel connected objects shows a minimum height of about 17 pixels, which is equal to one of the largest cylinders according to the 3D empirical distribution function. This is, in large part, an artifact of the coarseness of the objects. However, the fine-grained structure also shows that the choice of bounding box has an impact. Even though the bounding box always overrepresents the heights, the pixel connected objects misrepresent the heights even more so, weighted by the small and large observations, leading to an estimated distribution that is not at all representative of the true underlying distribution.

The choice of using the bounding box to represent the rectangle dimensions of non-rectangular objects overrepresents the objects' heights. In and of itself, this may not necessarily be a significant problem. It can be addressed by finding a different method to determine the rectangle dimensions. Using measurements like Ferret diameters or the major and minor axes of the ellipses of best fit, all quantities measured by image analysis programs like Fiji [62],

are reasonable alternatives to the bounding boxes. However, exploration of these quantities is beyond the scope of this work.

The problem arising from having no good means of determining the true connectivity of the observed objects on the cut plane is another issue that could be addressed to reduce the sensitivity of the model. Part of the problem comes from the image processing to convert the grey-scale micrograph into a binary image, as described in Chapter 2. One way this problem can be alleviated is by choosing a different method, a different means of thresholding or morphologically treating the image. Exploring this option, again, is beyond the scope of this work.

6.3.2 Normalized Symmetric Difference Volume (NSDV)

Throughout this chapter, the deviation of microstructural objects from the ideal geometric shapes has been discussed. However, there has been no means of quantifying how different the object is from the cylinders that are representing them. With some shapes, such as spheres, determining how much an object deviates from that shape is well established. For other objects, such as the cylinders used in this thesis, it is not immediately obvious how to quantify it. For this simulation, both the generating cylinder and the generated object of interest are known. The symmetric difference is one means of establishing how similar two objects are. Quantification of the similarity between two objects based on the symmetric difference is presented here and will be used throughout the rest of this chapter.

The symmetric difference between two sets is defined as set created from the union of the sets minus the intersection of the sets. The volume of the symmetric difference gives a measurable indication of how similar the two sets are. This idea can be applied to the cylinders and the objects of interest created in the Voronoi diagrams. However, since the volume of the symmetric difference is dependent upon the size of the objects being observed, dividing the volume of the symmetric difference by the volume of the union of the two objects removes this scale dependence, but increases the weight of the influence that small objects have on the results. This quantity is called the Normalized Symmetric Difference Volume (NSDV). When the NSDV is zero, the two objects are exactly the same. When the NSDV is one, the two objects have no overlap or nothing in common.

Figure 6.3.3 shows examples of varying symmetric differences. There are two sets represented by light and dark grey ovals. Their intersection is represented by the grey area of overlap between the two ovals. The union is single object created by the two ovals. The symmetric difference is represented by only the light and dark grey portions of the ovals still visible. The object on

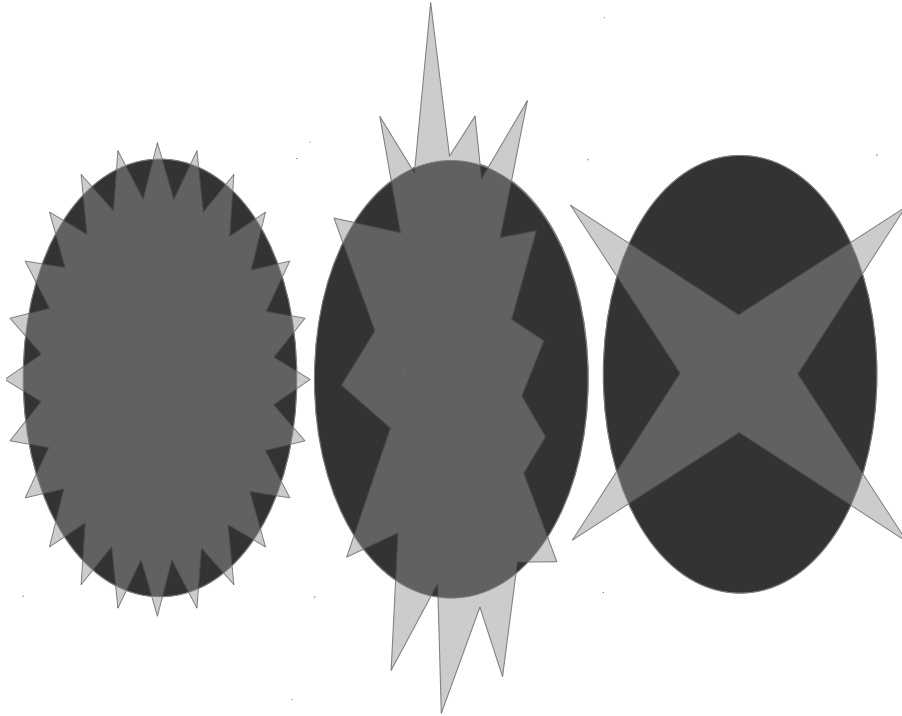


FIGURE 6.3.3: Example of two overlapping objects. The individual objects are light grey and dark grey. The intersection is represented by the medium grey portion in the center. The union is the combined object. The symmetric difference represented by only the light and dark grey areas. The left set has a NSDV of nearly zero. The right object has a NSDV of nearly one.

the left has a NSDV of nearly zero. The object on the right has a NSDV of nearly one.

To test the sensitivity of the cylinder model to deviations from ideal cylinders, comparison between microstructural objects and ideal cylinders is necessary. The NSDV can be used as a metric to determine how close the microstructural object is to ideal. The goal is to determine how far from ideal an object can deviate while the model still provides reliable estimates.

6.3.3 Correlating NSDV and Estimation Results

The union of 3D Voronoi diagrams and a box filled with cylinders is used to simulate dual phase microstructures whose features of interest are like circular cylinders. The union is created in the following way. A unit cube is uniformly

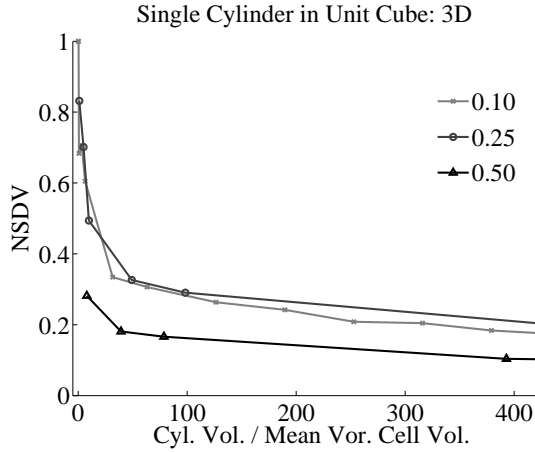


FIGURE 6.3.4: NSDV as a function of the ratio of the cylinder volume to mean Voronoi cell volume. Legend entries correspond to the radius and height (taken to be equal) of the cylinder.

and randomly filled with a number of points. These points are the generating sites for the Voronoi cells, which are also determined. Next, the box is filled, one at a time, with cylinders whose radii and heights are drawn from one of the distributions in eq. (4.3.1). Any Voronoi cell whose generating site falls inside of the cylinder is considered to be part of the object of interest, otherwise it is counted as part of the background. Finally, the box is cut at random in the direction of the axes of symmetry of the original cylinders, and the portions of the Voronoi objects and the cylinders observable on the plane are treated in the same way as the steel microstructures described in Chapter 4.

The NSDV is related to the size of the cylinders relative to the size of the Voronoi cells. An appropriate distribution of cylinder sizes and Voronoi densities must be determined for the simulation to span the range of NSDV and yield useful comparisons. To study the relationship between the NSDV and the size of the cylinders relative to the size of the Voronoi cells, a single cylinder, whose height and radius are equal, is placed inside of a unit box and the symmetric difference volume is assessed. Figure 6.3.4 shows a plot of the NVSD as a function of the ratio of the cylinder volume to the mean Voronoi cell volume for three different sized cylinders whose height and radius are, 0.10 (light grey x's), 0.25 (grey circles) and 0.50 (black triangles). The number of Voronoi points in the unit box ranges from 10 to 100,000 in steps of half-order of magnitude until 10,000, at which point the steps are in increments of 10,000. This gives a range of four orders of magnitude for the Voronoi

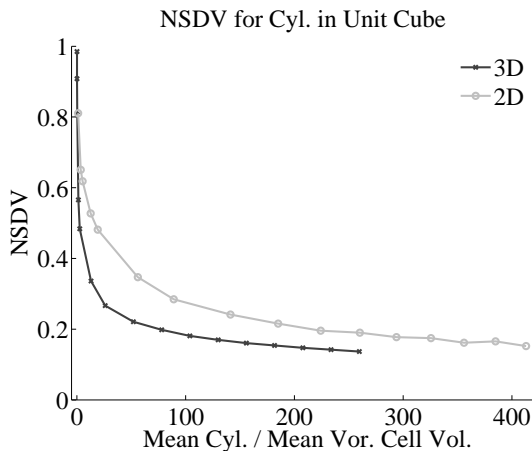
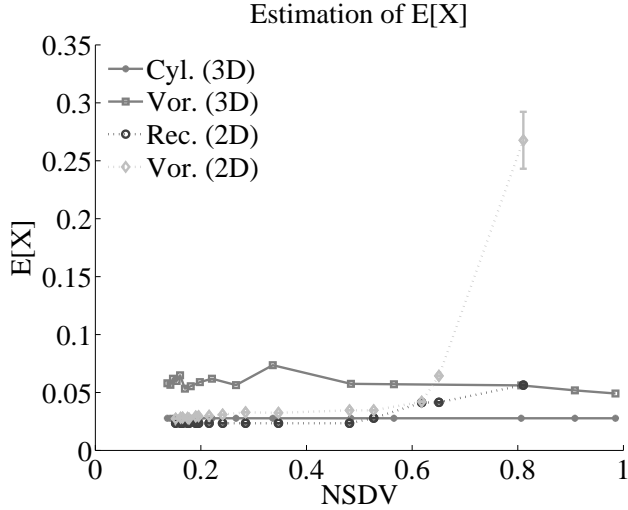


FIGURE 6.3.5: NSDV as a function of the ratio of the mean cylinder volume to Voronoi cell volume.

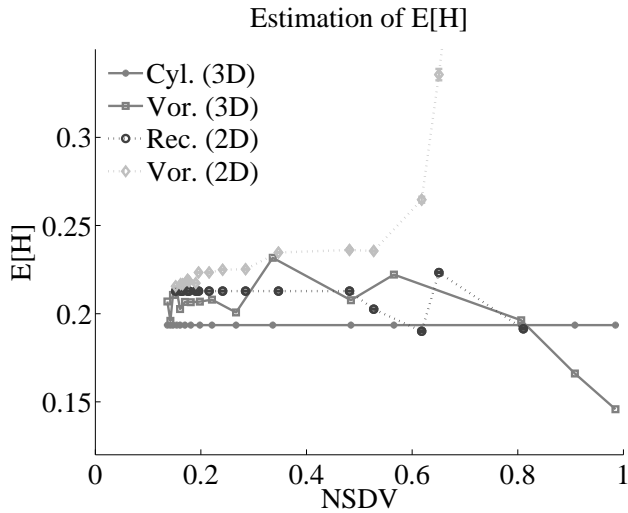
site density. As expected, the larger the cylinder is with respect to the mean Voronoi cell volume, the smaller the symmetric difference is, and so the NSDV is nearly zero. From Figure 6.3.4, a reasonable range of the cylinder volume to mean Voronoi cell volume is between 0 and 400. This provides nearly the full range of NSDVs. It also appears that a cylinder of size 0.25 and below will reasonably capture that range. This gives an appropriate distribution of cylinders and Voronoi cell densities for a full simulation.

Therefore, to test the sensitivity of the model to the NSDV, the box is now filled with 100 cylinders whose heights and radii are drawn independently and uniformly from the range $[0.10, 0.30]$ and $[0.05, 0.25]$, respectively. Figure 6.3.5 shows the results for the cylinders and for the observed rectangles on the cut plane. For the cut plane results, the mean rectangle area is compared to the density of Voronoi points in 2D, i.e. $N_{3D}^{2/3}$, where N_{3D} is the number of Voronoi points filling the box. There are two things to notice from this figure. The first is that the range of the NSDV for the rectangles is smaller than for the cylinders. The maximum NSDV is slightly higher than 0.8 for the rectangle, while it is nearly 1 for the cylinder. The second is that the ratio of the rectangle area to the mean Voronoi cell area is, in general, larger than that of the cylinder for similar NSDV. This implies that the object appears rougher in 2D than it might actually be in 3D.

To test the sensitivity of the model to the NSDV as a measure of how close to ideal the object of interest is, the expectations of the squared radius (show in Figure 6.3.6a), the height (show in Figure 6.3.6b), the surface area

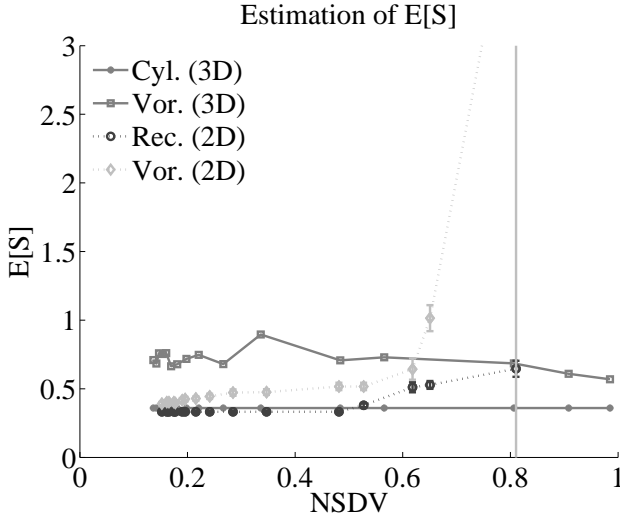


(A) Estimation of expected squared radius

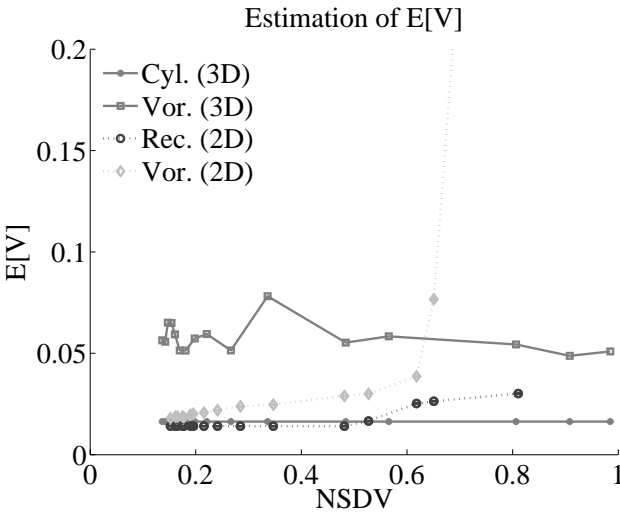


(B) Estimation of expected height

FIGURE 6.3.6: Estimation of the expectations of the quantities of interest. In all figures the grey line with dots represents the estimate from the 3D cylinder measurement. The grey line with squares represents the estimate from the bounding box around the 3D Voronoi structure. The dark grey circles represent the estimate from the 2D rectangle measurements and the light grey diamonds represent the estimate from the bounding box around the 2D Voronoi object. The error bars represent the constructed 95% confidence interval.



(A) Estimation of expected surface area



(B) Estimation of expected volume

FIGURE 6.3.7: Estimation of the expectations of the quantities of interest. In all figures the grey line with dots represents the estimate from the 3D cylinder measurement. The grey line with squares represents the estimate from the bounding box around the 3D Voronoi structure. The dark grey circles represent the estimate from the 2D rectangle measurements and the light grey diamonds represent the estimate from the bounding box around the 2D Voronoi object. The error bars represent the constructed 95% confidence interval.

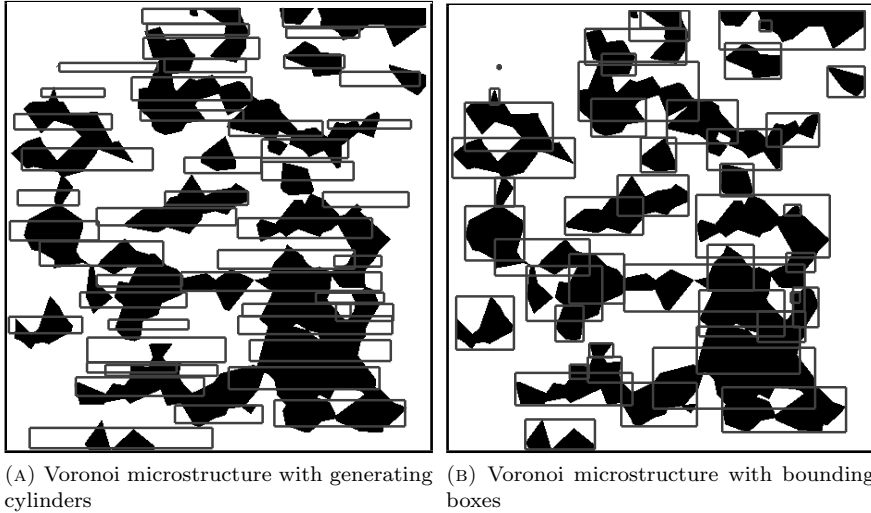


FIGURE 6.3.8: The cut plane for a simulated microstructure with 5000 Voronoi cells. The average NSDV for the box of Voronoi objects and cylinders is about 0.5. The model seems to be rather insensitive to deviations from ideal that are less than or roughly the same as this object.

(shown in Figure 6.3.7a) and the volume (shown in Figure 6.3.7b) are estimated for each of the 16 Voronoi cell densities and plotted, along with their constructed 95% confidence intervals. In all the plots the grey line with dots represents the estimation of the quantity from the 3D cylinder measurements. The grey line with squares represents the estimation from the bounding box of the 3D Voronoi object. The dark grey circles represent the estimation from the rectangles observed on the cut plane. The light grey diamonds represent the estimation from the bounding box of the portion of the observed Voronoi object on the cut plane.

From the results shown in Figures 6.3.6 and 6.3.7 it seems that the results are rather consistent for the rectangle and Voronoi object observed in 2D for NSDVs less than 0.5. This corresponds to the microstructure shown in Figure 6.3.8. The rectangles in Figure 6.3.8a represent the generating cylinders as if they were cut in the exact center, not as they are seen on the cut plane while Figure 6.3.8b shows the bounding boxes around the pixel connected objects. The Voronoi objects deviate from ideal, even with an NSDV of 0.5. The NSDV is an average over the individual NSDVs of all the objects in the box. Therefore, the model does not appear to be sensitive to the deviation since the results of the estimation are constant and the confidence intervals are small.

However, the inaccuracy of the results for the pixel connected bounding boxes comes from the problems discussed in Section 6.3.1 of objects merging and breaking up due to image processing and the limitations of binary images.

6.4 Conclusion

The results of this chapter show how sensitive the model is to deviations from ideal cylinders and parallel cut planes. In the first section, it has been shown that if the cylinders are plate-like and thin, i.e. their heights are relatively small, the model is insensitive to the cut plane deviating by small angles from exactly parallel to the cylinder axes of symmetry. Even large deviations in the cut plane angle only have a small effect, shifting the estimate to overestimate the heights. However, for thick plate-like cylinders, the model is quite sensitive to the cut plane angle. Even for angles as small as 5° , the results skew the estimate of the CDF of the height, giving it a completely different shape. Therefore, only when the objects can be considered thin plates is a cut plane deviation from parallel acceptable.

When the objects under consideration deviate from ideal cylinders, several issues arise and the model reacts differently to them. The model seems to be rather insensitive to the object deviating from ideal. Rather coarse Voronoi structures, for which the ideal cylinder shape given by the normalized symmetric difference volumes of 0.5 or less, seem to lead to reasonable estimates of the expected quantities of interest. Therefore, this model can be used on microstructures, where the objects observed tend to be non-ideal. However, as can be the case in real microstructures, the connectivity of the objects may not be well represented on the cut plane. This happens if an object is intersected in a place where it appears to be broken into smaller, unconnected objects, or if two objects are so close together that they cannot be distinguished in the image. If this is the dominating behavior for the observed objects, the model appears to be no longer reliable.

A

Appendix

A.1 CLT for Infinite Variance Random Variables

The theorem for infinite variance random variables, as given by Theorem 4 of Chapter 9 in Chow and Teicher [85] is stated here:

Theorem A.1.1. *If $\{Y_n, n \geq 1\}$ are i.i.d. random variables with non-degenerate distribution function K and Φ is the standard normal distribution function, then*

$$\lim_{n \rightarrow \infty} P \left(\frac{1}{B_n} \sum_{i=1}^n Y_i - A_n < y \right) = \Phi(y)$$

for some $B_n > 0$ and A_n iff

$$\lim_{c_n \rightarrow \infty} \frac{\int_{[|y| > c_n]} dK(y)}{c_n^{-2} \int_{[|y| < c_n]} y^2 dK(y)} = 0$$

where A_n and B_n may be taken to be

$$A_n = \frac{n}{B_n} \int_{[|y| < B_n]} y dK(y) \text{ and } B_n = \sup \left\{ c_n : \frac{1}{c_n^2} \int_{[|y| < c_n]} y^2 dK(y) \leq \frac{1}{n} \right\}.$$

A.2 Proof of some Lemmas and statements

A.2.1 Proof of Equation (3.4.4)

Proof. For $c = c_n$ and $M < c$,

$$\begin{aligned}
 \int_{y=0}^c y^2 dK(y) &= \int_{y=0}^c 2y [(1 - K(y)) - (1 - K(c))] dy \\
 &= \int_{y=0}^c 2y \left\{ \int_{z=0}^{\frac{1}{y^2}} \tau_q(z) dz - \int_{z=0}^{\frac{1}{c^2}} \tau_q(z) dz \right\} dy \\
 &= \int_{y=0}^c 2y \int_{z=\frac{1}{c^2}}^{\frac{1}{y^2}} \tau_q(z) dz dy \\
 &= \left\{ \int_{y=0}^M 2y + \int_{y=M}^c 2y \right\} \int_{z=\frac{1}{c^2}}^{\frac{1}{y^2}} \tau_q(z) dz dy \\
 &= I_1 + I_2.
 \end{aligned}$$

Looking at the individual integrals, first integral can be bounded as follows:

$$I_1 \leq \int_{y=0}^M 2y \int_{z=\frac{1}{c^2}}^{\infty} \tau_q(z) dz dy \leq \int_{y=0}^M 2y dy = M^2$$

Taking $M = [\ln(c)]^{1/4}$ gives $I_1 \leq \sqrt{\ln(c)}$.

Now, turn to the second integral.

$$\begin{aligned}
 I_2 &= \int_{y=M}^c 2y \int_{z=\frac{1}{c^2}}^{\frac{1}{y^2}} \tau_q(z) dz dy \\
 \text{let } p &= \frac{1}{y^2}, \text{ then } y = \frac{1}{\sqrt{p}} \text{ and } dy = -\frac{1}{2} p^{-3/2} dp \\
 &= \int_{p=\frac{1}{M^2}}^{\frac{1}{c^2}} p^{-2} \int_{z=\frac{1}{c^2}}^p \tau_q(z) dz dp = \int_{z=\frac{1}{c^2}}^{\frac{1}{M^2}} \tau_q(z) \int_{p=z}^{\frac{1}{M^2}} p^{-2} dp dz \\
 &= \int_{z=\frac{1}{c^2}}^{\frac{1}{M^2}} \tau_q(z) \left(\frac{1}{z} - M^2 \right) dz = \int_{z=\frac{1}{c^2}}^{\frac{1}{M^2}} \left(\frac{1}{z} - M^2 \right) \tau_q(z) dz.
 \end{aligned}$$

Applying the mean value theorem and using Assumption 3.4.4 yields

$$\begin{aligned}
 I_2 &= \int_{z=\frac{1}{c^2}}^{\frac{1}{M^2}} \left(\frac{1}{z} - M^2 \right) (\tau_q(0) + z\tau'_q(\xi)) dz \\
 &\leq \int_{z=\frac{1}{c^2}}^{\frac{1}{M^2}} \left(\frac{1}{z} - M^2 \right) \tau_q(0) dz + \int_{z=\frac{1}{c^2}}^{\frac{1}{M^2}} (1 - zM^2) K dz \\
 &= \left[\ln(c^2) - \ln(M^2) - 1 + \frac{M^2}{c^2} \right] \tau_q(0) + \left(\frac{1}{2M^2} - \frac{1}{c^2} + \frac{M^2}{2c^4} \right) K.
 \end{aligned}$$

Since $M = [\ln(c)]^{1/4}$,

$$\ln(M^2) = \ln\left(\sqrt{\ln(c)}\right) \ll \ln(c^2) \quad 1 \ll \ln(c^2) \quad \text{as } c \rightarrow \infty$$

$$\frac{M^2}{c^2} = \frac{\sqrt{\ln(c)}}{c^2} \rightarrow 0 \quad \text{as } c \rightarrow \infty \quad \frac{1}{2M^2} = \frac{1}{2\sqrt{\ln(c)}} \rightarrow 0 \quad \text{as } c \rightarrow \infty$$

$$\frac{1}{c^2} \rightarrow 0 \quad \text{as } c \rightarrow \infty \quad \frac{M^2}{2c^4} = \frac{\sqrt{\ln(c)}}{2c^4} \rightarrow 0 \quad \text{as } c \rightarrow \infty$$

and, therefore, $I_2 = \ln(c^2) \tau_q(0) + O(\ln(\ln(c))) + o\left(\frac{1}{\ln(c)}\right)$. This leads to

$$\int_{y=0}^c y^2 dK(y) = I_1 + I_2 = \ln(c^2) \tau_q(0) + O(\ln(\ln(c))).$$

□

A.2.2 Proof of Lemma 3.4.1

Proof. Starting with the Cramér-Wold device, for $s, t \in \mathbb{R}$ the (univariate) random variables $U_i^{(s,t)} = sZ_i^{-\frac{1}{2}} + tH_iZ_i^{-\frac{1}{2}}$. Considering this formulation in light of Theorem 3.4.1 and requiring $s, t > 0$ and $c \rightarrow \infty$, one obtains the following.

$$P\left(U^{(s,t)} > c\right) = P\left(Z < \left(\frac{s+tH}{c}\right)^2\right) = \int_{h=0}^{\infty} \int_{z=0}^{\left(\frac{s+th}{c}\right)^2} g(z, h) dz dh$$

The integral over h is broken into two parts and Assumption 3.4.2 is assumed to hold. The first part ranges over $[0, M_c)$ and the second over $[M_c, \infty)$. If

$M_c = c^{\frac{2}{5}} / \ln(c)$ is chosen, an upper bound for the second integral is:

$$\begin{aligned} P(H > M_c) &= P\left(H > \frac{c^{\frac{2}{5}}}{\ln(c)}\right) \leq \frac{E[H^{5+\epsilon}]}{\left(c^{\frac{2}{5}} / \ln(c)\right)^{5+\epsilon}} \leq \kappa c^{-2-\frac{\epsilon}{5}} (\ln(c))^{5+\epsilon} \\ &= o(c^{-2}). \end{aligned}$$

Turning now to the first integral and applying Taylor's theorem leads to

$$\int_{h=0}^{M_c} \int_{z=0}^{\left(\frac{s+th}{c}\right)^2} g(z, h) dz dh = \int_{h=0}^{M_c} \int_{z=0}^{\left(\frac{s+th}{c}\right)^2} \left(g(0, h) + z \frac{\partial}{\partial z} g(\xi_{z,h}, h)\right) dz dh$$

where $\xi_{z,h} \in (0, z)$. Therefore,

$$\int_{h=0}^{M_c} \int_{z=0}^{\left(\frac{s+th}{c}\right)^2} (g(z, h) - g(0, h)) dz dh = \int_{h=0}^{M_c} \int_{z=0}^{\left(\frac{s+th}{c}\right)^2} z \frac{\partial}{\partial z} g(\xi_{z,h}, h) dz dh$$

implying

$$\begin{aligned} \left| \int_{h=0}^{M_c} \left(\int_{z=0}^{\left(\frac{s+th}{c}\right)^2} g(z, h) dz - \left(\frac{s+th}{c}\right)^2 g(0, h) \right) dh \right| &= \\ &= \left| \int_{h=0}^{M_c} \int_{z=0}^{\left(\frac{s+th}{c}\right)^2} z \frac{\partial}{\partial z} g(\xi_{z,h}, h) dz dh \right|. \end{aligned}$$

The right hand side can be bounded under Assumption 3.4.6 by

$$\begin{aligned} \left| \int_{h=0}^{M_c} \int_{z=0}^{\left(\frac{s+th}{c}\right)^2} z \frac{\partial}{\partial z} g(\xi_{z,h}, h) dz dh \right| &\leq \int_{h=0}^{M_c} \int_{z=0}^{\left(\frac{s+th}{c}\right)^2} \left| \frac{\partial}{\partial z} g(\xi_{z,h}, h) \right| z dz dh \leq \\ &\leq \int_{h=0}^{M_c} \int_{z=0}^{\left(\frac{s+th}{c}\right)^2} Kz dz dh = \int_{h=0}^{M_c} K \frac{1}{2} \left(\frac{s+th}{c}\right)^4 dh = \frac{K}{2c^4} \int_{h=0}^{M_c} (s+th)^4 dh \\ &= \frac{K}{8tc^4} [(s+tM_c)^5 - s^5] \leq \frac{K}{8tc^4} \frac{t^5 c^2}{(\ln(c))^{\frac{2}{5}}} = o(c^{-2}) \end{aligned}$$

Putting everything back together, gives

$$\begin{aligned} \int_{h=0}^{\infty} \int_{z=0}^{\left(\frac{s+th}{c}\right)^2} g(z, h) dz dh &= \left\{ \int_{h=0}^{M_c} + \int_{h=M_c}^{\infty} \right\} \int_{z=0}^{\left(\frac{s+th}{c}\right)^2} g(z, h) dz dh \\ &= \int_{h=0}^{M_c} \left(\frac{s+th}{c}\right)^2 g(0, h) dh + o(c^{-2}) \end{aligned}$$

Now note that

$$E_g \left[U^{(s,t)} \right] = \int_{h=0}^{\infty} \int_{z=0}^{\infty} \frac{s+th}{\sqrt{z}} g(z, h) dz dh < \infty.$$

Finally, looking to the second moment in light of Assumption 3.4.5 results in

$$\begin{aligned} E_g \left[\left(U^{(s,t)} \right)^2 1_{U^{(s,t)} \in [0,c]} \right] &= \int_{h=0}^{\infty} \int_{z=(\frac{s+th}{c})^2}^{\infty} \frac{(s+th)^2}{z} g(z, h) dz dh \\ &\sim \ln(c^2) \int_{h=0}^{\infty} (s+th)^2 g(0, h) dh. \end{aligned}$$

Therefore, if $\bar{U}_n^{(s,t)}$ is the empirical mean, then $\sqrt{\ln(n)/n} \left(\bar{U}_n^{(s,t)} - E_g \left[U_i^{(s,t)} \right] \right) \rightsquigarrow \mathcal{N}(0, \kappa)$ where $\kappa = \int_{h=0}^{\infty} (s^2 + 2sth + t^2h^2) g(0, h) dh = s^2\xi_g^j + 2st\xi_g^j + t^2\xi_g^j$.

Finally, since $\sqrt{\frac{\ln(n)}{n}} \left(\sum_{i=1}^n \left[sZ_i^{-\frac{1}{2}} + tH_i Z_i^{-\frac{1}{2}} \right] - E \left[U^{(s,t)} \right] \right) \rightsquigarrow N(0, \kappa)$, the Cramér-Wold device (see van der Vaart [92], Section 2.3) implies eq. (3.4.8). \square

A.2.3 Proof of Relation (3.4.22)

Proof. Analogous to the proof of Lemma 3.4.1, use the Cramér-Wold device for the quantities $U_i^{(s,t)} = sZ_i^{-\frac{1}{2}} + tZ_i^{-\frac{1}{2}} 1_{[0,h]}(H_i)$. For $s, t, c > 0$

$$U_i^{(s,t)} > c \iff \left[Z_i < \left(\frac{s}{c} \right)^2 \text{ and } H_i \geq h \right] \text{ or } \left[Z_i < \left(\frac{s+t}{c} \right)^2 \text{ and } H_i < h \right]$$

Using that $P(U_i^{(s,t)} > c) \sim \kappa/c^2$ and $E \left[\left(U_i^{(s,t)} \right)^2 1_{U_i^{(s,t)} \in [0,c]} \right] \left(U_i^{(s,t)} \right) \sim \kappa \ln(c^2)$ for $c \rightarrow \infty$ with $\kappa = s^2g_Z(0) + (t^2 + 2st) \int_{y=0}^h g(0, y) dy$, Theorem 3.4.1 and Assumption 3.4.5 lead to eq. (3.4.22). For $E[T_n]$, note that from eq. (3.2.8)

$$\begin{aligned} E \left[Z_i^{-\frac{1}{2}} \right] &= \pi / (2m_F^+) \text{ and (requiring that Assumption 3.4.1 holds)} \\ E \left[Z_i^{-\frac{1}{2}} 1_{[0,h]}(H_i) \right] &= \int_{z=0}^{\infty} \int_{v=0}^h z^{-\frac{1}{2}} g(z, v) dv dz. \end{aligned}$$

\square

A.2.4 Relationships for the quantities of interest

Define the quantity of interest, squared radius, aspect ratio, surface area or volume, as t . Let (u, h) be the observed pair of variables. For a fixed $h > 0$,

define $t = p(h; u)$ for each quantity of interest. In eq. (3.2.4) the inverse of $p(h; u)$ is defined as $u = q(h; t)$. These can be calculated as follows:

$$p(h; u) = \begin{cases} \frac{u}{\sqrt{u}} & \text{(sqrd. rad.)} \\ \frac{h}{2\pi(u + h\sqrt{u})} & \text{(asp. ratio)} \\ \frac{h}{\pi hu} & \text{(surf. area)} \end{cases} \rightsquigarrow q(h; t) = \begin{cases} t & \text{(sqrd. rad.)} \\ (ht)^2 & \text{(asp. ratio)} \\ \left[\sqrt{\frac{h^2}{4} + \frac{t}{2\pi}} - \frac{h}{2} \right]^2 & \text{(surf. area)} \\ \frac{t}{\pi h} & \text{(volume).} \end{cases} \quad (\text{A.2.1})$$

It is important to note for all choices of $p(h; u)$ and $q(h; t)$ that $p(h; q(h; t)) = t$ and that $q(h; p(h; u)) = u$.

The derivative of these functions with respect to the second argument is also important. Denoting this partial derivative of p with respect to u by \dot{p} results in

$$\dot{p}(h; u) = \begin{cases} 1 & \text{(squared radius)} \\ \frac{1}{2h\sqrt{u}} & \text{(aspect ratio)} \\ 2\pi \left(1 + \frac{h}{2\sqrt{u}} \right) & \text{(surface area)} \\ \frac{1}{\pi h} & \text{(volume).} \end{cases} \quad (\text{A.2.2})$$

Denoting the partial derivative of q with respect to t by \dot{q} yields

$$\dot{q}(h; t) = \begin{cases} 1 & \text{(squared radius)} \\ \frac{1}{2h^2 t} & \text{(aspect ratio)} \\ \frac{1}{2\pi} \left(1 - \frac{h}{2\sqrt{\frac{h^2}{4} + \frac{t}{2\pi}}} \right) & \text{(surface area)} \\ \frac{1}{\pi h} & \text{(volume).} \end{cases} \quad (\text{A.2.3})$$

Denoting the second partial derivative of q with respect to t by \ddot{q} leads to

$$\ddot{q}(h; t) = \begin{cases} 0 & \text{(squared radius)} \\ \frac{1}{2h^2} & \text{(aspect ratio)} \\ \frac{h}{16\pi^2} \left(\frac{h^2}{4} + \frac{t}{2\pi} \right)^{-\frac{3}{2}} & \text{(surface area)} \\ 0 & \text{(volume).} \end{cases} \quad (\text{A.2.4})$$

It is also important to consider the relationship between \dot{p} and \dot{q} . Using the

linear approximation of q near t yields

$$\begin{aligned} \dot{p}(h; q(h; t)) &= \lim_{\epsilon \downarrow 0} \frac{p\left(h; q\left(h; t + \frac{\epsilon}{\dot{q}(h; t)}\right)\right) - p(h; q(h; t))}{\epsilon} = \lim_{\epsilon \downarrow 0} \frac{t + \frac{\epsilon}{\dot{q}(h; t)} - t}{\epsilon} \\ &= \frac{1}{\dot{q}(h; t)} \end{aligned} \tag{A.2.5}$$

Finally, note that $y > q(h; t)$ if and only if $t < p(h; y)$. Recall the expression for W_n can be written in terms of the function $\phi_{n,v}$. One can use the substitution $u = q(h; y)$ in the definition of $\phi_{n,v}$ and obtain, for z and h fixed

$$\phi_{n,v}(z, h) = \int_{y=t}^{(t+\delta_n v) \wedge p(h; z)} [z - q(h; y)]^{-\frac{1}{2}} dy = \int_{u=q(h; t)}^{q(h; t + \delta_n v) \wedge z} (z - u)^{-\frac{1}{2}} \dot{p}(h; u) du. \tag{A.2.6}$$

A.3 Estimation of the heights distribution

The estimation of the height distribution from the observed rectangles on the cut plane presents a unique dilemma. If the heights are known to be independent of the cylinder radius, then the biasing in the problem has no consequences for the distribution of observable heights and one may simply take the empirical distribution of the observed heights to be the estimate of the actual distribution

$$\widehat{F}_H(h) = \frac{1}{n} \sum_{i=1}^n 1_{[H_i \leq h]}. \tag{A.3.1}$$

This estimator is better than the one given in eq. (3.3.1) because it has a rate of convergence of $1/\sqrt{n}$ compared to the $\sqrt{\ln(n)}/n$. Figure A.3.1 shows the effect of the rate of convergence for the estimation procedure. Figure A.3.1a shows the 2D (light-grey line) and 3D (dark-grey line) empirical distributions for the heights of 500 uncorrelated (radii and cylinder heights), uniformly distributed cylinders. Figure A.3.1c shows the same for 5000 cylinders. The black solid line shows the estimation of the 3D distribution as calculated from eq. (3.3.1). The empirical distribution is a better choice than eq. (3.3.1) in this case because it has the faster rate of convergence. Contrarily, in Figures A.3.1b and A.3.1d where there is a correlation between the radii and heights of the cylinders, the biasing in the 2D distribution (light-grey lines compared to the dark-grey line for the 3D empirical distribution) is clear. In this case, the estimator from eq. (3.3.1) is necessary to accurately estimate the underlying 3D distribution.



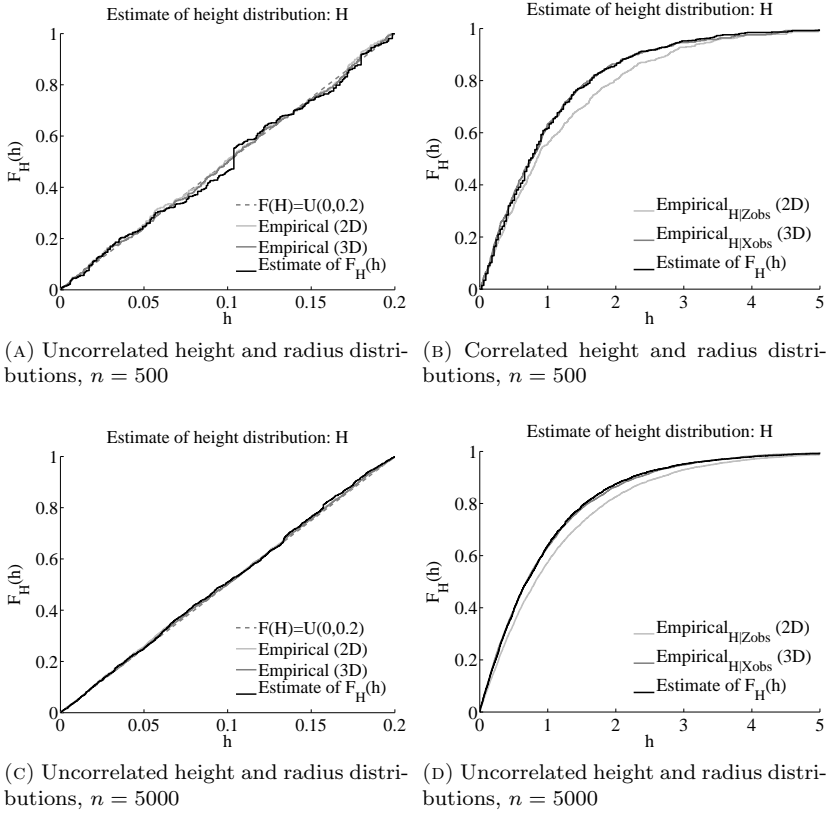


FIGURE A.3.1: Estimates of $F_H(h)$ for Correlated and uncorrelated height and radius distributions. The dark-grey lines show the 3D empirical distributions of the cylinder heights. The light-grey lines show the 2D empirical distributions. The black lines show the estimates of the 3D distributions as calculated from eq. (3.3.1). Note that for the uncorrelated data, the empirical estimator is sufficient and has a rate of convergence of $1/\sqrt{n}$. However, for the correlated data the estimator eq. (3.3.1) is necessary and has a rate of convergence of $\sqrt{\ln(n)/n}$.

B

Appendix

B.1 Calculation of CDFs, Moments and Isotonic Estimators

B.1.1 General Calculations

The cumulative distribution functions for the aspect ratio R , surface area S and volume V of the cylinders:

$$\begin{aligned} F_R(r) &= P(R \leq r) = P\left(\frac{\sqrt{X}}{H} \leq r\right) = P(X \leq (hr)^2) \\ &= \int_{h=0}^{\infty} \int_{x=0}^{(Hr)^2} f(x, h) dx dh \end{aligned}$$

$$\begin{aligned} F_S(s) &= P(S \leq s) = P\left(2\pi(X + \sqrt{X}H) \leq s\right) = P\left(X \leq \left(\sqrt{\frac{H^2}{4} + \frac{2}{2\pi}} - \frac{H}{2}\right)^2\right) \\ &= P(X \leq q(H; s)) = \int_{h=0}^{\infty} \int_{x=0}^{q(h; s)} f(x, h) dx dh \end{aligned}$$

$$\begin{aligned} F_V(v) &= P(V \leq v) = P(\pi XH \leq v) = P\left(H \leq \frac{v}{\pi X}\right) \\ &= \int_{x=0}^{\infty} \int_{h=0}^{x \wedge (v/\pi x)} f(x, h) dx dh \end{aligned}$$

The relationship between the moments from the 2D observations and the

2D to 3D Moment Relations					
3D	$E_f[\sqrt{X}]$	$E_f[X]$	$E_f[H]$	$E_f[\sqrt{XH}]$	$E_f[XH]$
2D	$\frac{\pi}{2m_G^-}$	$2\frac{E_g[Z^{\frac{1}{2}}]}{m_G^-}$	$\frac{E_g[Z^{-\frac{1}{2}}H]}{m_G^-}$	$\frac{\pi E_g[H]}{2m_G^-}$	$2\frac{E_g[Z^{\frac{1}{2}}H]}{m_G^-}$

TABLE B.1: Relationships between the 3D moments and the 2D moments. Recall $m_G^- = E_g[Z^{-\frac{1}{2}}]$ and $E_f[X^{\frac{1}{2}}] = m_F^+$

3D observations is explicitly calculated for $\alpha, \beta > -1$.

$$\begin{aligned}
 E_g[Z^\alpha H^\beta] &= \int_{h=0}^{\infty} \int_{z=0}^{\infty} z^\alpha h^\beta g(z, h) dz dh \\
 &= \frac{1}{2m_F^+} \int_{x=0}^{\infty} \int_{h=0}^{\infty} h^\beta f(x, h) \int_{z=x}^{\infty} z^\alpha (x-z)^{-\frac{1}{2}} dz dh dx \\
 &= \frac{1}{2m_F^+} \int_{x=0}^{\infty} \int_{h=0}^{\infty} h^\beta f(x, h) \int_{z=x}^{\infty} \left[x^{\alpha+\frac{1}{2}} B\left(\alpha+1, \frac{1}{2}\right) \right] dz dh dx \\
 &= \frac{B\left(\alpha+1, \frac{1}{2}\right)}{2m_F^+} \int_{x=0}^{\infty} \int_{h=0}^{\infty} x^{\alpha+\frac{1}{2}} h^\beta f(x, h) dh dx \\
 &= \frac{B\left(\alpha+1, \frac{1}{2}\right)}{2m_F^+} E_f[X^{\alpha+\frac{1}{2}} H^\beta] \\
 E_g[Z^\alpha H^\beta] &= \frac{\sqrt{\pi} \Gamma(\alpha+1)}{2m_F^+ \Gamma\left(\alpha+\frac{3}{2}\right)} E_f[X^{\alpha+\frac{1}{2}} H^\beta] \\
 &\text{alternatively} \\
 E_f[X^\alpha H^\beta] &= \frac{\sqrt{\pi} \Gamma(\alpha+1)}{m_G^- \Gamma\left(\alpha+\frac{1}{2}\right)} E_g[Z^{\alpha-\frac{1}{2}} H^\beta]
 \end{aligned}$$

The quantities ξ_g^j are calculated from the 2D bivariate density and the 3D

moments as follows:

$$\begin{aligned} \xi_g^j &= \int_{h=0}^{\infty} h^j g(0, h) dh = \int_{h=0}^{\infty} h^j \frac{1}{2m_F^+} \int_{x=0}^{\infty} (x-0)^{-\frac{1}{2}} f(x, h) dx dh \\ &= \frac{1}{2m_F^+} \int_{x=0}^{\infty} \int_{h=0}^{\infty} x^{-\frac{1}{2}} h^j dx dh = \frac{1}{2m_F^+} E_f \left[X^{-\frac{1}{2}} H^j \right] \end{aligned}$$

For calculating the optimal bandwidth for the estimator of the ξ_g^j 's, the function c_g^j can be calculated as follows:

$$\begin{aligned} c_g^j &= \frac{1}{2} \int_{h=0}^{\infty} h^j \left. \frac{\partial}{\partial z} g(z, h) \right|_{z=0} dh \\ &= \frac{1}{2} \int_{h=0}^{\infty} h^j \left. \frac{\partial}{\partial z} \frac{1}{2m_F^+} \int_{x=z}^{\infty} (x-z)^{-\frac{1}{2}} f(x, h) dx \right|_{z=0} dh \\ &= \frac{1}{4m_F^+} \int_{h=0}^{\infty} h^j \left. \frac{\partial}{\partial z} \int_{x=z}^{\infty} (x-z)^{-\frac{1}{2}} f(x, h) dx \right|_{z=0} dh \end{aligned}$$

For the empirical and isotonic estimators for the CDFs of the quantities of interest (using volume as the example) begin by defining the equation to estimate, recalling that $F_V(v) = 1 - N(v)/N(0)$,

$$N(v) = \int_{h=0}^{\infty} \int_{z=\frac{v}{\pi h}}^{\infty} \frac{g(z, h)}{\sqrt{z - \frac{v}{\pi h}}} dz dh$$

using the empirical estimator (for all quantities of interest)

$$\begin{aligned} N_n(v) &= \sum_{i=1}^n \left(Z_i - \frac{v}{\pi H_i} \right)^{-\frac{1}{2}} 1_{\{Z_i > \frac{v}{\pi H_i}\}} \\ N_n(r) &= \sum_{i=1}^n (Z_i - H_i^2 r^2)^{-\frac{1}{2}} 1_{\{Z_i > (H_i r)^2\}} \\ N_n(s) &= \sum_{i=1}^n \left(Z_i - \left[\sqrt{\frac{H_i^2}{4} + \frac{s}{2\pi}} - \frac{H_i}{2} \right]^2 \right)^{-\frac{1}{2}} 1_{\left\{ Z_i > \left[\sqrt{\frac{H_i^2}{4} + \frac{s}{2\pi}} - \frac{H_i}{2} \right]^2 \right\}} \end{aligned}$$

From here, define the function

$$\begin{aligned}
 U(v) &= \int_{y=0}^v N(y) dy \\
 &= \int_{y=0}^v \int_{h=0}^{\infty} \int_{z=\frac{y}{\pi h}}^{\infty} \frac{g(z, h)}{\sqrt{z - \frac{y}{\pi h}}} dz dh dy \\
 &= \int_{h=0}^{\infty} \int_{z=0}^{\infty} \int_{y=0}^{\pi h z \wedge v} g(z, h) \sqrt{\pi h} (\pi h z - y)^{-\frac{1}{2}} dy dz dh \\
 &= 2\sqrt{\pi} \int_{h=0}^{\infty} \sqrt{h} \int_{z=0}^{\infty} g(z, h) \sqrt{\pi h z - y} \Big|_{\pi h z \wedge v}^0 dz dh \\
 &= 2\sqrt{\pi} \int_{h=0}^{\infty} \sqrt{h} \left\{ \int_{z=0}^{\infty} g(z, h) \sqrt{\pi h z} dz - \int_{z=\frac{v}{\pi h}}^{\infty} g(z, h) \sqrt{\pi h z - v} dz \right\} dh \\
 &= 2\pi \int_{h=0}^{\infty} h \left\{ \int_{z=0}^{\infty} \sqrt{z} g(z, h) dz - \int_{z=\frac{v}{\pi h}}^{\infty} \sqrt{z - \frac{v}{\pi h}} g(z, h) dz \right\} dh
 \end{aligned}$$

and its empirical estimator

$$U_n(v) = \int_{y=0}^v N_n(y) dy = \frac{2\pi}{n} \sum_{i=1}^n H_i \left\{ \sqrt{Z_i} - \sqrt{Z_i - \frac{v}{\pi H_i}} 1_{\{Z_i > \frac{v}{\pi H_i}\}} \right\}.$$

For the aspect ratio and the surface area, these empirical functions are

$$\begin{aligned}
 U_n(r) &= \frac{1}{n} \sum_{i=1}^n \left[\frac{\pi}{2H_i} 1_{\{0 < Z_i < (rH_i)^2\}} + \frac{1}{H_i} \sin^{-1} \left(\frac{H_i r}{Z_i} \right) 1_{\{Z_i > (rH_i)^2\}} \right] \\
 U_n(s) &= \frac{4\pi}{n} \sum_{i=1}^n \left\{ \left(\sqrt{Z_i} + \frac{\pi H_i}{8} \right) + \frac{\pi H_i}{8} 1_{\{0 < Z_i < q(H_i; s)\}} \right. \\
 &\quad \left. - \left[\sqrt{Z_i - q(H_i; s)} + \frac{H_i}{4} \sin^{-1} \left(1 - \frac{2q(H_i; s)}{Z_i} \right) \right] 1_{\{Z_i > q(H_i; s)\}} \right\} \\
 \text{where } q(H_i, s) &= \left[\sqrt{\frac{H_i^2}{4} + \frac{s}{2\pi}} - \frac{H_i}{2} \right]^2.
 \end{aligned}$$

B.1.2 Numerical Simulation

For the numerical simulation the squared radius was chosen to have a gamma(3) distribution and the height, given $X = x$, to have a triangle distribution on

$[0, x]$ which leads to

$$f_X(x) = \frac{1}{2}x^2 e^{-x} \quad x \geq 0$$

$$f_{H|X}(h|x) = \frac{2}{x^2}(x-h) \quad h \in (0, x)$$

with a joint distribution function

$$f(x, h) = (x-h)e^{-x} \quad 0 < h < x < \infty.$$

From here, calculating the cumulative distribution functions (CDFs) for the various quantities of interest is straightforward. The CDFs for the marginal distributions of the squared radius and height are

$$F_X(x) = \int_{y=0}^x f_X(y) dy = 1 - \frac{1}{2} e^{-x} (x^2 + 2x + 2) \quad 0 < x < \infty$$

$$F_{H|X}(v|x) = \int_{v=0}^h f_{H|X}(v|x) dv = \frac{2}{x^2} \left(xh - \frac{1}{2}h^2 \right) \quad 0 < h < x.$$

In the following, the CDF for the volume is calculated from the bivariate density $f(x, h)$. The same can be done for the aspect ratio and surface area.

$$F_V(v) = \int_{x=0}^{\infty} \int_{h=0}^{x \wedge \frac{v}{\pi x}} f(x, h) dx dh = \int_{x=0}^{\infty} \int_{h=0}^{x \wedge \frac{v}{\pi x}} (x-h)e^{-x} dx dh$$

$$= \int_{x=0}^{\infty} e^{-x} \left(xh - \frac{1}{2}h^2 \right) \Big|_{h=0}^{x \wedge \frac{v}{\pi x}}$$

$$= \int_{x=0}^{\infty} e^{-x} \left(\left(x^2 \wedge \frac{v}{\pi} \right) - \frac{1}{2} \left(x^2 \wedge \frac{v^2}{\pi^2 x^2} \right) \right)$$

$$= \int_{x=0}^{\infty} e^{-x} \left(\frac{1}{2}x^2 \wedge \left(\frac{v}{\pi} - \frac{v^2}{2\pi^2 x^2} \right) \right)$$

$$= \int_{x=0}^{\sqrt{\frac{v}{\pi}}} \frac{1}{2} e^{-x} x^2 dx + \int_{x=\sqrt{\frac{v}{\pi}}}^{\infty} e^{-x} \left(\frac{v}{\pi} - \frac{v^2}{2\pi^2 x^2} \right) dx$$

$$= -\frac{1}{2} e^{-x} (x^2 + 2x + 2) \Big|_{x=0}^{\sqrt{\frac{v}{\pi}}}$$

$$- \left\{ \frac{v}{\pi} e^{-x} - \frac{v^2}{2\pi^2} \left[\frac{e^{-x}}{x} - E_i \left(\sqrt{\frac{v}{\pi}} \right) \right] \right\} \Big|_{\sqrt{\frac{v}{\pi}}}^{\infty}$$

$$\begin{aligned}
 F_V(v) &= \frac{1}{2} \left[2 - e^{-\sqrt{\frac{v}{\pi}}} \left(\frac{v}{\pi} + 2\sqrt{\frac{v}{\pi}} + 2 \right) \right] \\
 &\quad + \left(\frac{v}{\pi} - \frac{v^2}{2\pi^2} \sqrt{\frac{\pi}{v}} \right) e^{-\sqrt{\frac{v}{\pi}}} + \frac{v^2}{2\pi^2} E_i \left(\sqrt{\frac{v}{\pi}} \right) \\
 &= 1 - e^{-\sqrt{\frac{v}{\pi}}} \left(1 + \frac{v}{\pi} - \frac{v}{2\pi} + \frac{1}{2} \left(\frac{v}{\pi} \right)^{\frac{3}{2}} \right) + \frac{v^2}{2\pi^2} E_i \left(\sqrt{\frac{v}{\pi}} \right)
 \end{aligned}$$

where $E_i(x) = \int_{u=x}^{\infty} e^{-u} u^{-1} du$ is the exponential integral.

The same procedure can be followed for the aspect ratio and the surface area yielding:

$$\begin{aligned}
 F_R(r) &= e^{-\frac{1}{r^2}} - \frac{3\sqrt{\pi}}{4r} \operatorname{erfc} \left(\frac{1}{r} \right) \\
 F_S(s) &= 1 + \frac{s^2}{8\pi^2} \left[E_i \left(\frac{s}{2\pi} \right) - E_i(q) \right] \\
 &\quad + e^{-q} \left[\left(\frac{s}{2\pi} - \frac{3}{2} \right) (1 + \sqrt{q}) - \frac{3q}{2} - q^{\frac{3}{2}} - \frac{q^2}{2} \right] \\
 &\quad + e^{-\frac{s}{2\pi}} \left(\frac{1}{2} + \frac{3}{2} \left(\frac{s}{2\pi} \right)^{\frac{1}{2}} - \frac{s}{4\pi} \right) \\
 &\quad + \frac{\sqrt{\pi}}{2} \left(\frac{s}{2\pi} - \frac{3}{2} \right) \left[\operatorname{erfc}(\sqrt{q}) - \operatorname{erfc} \left(\sqrt{\frac{s}{2\pi}} \right) \right]
 \end{aligned}$$

where $\operatorname{erfc}(x) = \frac{2}{\sqrt{\pi}} \int_{u=x}^{\infty} e^{-u^2} du$ is the complementary error function, and q is the real root of the solution to the equation $x(\sqrt{x} + 1) = \frac{s}{2\pi}$:

$$\begin{aligned}
 \sqrt{q} &= \frac{\left(-8 + \frac{54s}{\pi} + 12\sqrt{81 \left(\frac{s}{2\pi} \right)^2 - \frac{6s}{\pi}} \right)^{\frac{1}{3}}}{6} \\
 &\quad + \frac{2}{3 \left(-8 + \frac{54s}{\pi} + 12\sqrt{81 \left(\frac{s}{2\pi} \right)^2 - \frac{6s}{\pi}} \right)^{\frac{1}{3}}} - \frac{1}{3}
 \end{aligned}$$

The 3D bivariate density function can be transformed via eq. (3.2.1) in the

following way.

$$\begin{aligned} g(z, h) &= \frac{1}{2m_F^+} \int_{x=z}^{\infty} (x-z)^{-\frac{1}{2}} f(x, h) dx = \frac{8}{15\sqrt{\pi}} \int_{x=z\vee h}^{\infty} (x-z)^{-\frac{1}{2}} e^{-x} (x-h) dx \\ &= \frac{8}{15\sqrt{\pi}} \left[\int_{x=z\vee h}^{\infty} e^{-x} x (x-z)^{-\frac{1}{2}} dx - \int_{x=z\vee h}^{\infty} e^{-x} h (x-z)^{-\frac{1}{2}} dx \right] \\ &= \frac{8}{15\sqrt{\pi}} [I_1 - h I_2] \end{aligned}$$

$$\begin{aligned} I_1 &= \int_{x=z\vee h}^{\infty} e^{-x} (x-z+z) (x-z)^{-\frac{1}{2}} dx \\ &= \int_{x=z\vee h}^{\infty} e^{-x} (x-z) (x-z)^{-\frac{1}{2}} dx + \int_{x=z\vee h}^{\infty} e^{-x} z (x-z)^{-\frac{1}{2}} dx \\ &= \int_{x=z\vee h}^{\infty} e^{-z} e^{-(x-z)} (x-z)^{\frac{1}{2}} dx + \int_{x=z\vee h}^{\infty} e^{-z} e^{-(x-z)} z (x-z)^{-\frac{1}{2}} dx \\ &= e^{-z} \int_{t=0\vee(h-z)}^{\infty} e^{-t} t^{\frac{1}{2}} dt + z e^{-z} \int_{t=0\vee(h-z)}^{\infty} e^{-t} t^{-\frac{1}{2}} dx \\ &= e^{-z} \Gamma\left(\frac{3}{2}, 0 \vee (h-z)\right) + z e^{-z} \Gamma\left(\frac{1}{2}, 0 \vee (h-z)\right) \end{aligned}$$

$$\begin{aligned} I_2 &= \int_{x=z\vee h}^{\infty} e^{-x} (x-z)^{-\frac{1}{2}} dx = e^{-z} \int_{t=0\vee(h-z)}^{\infty} e^{-t} t^{-\frac{1}{2}} dx \\ &= e^{-z} \Gamma\left(\frac{1}{2}, 0 \vee (h-z)\right) \end{aligned}$$

$$\begin{aligned} g(z, h) &= \frac{8}{15\sqrt{\pi}} [I_1 - h I_2] \\ &= \frac{8}{15\sqrt{\pi}} e^{-z} \left[\Gamma\left(\frac{3}{2}, 0 \vee (h-z)\right) + (z-h) \Gamma\left(\frac{1}{2}, 0 \vee (h-z)\right) \right] \end{aligned}$$

$$g(z, h) = \frac{8}{15\sqrt{\pi}} e^{-z} \begin{cases} \sqrt{\pi} \left(\frac{1}{2} - (h-z)\right) & z > h \\ \Gamma\left(\frac{1}{2}, h-z\right) \left(\frac{1}{2} - (h-z)\right) + \sqrt{h-z} e^{-(h-z)} & z < h \end{cases}$$

This leads to marginal and conditional densities of

$$g_Z(z) = \frac{4}{15} e^{-z} \left(z^2 + z + \frac{3}{4} \right) \quad z \geq 0$$

$$g_{H|Z}(h|z) = \frac{2}{\sqrt{\pi} \left(\frac{3}{4} + z + z^2 \right)} \begin{cases} \sqrt{\pi} \left(\frac{1}{2} - hz \right) & z > h \\ \Gamma \left(\frac{1}{2}, hz \right) \left(\frac{1}{2} - hz \right) + \sqrt{hz} e^{-hz} & z < h \end{cases}$$

where $hz = h - z$.

The expectations can be calculated in a similar way. Starting with expected radius, the explicit calculation is

$$\begin{aligned} E_f \left[\sqrt{X} \right] &= m_F^+ = \int_{x=0}^{\infty} \sqrt{x} f_X(x) dx = \frac{1}{2} \int_{x=0}^{\infty} e^{-x} \sqrt{x} x^2 dx \\ &= \frac{1}{2} \int_{x=0}^{\infty} e^{-x} x^{\frac{5}{2}} dx = \frac{1}{2} \Gamma \left(\frac{7}{2} \right) = \frac{1}{2} \frac{5}{2} \frac{3}{2} \frac{\sqrt{\pi}}{2} \\ &= \frac{15}{16} \sqrt{\pi} \end{aligned}$$

The quantities ξ_g^j are calculated for the numerical simulation as follows:

$$\begin{aligned} \xi_g^j &= \int_{h=0}^{\infty} h^j \frac{1}{2m_F^+} \int_{x=0}^{\infty} x^{-\frac{1}{2}} (x-h) e^{-x} dx dh \\ &= \frac{1}{2m_F^+} \int_{x=0}^{\infty} x^{-\frac{1}{2}} e^{-x} \int_{h=0}^x h^j (x-h) dh dx \\ &= \frac{1}{2m_F^+} \int_{x=0}^{\infty} x^{-\frac{1}{2}} e^{-x} \left[\frac{1}{j+1} x^{j+2} - \frac{1}{j+2} x^{j+2} \right] dx \\ &= \frac{1}{2m_F^+ (j+1)(j+2)} \int_{x=0}^{\infty} x^{j+\frac{3}{2}} e^{-x} dx \\ \xi_g^j &= \frac{\Gamma \left(j + \frac{5}{2} \right)}{2m_F^+ (j+1)(j+2)} \end{aligned}$$

To find the optimal bandwidth for the estimator of the ξ_g^j 's, the value for

c_g^j in the numerical simulation is determined as follows:

$$c_g^j = \frac{1}{4m_F^+} \int_{h=0}^{\infty} h^j \frac{\partial}{\partial z} \int_{x=z}^{\infty} (x-z)^{-\frac{1}{2}} (x-h)e^{-x} dx \Big|_{z=0} dh$$

$$c_g^j = \frac{1}{4m_F^+} \frac{\partial}{\partial z} \int_{x=z}^{\infty} (x-z)^{-\frac{1}{2}} e^{-x} \int_{h=0}^x h^j (x-h) dh dx \Big|_{z=0}$$

$$c_g^j = \frac{1}{4m_F^+} \frac{\partial}{\partial z} \int_{x=z}^{\infty} (x-z)^{-\frac{1}{2}} e^{-x} \frac{1}{(j+1)(j+2)} x^{j+2} dx \Big|_{z=0}$$

let $u = x^{j+2}e^{-x}$ $dv = (x-z)^{-\frac{1}{2}} dx$

$du = [(j+2)x^{j+1}e^{-x} - x^{j+2}e^{-x}]dx$ $v = 2\sqrt{x-z}$

$$c_g^j = \frac{1}{4m_F^+(j+1)(j+2)} \frac{\partial}{\partial z} \left\{ 2\sqrt{x-z}x^{j+2}e^{-x} \Big|_{x=z}^{\infty} - \int_{x=z}^{\infty} 2\sqrt{x-z}e^{-x} [(j+2)x^{j+1} - x^{j+2}] dx \right\} \Big|_{z=0}$$

$$c_g^j = \frac{1}{4m_F^+(j+1)(j+2)} \frac{\partial}{\partial z} \int_{x=z}^{\infty} 2\sqrt{x-z}e^{-x} [x^{j+2} + (j+2)x^{j+1}] dx \Big|_{z=0}$$

Using Leibniz rule gives

$$c_g^j = \frac{1}{4m_F^+(j+1)(j+2)} - 2\sqrt{z-z}e^{-z} [z^{j+2} + (j+2)z^{j+1}] + \int_{x=z}^{\infty} \frac{\partial}{\partial z} 2\sqrt{x-z}e^{-x} [x^{j+2} + (j+2)x^{j+1}] dx \Big|_{z=0}$$

$$c_g^j = \frac{1}{4m_F^+(j+1)(j+2)} \int_{x=z}^{\infty} (x-z)^{-\frac{1}{2}} e^{-x} [x^{j+2} + (j+2)x^{j+1}] dx \Big|_{z=0}$$

$$c_g^j = \frac{1}{4m_F^+(j+1)(j+2)} \int_{x=0}^{\infty} x^{-\frac{1}{2}} e^{-x} [x^{j+2} + (j+2)x^{j+1}] dx$$

$$c_g^j = \frac{1}{4m_F^+(j+1)(j+2)} \int_{x=0}^{\infty} e^{-x} [x^{j+\frac{3}{2}} + (j+2)x^{j+\frac{1}{2}}] dx$$

$$c_g^j = \frac{\Gamma(j+\frac{5}{2}) - (j+2)\Gamma(j+\frac{3}{2})}{4m_F^+(j+1)(j+2)}$$

The other moments can be found in exactly the same way. Table B.2 gives the underlying moment calculations for both the numerical and physical simulations (given in Section B.1.3).



Underlying Moment Results		
Moment	Value (Numerical)	Value (Physical)
$E_f \left[\sqrt{X} \right] = m_F^+$	$\frac{15}{16} \sqrt{\pi}$	$\frac{b+a}{2} = 0.25$
$E_f [X]$	3	$\frac{b^3-a^3}{3(b-a)} = 0.07$
$E_f [H]$	1	$\frac{c}{2} = 0.1$
$E_f \left[\sqrt{X} H \right]$	$\frac{32}{35} \sqrt{\pi}$	$\frac{c(b+a)}{4} = 0.025$
$E_f [XH]$	4	$\frac{c(b^3-a^3)}{6(b-a)} = 0.007$
$E_f \left[X^{-\frac{1}{2}} \right]$	$\frac{3}{8} \sqrt{\pi}$	$\frac{1}{b-a} \ln \left(\frac{b}{a} \right) = \frac{10}{3} \ln(4)$
$E_f \left[X^{-\frac{1}{2}} H \right]$	$\frac{5}{16} \sqrt{\pi}$	$\frac{c}{2(b-a)} \ln \left(\frac{b}{a} \right) = \frac{1}{3} \ln(4)$
$E_f \left[X^{-\frac{1}{2}} H^2 \right]$	$\frac{35}{64} \sqrt{\pi}$	$\frac{c^2}{3(b-a)} \ln \left(\frac{b}{a} \right) = \frac{4}{90} \ln(4)$
$E_g [Z]$	$\frac{7}{3}$	$\frac{b^2+a^2}{3} = 0.05\bar{6}$
$E_g \left[Z^{-\frac{1}{2}} \right] = m_G^-$	$\frac{8}{15} \sqrt{\pi}$	$\frac{\pi}{b+a} = 2\pi$
$E_g [H]$	$\frac{7}{6}$	$c(b+a) = 0.1$
$E_g \left[Z^{-\frac{1}{2}} H \right]$	$\frac{8}{15} \sqrt{\pi}$	$c\pi = 0.2\pi$
$E_g \left[Z^{\frac{1}{2}} \right]$	$\frac{16}{5\sqrt{\pi}}$	$\frac{2(b^3-a^3)}{3(b^2-a^2)} = 0.28$
$E_g \left[Z^{\frac{1}{2}} H \right]$	$\frac{15}{\sqrt{\pi}}$	$\frac{c(b^3-a^3)}{3(b^2-a^2)} = 0.028$
ξ_g^0	$\frac{8}{15\sqrt{\pi}} \frac{\Gamma(\frac{5}{2})}{(1)(2)} = \frac{1}{5}$	$\frac{1}{b^2-a^2} \ln \left(\frac{b}{a} \right) = \frac{\ln(4)}{0.15}$
ξ_g^1	$\frac{8}{15\sqrt{\pi}} \frac{\Gamma(\frac{7}{2})}{(2)(3)} = \frac{1}{6}$	$\frac{c}{2(b^2-a^2)} \ln \left(\frac{b}{a} \right) = \frac{\ln(4)}{1.5}$
ξ_g^2	$\frac{8}{15\sqrt{\pi}} \frac{\Gamma(\frac{9}{2})}{(3)(4)} = \frac{7}{24}$	$\frac{c^2}{3(b^2-a^2)} \ln \left(\frac{b}{a} \right) = \frac{4\ln(4)}{45}$
ξ_g^4	$\frac{8}{15\sqrt{\pi}} \frac{\Gamma(\frac{13}{2})}{(5)(6)} = \frac{231}{80}$	$\frac{c^4}{5(b^2-a^2)} \ln \left(\frac{b}{a} \right) = \frac{3\ln(4)}{4}$
c_g^0	$\frac{4}{15\sqrt{\pi}} \left(\frac{(2)\Gamma(\frac{3}{2})}{(1)(2)} - \frac{\Gamma(\frac{5}{2})}{(1)(2)} \right) = \frac{1}{30}$	$\frac{1}{8a^2b^2} = 78.125$
c_g^1	$\frac{4}{15\sqrt{\pi}} \left(\frac{(3)\Gamma(\frac{5}{2})}{(2)(3)} - \frac{\Gamma(\frac{7}{2})}{(2)(3)} \right) = \frac{1}{60}$	$\frac{c}{16a^2b^2} = 7.8125$
c_g^2	$\frac{4}{15\sqrt{\pi}} \left(\frac{(4)\Gamma(\frac{7}{2})}{(3)(4)} - \frac{\Gamma(\frac{9}{2})}{(3)(4)} \right) = \frac{1}{48}$	$\frac{c^2}{24a^2b^2} = 1.04$

TABLE B.2: Moments for the various quantities of interest for both the numerical and physical simulations.

B.1.3 Physical Simulation

For the physical simulation the radius and height were chosen to each have an independent uniform distribution. This leads to

$$f_X(x) = \frac{1}{2(b-a)\sqrt{x}} \quad x \in [a^2, b^2], \quad \text{and} \quad f_H(h) = \frac{1}{c} \quad h \in (0, c)$$

leading to a joint distribution function of $f(x, h) = \frac{1}{2(b-a)c\sqrt{x}} = \beta x^{-\frac{1}{2}}$. Therefore, the CDFs for the quantities of interest are:

$$F_X(x) = \frac{\sqrt{x} - a}{b - a} \quad x \in [a^2, b^2]$$

$$F_H(h) = \frac{h}{c} \quad h \in [0, c]$$

$$F_R(r) = \begin{cases} 0 & r < \frac{a}{c} \\ 1 - \beta \left(2cb - \frac{a^2}{r} - c^2 r \right) & \frac{a}{c} \leq r \leq \frac{b}{c} \\ 1 - \frac{1}{r} \frac{b+a}{2c} & \frac{b}{c} < r \end{cases}$$

$$F_S(s) = \beta \begin{cases} 0 & s < 2\pi a^2 \\ a^2 - \frac{s}{2\pi} \left[\ln \left(\frac{2\pi a^2}{s} \right) + 1 \right] & 2\pi a^2 \leq s < 2\pi(a^2 + ac) \\ c(q - 2a) + \frac{s}{2\pi} \ln \left(\frac{s}{2\pi q} \right) & 2\pi(a^2 + ac) \leq s < 2\pi b^2 \\ c(q - 2a) + \frac{s}{2\pi} \ln \left(\frac{s}{2\pi q} \right) + \frac{s}{2\pi} - b^2 & 2\pi b^2 \leq s < 2\pi(b^2 + bc) \\ \frac{1}{\beta} & 2\pi(b^2 + bc) \leq s \end{cases}$$

where $q = \left[\sqrt{\frac{h^2}{4} + \frac{s}{2\pi}} - \frac{h}{2} \right]^2$

B

$$F_V(v) = \begin{cases} \frac{v}{\pi c b a} & v \leq \pi c b^2 \\ 2\beta \left(2\sqrt{\frac{v c}{\pi}} - \frac{v}{\pi b} - c b \right) & \pi c b^2 < v \end{cases}$$

The joint probability density for the observed rectangles on the cut plane is

$$\begin{aligned} g(z, h) &= \frac{1}{2m_F^+} \int_{x=z}^{\infty} (x-z)^{-\frac{1}{2}} f(x, h) dx \\ &= \frac{\beta}{2m_F^+} \int_{x=z \vee a^2}^{b^2} (x-z)^{-\frac{1}{2}} x^{-\frac{1}{2}} dx \\ &= \frac{\beta}{2m_F^+} \int_{x=z \vee a^2}^{b^2} (x^2 - xz)^{-\frac{1}{2}} dx \\ &= \frac{\beta}{2m_F^+} \ln \left(\sqrt{x^2 - xz} + x - \frac{1}{2}z \right) \Big|_{x=z \vee a^2}^{b^2} \\ &= \frac{\beta}{m_F^+} \left[\ln \left(b\sqrt{b^2 - z} + b^2 - \frac{1}{2}z \right) - \ln \left(a\sqrt{a^2 - z} + a^2 - \frac{1}{2}z \right) 1_{[z < a^2]} \right. \\ &\quad \left. \ln \left(\frac{1}{2}z \right) 1_{[a^2 < z < b^2]} \right] \\ g(z, h) &= \frac{\beta}{m_F^+} \begin{cases} \ln \left(\frac{b\sqrt{b^2 - z} + b^2 - \frac{1}{2}z}{a\sqrt{a^2 - z} + a^2 - \frac{1}{2}z} \right) & z < a^2 \\ \ln \left(\frac{b\sqrt{b^2 - z} + b^2 - \frac{1}{2}z}{\frac{1}{2}z} \right) & a^2 \leq z < b^2 \end{cases} \end{aligned}$$

For the moments, ξ_g^j , c_g^j and the empirical estimators, the calculations are along the same line. Table B.2 shows the results as calculated for $a = 0.1$, $b = 0.4$ and $c = 0.2$, which are the quantities used in the simulation.

C

Appendix

C.1 Proof of equation (5.2.6)

Using that $t > 0$, $t > b_n$ for sufficiently large n , since $b_n \downarrow 0$ leads to

$$\begin{aligned}
 \tilde{N}_n^{vol}(t) &= \frac{1}{b_n n} \sum_{i=1}^n \int_{s=-\infty}^{\infty} K\left(\frac{t-s}{b_n}\right) \left[Z_i - \frac{s}{\pi H_i}\right]^{-\frac{1}{2}} 1_{[Z_i > \frac{s}{\pi H_i}]} ds \\
 &= \frac{1}{b_n n} \sum_{i=1}^n \int_{s=-\infty}^{\infty} K\left(\frac{t-s}{b_n}\right) \sqrt{\pi H_i} [Z_i H_i \pi - s]^{-\frac{1}{2}} 1_{[Z_i H_i \pi > s]} ds \\
 &= \frac{1}{b_n n} \sum_{i=1}^n \sqrt{\pi H_i} \int_{u=0}^{\infty} K\left(\frac{t - (Z_i H_i \pi - u)}{b_n}\right) u^{-\frac{1}{2}} du \\
 &= \frac{1}{b_n n} \sum_{i=1}^n \sqrt{\pi H_i} \int_{u=0}^{\infty} K\left(\frac{u + (t - Z_i H_i \pi)}{b_n}\right) \left(\frac{u}{b_n}\right)^{-\frac{1}{2}} b_n^{-\frac{1}{2}} d\left(\frac{u}{b_n}\right) b_n \\
 &= \frac{1}{\sqrt{b_n} n} \sum_{i=1}^n \sqrt{\pi H_i} \int_{u=0}^{\infty} K\left(u + \frac{t - Z_i H_i \pi}{b_n}\right) u^{-\frac{1}{2}} du \\
 &= \frac{1}{\sqrt{b_n} n} \sum_{i=1}^n \sqrt{\pi H_i} \bar{K}\left(\frac{t - \pi H_i Z_i}{b_n}\right)
 \end{aligned}$$

where $\bar{K}(v)$ is the same as that defined in eq. (5.2.4).

C.2 Convergence conditions for the proofs of Lemmas 5.2.1 and 5.3.1

For Lemma 5.2.1 (for the volume) it is necessary to show

$$I_{1,n} = \int_{u=-\epsilon/b_n}^c \int_h \bar{K}(u)^2 \left(g\left(\frac{t-b_n u}{\pi h}, h\right) - g\left(\frac{t}{\pi h}, h\right) \right) dh du = o(\ln b_n^{-1}).$$

For Lemma 5.3.1 it is necessary to show

$$I_{2,n} = \int_{u=-\infty}^1 \int_h \bar{K}'(u)^2 \left(g\left(\frac{t-b_n u}{\pi h}, h\right) - g\left(\frac{t}{\pi h}, h\right) \right) dh du = o(1).$$

In this integral, the function \bar{K}' occurs. The arguments given in Section 5.2 for the kernel \bar{K} can be extended to the derivative. Note that

$$\bar{K}'(u) = \lim_{h \rightarrow 0} \int_0^{-u+1} v^{-\frac{1}{2}} \frac{K(u+v+h) - K(u+v)}{h} dv.$$

From Condition 5.2.1, $\|K'\|_\infty \leq C$ follows and

$$\left| \frac{K(u+v+h) - K(u+v)}{h} \right| = \left| \frac{hK'(u+v+\xi h)}{h} \right| \leq C,$$

and

$$\int_0^{-u+1} v^{-\frac{1}{2}} C dv < \infty.$$

Using the differentiability of K (yielding that for $h \rightarrow 0$, $h^{-1}(K(u+v+h) - K(u+v)) \rightarrow K'(u+v)$), it follows by dominated convergence that

$$\bar{K}'(u) = \int_0^{-u+1} v^{-\frac{1}{2}} K'(u+v) dv.$$

Using integration by parts, for $u < -1$

$$\bar{K}'(u) = \int_{-u-1}^{-u+1} v^{-\frac{1}{2}} dK(u+v) = \frac{1}{2} \int_{-u-1}^{-u+1} v^{-\frac{3}{2}} K(u+v) dv$$

so that (following the same reasoning as with \bar{K} itself, for $u < -1$)

$$\frac{1}{2}(-u+1)^{-\frac{3}{2}} \leq \bar{K}'(u) \leq \frac{1}{2}(-u-1)^{-\frac{3}{2}}.$$

The bounded support condition in Assumption 5.2.2 means that there is some $M > 0$ such that for all (a, h) with $z > M$ or $h > M$, $g(z, h) = 0$. The Lipschitz continuous condition means that for some $0 < C < \infty$, for all (z_1, h_1) and (z_2, h_2) in $(0, \infty)^2$,

$$|g(z_2, h_2) - g(z_1, h_1)| \leq C\|(z_1 - z_2, h_1 - h_2)^T\|,$$

where $\|\cdot\|$ denotes the usual Euclidean norm on \mathbb{R}^2 .

Consider $I_{2,n}$. The integral in u can be split in two regions, $(-\infty, -1)$ and $[-1, 1]$. For the second region, it is clear that both \bar{K}' and g are bounded on the region of integration. For fixed (u, h) , the integrand tends to zero as n tends to infinity, so dominated convergence gives

$$\int_{u=-1}^1 \int_h \bar{K}'(u)^2 \left(g\left(\frac{t - b_n u}{\pi h}, h\right) - g\left(\frac{t}{\pi h}, h\right) \right) dh du \rightarrow 0$$

for $n \rightarrow \infty$. Now consider the first region of integration, $(-\infty, -1)$. For the integration in h , note that it can be restricted to the set where $h \in [0, M]$, $0 \leq t/(\pi h) \leq M$ and $0 \leq (t - b_n u)/(\pi h) \leq M$, leading to (note that $u < 0$ on this region of integration)

$$\frac{t}{\pi M} \leq h \leq M.$$

This gives

$$\begin{aligned} & \left| \int_{u=-\infty}^{-1} \int_{h=t/(\pi M)}^M \bar{K}'(u)^2 \left(g\left(\frac{t - b_n u}{\pi h}, h\right) - g\left(\frac{t}{\pi h}, h\right) \right) dh du \right| \\ & \leq \int_{u=-\infty}^{-1} \int_{h=t/(\pi M)}^M \frac{1}{4}(-1 - u)^{-3} \left| g\left(\frac{t - b_n u}{\pi h}, h\right) - g\left(\frac{t}{\pi h}, h\right) \right| dh du \\ & \leq \int_{u=-\infty}^{-1} \int_{h=t/(\pi M)}^M \frac{1}{4}(-1 - u)^{-3} C \frac{b_n |u|}{\pi h} dh du \leq \frac{CM^2 b_n}{4t} \int_1^\infty \frac{u}{(1 + u)^3} du \\ & = O(b_n). \end{aligned}$$

Now consider the condition needed in Lemma 5.2.1, for the volume. Recall that $c < -1$. Imposing Condition 5.2.1 and under Assumption 5.2.2, the region of integration of h can be restricted to $[t/(\pi M), M]$

$$\begin{aligned} |I_{n,1}| & \leq \int_{u=-\epsilon/b_n}^c \bar{K}(u)^2 \int_{h=t/(\pi M)}^M \left| \frac{Cb_n u}{\pi h} \right| dh du \\ & \leq \frac{Cb_n M^2}{t} \int_{u=-\epsilon/b_n}^c |u| \bar{K}(u)^2 du \leq \frac{Cb_n M^2}{t} \int_{-c}^{u=\epsilon/b_n} \frac{u}{u+1} du \leq \frac{C\epsilon M^2}{t}. \end{aligned}$$

This shows that $I_{n,1} = O(1)$, and therefore certainly $o(\log b_n^{-1})$.

C.3 Proof of equation (5.2.9) for Volume

Proof. Following exactly the same reasoning as for \tilde{N}_n^{sr} , yields

$$n \text{Var} \left(\tilde{N}_n^{vol}(t) \right) = b_n^{-1} \pi E \left[H_1 \bar{K} \left(\frac{t - \pi Z_1 H_1}{b_n} \right)^2 \right] - N^{vol}(t)^2 + o(1).$$

Again, for $\epsilon > 0$ and n sufficiently large such that $b_n < \epsilon$,

$$\begin{aligned} & b_n^{-1} \pi E \left[H_1 \bar{K} \left(\frac{t - \pi Z_1 H_1}{b_n} \right)^2 \right] \\ &= b_n^{-1} \int_{h=0}^{\infty} \pi h \left(\int_{z=\frac{t-b_n}{\pi h}}^{\frac{t+\epsilon}{\pi h}} + \int_{z=\frac{t+\epsilon}{\pi h}}^{\infty} \right) \bar{K} \left(\frac{t - zh\pi}{b_n} \right)^2 g(z, h) dz dh \\ &= I_1 + I_2. \end{aligned}$$

For I_2 we have, squaring the upper bound on \bar{K} given in eq. (5.2.7) and using that for $zh\pi > t + \epsilon > t + b_n$, $(t - zh\pi)/b_n < -1$

$$\begin{aligned} I_2 &\leq b_n^{-1} \int_{h=0}^{\infty} \pi h \int_{z=\frac{t+\epsilon}{h\pi}}^{\infty} b_n (zh\pi - t - b_n)^{-1} g(z, h) dz dh \\ &\leq \int_{h=0}^{\infty} \pi h (t + \epsilon - t - b_n)^{-1} \int_{z=\frac{t+\epsilon}{h\pi}}^{\infty} g(z, h) dz dh \\ &\leq \frac{1}{\epsilon - b_n} \int_{h=0}^{\infty} \pi h \int_{z=\frac{t+\epsilon}{h\pi}}^{\infty} g(z, h) dz dh \\ &\leq \frac{2}{\epsilon} \pi E_g[H] \end{aligned}$$

for all n sufficiently large. For I_1 we have for n sufficiently large

$$\begin{aligned} I_1 &= b_n^{-1} \int_{h=0}^{\infty} \pi h \int_{z=\frac{t-b_n}{\pi h}}^{\frac{t+\epsilon}{\pi h}} \bar{K} \left(\frac{t - zh\pi}{b_n} \right)^2 g(z, h) dz dh. \\ &= \int_{h=0}^{\infty} \int_{v=-\epsilon/b_n}^1 \bar{K}(v)^2 g \left(\frac{t - b_n v}{\pi h}, h \right) dv dh. \end{aligned}$$

Following the exact same reasoning as for the squared radius and using the continuity of g at t yields

$$I_1 \approx \int_{h=0}^{\infty} g \left(\frac{t}{\pi h}, h \right) dh \ln(b_n^{-1}) = \tau_q(0) \ln(b_n^{-1}).$$

□

C.4 Calculation of asymptotically MSE optimal bandwidth

Starting with the results from Theorem 5.2.1 and dropping the lower order terms yields

$$\text{MSE}(\tilde{N}_n(t)) = \frac{1}{4}b_n^4 N''(t)^2 \left(\int u^2 K(u) du \right)^2 + \frac{\tau_q(0) \ln(b_n^{-1})}{n}.$$

Minimizing the MSE with respect to the bandwidth yields:

$$0 = \frac{\partial}{\partial b_n} \text{MSE}(\tilde{N}_n(t)) = \frac{\partial}{\partial b_n} \left[\frac{1}{4}b_n^4 \left(N''(t) \int u^2 K(u) du \right)^2 - \frac{\tau_q(0) \ln(b_n)}{n} \right]$$

$$0 = \frac{1}{4}4b_n^3 \left(N''(t) \int u^2 K(u) du \right)^2 - \frac{\tau_q(0) \left(\frac{1}{b_n} \right)}{n}$$

$$b_n^4 = \frac{\tau_q(0)}{n \left(N''(t) \int u^2 K(u) du \right)^2}$$

and the optimal bandwidth is

$$b_n = n^{-\frac{1}{4}} \tau_q(0)^{\frac{1}{4}} \left(N''(t) \int u^2 K(u) du \right)^{-\frac{1}{2}}.$$

This leads to an MSE of

$$\begin{aligned} \text{MSE}(\tilde{N}_n(t)) &= \frac{1}{4}b_n^4 N''(t)^2 \left(\int u^2 K(u) du \right)^2 - \tau_q(0) \ln(b_n) n^{-1} \\ &= \frac{1}{4}n^{-1} \tau_q(0) - \frac{1}{4} \tau_q(0) \ln \left(\frac{\tau_q(0)}{n \left(N''(t) \int u^2 K(u) du \right)^2} \right) n^{-1} \\ &= \frac{1}{4} \tau_q(0) \frac{\ln(n)}{n} + o \left(\frac{\ln(n)}{n} \right). \end{aligned}$$

C.5 Proof of equation (5.2.10)

Proof. Denote by \mathbb{G}_n the empirical distribution function of a sample X_1, \dots, X_n from the distribution function G . Choose $t \in \mathbb{R}$ and assume that G is twice

C

continuously differentiable at t . Let K be the kernel and $b = b_n > 0$ the bandwidth and define

$$\hat{G}_n(t) = \frac{1}{b} \int K\left(\frac{t-x}{b}\right) \mathbb{G}_n(x) dx.$$

Then the bias of this estimator is given by

$$\begin{aligned} E[\hat{G}_n(t)] - G(t) &= \frac{1}{b} \int K\left(\frac{t-x}{b}\right) (G(x) - G(t)) dx \\ &= \frac{1}{2} b^2 g'(t) \int_{-1}^1 u^2 K(u) du + o(b^2). \end{aligned} \quad (\text{C.5.1})$$

For the variance, writing $\mathbb{K}(u) = \int_{-1}^u K(v) dv$, note that

$$\hat{G}_n(t) = - \int \mathbb{G}_n(x) d\mathbb{K}\left(\frac{t-x}{b}\right) = \int \mathbb{K}\left(\frac{t-x}{b}\right) d\mathbb{G}_n(x),$$

giving

$$\begin{aligned} \text{Var}(\hat{G}_n(t)) &= \frac{1}{n} \text{Var}\left(\mathbb{K}\left(\frac{t-X_1}{b}\right)\right) \\ &= \frac{1}{n} \left\{ E\left[\mathbb{K}\left(\frac{t-X_1}{b}\right)^2\right] - \left(E\left[\mathbb{K}\left(\frac{t-X_1}{b}\right)\right]\right)^2 \right\} \end{aligned}$$

Note that

$$\begin{aligned} E\left[\mathbb{K}\left(\frac{t-X_1}{b}\right)^2\right] &= \left(\int_{-\infty}^{t-b} + \int_{t-b}^{t+b}\right) \mathbb{K}\left(\frac{t-x}{b}\right)^2 g(x) dx \\ &= \int_{-\infty}^{t-b} g(x) dx + b \int_{-1}^1 \mathbb{K}(u)^2 g(t-bu) du \\ &= G(t-b) + bg(t) \int_{-1}^1 \mathbb{K}(u)^2 du + O(b^2) \\ &= G(t) - g(t) \left(1 - \int_{-1}^1 \mathbb{K}(u)^2 du\right) b + O(b^2). \end{aligned}$$

Furthermore, from eq. (C.5.1) it follows that

$$E\left[\mathbb{K}\left(\frac{t-X_1}{b}\right)\right] = G(t) + \frac{1}{2} b^2 g'(t) \int u^2 K(u) du + o(b^2).$$

This implies, for $0 < b = b_n \rightarrow 0$,

$$\begin{aligned} \text{Var}(\hat{G}_n(t)) &= \frac{1}{n} \left(G(t) - g(t) \left(1 - \int_{-1}^1 \mathbb{K}(u)^2 du \right) b - G(t)^2 + O(b^2) \right) \\ &\sim \frac{1}{n} G(t)(1 - G(t)) - \frac{b}{n} g(t) \left(1 - \int_{-1}^1 \mathbb{K}(u)^2 du \right) \\ &= \frac{\sigma_t^2}{n} - c_{G,K}^{(1)} \frac{b}{n}. \end{aligned}$$

Therefore, for $b = b_n \downarrow 0$,

$$\text{MSE} \sim \frac{\sigma_t^2}{n} - c_{G,K}^{(1)} \frac{b}{n} + c_{G,K}^{(2)} b^4$$

where

$$c_{G,K}^{(2)} = \frac{1}{4} g'(t)^2 \left(\int u^2 K(u) du \right)^2$$

□

C.6 Proof of equation (5.3.4) for Volume

Proof.

$$\begin{aligned} \text{Var}(\tilde{\nu}(t)) &= \text{Var} \left(b_n^{-\frac{3}{2}} n^{-1} \sum_{i=1}^n \sqrt{H_i \pi \bar{K}'} \left(\frac{t - Z_i H_i \pi}{b_n} \right) \right) \\ &= b_n^{-3} n^{-1} \text{Var} \left(\sqrt{H_1 \pi \bar{K}'} \left(\frac{t - Z_1 H_1 \pi}{b_n} \right) \right) \\ n b_n^2 \text{Var}(\tilde{\nu}(t)) &= b_n^{-1} \left\{ E \left[H_1 \pi \bar{K}' \left(\frac{t - Z_1 H_1 \pi}{b_n} \right)^2 \right] \right. \\ &\quad \left. - \left(E \left[\sqrt{H_1 \pi \bar{K}'} \left(\frac{t - Z_1 H_1 \pi}{b_n} \right) \right] \right)^2 \right\} \end{aligned}$$

$$\begin{aligned}
E \left[H_1 \pi \overline{K}' \left(\frac{t - Z_1 H_1 \pi}{b_n} \right)^2 \right] &= \int_{h=0}^{\infty} \pi h \int_{z=0}^{\infty} \overline{K}' \left(\frac{t - zh\pi}{b_n} \right)^2 g(z, h) dz dh \\
&= b_n \int_{h=0}^{\infty} \int_{v=-\infty}^{\frac{t}{b_n}} \overline{K}'(v)^2 g \left(\frac{t - b_n v}{b_n}, h \right) dv dh \\
&= b_n \int_{h=0}^{\infty} g \left(\frac{t - b_n v}{b_n}, h \right) dh \int_{v=-\infty}^1 \overline{K}'(v)^2 dv \\
&= b_n \tau_q(0) \int_{v=-\infty}^1 \overline{K}'(v)^2 dv
\end{aligned}$$

Therefore,

$$\begin{aligned}
nb_n^2 \text{Var}(\tilde{\nu}(t)) &= b_n \tau_q(0) \int_{v=-\infty}^1 \overline{K}'(v)^2 dv - b_n^2 \nu(t)^2 + o(b_n^2) \\
&= b_n \tau_q(0) \int_{v=-\infty}^1 \overline{K}'(v)^2 dv + O(b_n^2)
\end{aligned}$$

leads to

$$\text{Var}(\tilde{\nu}(t)) = (b_n n)^{-1} \tau_q(0) \int_{v=-\infty}^1 \overline{K}'(v)^2 dv + O(n^{-1}).$$

□

Summary

Microstructural banding is explored in 2D and 3D using serial sectioned micrographs. The banding is quantified using two parameters called the Band Continuity Index C_b and the Perpendicular Continuity Index C_p . The indexes determined from the 2D micrographs is shown to be sufficient for estimating the distribution of the bands in 3D.

A stereological model employing oriented circular cylinders is established to represent the bands in steel microstructures. This model assumes that cylinders are distributed randomly inside of a box with their symmetry axes oriented in the same direction. The box is then cut parallel to the symmetry axes and rectangles are observed on the cut plane. The inverse relationship between the rectangles and the cylinders is established, and the distribution functions and expectations various quantities of interest, such as the cylinder radius, height, surface area and volume, as well as the covariance between the radius and height, are estimated directly from the rectangle observations. The asymptotic behavior of the empirical, isotonic and kernel smoothed estimators is determined and used to obtain confidence intervals for the expectations of the quantities of interest when the model is applied to the steel microstructures.

The limitations of the model are explored and the model is shown to be reasonably robust against deviations from its rather stringent requirements. This makes the model useful in a practical setting, and the results obtained for the steel microstructures are reasonable. This model is not limited in application to banded microstructures, but can also be used for any microstructural feature that can be thought of as being plate-like, rod-like or needle-like. Features such as inclusions, voids and dendrites often take on these shapes.

Samenvatting

Microstructurele banden worden in 2D en 3D bestudeerd, door gebruik te maken van micrografieën van seriele doorsnedes. De banden worden gekwantificeerd door twee parameters: de Bands Continuïteitsindex C_b en de Orthogonale Continuïteitsindex C_p . We laten zien dat de indices die geschat zijn aan de hand van de 2D-micrografieën toereikend zijn voor het bepalen van de 3D-bandenverdeling.

Een stereologisch model, op basis van gerichte cilinders (met cirkelvormige doorsnede), wordt opgezet om de banden in stalen microstructuren te vertegenwoordigen. Dit model gaat er van uit dat de cilinders willekeurig verdeeld zijn binnen een doos, met hun symmetrieassen dezelfde richting op georiënteerd. De doos wordt dan parallel aan de symmetrieassen doorgesneden, wat rechthoeken oplevert in het doorsneevlak. De inverse relatie tussen de rechthoeken en de cilinders wordt afgeleid, en de verdelingsfuncties en verwachtingswaarden van verschillende interessante grootheden zoals de cilinderstraal, de hoogte, de oppervlakte en het volume, en ook de covariantie tussen de straal en hoogte, worden vervolgens direct aan de hand van de waarnemingen van rechthoeken ingeschat. Het asymptotisch gedrag van de empirische, isotone, en kernel-smoothed schatters wordt bepaald, en gebruikt om betrouwbaarheidsintervallen te verkrijgen voor de verwachtingswaarden van de interessante grootheden wanneer het model toegepast wordt op stalen microstructuren.

De beperkingen van het model worden verkend, welke redelijk robuust bestand blijken te zijn tegen afwijkingen van de vrij strenge voorwaarden van het model. Dit zorgt ervoor dat het model bruikbaar is in realistische (bijv. industriële) settings, en dat de resultaten voor de stalen microstructuren redelijk zijn. Het model is niet beperkt in toepassing tot banden in microstructuren, maar kan ook toegepast worden op willekeurige microstructurele eigenschappen, zolang die bij benadering plaatvormig, staafvormig of naaldvormig zijn. Eigenschappen zoals inclusies, holtes en dendrietten vallen hier vaak onder.

References

- [1] P. Hall and R. L. Smith, *The Kernel Method for Unfolding Sphere Size Distributions*, Journal of Computational Physics **74**, 409 (1988).
- [2] T. A. Kop, J. Sietsma, and S. van der Zwaag, *Anisotropic dilatation behaviour during transformation of hot rolled steels showing banded structure*, Materials Science and Technology **17**, 1569 (2001).
- [3] J. D. Verhoeven, *A review of Microsegregation Induced Banding Phenomena in Steels*, Journal of Materials Engineering and Performance **9**, 286 (2000).
- [4] T. M. Mayhew, *The new stereological methods for interpreting functional morphology from slices of cells and organs*, Experimental physiology **76**, 639 (1991).
- [5] J. Russ and R. Dehoff, *Practical stereology* (Kluwer Academic/Plenum Publishers, 2000).
- [6] J. Alkemper and P. W. Voorhees, *Quantitative serial sectioning analysis*, Journal of Microscopy **201**, 388 (2001).
- [7] M. Groeber, B. Haley, M. Uchic, D. Dimiduk, and S. Ghosh, *3D reconstruction and characterization of polycrystalline microstructures using a FIB-SEM system*, Materials Characterization **57**, 259 (2006).
- [8] A. Lewis, J. Bingert, D. Rowenhorst, A. Gupta, A. Geltmacher, and G. Spanos, *Two- and three-dimensional microstructural characterization of a super-austenitic stainless steel*, Materials Science and Engineering A **418**, 11 (2006).
- [9] A. D. Rollett, S.-B. Lee, R. Campman, and G. S. Rohrer, *Three-dimensional characterization of microstructure by electron back-scatter diffraction*, Annu Rev Mater Res **37**, 627 (2007).
- [10] G. Spanos, D. J. Rowenhorst, A. C. Lewis, and A. B. Geltmacher, *Combining serial sectioning, EBSD analysis, and image-based finite element modeling*, MRS Bulletin **33**, 597 (2008).

-
- [11] F. Lin, A. Godfrey, D. J. Jensen, and G. Winther, *3D EBSD characterization of deformation structures in commercial purity aluminum*, Materials Characterization **inpress** (2010).
- [12] B. Gault, M. P. Moody, J. M. Cairney, and S. P. Ringer, *Atom Probe Microscopy*, vol. 160 of *Springer Series in Materials Science* (Springer, 2012), 1st ed.
- [13] T. F. Kelly and D. J. Larson, *Atom Probe Tomography 2012*, Annu Rev Mater Res **42**, 1:31 (2012).
- [14] S. Offerman, N. van Dijk, J. Sietsma, S. Grigull, E. Lauridsen, L. Margulies, H. Poulsen, M. Rekveldt, and S. van der Zwaag, *Grain nucleation and growth during phase transformations*, Science **298**, 1003 (2002).
- [15] D. J. Jensen, S. E. Offerman, and J. Sietsma, *3DXRD Characterization and Modeling of Solid-State Transformation Process*, MRS Bulletin (2008).
- [16] J. Buffière, P. Cloetens, W. Ludwig, E. Maire, and L. Salvo, *In situ X-ray tomography studies of microstructural evolution combined with 3D modeling*, MRS Bull **33**, 611 (2008).
- [17] S. A. Saltykov, *Stereometric Metallography* (Metallurgizdat, Moscow, 1958), 2nd ed.
- [18] P. L. Goldsmith, *The calculation of true particle size distributions from the sizes observed in a thin slice*, British Journal of Applied Physics **18**, 813 (1967).
- [19] W. L. Nicholson and K. R. Merckx, *Unfolding Particle Size Distributions*, Technometrics **11**, 707 (1969).
- [20] H. Cruz-Orive, Luis M. and Hoppeler, O. Mathieu, and E. R. Weibel, *Stereological Analysis Of Anisotropic Structures Using Directional Statistics*, Journal of the Royal Statistical Society: Series C (Applied Statistics) **34**, 14 (1985).
- [21] B. van Es and A. Hoogendoorn, *Kernel estimation in Wicksell's corpuscle problem*, Biometrika **77**, 139 (1990).
- [22] P. Groeneboom and G. Jongbloed, *Isotonic Estimation and Rates of Convergence in Wicksell's Problem*, The Annals of Statistics **23**, 1518 (1995).

- [23] D. G. Jensen, *Estimation of the size distribution of spherical, disc-like or ellipsoidal particles in thin foil*, Journal of Physics D: Applied Physics **28**, 549 (1995).
- [24] S. Mase, *Stereological estimation of particle size distributions*, Advances in Applied Probability **27**, 350 (1995).
- [25] D. L. Sahagian and A. A. Proussevitch, *3D particle size distributions from 2D observations: stereology for natural applications*, Journal of Volcanology and geothermal research **84**, 173 (1998).
- [26] M. D. Thouless, B. J. Dalgleish, and A. G. Evans, *Determining the Shape of Cylindrical Second Phases by Two-dimensional Sectioning*, Materials Science and Engineering A **102**, 57 (1988).
- [27] M. Li, S. Ghosh, O. Richmond, H. Weiland, and T. Rouns, *Three dimensional characterization and modeling of particle reinforced metal matrix composites: part I Quantitative description of microstructural morphology*, Materials Science and Engineering A **A265**, 153 (1999).
- [28] M. D. Higgins, *Measurement of crystal size distributions*, American Mineralogist **85**, 1105 (2000).
- [29] D. Dierickx, B. Basu, J. Vleugels, and O. van der Biest, *Statistical extreme value modeling of particle size distributions: experimental grain size distribution type estimation and parameterization of sintered zirconia*, Materials Characterization **45**, 61 (2000).
- [30] S. Zhou, Y. Murakami, S. Beretta, and Y. Fukushima, *Experimental investigation on statistics of extremes for three-dimensional distribution of non-metallic inclusions*, Materials Science and Technology **18**, 1535 (2002).
- [31] J. Gegner, in *Proceedings of MMT-2006 conference* (Ariel, Israel, 2006), vol. 3, pp. 109–120.
- [32] S. J. Andersen, B. Holme, and C. D. Marioara, *Quantification of small, convex particles by TEM*, Ultramicroscopy **108**, 750 (2008).
- [33] J. Jeppsson, K. Mannesson, A. Borgenstam, and J. A. gren, *Inverse Saltykov analysis for particle-size distributions and their time evolution*, Acta Materialia **59**, 874 (2011).

- [34] B. Sen and M. Woodroffe, *Bootstrap confidence Intervals for Isotonic Estimators in a Stereological Problem*, Bernoulli **arXiv:math.PR/0000000** (2011).
- [35] H. M. Howe, *The Metallography of Steel and Cast Iron* (McGraw-Hill Book Company, 1916).
- [36] R. D. Knutsen, *Influence of compositional banding on grain anisotropy in 3CR12 steel*, Materials Science and Technology **8**, 621 (1992).
- [37] S. Thompson and P. Howell, *Factors Influencing Ferrite Pearlite Banding and Origin of Large Pearlite Nodules in a Hypoeutectoid Plate Steel*, Mater Sci Tech Ser **8**, 777 (1992).
- [38] F. Khalid, M. Farooque, A. ul Haq, and A. Q. Khan, *Role of ferrite/pearlite banded structure and segregation on mechanical properties of microalloyed hot rolled steel*, Materials Science and Technology **15**, 1209 (1999).
- [39] S. Offerman, N. van Dijk, M. Rekveldt, J. Sietsma, and S. van der Zwaag, *Ferrite/pearlite band formation in hot rolled medium carbon steel*, Mats. Sci. Tech. **18**, 297 (2002).
- [40] T. F. Majka, D. K. Matlock, and G. Krauss, *Development of Microstructural Banding in Low-Alloy Steel with Simulated Mn segregation*, Metallurgical and Materials Transactions A **33A**, 1627 (2002).
- [41] G. Krauss, *Solidification, Segregation, and Banding in Carbon and Alloy Steels*, Metallurgical and Materials Transactions B **34B**, 781 (2003).
- [42] A. Stauffer, D. Koss, and J. McKirgan, *Microstructural banding and failure of a stainless steel*, Metall Mater Trans A **35A**, 1317 (2004).
- [43] R. A. Grange, *Effect of Microstructural Banding in Steel*, Metallurgical Transactions **2**, 417 (1971).
- [44] R. G. Davies, *Influence of Martensite Composition and Content on the Properties of Dual Phase Steels*, Metallurgical Transactions A **9A**, 671 (1978).
- [45] A. R. Marder, *Deformation Characteristics of Dual-Phase Steels*, Metallurgical Transactions A **13A**, 85 (1982).

- [46] J. Komenda and R. Sandström, *Assessment of Pearlite Banding Using Automatic Image Analysis: Application to Hydrogen-Induced Cracking*, *Materials Characterization* **31**, 143 (1993).
- [47] J. Komenda and R. Sandström, *Automatic Assessment of a Two-Phase Structure in the Duplex Stainless-Steel SAF 2205*, *Materials Characterization* **31**, 155 (1993).
- [48] B. Hwang, H. Lee, Y. Kim, and S. Lee, *Analysis and prevention of side cracking phenomenon occurring during hot rolling of thick low-carbon steel plates*, *Mat Sci Eng A-Struct* **402**, 177 (2005).
- [49] M. Mazinani and W. J. Poole, *Effect of Martensite Plasticity on the Deformation Behavior of a Low-Carbon Dual-Phase Steel*, *Metallurgical and Materials Transactions A* **38A**, 328 (2007).
- [50] C. Gupta, J. Nagchaudhury, J. K. Chakravartty, and R. C. Prasad, *Cyclic stress-strain characteristics of two microalloyed steels*, *Mats. Sci. Tech.* **25**, 760 (2009).
- [51] C. C. Tasan, J. P. M. Hoefnagels, and M. G. D. Geers, *Microstructural banding effects clarified through micrographic digital image correlation*, *Scripta Materialia* **62**, 835 (2010).
- [52] P. E. J. Rivera-Díaz-Del-Castillo, J. Sietsma, and S. van der Zwaag, *A Model for Ferrite/Pearlite Band Formation and Prevention in Steels*, *Metallurgical and Materials Transactions A* **35A**, 425 (2004).
- [53] W. Xu, P. E. J. Rivera-Díaz-Del-Castillo, and S. van der Zwaag, *Ferrite/Pearlite Band Prevention in Dual Phase and TRIP Steels: Model Development*, *ISIJ International* **45**, 380 (2005).
- [54] A. From and R. Sandström, *Assessment of Banding in Steels by Using Advanced Image Analysis*, *Materials Characterization* **41**, 11 (1998).
- [55] ASTM, ed., *Annual Book of ASTM Standards* (ASTM, 2000), vol. 03.01 of *Metals-Mechanical Testing; Elevated and Low-Temperature Tests: Metallography*, chap. E 1268-99 Standard Practice for Assessing the Degree of Banding or Orientation of Microstructures (reapproved 2001, 2007), pp. 820–848.
- [56] J. Chmiela, D. Słota, and J. Szala, *Multiscale description of the inhomogeneity of multiphase materials*, *Materials Characterization* **60**, 1145 (2009).

- [57] B. Krebs, A. Hazotte, L. Germain, and Gouné, *Quantitative analysis of banded structures in dual-phase steels*, Image Analysis and stereology **29**, 85 (2010).
- [58] F. B. Pickering, *The Basis of Quantitative Metallography*, Institute of Metallurgical Technicians monograph no. 1 (Institution of Metallurgists, 1990).
- [59] J. Ohser and F. Mücklich, *Statistical Analysis of Microstructures in Materials Science* (John Wiley & Sons, Ltd, 2000).
- [60] T. L. Wolfson, W. H. Bender, and P. W. Voorhees, *The Morphology of High Volume Fraction Solid-Liquid Mixtures: An Application of Microstructural Tomography*, Acta Materialia **45**, 2279 (1997).
- [61] M. V. Kral and G. Spanos, *Three-dimensional analysis of proeutectoid cementite precipitates*, Acta Materialia **47**, 711 (1999).
- [62] W. S. Rasband, *ImageJ*, U.S. National Institutes of Health, Bethesda, Maryland, USA (1997-2009), URL <http://rsb.info.nih.gov/ij/>.
- [63] B. J. Thijsse and B. W. Rust, *Freestyle data fitting and global temperatures*, Computing in Science and Engineering **10**, 49 (2008).
- [64] T. W. Ridler and S. Calvard, *Picture Thresholding Using an Iterative Selection Method*, IEEE Transactions on Systems, Man, and Cybernetics **8**, 630 (1978).
- [65] L. G. Shapiro and G. Stockman, *Computer Vision* (Prentice Hall, 2002).
- [66] B. Schmid, J. Schindelin, A. Cardona, M. Longair, and M. Heisenberg, *A high-level 3D visualization API for Java and ImageJ*, BMC Bioinformatics **11**, 274 (2010).
- [67] S. D. Wicksell, *A Mathematical Study of a Biometric Problem*, Biometrika **17**, 84 (1925).
- [68] L. M. Cruz-Orive and E. R. Weibel, *Recent stereological methods for cell biology: a brief survey*, American Physiological Society **258**, L148 (1990).
- [69] B. W. Silverman, M. C. Jones, J. D. Wilson, and D. W. Nychka, *A Smoothed EM Approach to Indirect Estimation Problems, with Particular Reference to Stereology and Emission Tomography*, Journal of the Royal Statistical Society: Series B (Methodological) **52**, 271 (1990).

- [70] K. Miyamoto, *Research of Pattern Formation* (KTK Scientific Publishers, 1994), chap. 8.3 Particle Number and Sizes Estimated from Sections - A History of Stereology, pp. 507–516.
- [71] R. M. German, *The contiguity of Liquid Phase Sintered Microstructures*, Metallurgical Transactions A **16**, 1247 (1985).
- [72] B. Roebuck and E. G. Bennett, *Phase size distribution in WC/Co Hard-metal*, Metallography **19**, 27 (1986).
- [73] A. K. Giumelli, M. Militzer, and E. B. Hawbolt, *Analysis of the Austenite Grain Size Distribution in Plain Carbon Steels*, ISIJ International **39**, 271 (1999).
- [74] A. Tewari and A. M. Gokhale, *Estimation of three-dimensional grain size distribution from microstructural serial sections*, Materials Characterization **46**, 329 (2001).
- [75] J. Wosik, B. Dubiel, A. Kruk, H.-J. Penkalla, F. Schubert, and A. Czyska-Filemonowicz, *Stereological estimation of microstructural parameters of mickel-based superalloy Waspaloy using TME methods*, Materials Characterization **46**, 119 (2001).
- [76] Y. Sidor and F. Kovac, *Quantification of microstructure and evaluation of mechanical properties in non-oriented electrical steels*, Metalurgija **42**, 153 (2003).
- [77] M. Spiess and E. Spodarev, *Anisotropic Poisson Processes of Cylinders*, Methodology and Computing in Applied Probability **13**, 801 (2010).
- [78] R. L. Fullman, *Measurement of Particle Sizes in Opaque Bodies*, Transactions AIME (Journal of Metals) **197**, 447 (1953).
- [79] R. L. Fullman, *Measurement of Approximately Cylindrical Particles in Opaque Samples*, Transactions AIME (Journal of Metals) **197**, 1267 (1953).
- [80] R. B. S. Oakershott and S. F. Edwards, *On the stereology of ellipsoids and cylinders*, Physica A **189**, 208 (1992).
- [81] K. Mehnert, J. Ohser, and P. Klimanek, *Testing stereological methods for the estimation of spatial size distributions by means of computer-simulated grain structures*, Materials Science and Engineering A **A246**, 207 (1998).

- [82] I. Saxl, K. Sülleiová, and P. Ponížil, *Simulating Grain Size Estimation*, *Kovové Materiály* **39**, 396 (2001).
- [83] D. Anevski and P. Soulier, *Monotone spectral density estimation*, *The Annals of Statistics* **39**, 418 (2011).
- [84] P. Groeneboom and G. Jongbloed, *Generalized continuous isotonic regression*, *Statistics and Probability Letters* **80**, 248 (2011).
- [85] Y. S. Chow and H. Teicher, *Probability Theory, Independence, Interchangeability, Martingales*, *Spring Texts in Statistics* (Springer Verlag, 1988), 2nd ed.
- [86] T. Robertson, F. W. Wright, and R. L. Dykstra, *Order Restricted Statistical Inference*, *Wiley Series in Probability and Statistics* (John Wiley & Sons, Ltd, 1988).
- [87] M. R. Kosorok, *Introduction to Empirical Processes and Semiparametric Inference*, *Springer Series in Statistics* (Springer Verlag, 2008), 1st ed.
- [88] S. Bolte and P. Cordelières, *A guided tour into subcellular colocalization analysis in light microscopy*, *Journal of Microscopy* **224**, 213 (2006).
- [89] C. C. Taylor, *A new method for unfolding sphere size distributions*, *Journal of Microscopy* **132**, 57 (1983).
- [90] F. Aurenhammer, *Voronoi diagrams—a survey of a fundamental geometric data structure*, *ACM Computing Surveys (CSUR)* **23**, 405 (1991).
- [91] P. J. J. Kok, *Personal correspondence*, email (2013).
- [92] A. W. van der Vaart, *Asymptotic Statistics*, no. 3 in *Series in Statistical and Probabilistic Mathematics* (Cambridge Press, www.few.vu.nl/~bt.knapik/as/index.htm, 1998), lecture notes fall 2011 ed.

Curriculum Vitæ

Kimberly Sue McGarrity

Mar. 9, 1980 Born in St. Cloud, Minnesota, USA.

Education

- 1998–2002 Undergraduate in Physics & Spanish
Concordia College, Moorhead, Minnesota
- 2002 Study Abroad and Internship
Universidad de Las Americas, Mexico City, Mexico
- 2002–2004 Masters of Science
Michigan State University, East Lansing, Michigan
- 2009–2013 Ph.D. thesis *Stereological Estimation of Anisotropic
Microstructural Features*
Delft University of Technology, Delft
Promotor: Prof. dr. ir. G. Jongbloed
Promotor: Prof. dr. ir. J. Sietsma

List of Publications

5. G. Jongbloed, K. S. McGarrity, J. Sietsma *Smooth estimation of size distributions in an oriented cylinder model*, submitted
4. K. S. McGarrity, J. Sietsma, G. Jongbloed *Nonparametric Inference in a Stereological Model with Oriented Cylinders Applied to Dual Phase Steel*, submitted
3. K. S. McGarrity *A glimpse beneath the surface: modeling 3D material with 2D data*, MaCHazine **17** (2), 26 (2012).
2. K. S. McGarrity, J. Sietsma, G. Jongbloed *Characterisation and Quantification of Microstructural Banding in Dual Phase Steels Part II: A case study extending to 3D*, Materials Science and Technology **28** (8), 903 (2012).
1. K. S. McGarrity, J. Sietsma, G. Jongbloed *Characterisation and Quantification of Microstructural Banding in Dual Phase Steels Part I: A general 2D study*, Materials Science and Technology **28** (8), 903 (2012).

THE ROAD NOT TAKEN

*TWO roads diverged in a yellow wood,
And sorry I could not travel both
And be one traveler, long I stood
And looked down one as far as I could
To where it bent in the undergrowth;
THEN took the other, as just as fair,
And having perhaps the better claim,
Because it was grassy and wanted wear;
Though as for that the passing there
Had worn them really about the same,
AND both that morning equally lay
In leaves no step had trodden black.
Oh, I kept the first for another day!
Yet knowing how way leads on to way,
I doubted if I should ever come back.
I SHALL be telling this with a sigh
Somewhere ages and ages hence:
Two roads diverged in a wood, and I
I took the one less traveled by,
And that has made all the difference.*

– Robert Frost

Postscript: Reflections on a Journey

*But the plans I have made will not happen right away.
Slowly, steadily, surely the time approaches for the vision to be fulfilled.
If it seems slow do not despair, for these things will surely come to pass.
Just be patient! They will not be overdue a single day.*

Habakkuk 2:3 (TLB)

When I began this journey towards a PhD one third of my life ago I was told that earning my PhD is about nothing more than determination. Dr. Richard White, while I believed you when you said that to me, I could not have imagined what that would mean. This journey has taken me places I would never have imagined I would go. I rarely do things in the conventional way, and in this case, I took the long way around. I started out trying to be a physicist and ended up as a statistician and materials scientist. As I walked down this road, often not seeing any end in sight, there were many times I wanted to give up. There were many times I felt lost and hopeless. If it had not been for the support and encouragement of the wonderful people around me, I would have never been able to persevere.

First and foremost, I need to express my deepest gratitude to Geurt and Jilt. If you had not been willing to take a chance on me, I would certainly not be here and most likely I would not be finishing my PhD at all. As it is, I would not be finishing this PhD without all the support and guidance you both gave. I have learned much from each of you about your respective disciplines, neither of which were really mine when I started. Often, when there are multiple advisers on a project problems arise. There are scheduling conflicts, language barriers, strong wills and conflicting interests. With the two of you, none of these was ever a problem, and I know it is because both of you were committed to the success of the project. You were willing to learn the language of the other, and to accept the expertise of the other when in that domain. This, of course, made my life infinitely easier and I was able to learn much more because of it. Geurt, I need to thank you, in particular, for your boundless patience with me as I learned everything that a physicist

should, but does not know about mathematics. Thank you for all the time you invested, sitting for hours sometimes, to help me through this project. On top of all this, you and Jilt were incredibly supportive of me especially during this last year when Erin and I had to be apart. Thank you for making time to talk with me across the ocean, over a quarter of a day apart. You were willing to go further than I could have ever dared to ask and I cannot thank you enough. To say that I was extremely lucky to have you both as my advisers is an understatement, and I am not sure that there is a way to make that an overstatement. Heel hartelijk bedankt voor de afgelopen vier jaar!

Of course, nothing would ever get done without the fabulous support staff that we have. Cindy, Carl, Evelyn, Roniet, and Léonie (I would be remiss to not include Cathy and Lisa here) thank you for your dedication. Thank you for always being there to help us, for taking care of things and for being willing to go the extra mile. Everything always ran smoothly because of you. There are not enough ways to express my appreciation for all you do.

I also need to thank the wonderful people at Tata Steel for all the help and the useful discussions. I had the fortune of talking with and working around many intelligent and interesting people. Among them were many who had a direct impact on this project. Jan Wörmann, thank you for all the help you gave me when I first came to take the serial sectioned data. Karin de Moel, Koen Lammers and Piet Kok, thank you for all the help, important discussions and time that you gave to me and this project. I have learned quite a bit from all of you, especially about the industrial side of this project.

I am grateful to M2i and all the wonderful people that work so hard to make everything run so smoothly. I appreciate the opportunity M2i provided for me to work on a project that extended beyond the university to industry. It has been a privilege to work with such a dedicated organization. In particular, I want to say “Thank you” to Monica Reulink. Your enthusiasm is contagious; it is impossible to be unhappy in your presence. Thank you for caring about all of us, for taking the time to get to know us and for investing in us.

Next, I owe an inestimable debt of gratitude to my parents. You have always believed in me and supported me, regardless of whatever crazy ideas I tried. You have always been there, sharing your wisdom and knowledge. I may not have always recognized it as such in the moment, but know that now, and especially after being a pseudo-parent myself, I realize how much you sacrificed and how much you gave to me. Not the least of which was the freedom to try all these crazy things. I know it is sometimes difficult to have both Chad and I so far away, but I also know that you share in the joys and support us through the difficulties these experiences bring. I could have never made it to where I am without your unconditional love and support. I hope

that you know love you both very much, more than I can ever fully express.

George and Gail, I want to thank you for all the love and support you have given to Erin and me as a couple, especially with all your help when we moved to the Netherlands, and also to me as I moved towards finishing my PhD. Even though I am not your daughter, you have embraced me as such and thrown yourselves into forming our relationship. I am excited to have you back so close to us again! I love you both very much.

Jos Thijssen, thank you for making the effort to find a way for me to come to Delft along with Erin. I learned a lot by working with you. I would say it was from you that I learned what it meant to be a real scientist, how to really think about a problem and how to be critical of the results. I wrote my first article under your guidance and I believe the success I have had is in no small part because of your careful instruction.

Elena, Henri (and Aimo), Bora, Tungky, Joost, Vanessa and Chris, you have all be amazing friends throughout the last four years. Our paths are diverging now, but I hope this will not be the last steps we take together. Neil, Carol, Ana, Shannon, Jim, Connor and Jo, I am so glad to be coming back home to you all. I missed you.

Fateme, Catherine and Tammy you have been the truest friends I could have ever hoped to find. Thank you for your friendship and support over the various number of years I have been fortunate to have you in my life. In particular, Fateme, thank you for living with me this last year. I would not have survived without you.

Chad, I am glad that we are not only siblings but also friends. You are one of the most influential people in my life because you have essentially always been there. The oceans that separated us are not deep enough to exemplify my respect and love for you.

Erin, my love, I could have never finished this without you. You are the biggest reason I have not given up. You have been there cheering me on, having blazed the trail yourself. You are my cairn, my compass and my shelter. Even more than that, you are my constant travelling companion. You make the journey worth it.

The wonderful part of this peregrination has been meeting all the other travelers along the way. There are so many people who have come in to and out of my life. Some have gone on, some were left behind, and some remain traveling with me along this road, companions I do not want to be without. While there are far too many of you to name here, I hope that you understand I am grateful for your presence in my life, that my life is far better and richer for the steps we have taken, are taking and will take together along the way.

Kimberly Sue McGarrity

Delft, December 2013